INFORMATION TO USERS

This manuscript has been reproduced from the microfilm master. UMI films the text directly from the original or copy submitted. Thus, some thesis and dissertation copies are in typewriter face, while others may be from any type of computer printer.

The quality of this reproduction is dependent upon the quality of the copy submitted. Broken or indistinct print, colored or poor quality illustrations and photographs, print bleedthrough, substandard margins, and improper alignment can adversely affect reproduction.

In the unlikely event that the author did not send UMI a complete manuscript and there are missing pages, these will be noted. Also, if unauthorized copyright material had to be removed, a note will indicate the deletion.

Oversize materials (e.g., maps, drawings, charts) are reproduced by sectioning the original, beginning at the upper left-hand corner and continuing from left to right in equal sections with small overlaps.

Photographs included in the original manuscript have been reproduced xerographically in this copy. Higher quality 6" x 9" black and white photographic prints are available for any photographs or illustrations appearing in this copy for an additional charge. Contact UMI directly to order.

ProQuest Information and Learning
300 North Zeeb Road, Ann Arbor, MI 48106-1346 USA
800-521-0600

UMI®

EXPERIMENTAL AND ANALYTICAL STUDY OF A FRUSTUM CONFINING VESSEL

By

GABRIEL SEDRAN, Const. Eng., M. Eng.

A thesis
Submitted to the School of Graduate Studies
in Partial Fulfilment of the Requirements for
the Degree
Doctor of Philosophy

McMaster University

THE STUDY OF A
FRUSTUM CONFINING VESSEL

DOCTOR OF PHILOSOPHY (1999) McMaster University

(Civil Engineering) Hamilton, Ontario

TITLE: Experimental and Analytical Study of a Frustum Confining Vessel

AUTHOR: Gabriel Sedran, Const. Eng. (Universidad Tecnologica Nacional)
M.Eng. (McMaster University)

SUPERVISOR: Professor Dieter F.E. Stolle

NUMBER OF PAGES: xviii, 212

ABSTRACT

A Frustum Confining Vessel (FCV) was developed by McMaster University and Berminghammer Foundation Equipment Ltd., which provides an environment for the testing of reduced-scale piles (physical model). This vessel is intended to produce stress distributions within sand specimens, which resemble field conditions, however at a smaller geometric scale.

This thesis presents the findings of the experimental and analytical investigations conducted on the FCV device. A technique for measuring normal stresses in dry sand is developed, and the stresses and displacements measured at specific locations within the sand specimens are used to calibrate the finite element model. Finite element simulations are used to evaluate different aspects of the responses, which cannot be directly measured in the experiments.

The fundamentals of dimensional analysis are reviewed and a set of primitive variables for the pile-soil system is presented. Using the Buckingham-π theorem, a derived set of dimensionless groups is thereby proposed for the study of pile-soil interaction.

The scaling factors necessary for the extrapolation of results from model to prototype conditions are obtained via similarity analysis. It is suggested that the lack of gravity scaling in the FCV device does not introduce significant distortions in the physical model provided that stress distributions, particularly horizontal stresses, are properly controlled by FCV loading.

In relation to physical modeling of piles, a criterion for the acceptance of testing conditions is established, and the suitability of the current device is assessed in terms of the mentioned criterion. It is found that the current device does not completely meet the acceptance criteria. The improvement on testing condition is thereby sought by redesigning the vessel's shape. Alternative shapes for the vessel are investigated by means of finite element modeling. A redesigned shape, which offers optimal stress conditions for the purposes of physical modeling, is presented.

ACKNOWLEDGEMENTS

The author wishes to express his gratitude to the members of the supervisory committee Dr. A.N. Hrymak and Dr. R.H. Horvath for their valuable input during the completion of the thesis. The author would also like to express his gratitude for the help provided by Mr. P. Koudys during the experimental part of the work. Without his expertise and technical advice the author's tasks in the laboratory would had been much more harder and lengthy.

Modifications of the Frustum Confining Vessel were promptly completed by Berminghammer Foundation Equipment Ltd, thanks to the help provided by Mr. P. Bermingham and Mr. K. Vandehei. Their effort is greatly appreciated.

The present study was financially supported by McMaster University through the Department of Civil Engineering. This support is hereby acknowledged.

Finally, the author would like to thank the supervisor of the thesis. By far the greatest burden in supporting the completion of the thesis was borne by Dr. D.F.E. Stolle, who encouraged the author through every stage of the study. The author is profoundly indebted to him.

TABLE OF CONTENT

Chapter 1 INTRODUCTION

Chapter 2 EXPERIMENTAL TESTING SERIES

Chapter 3 MATHEMATICAL MODELING

Chapter 4 NUMERICAL ANALYSES

LIST OF FIGURES

LIST OF TABLES & BOXES

LIST OF SYMBOLS

Chapter 2: Experimental Testing Series

A	Hardening parameter for plasticity
A_0, A_{corr}	Initial and corrected cross sectional areas of triaxial samples
B	Skempton pore pressure parameter
C_U	Coefficient of uniformity
C_C	Coefficient of curvature
d_0	Initial diameter of a triaxial sample
D_{10}, D_{50}	Effective and mean grain sizes
D_R	Relative density of sand
e	Void ratio
e_{max}, e_{min}	Maximum and minimum void ratios
e_0, e_{ssl}	Void ratios at initial conditions and at the steady state line
E	Elastic modulus of the soil
E_{ref}	Reference elastic modulus
G_S	Specific gravity
h_0	Initial height in a triaxial sample
H	Height of FCV sand specimens
k	Stress ratio

K	Bulk modulus
p'	Effective confining stress
Q	Axial load in triaxial tests
q	Deviatoric stress
u_w	Backpressure in triaxial tests
V_0	Initial volume of triaxial samples
z	Depth coordinate at the centerline of FCV sand specimens
z'	Depth coordinate along the inclined wall of FCV sand specimens
$\Delta\sigma'_1$	Deviatoric stress change in triaxial tests
ΔV	Net volume change in triaxial tests
Δy	Vertical or axial displacement in triaxial tests
ε_{axial}	Average axial strain in triaxial tests
ε_q, $\varepsilon_q^{\,e}$, $\varepsilon_q^{\,p}$	Total, elastic, and plastic deviatoric strains
ε_{vol}	Average volumetric strain in triaxial tests
ϕ_{cs}, ϕ_f	Friction angles at critical state and at failure conditions
γ_{dry}	Dry unit weight of sand in triaxial samples
η_f	Stress ratio at failure
η_{cs}	Stress ratio at critical state conditions
ψ	Angle of dilatancy
Ψ	State parameter
σ'_0	Initial confining stress in triaxial tests
σ'_3, σ_3	Effective and total confining stresses in triaxial tests

$\sigma_{vertical}$, σ_{radial}	Vertical and radial stresses in FCV sand specimens
σ'_n	Normal stress acting at the inclined wall of a sand FCV specimens
ν	Poisson's ratio

Chapter 3: Mathematical Modeling

$\boldsymbol{a}$	Nodal displacement vector
$\boldsymbol{b}$	Body forces vector
$\boldsymbol{B}$	Strain-displacement matrix
$\boldsymbol{C}$	Compliance matrix
$\boldsymbol{D}$	Constitutive matrix
$\boldsymbol{D}_L$, $\boldsymbol{D}_P$	Constitutive matrices in the local and principal stress systems
E_1, E_2, E_3	Elastic moduli in the principal stress directions (sand)
f	Yield function
$g_1(\theta), g_2(\theta)$	Failure and plastic potential envelopes in the π-plane
G_{13}	Shear modulus in the plane containing the major and minor principal stresses
G_{ref}	Reference shear modulus
H_p, H_e	Plastic and elastic hardening parameters
$\boldsymbol{K}_T$	Tangential stiffness matrix
$\boldsymbol{L}$, $\boldsymbol{L}_\sigma$	Differential operators for strains and stresses
$\boldsymbol{N}$	Matrix of the interpolation functions
r, z, θ	Cylindrical coordinates
$\boldsymbol{R}$	Residual load vector

$\boldsymbol{t}$	Surface traction vector
$\boldsymbol{T}$, $\boldsymbol{T}_d$	Stress and strain transformation matrices
$\boldsymbol{T}_S$	Surface traction force vector
$\boldsymbol{u}_s$	Prescribed displacement vector, applied at the boundary S
α	Rotation angle from the local stress system to the principal stress system
Δ	Determinant of the compliance matrix
$\Delta\boldsymbol{a}$	Nodal displacement increment vector
$\Delta\boldsymbol{D}$	Incremental elastic constitutive matrix
$\Delta\varepsilon, \Delta\varepsilon^e, \Delta\varepsilon^p$	Total, elastic, and plastic strain increment vectors
$\Delta\boldsymbol{f}$	Incremental external force vector
$\Delta\lambda$	Plastic scale factor
$\Delta\sigma$	Stress increment vector
ε	Total strain vector
ε_q^p	Plastic deviatoric strain invariant
ν_1 , ν_2 , ν_3	Poisson's ratios in the principal stress directions
Ψ	Plastic potential
σ	Stress vector
σ_P , σ_L	Principal and local stress vectors
σ_1 , σ_2 , σ_3	Major, intermediate, and minor principal stresses
σ_m	Mean stress invariant
$\bar{\sigma}$	Deviatoric stress invariant
$\bar{\sigma}_c$	Confining stress

Chapter 4: Numerical Analyses

C_1, C_2	Vessel parameters accounting for shape and loading conditions
$E_{\max}$, $E_{\min}$	Maximum and minimum elastic moduli for the soil
E_{st}	Elastic modulus for the steel
f_{int}	Unit friction acting at the FCV walls
p_{app}, $p_{\max}$	Applied basal pressure and maximum applied pressure in the FCV device
$\tan\delta$	Steel-sand friction coefficient
u, v	Horizontal and vertical displacements
V^{U}, V^{NU}	Uniform and non-uniform variables for statistical analysis
Δ, $\varepsilon\%$	Mean absolute and relative dispersion norms
β	Wall inclination
ϕ_f	Peak friction angle
σ'_n	Normal stresses acting at the FCV walls
σ_r, σ_z, σ_{zr}	Radial, vertical, and shear stresses within the FCV device
σ_h, σ_v, σ_{vh}	Radial, vertical, and shear stresses in field conditions

Chapter 5: Physical Modeling

A_{OCR}	Overconsolidation parameter
d	Pile diameter
E_p	Pile elastic modulus
E_s	Reference elastic modulus of sand
f_s	Unit skin friction at the pile-soil interface

f_{s_p}, f_{s_m}	Unit skin frictions for prototype and model systems
$F(e)$	Void ratio parameter
$\boldsymbol{F}_p(t_p)$, $\boldsymbol{F}_m(t_m)$	Force vectors for prototype and model systems
g	Gravity acceleration
L_p	Embedded length of the pile
$\boldsymbol{M}_p$, $\boldsymbol{C}_p$, $\boldsymbol{K}_p$	Mass, damping and stiffness matrices for prototype system
$\boldsymbol{M}_m$, $\boldsymbol{C}_m$, $\boldsymbol{K}_m$	Mass, damping and stiffness matrices for model system
$\sin\phi_f$	Friction coefficient at failure
$\sin\phi_{cs}$	Friction coefficient at critical state
$\tan\delta$	Friction coefficient at the pile-soil interface
T_L	Loading interval
w	Axial displacement of pile at a given depth
λ	Generic scaling factor
ν_s	Poisson's ratio for the sand

Chapter 1

INTRODUCTION

1.1 Reduced Scale Testing of Pile Foundations

The reduced scale testing of deep foundations has been recognized as a valuable tool to study the load-displacement characteristics of pile-soil systems. An important advantage of using physical modeling of deep foundation systems is that comprehensive testing programs can be carried out at reasonable cost. Also, from an experimental point of view, physical modeling allows one to isolate the effects of a particular variable by varying one parameter at the time in a series of otherwise identical models. These advantages are not usually available when testing prototypes or full-scale models.

Traditional techniques employed in the physical modeling of pile foundations make use of either centrifuge devices, or the so-called 1g devices. Even though centrifuge testing can be more economical than full scale load tests, such testing programs may still be expensive. Furthermore, centrifuge devices are not readily available everywhere (Franke & Muth, 1985). Reduced scale testing in 1g environments is inexpensive and specimens can be easily set up. However, an important limitation of 1g devices is that they are unable to properly scale gravity, thereby introducing model distortions. These distortions prevent direct extrapolation of test results to large-scale situations, which in turn limits the usefulness of the tests. There is also a less conventional approach to physical modeling, known as the increased stress-gradient method, where effective stresses can be increased by means of a downward gradient of the pore fluid; see, e.g. Altaee & Fellenius (1994). The use of this method, however, is limited to specific applications and soil types, and will not be considered in this study.

With regards to pile foundations, physical modeling offers the possibility of studying both theoretical and practical aspects including, for instance: load transfer mechanisms; pile group interaction (Hassini & Woods 1989); failure mechanisms for short and long piles; influence of rate of loading for piles in clay (Horvath 1995); influence of pile installation on the bearing capacity (Steenfelt et al. 1981, and Craig 1985); dynamic responses of piles; influence of overconsolidation ratio on pile bearing capacity (Foray et al. 1998); influence of pile rigidity in the mobilization of skin friction in cohesionless soils; limiting skin friction ; dependency of soil strength parameters on the levels of confinement (Craig & Sabagh 1994); and pile response to lateral loading (Scott 1981, and Agaiby et al. 1996).

This thesis investigates the suitability of using a confining vessel, namely the Frustum Confining Vessel (FCV), as a reduced scale environment to study different aspects related to the behaviour of piles.

1.2 The FCV Device

Given the wide range of applications for which physical modeling is used in the study of pile foundations, it is considered desirable to explore the feasibility of using possibly better and more efficient environments than those already available for the testing of model piles. In this regard, the Frustum Confining Vessel (FCV) has been developed by McMaster University and Berminghammer Foundation Corporation as an alternative device for reduced scale modeling of pile foundations; see e.g. Horvath (1995), and Horvath & Stolle (1996). This vessel, which is to be further described in Chapter 2, offers the possibility of controlling the net levels of confinement in sand specimens while producing approximately constant stress gradients with depth, similar in nature to those encountered in field conditions, as shown in Figure 1.1. These characteristics are important as they enforce necessary requirements for the extrapolation of model behaviour to full-scale behaviour.

Owing to its simplicity, the FCV device presents a practical and economical alternative to centrifuge devices. In addition, the most critical gravity related limitations associated with $1g$ devices can be eliminated when model piles are tested in the FCV device.

1.3 Objectives of the Thesis

The motivation for the reported research was to gain a clear understanding of the fundamental concepts involved in the physical modeling of piles when using the FCV device. Towards that end, an experimental testing program, complemented with mathematical modeling, was undertaken to acquire data and to produce knowledge relevant to the problem. To limit the scope of this thesis, the focus of this investigation was placed on the FCV device and its ability to produce appropriate stress distributions in the sand specimens. The actual testing of model piles was not considered in the present work.

The objectives of the study were to:

(i) further develop the FCV testing technique;

(ii) optimize the shape of the vessel to improve the stress field within sand specimens;

(iii) establish guidelines for the extrapolation of results from tests on FCV models to prototype or full scale conditions; and

(iv) evaluate soil constitutive relations and working assumptions using the responses of sand specimens tested under FCV loading conditions as benchmark problems.

1.4 Outline of the Thesis

Chapter 2 describes the experiments carried out on sand specimens using the existing FCV device, as well as the series of drained triaxial compression tests on saturated sand samples, which was used to determine elasto-plastic material properties of the sand utilized in the testing program. Details of the instrumentation and stress measuring techniques used during the laboratory experiments are also discussed.

Chapter 3 formally defines the boundary-valued problems representing the loading of sand specimens under triaxial and FCV testing conditions. A mathematical model is introduced in terms of the differential equations of equilibrium, the kinematic equations, the constitutive relations, completed with the necessary boundary conditions. The principle of virtual work is used to set up the system of equations necessary for the finite element discretization.

Since most parts of FCV specimens are affected by increasing levels of confinement, the stress-strain relations of the sand within the vessel are basically dominated by quasi-elastic behaviour. For that reason, the emphasis of Chapter 3 is placed on the description of elastic deformations. Nevertheless, plasticity is also included in the description of material behaviour in order to accommodate slippage and distortion of the sand specimens close to the FCV wall.

Chapter 4 describes the numerical analyses of triaxial and FCV tests and the results are compared with the measured responses. The purpose of these simulations is a) to calibrate the numerical model; b) to obtain adequate model parameters; and c) to evaluate different aspects of the responses that can not be directly measured in the experiments. Simulations are also conducted for sand specimens with random variation of initial density in order to evaluate the effects of inhomogeneous material properties on the measured responses. The calibrated numerical model is then used to study the effect of the vessel geometry on the stress field produced within the FCV specimens. This exercise is utilized to optimize the shape of the vessel.

Chapter 5 introduces the theoretical and technical aspects necessary for the definition of the similarity conditions between the model and prototype problems. The advantages and limitations of centrifuge, 1*g*, and FCV devices are compared for the case of the physical modeling of pile foundations. The numerical simulation of a dynamic load test on a single pile is used as a benchmark problem to verify the scaling relations and to validate thereby the suitability of the FCV device for physical modeling of piles. The dimensional analysis of the pile foundation problem is also addressed in this chapter, and a set of dimensionless π-groups suitable for the problem is proposed.

Chapter 6 completes the thesis by summarizing the findings and conclusions of the present research. Recommendations for the use of an optimal FCV device for physical modeling of pile foundations are also issued in the closure of this chapter.

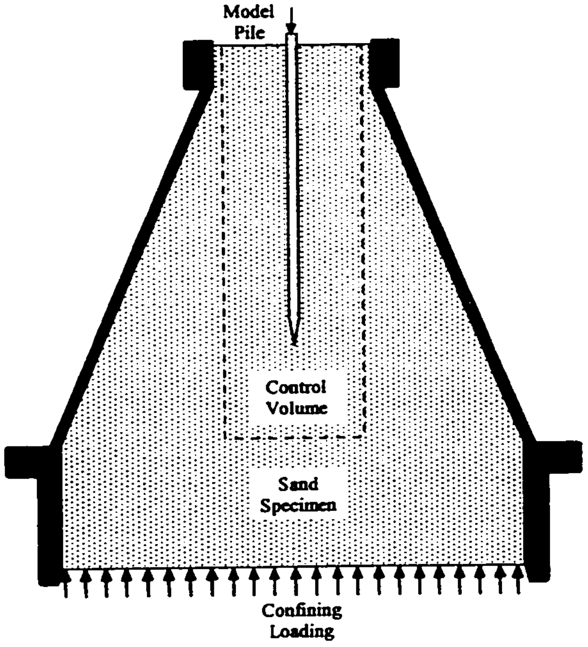

(a) Schematic of the Frustum Confining Vessel.

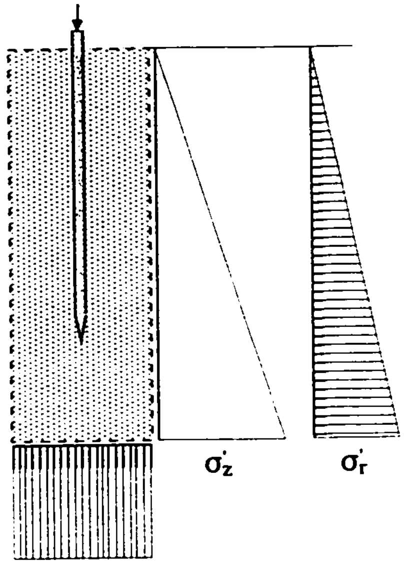

(b) Idealized distribution of stresses within a control volume. The purpose of the device is to produce within the control volume a state of stresses similar to those typically found in the field, while controlling the stress levels simultaneously.

Figure 1.1. The Frustum Confining Vessel (FCV)

Chapter 2

EXPERIMENTAL TESTING SERIES

2.1 Laboratory Investigation

The experiments conducted in this study addressed the behaviour of sand under triaxial and FCV testing conditions. To begin with, a series of triaxial tests were completed with the specific objective of evaluating material properties of the Ottawa sand employed in the experiments. The triaxial responses observed in the experiments were treated as boundary-valued problems when calibrating the numerical models developed in this thesis.

A series of preliminary FCV tests was conducted to develop procedures for the preparation and testing of FCV specimens. Different types of loading were also evaluated in relation to the reproducibility of the tests. In general, the measured responses were analyzed in terms of displacements and normal stresses measured at different locations within the specimens. The measuring techniques utilized in the FCV testing series are briefly discussed in this chapter.

As previously mentioned, the objective of this FCV testing series was to investigate the response of the sand specimens within FCV, in particular, the distribution of stresses under basal loading. The testing of reduced-scale pile models was not directly considered.

2.1.1 Definitions

The behaviour of soils under any given loading can be analyzed in terms of the following factors: (a) state of the soil mass, (b) intrinsic properties, and (c) behavioral properties of the soil (Been et al. 1991). To avoid any confusion or ambiguity related to the interpretation of these concepts, we need to define the corresponding terminology.

The state conditions of any soil are considered to be uniquely defined by void ratio, confining stresses, and deviatoric stresses, or $(e, p', q)^1$, respectively. These are known as state parameters. An additional state parameter, Ψ may be introduced to describe the state of a soil, given by (e_i, p_i', q_i), relative to a reference state represented by the steady state line (e_{ssl}, p_i', q_i), for instance, $\Psi_i = e_i - e_{ssl}$ (see, e.i., Been & Jefferies, 1985).

Intrinsic material properties are directly related to the particulate nature of a soil, including specific gravity, characteristics of the grain-size distributions, mineral composition, and grain shape. Intrinsic properties are, by definition, independent of the state conditions.

Behavioral properties, on the other hand, depend on the stress paths associated with a given type of testing device. Behavioral properties also depend on initial state conditions and intrinsic properties. For the case of the triaxial testing series, behavioral properties include peak deviatoric stresses and volumetric changes. In essence, the behavioral properties are considered test-dependent.

While intrinsic and behavioral properties of a soil are strictly physical properties, the properties required to describe soil behavior within a mathematical context depend on the

---

[1] We limit our considerations to quasi-static and isothermal loading conditions.

assumptions adopted by the any given constitutive model. These properties are typically referred to as constitutive parameters.

2.1.2 Intrinsic Material Properties

All triaxial samples and FCV specimens tested during the experimental work were made with the same batch of Ottawa C-109 sand. The physical characteristics of this sand, evaluated in the laboratory, are given by:

- the specific gravity: $G_S = 2.65$;
- estimated values of the limiting void ratios: $e_{min} = 0.48$ and $e_{max} = 0.71$;
- the grain size distribution, characterized by the coefficient of uniformity $C_U = 1.91$ and by the coefficient of curvature $C_C = 1.21$. The effective and mean grain sizes are $D_{10} = 0.22\ mm$ and $D_{50} = 0.39\ mm$, respectively.

Since the same batch of sand was used in every FCV test, it was considered that the possibility of particle crushing might have resulted in some changes on the grain size distribution, thereby affecting material properties. However, based on comparisons of grain-size analyses conducted on the new untested sand and on the FCV-tested sand, little difference in the grain-size distribution was observed, suggesting that particle crushing in FCV testing was limited and need not be considered as an important factor in any analysis of responses.

2.2 Triaxial Testing

Samples of Ottawa sand were tested under triaxial compression to study the behavioral properties, including

- shear strength characteristics under drained conditions,
- characteristics of volumetric changes under testing conditions,
- sensitivity of sand behaviour to different initial confining stresses, and
- sensitivity of sand behaviour to different values of initial void ratio.

The triaxial series consisted of over 20 consolidated-drained compression tests on saturated samples of Ottawa sand, carried out using five different levels of effective confinement, namely σ_3' equal to 50, 100, 200, 500, and 1050 *kPa*. A minimum of three samples were tested for each confining level. Only the results from five typical tests, designated here as TT50, TT100, TT200, TT500 and TT1050, are described in the discussion. The observed results are illustrated in terms of the strength and volumetric characteristics of the Ottawa sand. With regard to the density of the samples and the levels of confinement, these triaxial tests were intended to be conducted under state conditions similar to those expected to occur in the sand under FCV testing conditions.

2.2.1 Behavioral Properties

(i) Testing Procedures. The nominal dimensions of the triaxial samples were 75 *mm* in height by 35 *mm* in diameter. All samples were prepared by pluviation of saturated sand into a rubber membrane, which was stretched by a split cylindrical mold filled with deaerated water; see, for example, Kenneth et al. (1967) and Bishop & Henkel (1962). During the formation of the samples, no tamping was used, however, vibration was applied to the pedestal for a controlled period of time. Once the membrane was sealed at the ends with o-rings, the samples were initially consolidated by applying a vacuum equivalent to an effective confining pressure no higher than 50 *kPa*. At this stage and prior to the final consolidation, the diameter and height of the sample were measured. The diameter d_0 was obtained by averaging the measurements taken at the top, middle, and bottom sections of the sample using a caliper with a resolution of 0.01 *mm*. At each section two measurements were taken 90° apart. The height of a sample was determined with a dial gauge (0.01 *mm* resolution), i.e., using the dummy sample method, and averaging the readings from three locations, 120° apart. The height h_0 was then taken as the average of the three readings.

With the triaxial cell in place and with the instrumentation readily activated, each sample was isotropically consolidated to the specified effective confinement. It is considered that all samples within this triaxial series were tested in a normally consolidated state. Backpressure ranging from 20 to 40 *kPa* was applied to all samples. Values of the Skempton's B parameter higher than 0.94 were ensured prior to proceed to the axial loading stage. Deviatoric loading was applied using a displacement-controlled loading mode at a rate of 0.15 *mm/min*.

(ii) Measurements. The applied load Q and axial displacements Δy were recorded by means of a load cell and an LVDT (linear variable displacement transducer), respectively. Cell pressure σ_3 and pore water pressure u_w, were monitored through pressure transducers. Net volumetric changes ΔV were measured by means of a differential pressure transducer connected to the drainage lines. The time was also recorded in order to keep track on the rate of axial displacement. The soil mechanics sign convention is adopted in this chapter for the description of the experimental results; i.e., compressive stresses and strains are positive.

(iii) Results. The responses measured from the samples tested at five different levels of confinement are presented in terms of the following plots:

- Deviatoric stress q versus axial strain ε_{axial}, shown Figure 2.1(a),

where the average axial strain was calculated with

$$\varepsilon_{axial} = \frac{\Delta y}{h_0} \quad , \tag{2.1}$$

the deviatoric stress is given by

$$q = \Delta\sigma'_1 = \frac{Q}{A_{corr}} \quad , \tag{2.2}$$

with A_{corr} as the corrected cross-sectional area of the sample, and $\Delta\sigma'_1$ as the deviatoric stress increase.

- Volumetric strain ε_{vol} versus deviatoric strain ε_{axial}, shown in Figure 2.1(b).

The average volumetric strain was calculated with

$$\varepsilon_{vol} = \frac{\Delta V}{V_0} \quad , \tag{2.3}$$

with ΔV being the measured net volume change, and V_0 as the initial volume of the sample measured prior to the final consolidation stage of the triaxial test. For all five levels of confinement the specimens initially showed a small amount of volume compression followed by a marked volume dilation, normally observed in medium-dense to dense samples; see e.g., Kenneth et al. (1967), Bishop et al. (1962), and Kolymbas et al. (1990).

- Effective stress path q versus p', illustrated in Figure 2.2(a).

The effective confining stress was evaluated with

$$p' = \frac{\Delta\sigma'_1}{3} + \sigma'_3 \quad . \tag{2.4}$$

The Mohr-Coulomb failure envelope was defined by the locus of stress points (q, p') corresponding to the peak deviatoric stress $(q_{\max})$.

- Normalized deviatoric stress q/p' versus axial strain ε_{axial}, shown in Figure 2.2(b).

The stress ratio at failure, $\eta_f = q_{\max}/p'$, showed a slight decrease for increasing levels of confinement.

(iv) Some Errors and Corrections. The corrected cross-sectional area used in equation (2.2) is defined by

$$A_{corr} = A_0 \, \frac{(1 - \varepsilon_{vol})}{(1 - \varepsilon_{axial})} \quad . \tag{2.5}$$

In this expression it was assumed that the deformed specimen had the shape of a cylinder, where in reality the deformed specimen takes the shape of a barrel, Bowles (1986). The consequences of this simplifying assumption are that axial stresses are slightly overestimated at the mid-height of the sample. This error, however, is small and may be safely neglected.

It should also be mentioned that a sample's initial area was calculated with the net diameter, that is, the measured diameter minus two times the membrane thickness. Omitting this correction on the diameter would lead to low estimations of density.

Based on evidence presented by Bishop and Henkel (1962), systematic errors introduced by means of membrane penetration are small when compared with the other sources of error. Been et al. (1990), on the other hand, suggest that membrane penetration introduces significant errors in the case of drained tests where, for instance, the amount membrane penetration is directly related to changes on the effective confinement. In the present study, the error associated with membrane penetration is indirectly corrected by considering the amount of volume changes occurring during the final stage of consolidation, as it will be explained in the next section.

A source of error related to the measurement of the applied axial load is due to the friction developed between the loading rod and the bushing. This error is not considered to be strictly systematic as the friction along the bushing was observed to change from test to test. This type of error can be minimized or eliminated by offsetting the axial load applied to the sample with respect to the sitting or bedding load.

2.2.2 State Properties

(i) Void Ratios. As mentioned previously, the volume of the triaxial samples were measured under vacuum prior to the final consolidation, and the oven-dried weight was taken after the samples were tested. With this data, the calculation of void ratios is straightforward. Table 2.1 summarizes the void ratios and related properties for the five samples, TT50 to

TT1050, prior to the final consolidation stage.

Table 2.1 Densities of tested samples prior to final consolidation $G_s = 2.65$

Test Designation	Effective Confinement σ'_0 [kPa]	Dry Unit Weight γ_{dry} [kN/m^3]	Void Ratio e_0	Relative Density D_R [%]
TT50	25	16.93	0.535	76.2
TT100	40	17.03	0.526	79.9
TT200	40	17.06	0.523	81.1
TT500	40	17.05	0.524	80.7
TT1050	60	17.16	0.515	85.0

The values of e_0 for this stage, however, were not the initial void ratios corresponding to the beginning of the shear stage. During the final consolidation stage of the triaxial tests the density of the specimens increased according to the consolidation characteristics of the Ottawa sand; see i.e., Been et al. (1991), Kolymbas et al. (1990), and Schanz & Vermeer (1996).

The consolidation properties of the Ottawa sand, which are shown in Figure 2.3, were determined from a series of isotropic consolidation tests. Six triaxial samples were prepared at different states of density and isotropically loaded, for example with $p' = \sigma'_3$. Once the consolidation properties were known, it was possible to estimate the initial void ratio at the beginning of the shearing stage of a triaxial test by using the following expression:

$$e_i \approx e_0 - M \ln\left(\frac{\sigma'_3}{\sigma'_0}\right) , \qquad (2.6)$$

where $M = 0.00638$ indicates the slope of the consolidation curves in a semi-logarithmic plot of e versus p'. The calculated values of initial void ratio corresponding to the shearing stage are shown in Table 2.2.

Table 2.2 Densities of tested samples after final consolidation

Test Designation	Effective Confinement σ'_3 [*kPa*]	Dry Unit Weight γ_{dry} [kN/m^3]	Void Ratio $e_{initial}$	Relative Density D_R [%]
TT50	50	16.97	0.531	77.8
TT100	100	17.10	0.520	82.6
TT200	200	17.18	0.513	85.7
TT500	500	17.23	0.508	87.8
TT1050	1050	17.36	0.497	92.6

A maximum difference of 17 % in values of relative density was observed between tests TT50 and TT1050. The preparation of the triaxial samples with equal or similar void ratios e_i at the end of the final consolidation stage is known to be a difficult task, and particularly so when the samples are tested at varying levels of confinement. Techniques for preparing samples of similar initial void ratios were considered to be beyond the scope of the present study. Notwithstanding, it is recognized from the results presented in Section 2.2.1, Paragraph *iii*, that is not possible to isolate the effects of increasing confinement from the effects associated with different initial void ratio on the responses. Since the influence of varying void ratios could not be eliminated nor isolated, it was necessary to determine, in a qualitative manner, the severity of the effects of density variations on the triaxial responses.

The influence of initial void ratios in the behaviour of sandy soils has been widely reported in the literature: see, i.e., Wood (1990), and Altaee & Fellenius (1994). As explained by Garga & Zhang (1997) the strength and volumetric characteristics of a sandy soil strongly depend on how far the soil's void ratio is from that corresponding to the steady-state line. Owing to the fact that steady-state lines for sands are quite flat within a normal range of stresses [2], small variations in the void ratio usually leads to substantial changes in the behaviour of the sands. This relation between variations in void ratio and soil properties is best described by the state parameter Ψ, as it is explained by Been & Jefferies (1985); also see Atkinson & Bransby (1978).

With regard to the present series of triaxial tests, Figure 2.4 shows the responses observed from three triaxial samples which had slightly different initial void ratios. These samples were tested under the same effective confinement of 500 *kPa*. It is evident from these plots that the responses of the tested Ottawa sand were highly sensitive to small changes in initial void ratio. In approximate percentages, a 4 % increase in the initial void ratio resulted in a 15 % decrease in peak stress and a 56 % decrease in the rate of dilation.

These differences are strictly applicable for Ottawa sand and for the particular level of confinement applied to these three samples. Because of the response sensitivity to variation of void ratio, it is clear that care must be exercised in the interpretation of these experimental results.

(ii) Stress and Strain Homogeneity. A typical shortcoming of triaxial tests is the frictional constraints imposed by the end platens. Experimental evidence presented by Kolymbas & Wu (1990), and Garga & Zhang (1997), clearly show that, even in the case that platens are carefully designed to eliminate or reduce platen friction, end effects can not be neglected. As explained by Kolymbas et al. (1989), constrained end effects are responsible for

---

[2] Steady-state lines are represented by variations of void ratio versus confining stress, usually plotted using semi-logarithmic scales.

remarkable inhomogeneous deformations occurring even at early stages of a triaxial test.

Since the present triaxial testing series was conducted using porous stones at the platens, the tested samples were fully constrained at the platens. Even though stress conditions in the mid-section of the samples were relatively uniform, close to the frictional platens non-uniform stresses were to be expected as a result of restraint on the sample's deformations. Furthermore, strong deviations between actual and average stresses were expected. The numerical simulations, discussed in Chapter 4, show the severity of the deviations.

The volumetric strains calculated as the ratio between the amount of drained pore water and the initial volume of the sample are also average values. With regard to undrained triaxial tests, an overall zero volumetric strain does not guarantee that volumetric strains were zero locally, (Garga et al., 1997). For instance, while those portions of a sample near to the platens may be contracting, the central portion of a sample, the portion that actually fails, might be dilating with the result that the net or overall volume change is equal to zero.

The general conclusion is that results from the present triaxial series have inherited shortcomings, and that the interpretation of the results can not completely take into account the actual behavioral properties of the soil samples.

2.2.3 Constitutive Parameters

According to the mathematical description of stress-strain responses in triaxial and FCV testing, to be considered in Chapter 3, the basic constitutive law requires five parameters to describe the behaviour of the sand samples. These constitutive parameters depend on the assumptions implicitly adopted by the constitutive law, and may not necessarily take into consideration every aspect of the observed phenomena. In the mathematical description, elastic deformations depend on the elastic modulus E and Poisson's ratio ν, while the plastic behaviour is characterized by the stress ratio at failure η_f, the stress ratio at critical state conditions η_{cs}, and the hardening parameter A.

(i) Elastic Modulus E. Values of the elastic modulus E can be measured from the initial slope of the q versus ε_{axial} curve as shown in Figure 2.5(a). It is observed in Figure 2.1(a) that the initial slope of these curves increases proportionally with the confinement. This relation between the elastic modulus and confining stress, plotted in Figure 2.6, can be approximated with the following expression:

$$E = E_{ref} \left\{ 1 - e^{-r} \right\} \quad , \tag{2.7}$$

where the exponent r is given by

$$r = \frac{1000}{E_{ref}} \sigma'_3 \quad . \tag{2.8}$$

The stress dependency of the elastic modulus may also be represented by other empirical relations, for instance, the power law proposed by Janbu (1963)

$$E = K \, p_a \left\{ \frac{\sigma'_3}{p_a} \right\}^n \quad , \tag{2.9}$$

where K and n are material properties and p_a is a reference pressure; see, i.e., Kolymbas et al.(1990). This power law, however, can not properly reproduce the stress dependency of the elastic moduli observed in the present triaxial series. As shown in Figure 2.6, while the experimental data points exhibit a tendency to flatten out for confining stresses above 600 *kPa*, the power law predicts ever increasing values of E. Within the range of confining stresses considered in the present study, the exponential function in equation (2.7) provided a reasonable fit for the experimental data.

(ii) **Poisson's Ratio** ν. Values of the Poisson's ratio were estimated from the volumetric change characteristics of the responses, as shown the plot of ε_{vol} versus ε_{axial} in Figure 2.5(c). Owing to the fact that volume changes measured at early stages of the tests were not very accurate, as volume contraction tended to be very small, some uncertainty in the estimation of ν was to be expected.

(iii) **Stress Ratio at Failure** η_f. This parameter, which corresponded to the peak deviatoric stresses, represents failure conditions of the sand, as shown in Figure 2.5(b). By inspection of the experimental results plotted in Figure 2.2(b), it is observed that values of η_f exhibit a tendency to decrease as the levels of confinement increase (Wood 1990). Based on the experimental data, the relation between the values of the stress ratio at failure and confining stresses was observed to be very subtle, and it was not possible to establish an accurate empirical relationship.

(iv) **Stress Ratio at Critical State Conditions** η_{cs}. This parameter corresponds to the rate of zero volume change, and is defined in terms of the friction angle ϕ_{cs} at the critical state

$$\eta_{cs} = \frac{6 \sin\phi_{cs}}{3 - \sin\phi_{cs}} \quad . \tag{2.10}$$

For granular materials with an angle of dilatancy ψ, the following expression relates the friction angles at failure ϕ_f and at critical state ϕ_{cs} with ψ,

$$\phi_{cs} = \phi_f - \psi \quad . \tag{2.11}$$

Based on the experimental data and as shown in Figure 2.5(c) Schanz & Vermeer (1996) proposed the following expression

$$\tan\alpha = \frac{2 \sin\psi}{1 - \sin\psi} = \frac{\Delta\varepsilon_{vol}}{\Delta\varepsilon_{axial}} \quad . \tag{2.12}$$

Equation (2.12) was used to determine values of ψ from the experimental data shown in Figures 2.1(b) and 2.5(c). Suitable values of η_{cs} were then calculated , using equations (2.10) and (2.11). It is also possible to determine the values of η_{cs} with the following approximation

$$\eta_{cs} \cong \eta_f - \tan\alpha \quad . \tag{2.13}$$

In practice, the values of η_{cs} were calculated using equation (2.13) with tanα measured from Figure 2.1(b). It should be noted that in the case where volumetric and deviatoric strains were uniformly distributed within the sample, the estimation of η_{cs} would be accurate. However, as stated previously, the volumetric changes measured during the tests represented net volume changes, concluding that the calculation of η_{cs} provided approximate estimates.

(v) Plasticity Parameter A. The parameter A accounts for the rate of plastic deformations, thereby controlling whether the type of failure is of a ductile or brittle nature. The hardening rule is expressed in terms of the parameters A and η_f

$$\eta = \eta_f \frac{\varepsilon_q^{\,p}}{\left(\varepsilon_q^{\,p} + A\right)} \quad , \tag{2.14}$$

where $\varepsilon_q^{\,p}$ is the plastic deviatoric strain, which is related to the total strain by

$$\varepsilon_q^{\,p} = \varepsilon_q - \varepsilon_q^{\,e} \quad , \tag{2.15}$$

with $\varepsilon_q^{\,e}$, the elastic component of the deviatoric stresses, calculated as

$$\varepsilon_q^{\,e} = -\frac{q}{E} + \frac{1}{3}\frac{p'}{K} \quad , \tag{2.16}$$

see Wood (1990). The elastic modulus E and the bulk modulus K are determined from the experimental data shown in Figures 2.5(a) and 2.5(e), respectively. The total deviatoric strain ε_q in equation (2.15) is calculated from the measured axial and volumetric deformations as

$$\varepsilon_q = -\,\varepsilon_{axial} + \frac{1}{3}\varepsilon_{vol} = -\frac{\Delta y}{y} + \frac{1}{3}\frac{\Delta V}{V} \tag{2.17}.$$

Substituting equations (2.16) and (2.17) in (2.15), the plastic deviatoric strains can be calculated from experimental data using

$$\varepsilon_q^{\,p} = -\left(\varepsilon_{axial} - \frac{q}{E}\right) + \frac{1}{3}\left(\varepsilon_{vol} - \frac{p'}{K}\right) \quad . \tag{2.18}$$

The determination of parameter A using experimental data from the triaxial compression tests may now be attempted with the help of equations (2.14) and (2.18). Since equation (2.14) is a typical saturation-growth-rate function, a linearization of the hardening rule is obtained by plotting the experimental data in terms of $1/\eta$ versus $1/\varepsilon_q^{\,p}$, as shown in Figure 2.5(d). The plastic parameter A may then be measured from the slope of the linearized hardening rule. As may be seen from equation (2.18) and from Figure 2.5(d), the determination of parameter A requires the previous determination of E, K, and η_f. Ductile failure conditions are represented by high values of A, for instance 0.00100 or higher, while for brittle failure the values of A are 0.00020 or lower.

(vi) Summary of Constitutive Parameters. Table 2.3 lists the constitutive parameters as they were determined from each test of the triaxial series.

Table 2.3 **(a) Summary of Constitutive Parameters**

Test Designation	σ_3' [kPa]	E [MPa]	ν	η_f	η_{cs}	A
TT50	50	31	0.37	1.53	0.98	0.00043
TT100	100	62	0.36	1.49	0.96	0.00046
TT200	200	110	0.38	1.49	1.07	0.00083
TT500	500	203	0.36	1.39	1.07	0.00049
TT1050	1050	232	0.37	1.45	1.10	0.00065

Table 2.3 (b) Associated Constitutive Parameters

Test Designation	σ_3' [*kPa*]	K [*MPa*]	$\tan\alpha$	ϕ_f [*degrees*]	ϕ_{cs} [*degrees*]	ψ [*degrees*]
TT50	50	41	0.55	37.6	24.9	12.7
TT100	100	54	0.53	36.6	24.4	12.2
TT200	200	71	0.41	36.6	27.0	9.6
TT500	500	102	0.32	34.4	27.0	7.4
TT1050	1050	290	0.35	35.7	27.7	8.0

In this Table 2.3, it is observed that values of the plasticity parameters η_f, η_{cs} and A showed some dependency on the levels of confinement, but to a much lesser degree when compared with the stress-dependency of the elastic moduli. The values of Poisson's ratio ν do not shown any significant dependency of the level of confinement. It is possible that the experimental data was not sufficiently accurate to detect a stress-dependency. The topic of constitutive parameters will be further discussed, from a mathematical viewpoint, in Chapters 3 and 4.

2.3 FCV Testing Procedures

The initial experiments involving the FCV were used to establish appropriate preparation and loading procedures for FCV specimens. These experiments were primarily concern with the development of testing techniques that could reproduce specific aspects in the response of FCV specimens.

Two loading configurations were used throughout the FCV testing program. The uniform displacement configuration of the FCV device, shown in Figure 2.7(a), was the first one available for experimentation. At a latter stage of the experimental study, the original device was modified by replacing the piston with a membrane in order to apply a uniform pressure at the bottom of the specimens. The principles of operation for each configuration can be readily seen in the figure. In its existing form, the device can be easily converted from one configuration to the other. The frustum vessel itself is made of steel and its general dimensions are shown in Figure 2.7(c).

2.3.1 Preparation of FCV Sand Specimens

FCV specimens were prepared by pouring dry Ottawa sand through a funnel into the vessel. The bulk or average density of a specimen was controlled by varying the compaction effort. With respect to the imparted effort, five levels of compaction were considered.

(i) **No Compaction.** In this approach, the dry sand was poured into the vessel with no compaction.

(ii) **Low Compaction.** Specimens were compacted by blows of a rubber mallet to the sides of the vessel until the metal plate, placed on top of the specimen, become aligned with a reference line. Since the volume of the vessel does not change and the same amount of sand was used in all tests, the bulk density of the specimens could be accurately calculated.

(iii) **Medium Compaction**. In this case, the specimens were compacted by prodding the sand with a vibratory rod prior to the placement of the metal plate. After vibration was completed, the top metal plate was placed and brought to the reference line by means of applying blows with a rubber mallet to the side of the vessel.

(iv) **High Compaction.** In this procedure the specimens were compacted by layers, using a circular tapper, which consisted of a plate of 75 *mm* in diameter attached to a rod. Each lift was about 50 *mm* thick.

(v) **Cyclic Compaction.** In this procedure, the specimens were subjected to series of load-unload cycles after having been prepared using the medium compaction procedure. At the end of each cycle, all LVDT sensors were reset.

The average values of bulk unit weight, initial void ratio, and relative density, typically produced by each compaction procedure are listed in Table 2.4.

Table 2.4 **Bulk Density** $G_s = 2.65$

Compaction Procedure	Dry Unit Weight γ_{dry} [kN/m^3]	Initial Void Ratio $e_{initial}$	Relative Density D_R [%]
No Compaction	16.2	0.60	46
Low Compaction	16.5	0.57	58
Medium Compaction	16.8	0.55	69
High Compaction	17.2	0.50	83
Cyclic Compaction	>17.0	<0.53	>76

2.3.2 Loading Procedures

In terms of the rate of loading, three loading procedures were considered. The first procedure consisted of applying a monotonically increasing load. The second procedure used a cyclic load of constant peak amplitude, and the third procedure used cyclic loads of linearly increasing peak amplitude. The load histories for the three procedures are illustrated in Figures 2.8(a), (b), and (c), respectively. Although Figure 2.8 only shows loading procedures using the piston loading, these procedures have also being applied to FCV specimens tested under the uniform pressure configurations (membrane loading).

In the case of the uniform displacement configuration, the hydraulic actuator was capable of delivering a maximum peak load of 195 *kN*. In the case of membrane loading, the peak pressure was limited to 650 *kPa*

With regard to the uniform displacement configuration, two LVDT's were attached at diametrically opposed locations on the piston to measure bottom displacements. These measurements clearly indicated the tilting of the piston during loading. The tilting was observed to be greatest for the case of low density specimens.

2.3.3 Reproducibility of FCV Tests

For any testing device, the capability of reproducing responses for any specific type of condition is an essential requirement that must be satisfied. The successful development of the FCV testing device, therefore, depended on its ability to produce repeatable specimen responses for various testing conditions.

The repeatability of a given test was established by comparing the load-displacement characteristics observed from several identical tests. The assumption was made that if similar preparation and loading procedures were used, then, the responses could be considered reproducible only if they exhibit similar load-displacement characteristics.

From the test results, it became evident that specimens with loose to medium densities tended to show signs of localized collapse or break with sudden jumps in unpredictable displacement patterns, while tests on dense specimens showed clearly a repeatable response. It was therefore concluded that only higher density specimens were suitable for FCV testing.

It was also observed that specimen behaviour showed a slight dependency on the rate of loading. For instance, the behaviour of specimens with similar densities appeared to be stiffer in the case of a quickly applied load than for the case of a slowly applied load. This dependency on the rate of loading was observed to rapidly diminish at lower rates of loading. Specifically, when loading periods were longer than 400 seconds, the rate-dependency was observed to be negligible

Based on repeatability considerations, the No Compaction and Low Compaction procedures, as well as loading periods shorter than 400 seconds were considered not to be appropriate testing procedures, and therefore were not used in subsequent testing. The preparation of specimens with Cyclic Compaction was also discarded since it was believed that cyclic loading tended to densify specimens in a highly non-uniform manner.

Figure 2.9 exhibits the characteristics of test reproducibility for specimens prepared with the Medium Compaction method and for the three loading procedures shown in Figure 2.8. In this FCV testing series, at least four tests were carried out for each loading procedure. The small amount of scattering exhibited in these Figures 2.9 (a)-(c), clearly indicates that reproducibility of responses was feasible when using the uniform displacement configuration. It should be noted, however, that repeatability of load-displacement aspects of the responses may not directly imply that local stress-strain conditions were also reproduced. As it will be shown through numerical simulations, it is possible to have two tested specimens with similar load-displacement characteristics, while the corresponding stress distributions are different.

2.4 Measurement of Displacements on FCV Tests

The objective of the third testing series was to measure displacements within FCV specimens, with the purpose of observing patterns of displacements inside the specimens.

2.4.1 Procedures

The measurement of internal displacements was conducted by placing telltales inside FCV specimens. The telltales were made with a circular plastic plates[3] attached to thin flexible steel rod that was connected on the free end to LVDT sensors located outside the vessel. As an intrusive measurement technique, telltales introduce some distortions in the response of a specimen, and because of this, measured displacements in FCV tests provided only approximate estimations of free-field displacements. The distortions were reduced by covering the connecting rods with small tubing to prevent friction along the shaft of the telltale.

A mapping of the displacement field was completed by measuring displacements at 15 different positions within FCV specimens. To avoid the crowding of telltales inside a particular specimen, each mapping test was conducted with only three telltales at a time, and several specimens had to be tested to complete the mapping of displacements. The main assumption was that these measurements were taken from a series of reproducible tests. To ensure the applicability of this assumption, the load and displacement at the piston were monitored for every test of the series. The specimens were prepared with the medium compaction procedure and tested under the one cycle-ramp loading. Differential displacements due to the tilting of

---

[3] The plates are 24 *mm* in diameter and 0.6 *mm* thick.

the piston were observed to be less than 0.3 *mm* for an average piston displacement of 2.5 *mm*.

2.4.2 Displacement Fields

Figure 2.10 shows the displacement observed at three elevations and at three loading stages, namely at 100, 150, and 195 *kN*. The diagrams indicate the approximate direction and magnitude of the displacements at 15 different positions within FCV specimens. Owing to the errors associated with the intrusive measurements and scattering from test to test, it is acknowledged that the displacements shown in Figure 2.10 are representative of approximate deformations occurring in the specimens. Nevertheless, a consistent pattern of displacements can be observed, and it is clear that these aspects of the deformation can not be easily inferred with non-intrusive measurements; i.e., measurements at the surface.

The displacements measured at the top, bottom and at the wall were used to compare responses produced by the piston and membrane configurations. The responses at various locations are shown in Figure 2.11(a) for the case of uniform displacements, and (b) uniform loading configurations. A common problem associated to testing of FCV specimens with the piston loading was the occurrence of sudden jumps, as seen in Figure 2.11(a) at about 150 *kN* load level. In addition, it was observed that the jumps occurred at any stage of loading, in a unpredictable manner. With respect to Figure 2.11(a), it may also be observed that the amount of jumping was more severe in the upper part than at the bottom and at the mid-height of the wall, suggesting that a brittle type of stick-slip failure may have been occurring close to the top. Although jumps were also observed during tests with membrane loading, these were rare and rather small. Another disadvantage of piston loading was the tilting of the piston, which was observed to increase as the loading progressed, as is shown in Figure 2.11(a).

2.4.3 Observations on Measured Displacements

From the third testing series, measured displacements provided the following information:

- The displacement measured along the wall indicated the order of magnitude of the relative sliding between the specimen and the wall.
- Using the uniform displacement configuration, tilting of the piston was observed. The tilting effect decreased in the case of specimens prepared with medium to high initial densities. In addition, piston loading often produced unpredictable jumps. Once a jump occurred, the test was considered to have ended.
- In terms of measured displacements, tests were satisfactorily reproduced for both loading configurations, concluding that repeatability is attainable.
- Based on the measured displacement volume changes corresponding to changes in density were inferred. For instance, approximate increases in density of 2.6, 0.7, and 1.0% were estimated for the lower, middle, and upper portions, respectively.

The observed displacement field indicated that responses of FCV specimens tested under the uniform displacement configuration were not as simple as intuition might suggest. Owing to the peculiar patterns of deformation, the decision was made to measure stresses directly inside FCV specimens.

2.5 Measurement of Stresses in FCV Tests

The objectives of the fourth testing series were to measure stresses within FCV sand specimens, and to assess the effect of loading configuration on stress distribution. The stresses were measured at three specific locations within the specimens, namely: along the centerline; along the inclined walls; and at the bottom of the vessel.

For the case of the uniform pressure configuration, two types of rubber membranes were considered. One membrane was made with a stiff rubber pad 7 *mm* thick and reinforced with two inner layers of fabric material. The second type of membrane was cut out of a thin pad of soft rubber 2.5 *mm* thick with no reinforcement. Identical tests were conducted, measuring displacements and stresses. It was observed that the FCV specimen responses using the thick and thin membranes were very similar. Since the soft rubber membrane was likely to have less membrane effect than the reinforced one, it was concluded that, technically, the soft rubber membrane would be the best choice for the uniform loading configuration. In order to limit the magnitude of the displacements at the bottom, and therefore minimize the effects of membrane action on the stresses, the sand specimens were prepared with the High Compaction procedure, i.e. compaction by layers, with values of relative density D_R about 83%. Tests with dense specimens had an additional advantage of improving conditions for test reproducibility.

The measurement of stresses within FCV specimens was performed by two approaches. In one approach the stresses were measured by means of either force sensing resistors (FSR®) or the capacitive stress sensors (CSS). The description of these sensors and their ability to measure stresses in sand is presented in Appendix A. The second, but less direct, approach to the measurement of stresses consisted of cone penetration probing in FCV specimens along the centerline. The penetration probe was instrumented with a load cell on its tip in order to measure tip resistance.

During this testing series, LVDTs were used, in order to measure displacements at the bottom and the top of the specimens. Once again, the purpose of measuring top and bottom displacements was to monitor test reproducibility.

2.5.1 Stresses along the Centerline

(i) Stress Distributions Estimated with Force Sensing Resistors. FSR sensors were used to estimate vertical and radial stress distribution along the centerline. In the first test, for instance, eight sensors were placed in horizontal position along the centerline while in the second test the sensors were placed in vertical position at approximately the same elevation as in the previous test, in order to measure axial and radial stresses, respectively. These measurements were then used for the calculation of values of the stress ratio, $k = \sigma_{radial} / \sigma_{vertical}$. The loading procedure consisted of an increasing load from 0 to 600 *kPa* for the membrane loading, and from 0 to 190 *kN* for the piston loading.

Figures 2.12(a) and (b) show the variation of vertical and radial stresses at the centerline for the case of membrane loading. Figure 2.12(c) shows the approximate variation for values of the stress ratio *k*. The figure illustrates the distribution of stresses at three stages of the loading, that is, for 100, 300, and 500 *kPa* of pressure applied to the membrane. Similar measurement of stresses, shown in Figure 2.13, was carried out for the case of the uniform displacement configuration , however, at stress levels corresponding to 16, 48, and 80 *kN* load applied to the piston. The stresses were then normalized with respect to the applied load and shown in Figure 2.14 and 2.15 for the cases of membrane and piston loading, respectively.

Although measured stress levels varied from one loading mode to the other, the stress distributions are somewhat similar. A common feature in the vertical and radial stress distributions is that stresses along the centerline increase steadily from the top down to bottom of the vessel, exhibiting values of the stress ratio *k* which evolve during loading.

The value of the stress ratio is initially approximately equal to one. In the case of membrane loading, the values of *k* increase with loading for the upper part of the vessel and decrease for the lower part. In the case of the piston loading, the values of *k* tends to increase along the entire centerline. From these results, it may be observed that the two loading procedures produced values of the stress ratio above one, particularly in the upper part of the vessel.

Regarding the accuracy of stress measurements using Force Sensing Resistors, each sensor was observed to have a certain amount of scatter. As discussed in Appendix A, the amount of dispersion for each sensor was evaluated from a series of calibration tests. These tests provided average calibration curves that were used to process the data acquired from the FCV tests into stress measurements. The uncertainty associated with the readings for each sensor is shown in Figures 2.16 and 2.17, for the membrane and piston loading, respectively.

(ii) Stress distributions via a Capacitive Stress Transducer. Figure 2.18 illustrates the stresses measured along the centerline with a capacitive stress sensor. The vertical and radial stresses, and values of the stress ratio are shown in plots (a), (b), and (c), respectively. These stresses were measured from specimens tested with piston loading. The specimens were prepared using vibration rather than compaction by layers, and the loading period for this test series was 100 seconds. Owing to differences in density and loading period, the stresses measured with the capacitive sensor cannot be directly compared with those stresses measured with the FSR sensors. However, it may be seen that the trends in the radial and vertical stress distributions are similar to those of Figure 2.13. It should be noted that the stress data points shown in Figure 2.18 were taken from 14 separate tests. Considering possible small differences in density distributions among the tested specimens, some scattering of stress measurements should be expected. In general, the stresses measured with the capacitive stress sensor were helpful to confirm the patterns of stress distributions along the centerline.

(iii) Cone Penetration Probing. Cone Penetration Probing was conducted in FCV specimens tested under the piston loading. The results from cone penetration probing along the centerline, as shown in Figure 2.19, indicated that the distribution of tip resistance values resembled the pattern of stress distribution observed for the distribution of radial stress, shown in Figures 2.12 and 2.13. Although under field conditions it may be possible to correlate horizontal stresses from values of tip resistance, see i.e., Robertson & Campanella (1983); Sully & Campanella (1991); and Konrad (1997), problems associated with the close boundaries of the FCV device were believed to affect stress-tip resistance correlations. Experimental evidence of cone penetration tests in calibration chambers presented by Houlsby & Hitchman (1988), and Schnaid & Houlsby (1991) indicated that cone penetration readings are influenced by nearby boundaries as well as by horizontal stress levels. Furthermore, cone penetrometer readings from calibration chambers may not be directly correlated to free-field stresses. Owing to the close boundary effects, no attempt was made in the present analysis to compare stress levels with values of tip resistance. However, it is worthwhile to note that these two very different measurement procedures, passive stress transducers and active probing, provided similar trends for stresses and resistance, respectively.

2.5.2 Stresses at the Inclined Wall

Normal stresses acting along the inclined wall were measured with the force sensing resistors for both piston and the membrane loading conditions. The sensors were placed along the inclined wall of the vessel with a 10 to 15 *mm* separation from the metal surface. The reason for placing the sensors away from the wall was to avoid as much as possible the distortion and bending of the sensor pads due to the shear stresses developing close to the wall.

For the case of the membrane loading, Figure 2.20 shows (a) the measured normal stresses, and (b) the normalized stresses acting along the wall at different stages of loading; namely, at 100, 300, and 500 *kPa* pressure applied to the loading membrane. The plots illustrate how the normal stress distributions evolve with loading. It is observed that normal stresses had a clear trend to increase with respect to the normalized depth z'/H, where z' refers to the distance measured in the direction of the inclined wall. Figure 2.20(c) exhibits the values of the uncertainties associated to the reading of stresses with force sensing resistors.

For specimens tested with piston loading, Figure 2.21 shows (a) the normal stresses and (b) the normalized stress distributions acting at the wall, with the uncertainty bars being show in plot (c) for the normalized stresses corresponding to a load applied to the piston of 500 *kPa*. The stress peak observed at the bottom may be attributed to stress concentrations. It is conjectured that anomalies related to the stress concentration or high stress gradients were responsible for the occurrence of the jumps, typically observed in specimens tested with piston loading. Based on intuition and on the patterns of measured stresses, it is believed that soil arching and zones of stress concentration develop as shown in Figure 2.22.

2.5.3 Stresses at the Bottom

Vertical stresses at the bottom of FCV sand specimens were measured by placing the force sensing resistors horizontally about 30 *mm* above the plate or the membrane. At least two specimens were tested for each loading configuration. Figure 2.23(a) illustrates a plan view of the bottom of the vessel showing the approximate position of the eight force sensing resistors. The vertical stresses measured at peak loading conditions, with their corresponding estimated variation, are summarized in Figure 2.23(b) for the case of the specimens tested with membrane loading. The stress measurements merely confirmed the uniformity of the stress distributions acting on the bottom for membrane loading. The vertical stresses measured in specimens tested with piston loading, indicated that the vertical stresses were significantly lower in the inner region than in the outer region, as is presented in Figure 2.23(c).

2.6 Concluding Remarks on FCV Testing

Based on the experimental information presented in the previous sections the following conclusions may be drawn:

- Regarding test reproducibility and the preparation of specimens, it is concluded that compaction by layer results in dense specimens which are more appropriate than those specimens formed by vibration.

- The application of cyclic loading increased the density of the specimens. The resulting density distributions within a specimen are believed to be non-uniform, as the soil in the bottom part of the specimens is subjected to confining stresses that are higher than those in the upper part of the specimens.
- Stress measurements provided useful information on the patterns of stress distributions. Estimated uncertainties associated with the force sensing resistors indicated that measured values of normal stresses would not be as accurate as desired. However, the observed stress distributions are considered to be representative of the stress conditions in FCV specimens.
- The stress distributions along the centerline obtained with membrane loading were smoother than in the case of piston loading.
- The maximum bottom displacement observed in the specimens tested with the membrane loading was less than 3 *mm* at full applied pressure of 650 *kPa*. For this magnitude of displacement pulling effects on the membrane can be considered negligible.
- Stress measurements on specimens tested with the piston loading exhibited concentration of high stresses where the piston meets the bottom of the vessel.
- The experimental data obtained from the tests is not sufficient to properly identify the formation of soil arching. However, the occurrence of jumps suggested that some kind of arching mechanism may be breaking in a brittle manner at the time of a jump.
- The inferred values of the stress ratio k were substantially higher than typical k values in the field, regardless of the loading configurations.

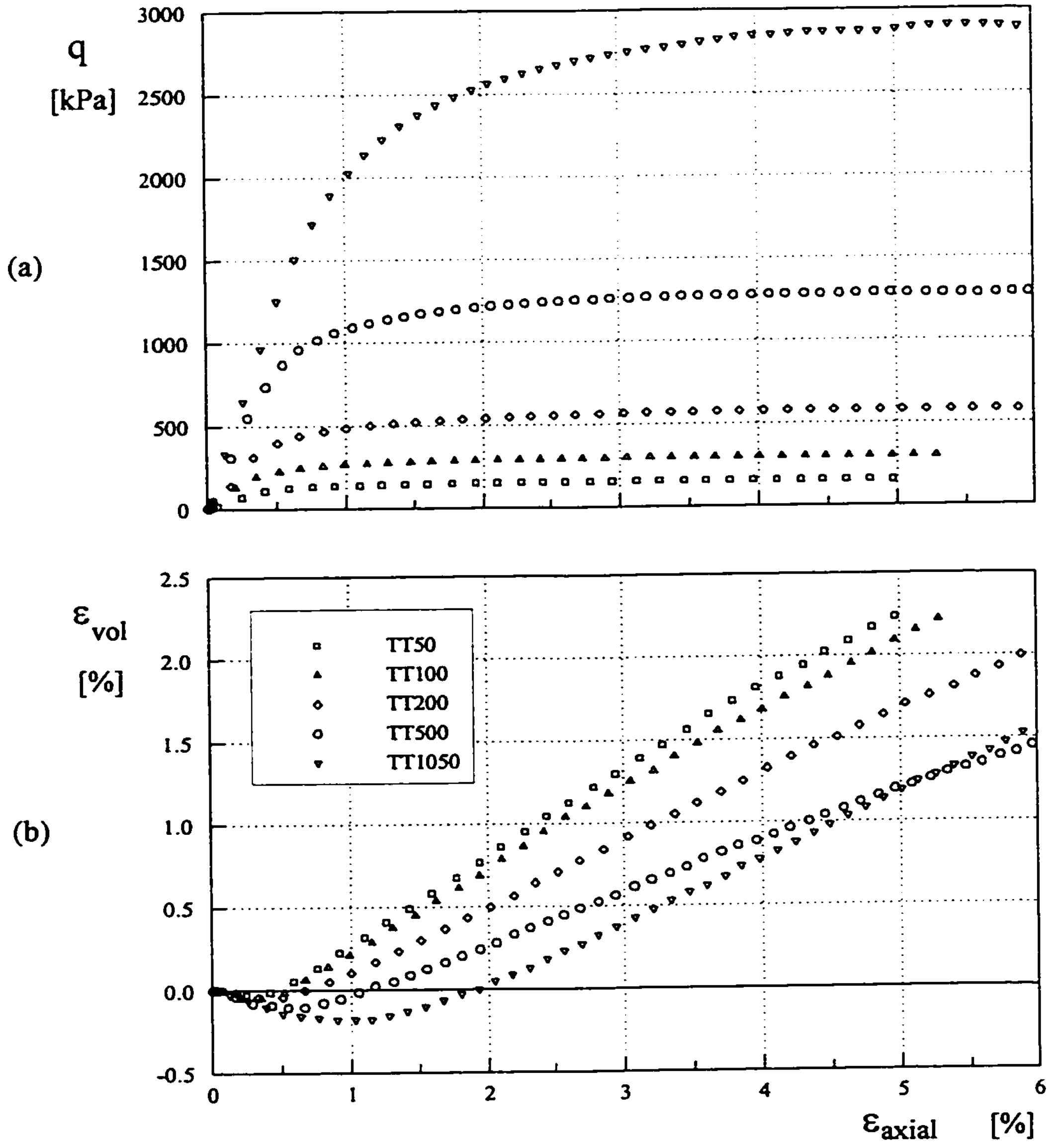

Typical results from a series of drained triaxial compression tests conducted on saturated samples of Ottawa sand and tested at five different levels of effective confinement: (a) deviatoric stresses versus axial strains, and (b) volumetric strains versus axial strains.

Figure 2.1. Triaxial test results: Experimental data

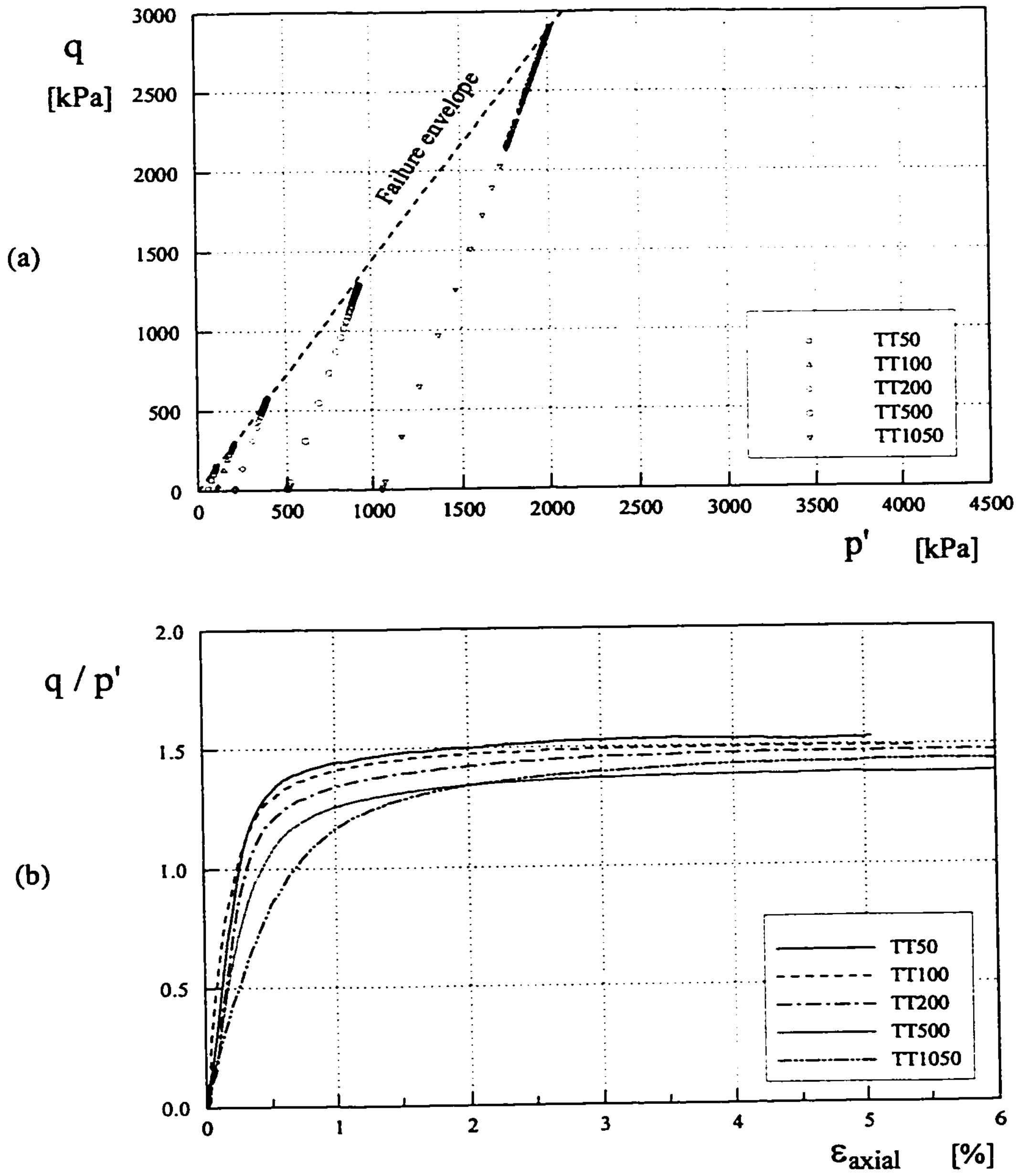

(a) Effective stress paths, and (b) normalized deviatoric stresses versus axial strains

Figure 2.2. Triaxial test results: Normalized data

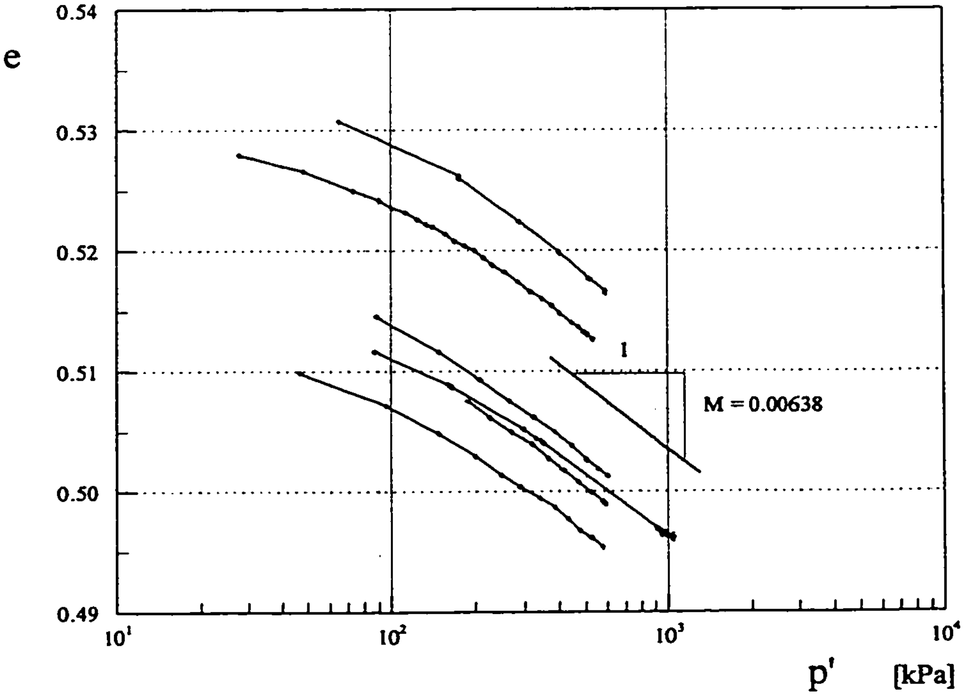

Consolidation characteristics of the Ottawa sand obtained from the isotropic consolidation of six triaxial samples. The samples were prepared with different values of initial void ratio. The slopes of the consolidation curves are approximately equal.

Figure 2.3. Consolidation test results

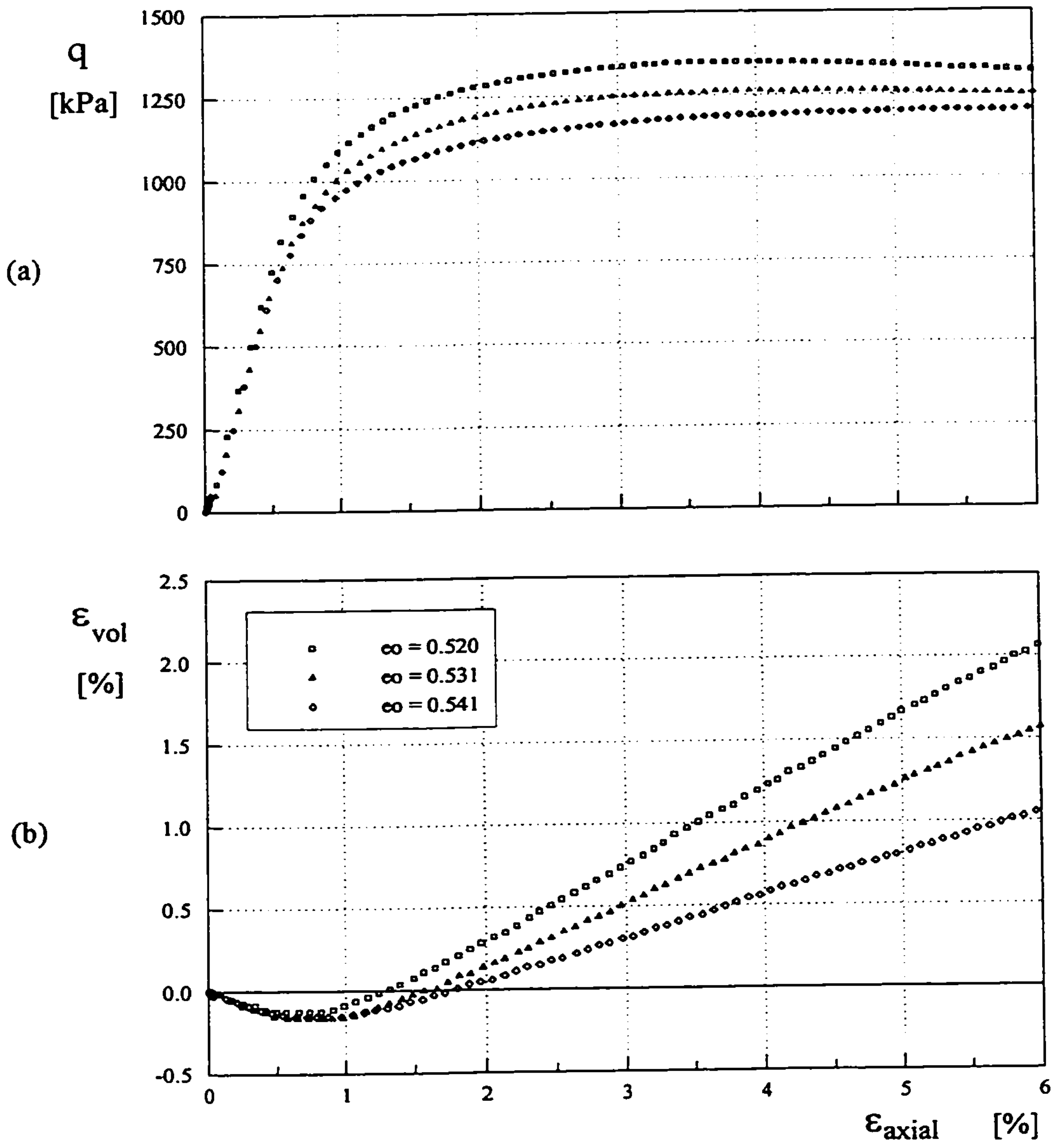

Differences in triaxial responses due to variations of initial void ratio. The three samples were tested under the same effective confinement of $\sigma_3' = 500$ *kPa*: (a) deviatoric stresses versus axial strains, and (b) volumetric strains versus axial strains.

Figure 2.4. Effect of different initial void ratios

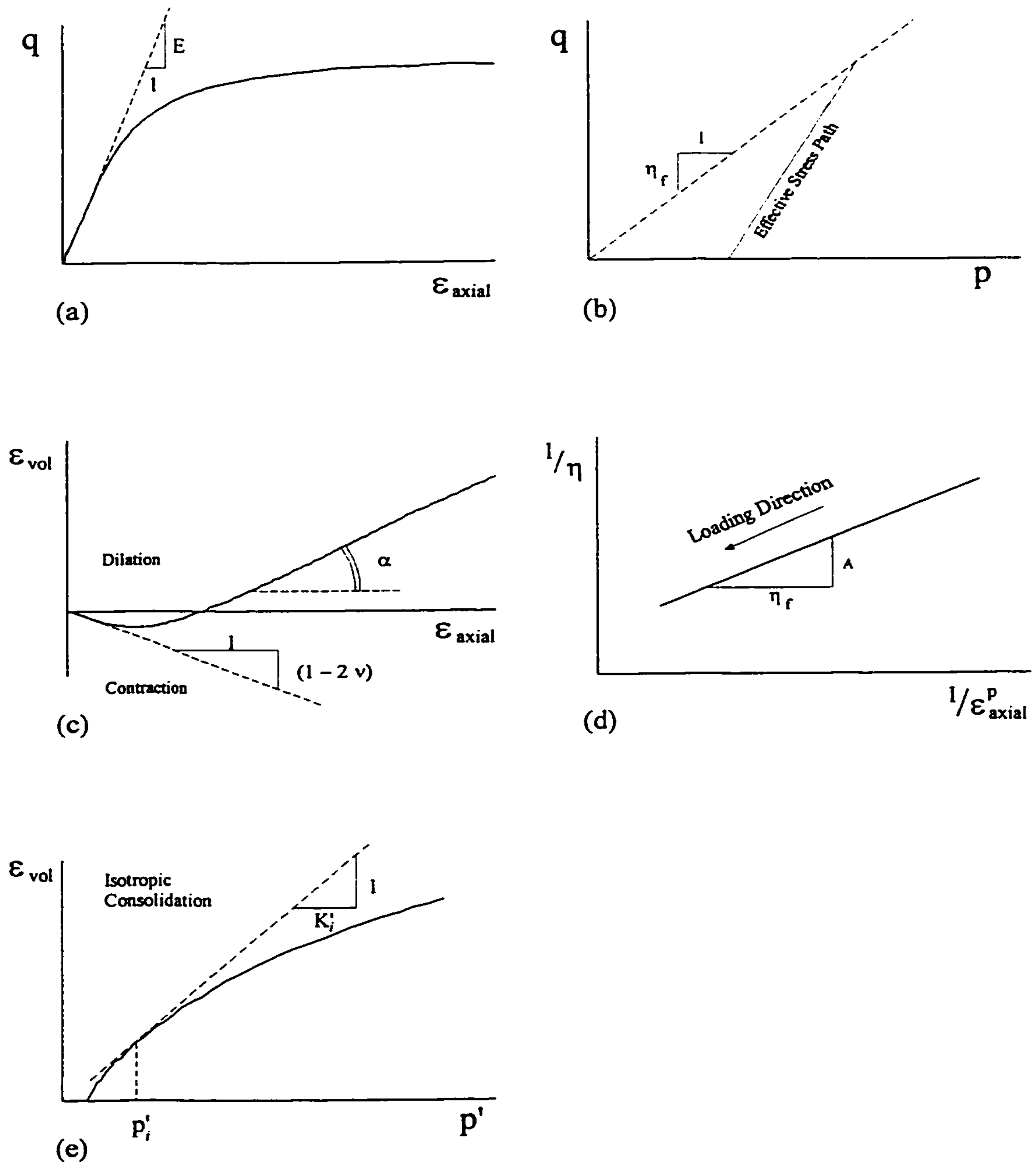

Determination of constitutive parameters using the results from triaxial compression and isotropic consolidation tests: (a) elastic modulus E, (b) stress ratio at failure η_f, (c) Poisson's ratio ν and stress ratio at critical state η_α, (d) hardening parameter A, and (e) bulk modulus K.

Figure 2.5. Determination of constitutive parameters

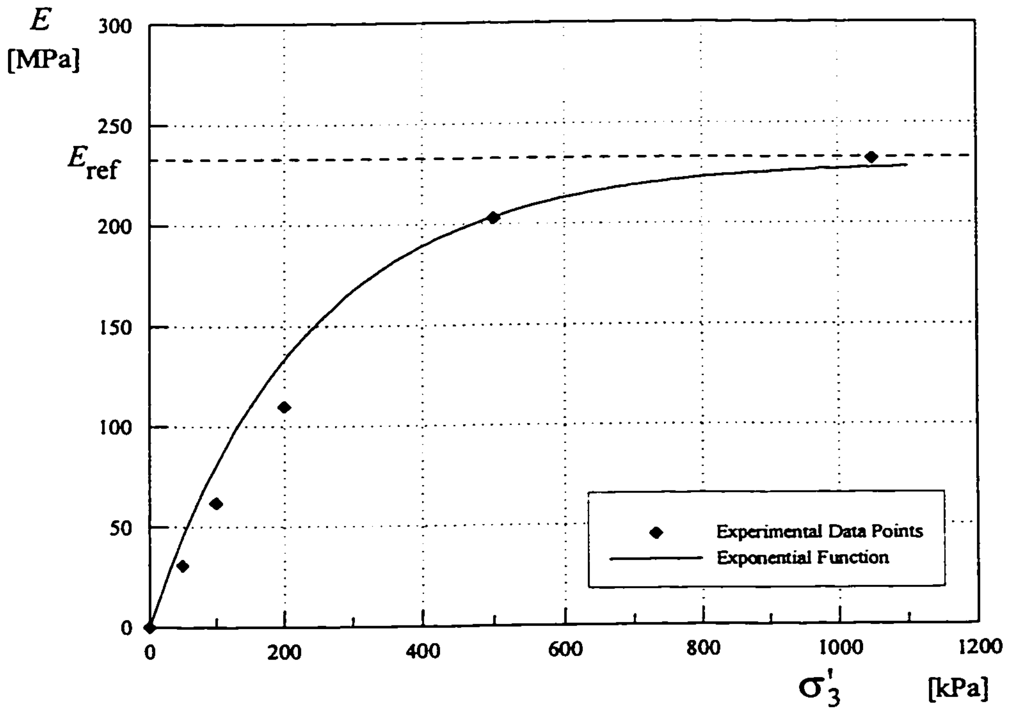

$$E = E_{ref} \left\{ 1 - e^{-r} \right\}$$

$$r = \frac{1000}{E_{ref}} \sigma'_3$$

Figure 2.6. Stress dependency of the elastic modulus

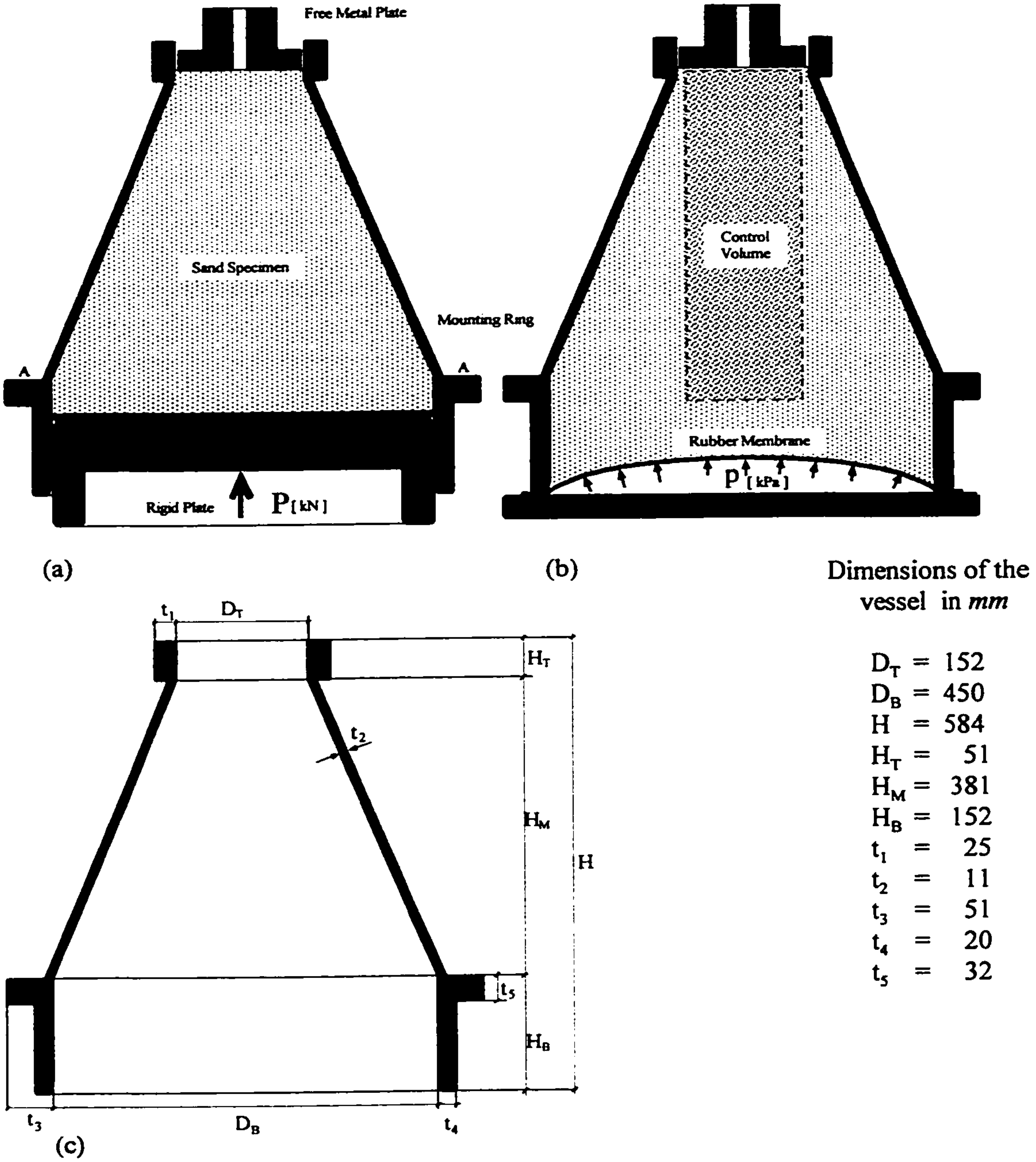

Dimensions of the vessel in *mm*

D_T = 152
D_B = 450
H = 584
H_T = 51
H_M = 381
H_B = 152
t_1 = 25
t_2 = 11
t_3 = 51
t_4 = 20
t_5 = 32

Frustum Confining Vessel using (a) the piston and (b) the membrane loading configurations. The general dimensions of the vessel are shown in (c).

Figure 2.7. FCV loading configurations

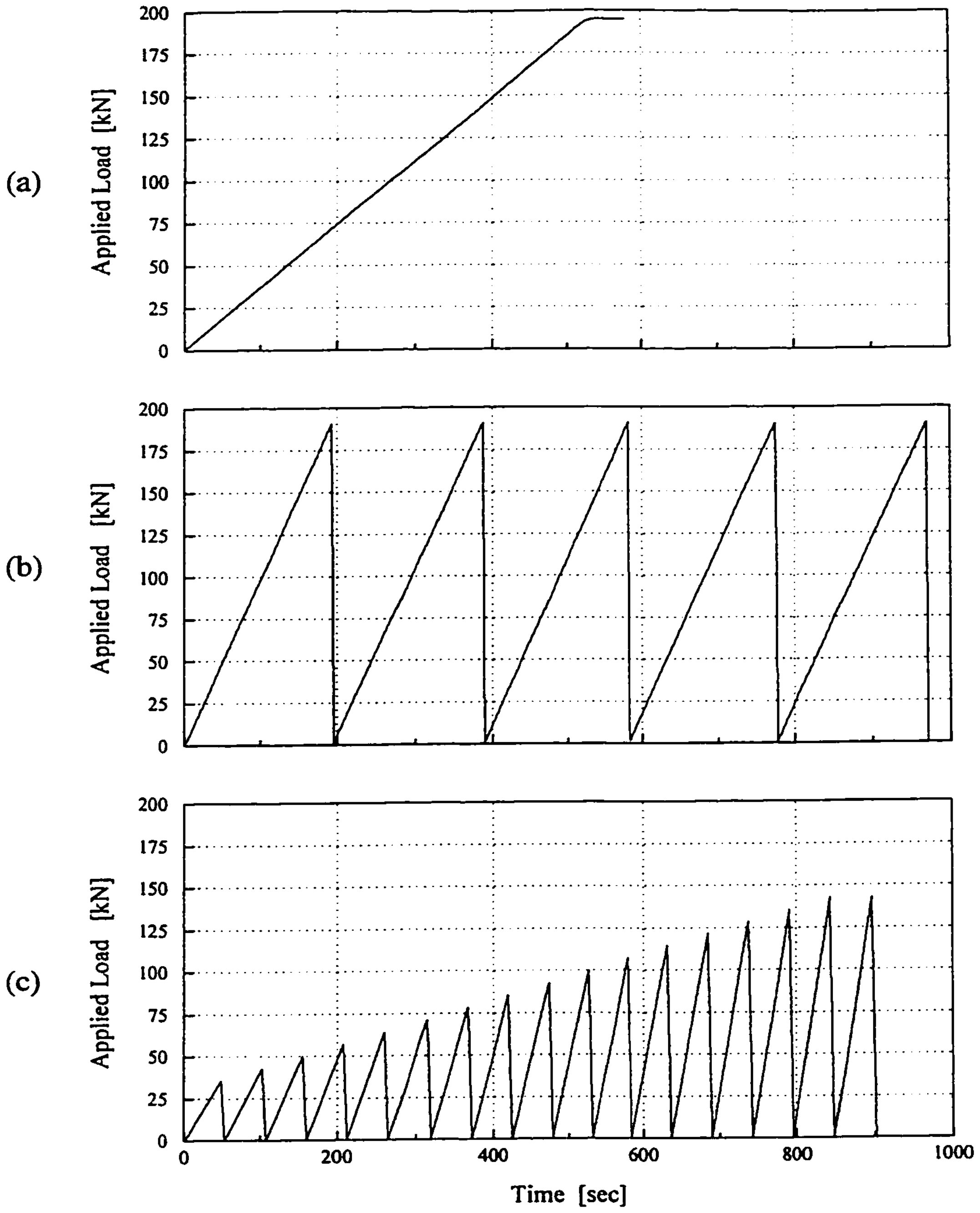

Different loading procedures applied to FCV specimens using the piston configuration: (a) one-cycle ramp load, (b) multiple-cycle ramp load, and (c) multiple-cycle scaled loading.

Figure 2.8. FCV loading procedures

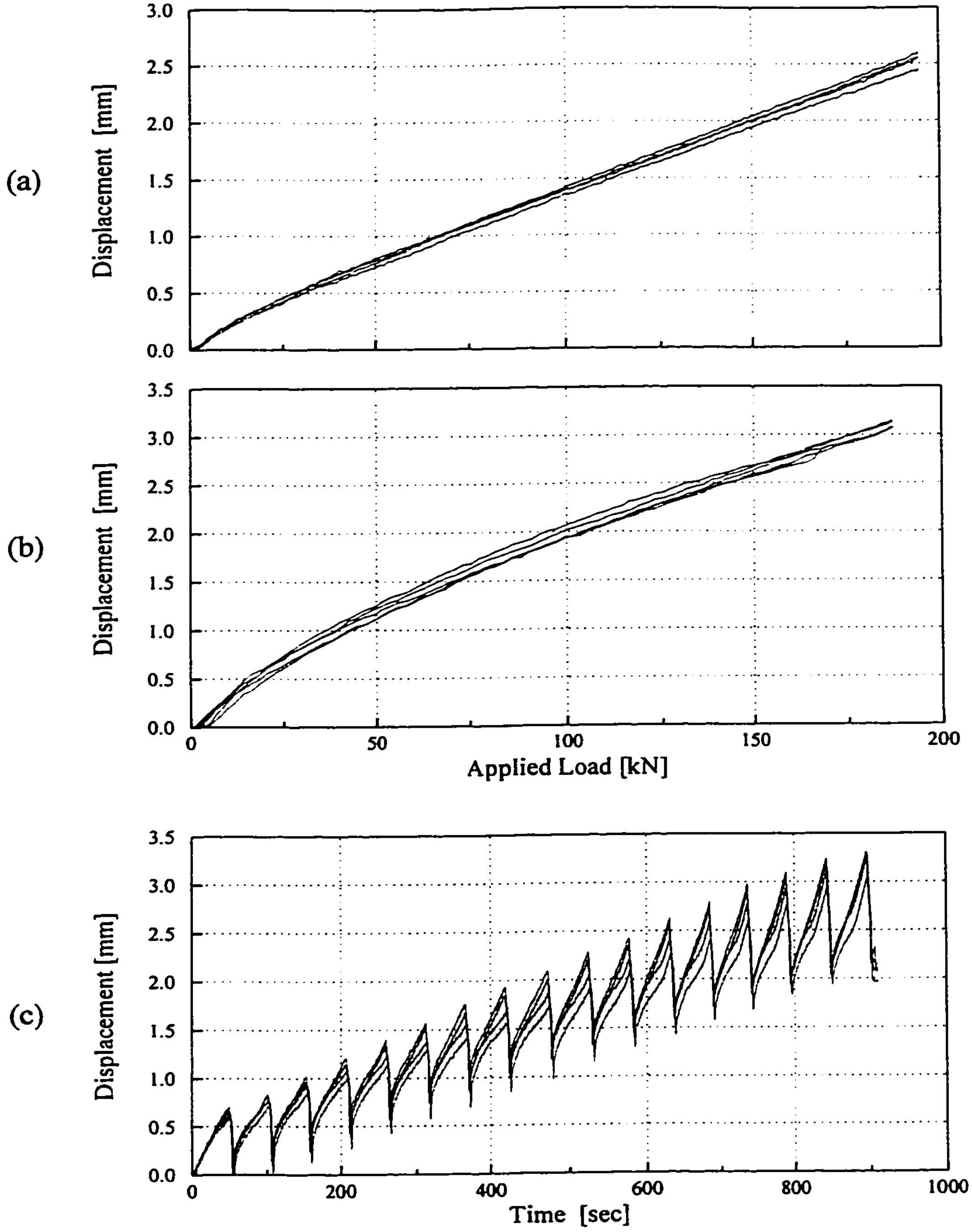

Reproducibility of test responses for the cases of (a) one-cycle ramp load, (b) reset multiple-cycle ramp load, and (c) multiple-cycle scaled load without reset. The responses are shown in terms of piston displacements.

Figure 2.9. FCV test reproducibility

Measured Displacements in *mm*			
Position	Piston Load [kN]		
	100 ◇	150 ○	195 △
Piston	1.31	2.00	2.51
Top Plate	1.32	1.90	2.47
1	1.08	1.33	1.52
2	1.15	1.71	2.25
3	1.25	1.79	2.29
4	0.65	1.17	1.63
5	0.71	1.18	1.67
6	0.85	1.13	1.30
7	1.40	2.05	2.55
8	1.15	1.70	2.25
9	1.00	1.60	2.10
10	0.65	1.00	1.32
11	1.70	2.50	3.13
12	1.91	2.77	3.47
13	1.27	1.87	2.40
14	0.93	1.27	1.53
15	1.13	1.70	2.27

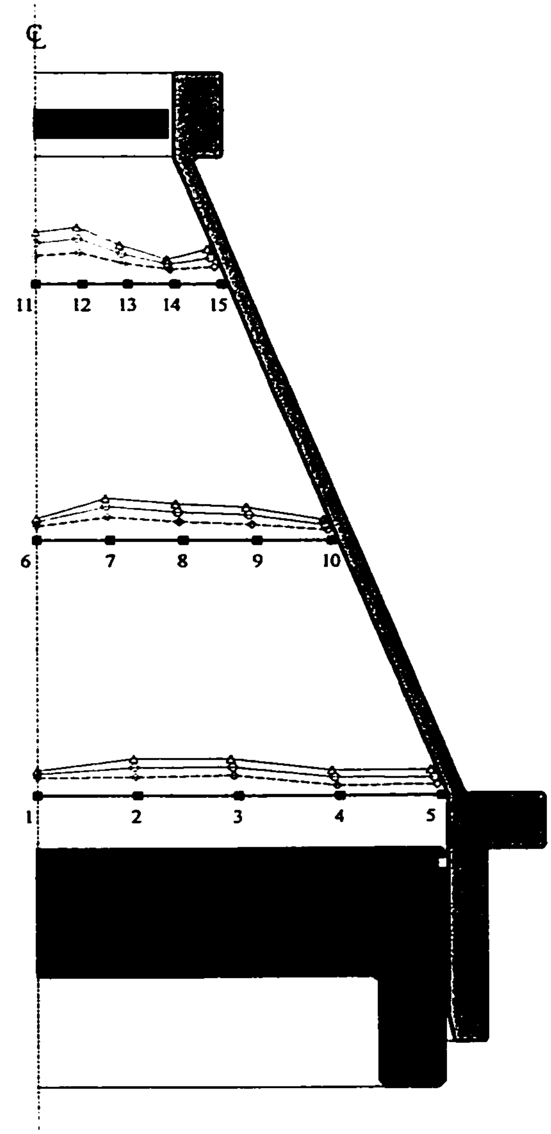

Displacements measured within FCV specimens at three different stages of loading, corresponding to piston displacements of 1.31 *mm* (◇), 2.00 *mm* (○), and 2.51 *mm* (△). The initial position of the telltales are indicated with (■). The displacements are magnified by a factor of 10.

Figure 2.10. Displacements measured in FCV specimens

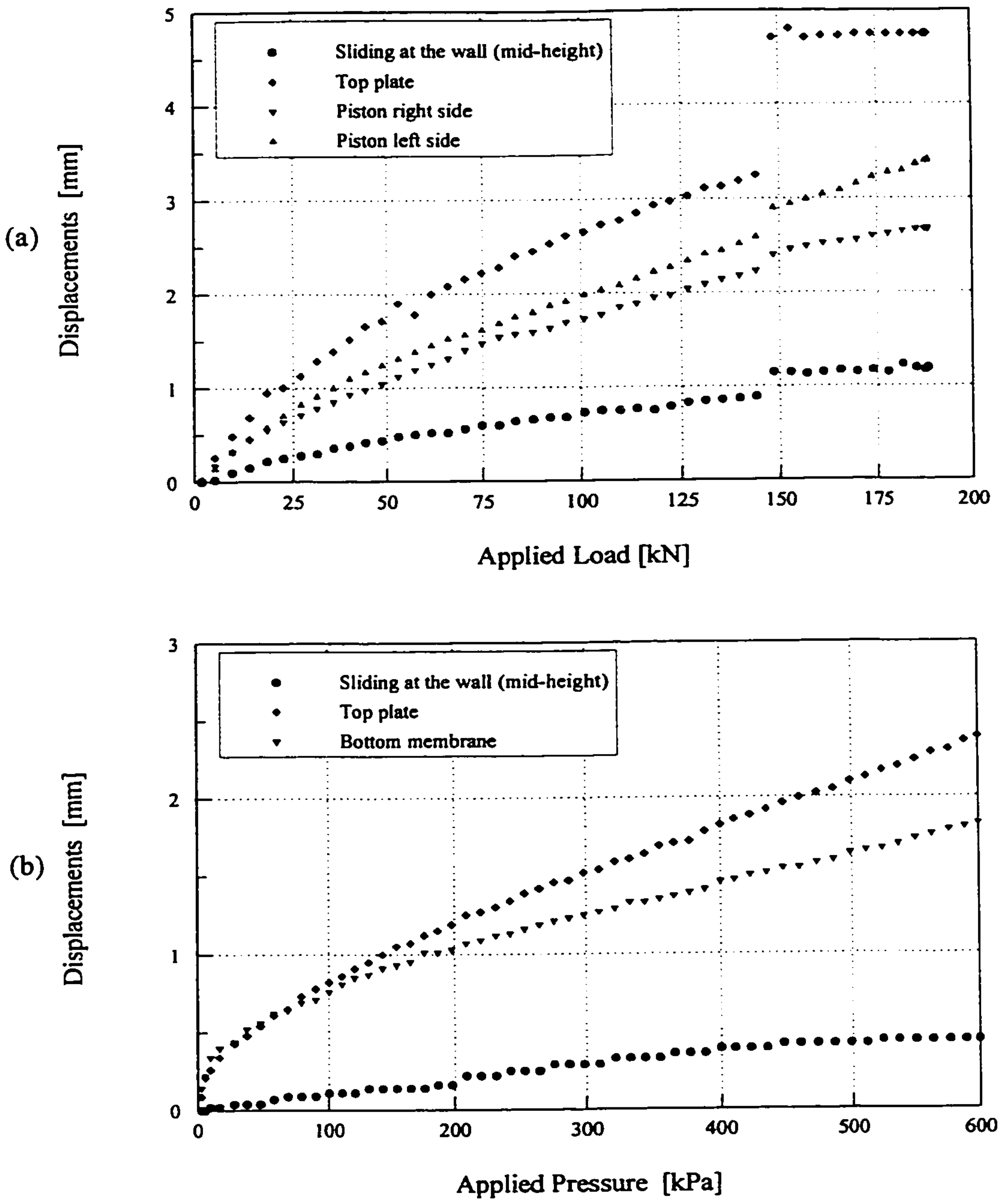

Observed responses from (a) the piston and (b) membrane loading configurations shown in terms of displacements at the top, bottom, and wall (mid-height). In the case of piston loading, displacements exhibit a typical jump at about 150 *kN*.

Figure 2.11. Responses from piston and membrane loading configurations

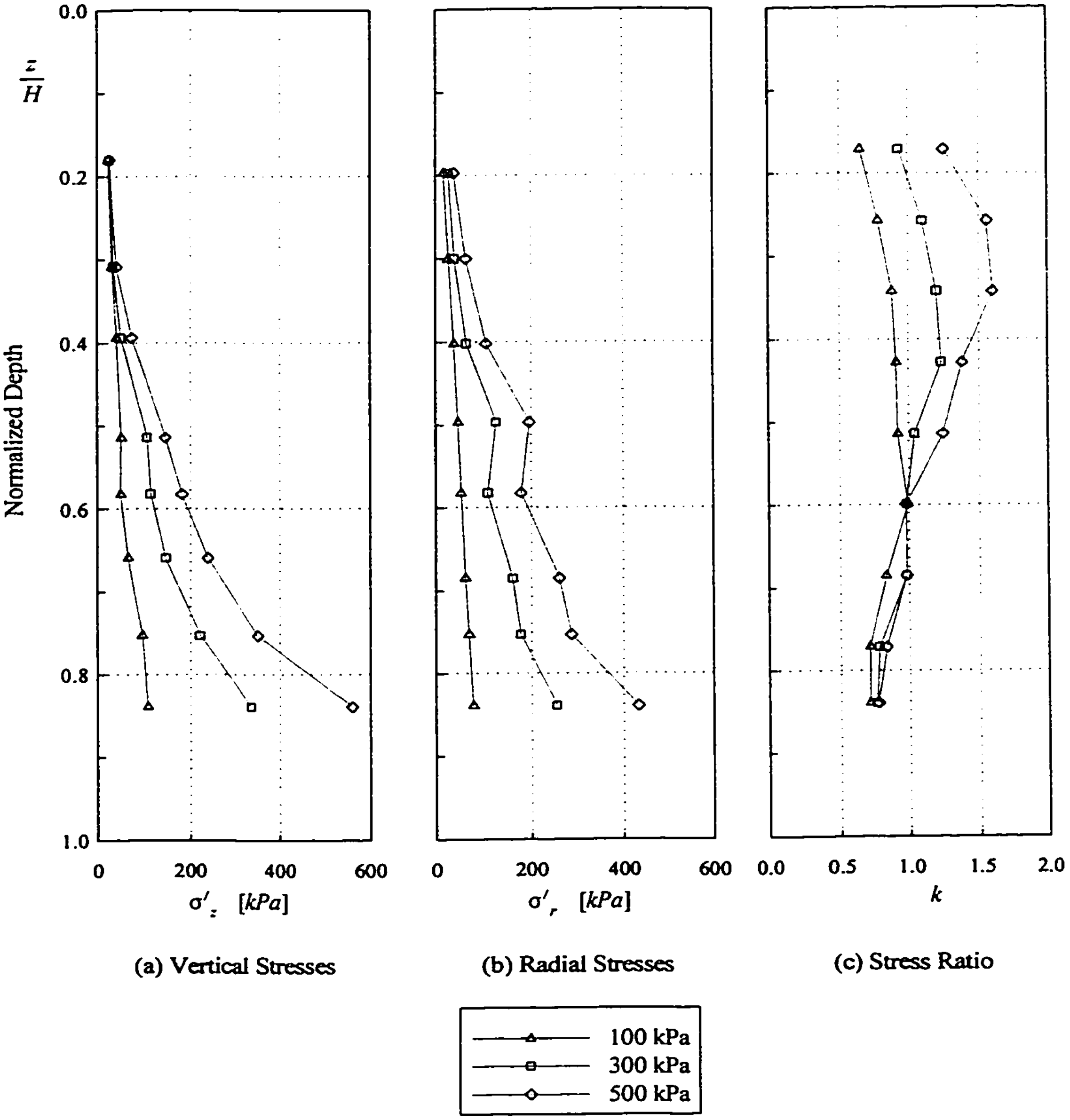

(a) Vertical Stresses

(b) Radial Stresses

(c) Stress Ratio

The stresses measured along the centerline of FCV specimens tested with the membrane loading are shown for (a) vertical stresses, (b) radial stresses, and (c) calculated values of the stress ratio, in function of the normalized depth *z/H*. The stresses are shown at three different stages of loading: 100, 300, and 500 *kPa* of applied pressure.

Figure 2.12. Centerline stresses measured with FSR sensors: Membrane loading

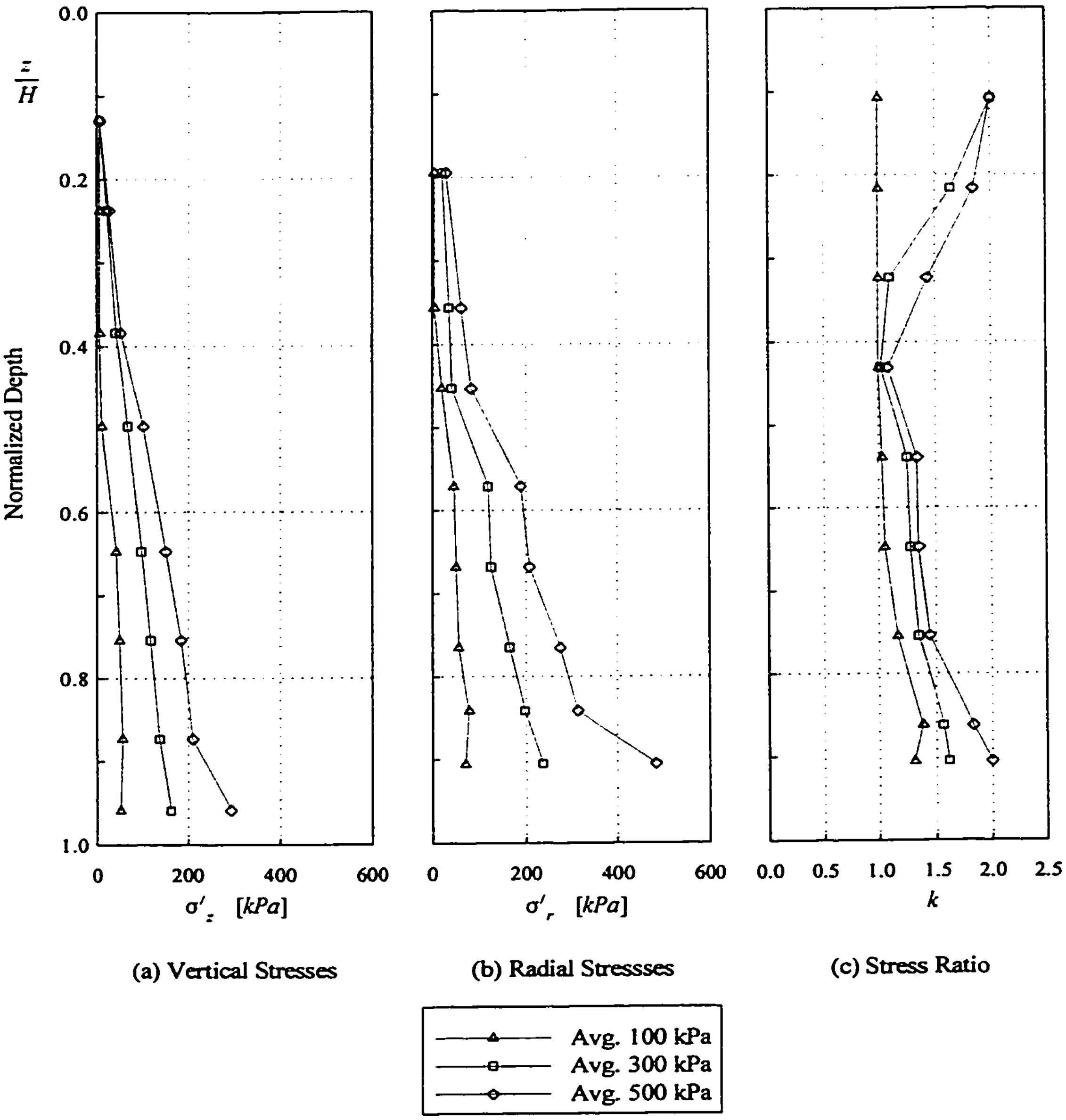

(a) Vertical Stresses

(b) Radial Stressses

(c) Stress Ratio

The stresses measured along the centerline of FCV specimens tested with the piston loading are shown for (a) vertical stresses, (b) radial stresses, and (c) calculated values of the stress ratio, in function of the normalized depth *z/H*. The stresses are shown at three different stages of loading: 16, 48, and 80 *kN* of applied load (with the equivalent pressures of 100, 300, and 500 *kPa*, respectively).

Figure 2.13. Centerline stresses measured with FSR sensors: Piston loading

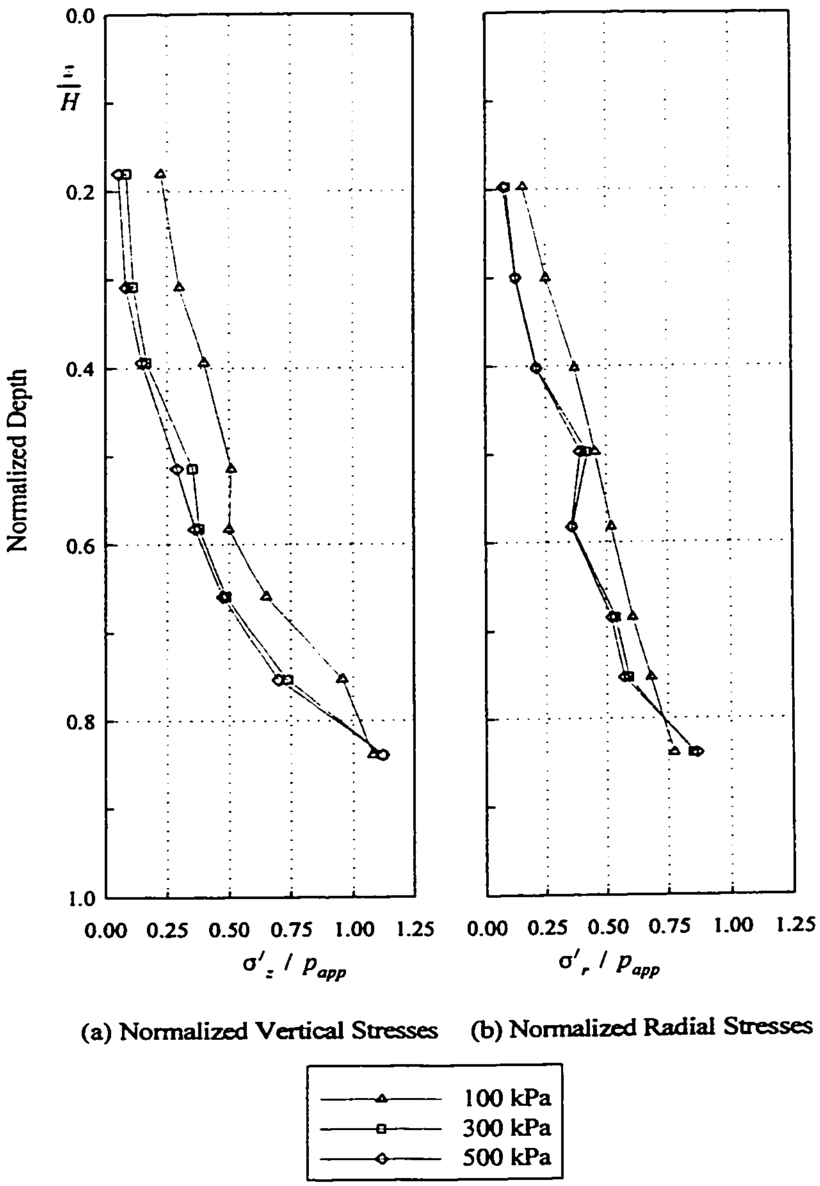

(a) Normalized Vertical Stresses (b) Normalized Radial Stresses

The stresses measured along the centerline of FCV specimens tested with the membrane loading are shown for (a) normalized vertical stresses, and (b) normalized radial stresses in function of the normalized depth *z/H*. The stresses, which are normalized with respect to the applied pressure, are shown at three different stages of loading: 100, 300, and 500 *kPa* of applied pressure.

Figure 2.14. Centerline normalized stresses: Membrane loading

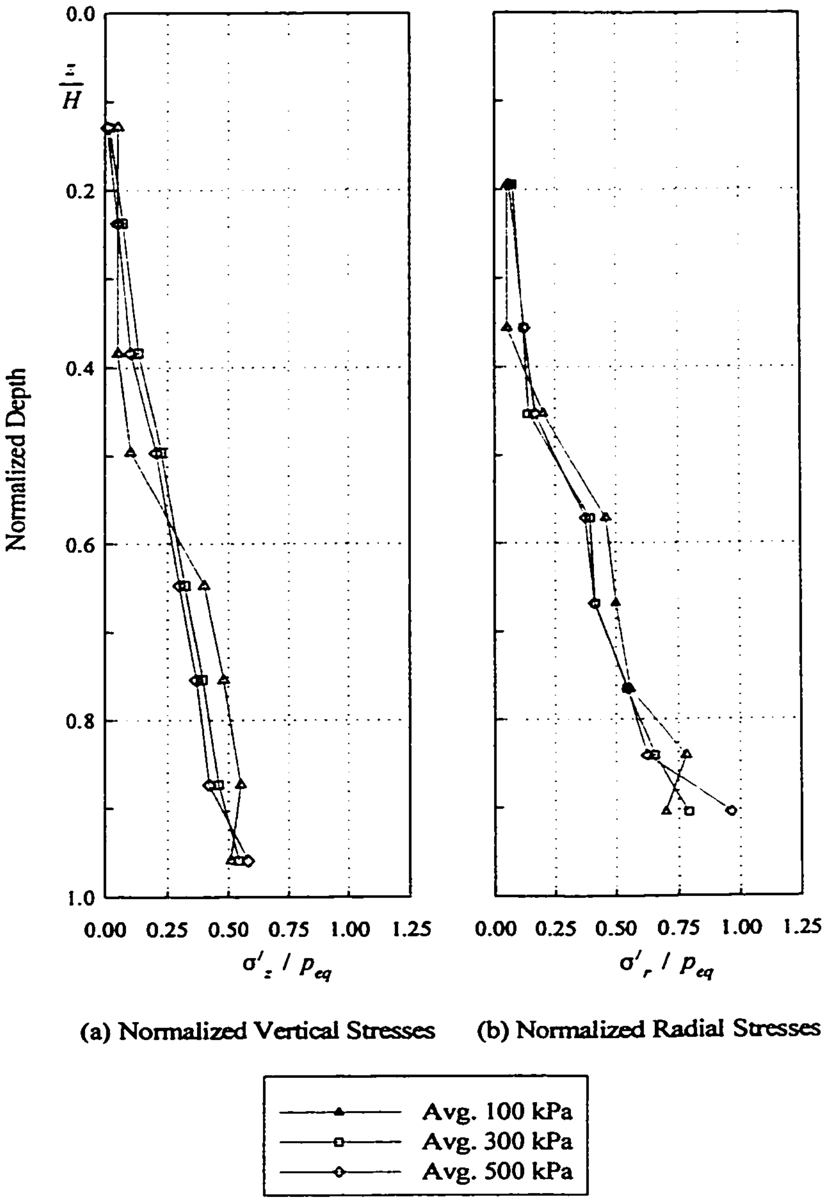

(a) Normalized Vertical Stresses (b) Normalized Radial Stresses

The stresses measured along the centerline of FCV specimens tested with the piston loading are shown for (a) normalized vertical stresses, and (b) normalized radial stresses in function of the normalized depth z/H. The stresses, which are normalized with respect to the average applied pressure, are shown at three stages of loading: 16, 48, and 80*kN* of applied load.

Figure 2.15. Centerline normalized stresses: Piston loading

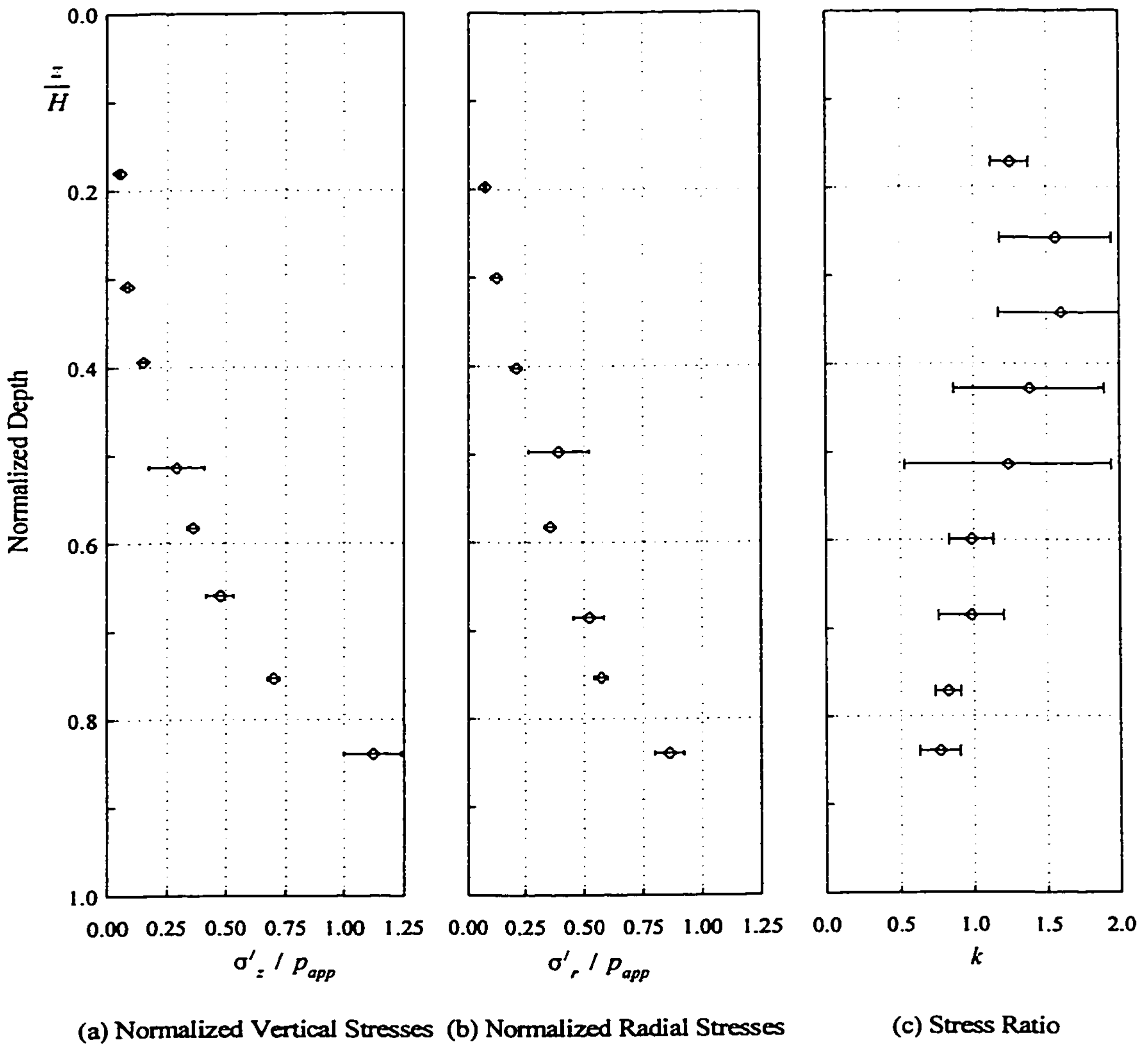

The uncertainties associated with the measured stresses are indicated as error bars for the case of (a) normalized vertical stresses, (b) normalized radial stresses, and (c) values of the stress ratio in a FCV specimen tested with the membrane loading at 500 *kPa* of applied pressure. The uncertainties were estimated from a series of calibration tests conducted on the FSR sensors.

Figure 2.16. Uncertainties associated with the measured stresses: Membrane loading

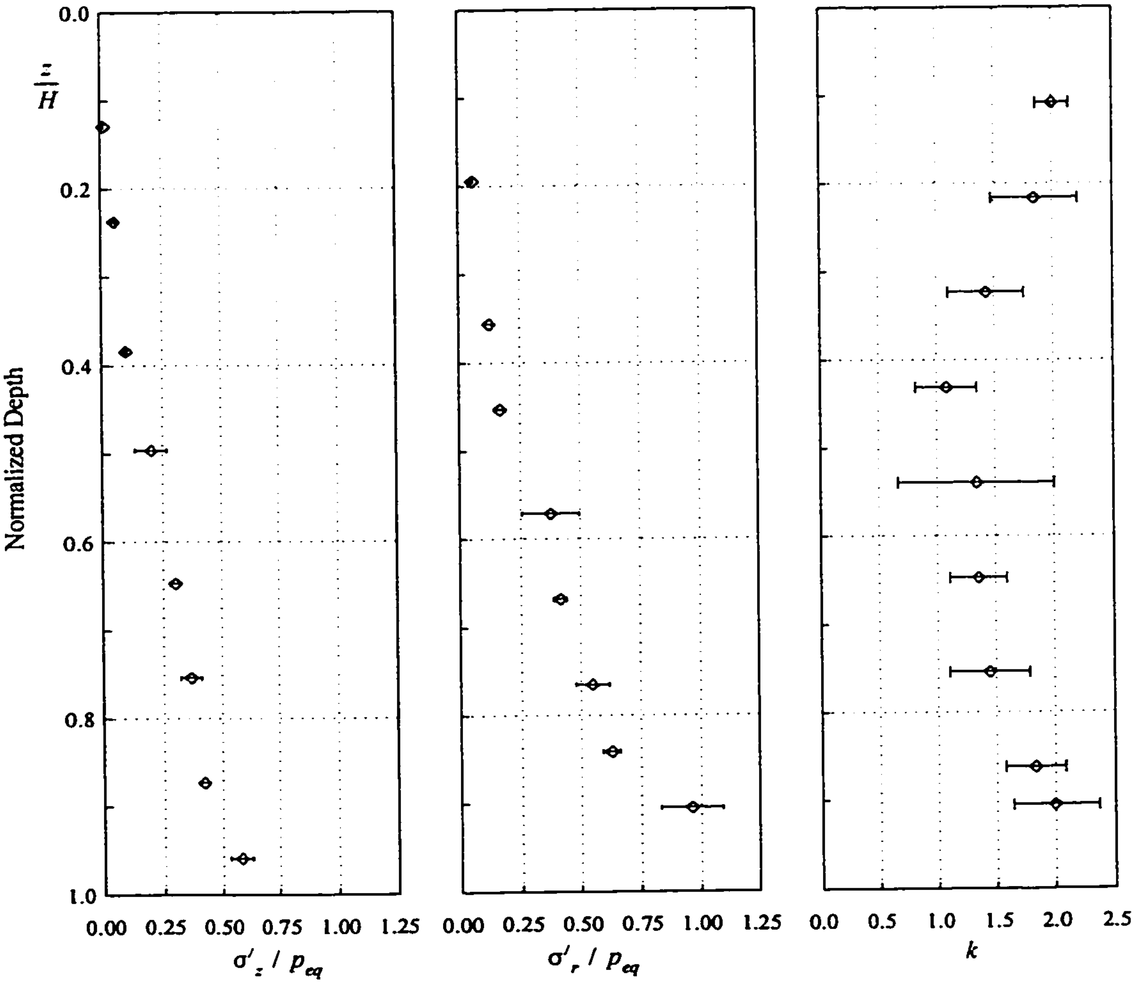

(a) Normalized Vertical Stresses (b) Normalized Radial Stresses (c) Stress Ratio

The uncertainties associated with the measured stresses are indicated as error bars for the case of (a) normalized vertical stresses, (b) normalized radial stresses, and (c) values of the stress ratio in a FCV specimen tested with the piston loading at 80 *kN* of applied load. The uncertainties were estimated from a series of calibration tests conducted on the FSR sensors.

Figure 2.17. Uncertainties associated with the measured stresses: Piston loading

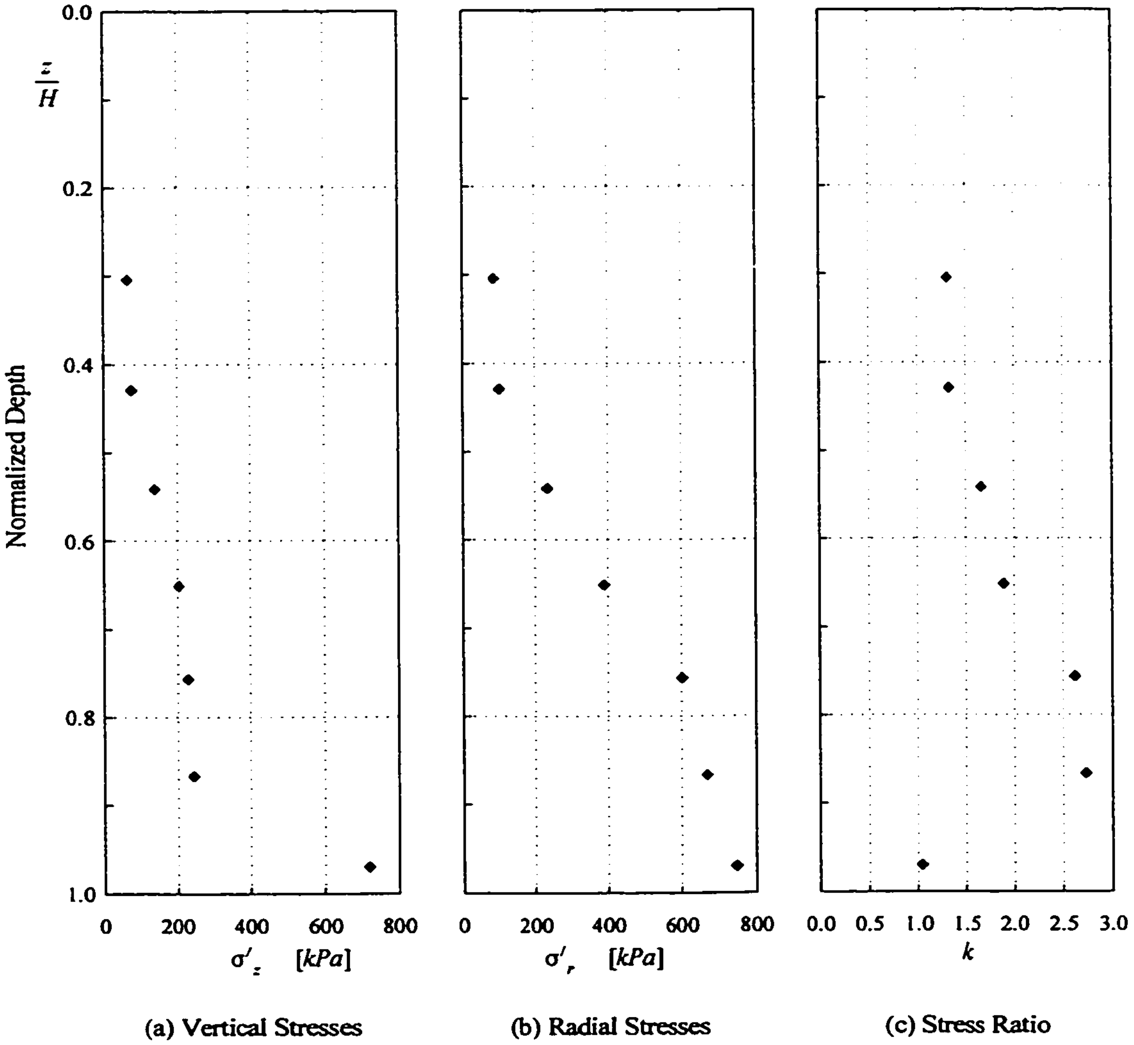

(a) Vertical Stresses (b) Radial Stresses (c) Stress Ratio

Stresses measured along the centerline with a capacitive stress sensor. Each stress data point on the (a) vertical and (b) radial stress distributions represent a separate test. The calculated values of the stress ratio are shown in (c). Measured stresses correspond to a piston load of 195 *kN*.

Figure 2.18. Centerline stresses measured with a capacitive sensor: Piston loading

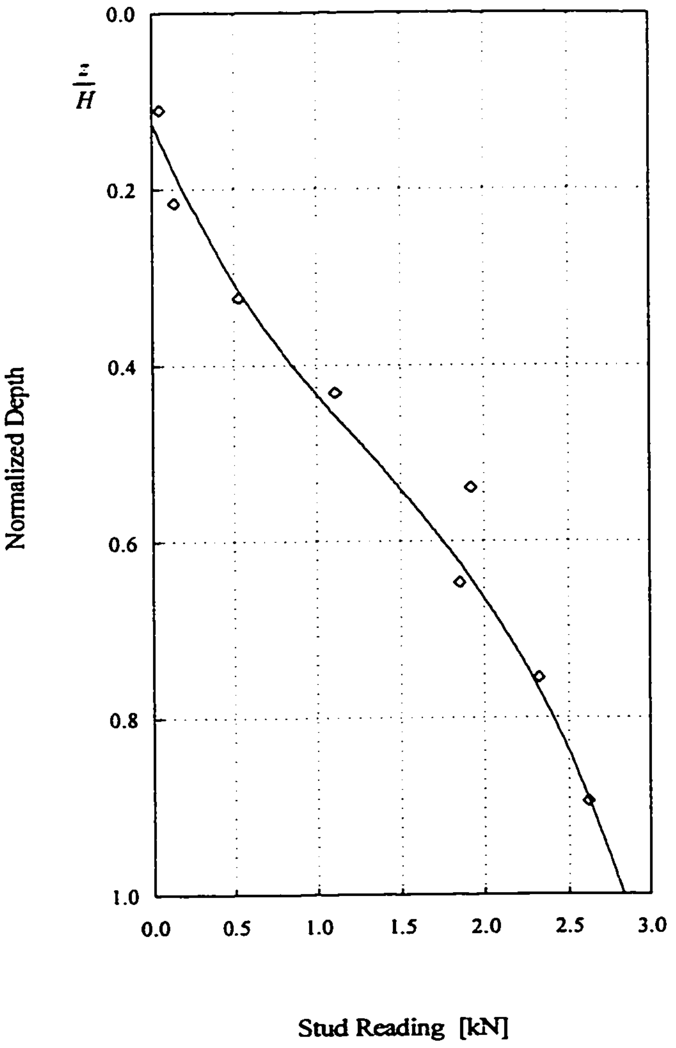

The stress conditions along the centerline of a FCV specimen tested with the piston loading are shown in terms of values of tip resistance versus normalized depth z/H.

Figure 2.19. Results from cone-penetration probing

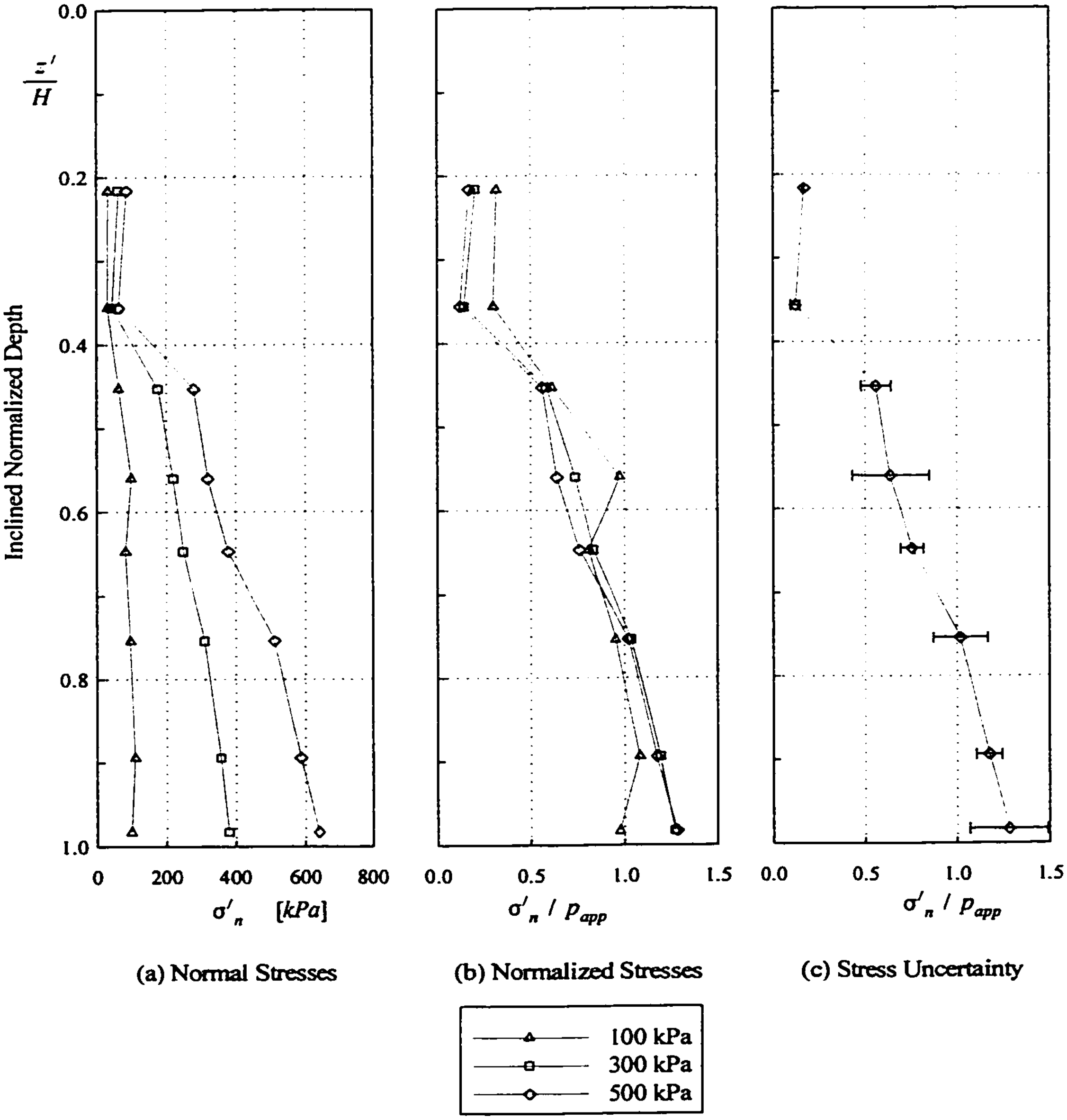

The normal stresses acting at the wall of a FCV specimen tested with the membrane loading were measured with FSR sensors, at three different stages of loading: 100, 300, and 500 *kPa*. The plots shown (a) normal stresses, (b) normalized stresses, and (c) uncertainties in the stress measurements versus normalized depth *z'/H*.

Figure 2.20. Stresses at the wall: Membrane loading

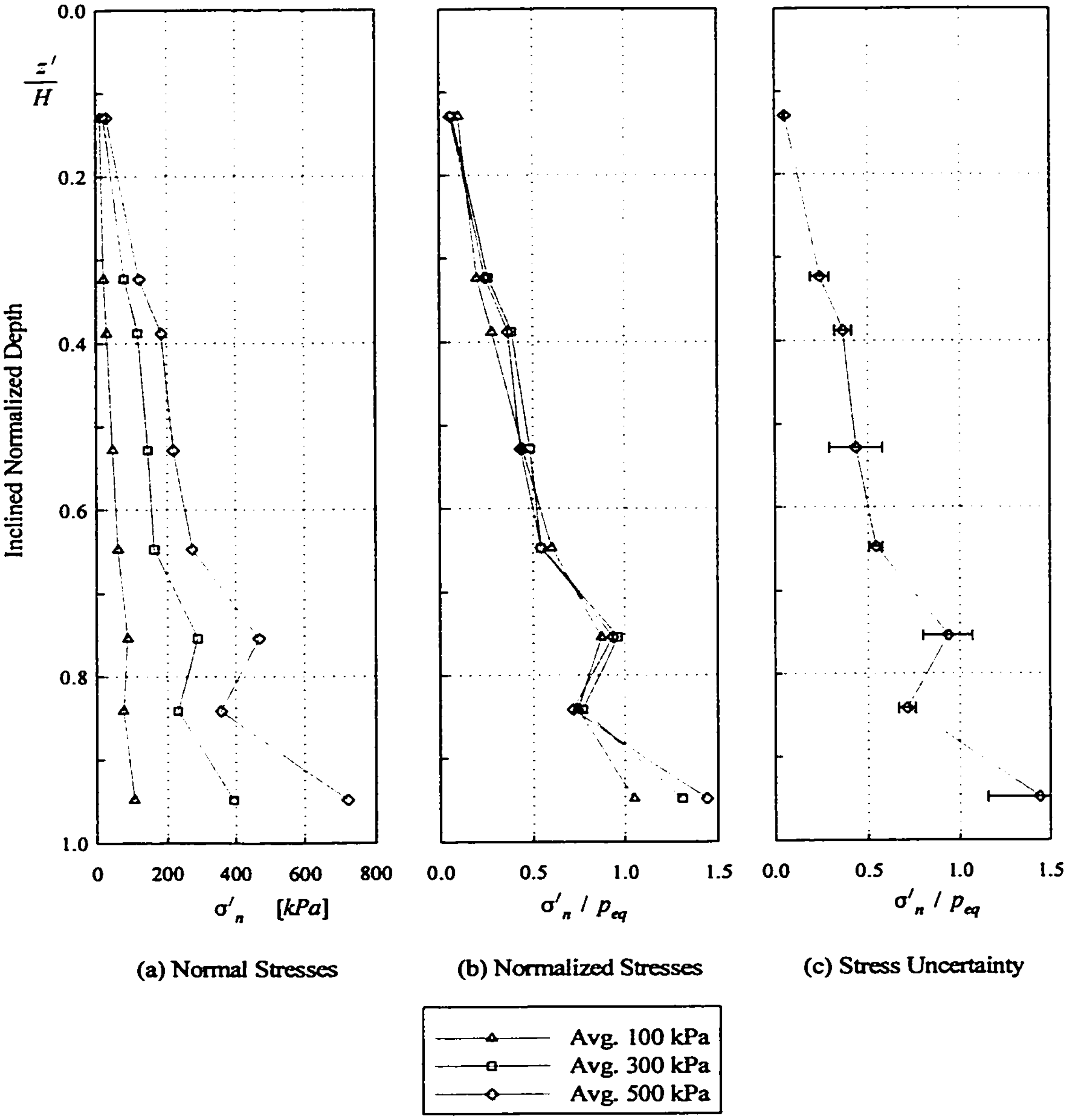

(a) Normal Stresses (b) Normalized Stresses (c) Stress Uncertainty

The normal stresses acting at the wall of a FCV specimen tested with the piston loading were measured with FSR sensors, at three different stages of loading: 16, 48, and 80 *kN*, which correspond to 100, 300, and 500 *kPa* of average applied pressure. The plots shown (a) normal stresses, (b) normalized stresses, and (c) uncertainties in the stress measurements versus normalized depth z'/H.

Figure 2.21. Stresses at the wall: Piston loading

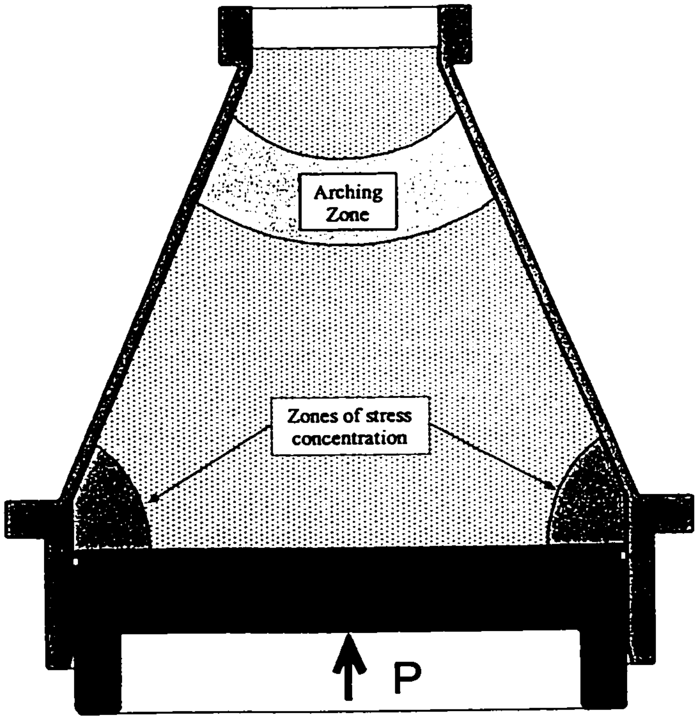

Figure 2.22. Stress concentration and arching in FCV specimens

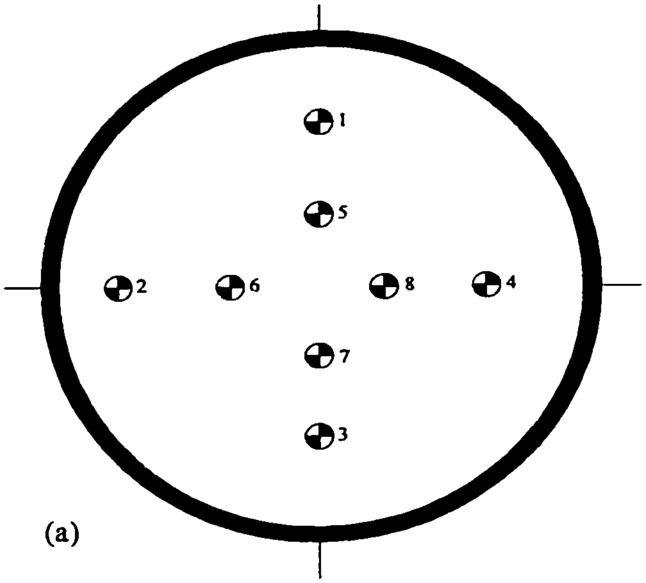

Membrane Loading Applied Pressure: 510 *kPa*			
Position	Normal Stress [*kPa*]	Normalized stress	Uncertainty [*kPa*]
1	550	1.08	±151
2	517	1.01	±83
3	489	0.95	±80
4	470	0.92	±5
5	508	1.00	±47
6	491	0.96	±30
7	480	0.94	±68
8	474	0.93	±43

(b)

Piston Loading Applied Force: 80 *kN*			
Position	Normal Stress [*kPa*]	Normalized stress	Uncertainty [*kPa*]
1	620	1.24	±150
2	523	1.05	±32
3	568	1.14	±75
4	514	1.03	±52
5	248	0.50	±103
6	254	0.51	±54
7	221	0.44	±59
8	238	0.47	±42

(c)

Stresses acting at the bottom of FCV specimens were measured at the positions indicated in the plan view shown in (a), for the case of (b) membrane and (c) piston loading. Normal stresses were measured with FSR sensors.

Figure 2.23 Stresses acting at the bottom of FCV specimens

Chapter 3

MATHEMATICAL MODELING

3.1 Description of the Boundary-Valued Problems

The soil behaviour observed during the experimental triaxial and FCV testing series is further studied in this chapter from a mathematical point of view. The measured responses are defined and treated as boundary-valued problems. This chapter presents the mathematical formulation of the general boundary-valued problem in a formal manner, considering the following basic features

- quasi-static monotonic loading conditions;
- axisymmetric stress-strain state; and
- elasto-plastic stress-strain behaviour.

A mathematical formulation was initially developed to model the problem of drained triaxial compression tests. In terms of the main characteristics of triaxial responses observed during the testing, the formulation assumes that,

- there is no slippage at the loading platens;
- the confining stresses remain constant throughout loading; and

- the principal stress and strain directions do not rotate significantly under loading.

In terms of the constitutive law adopted for the simulation of triaxial tests the following assumptions were made

- the material properties are homogeneous and isotropic, and
- the material properties remain constant during the tests.

Because of its simplicity, the constitutive relation used for simulating the triaxial tests is designated as the *basic constitutive law*.

The initial formulation, based on the *basic constitutive law*, however, was not adequate to model sand behaviour under FCV testing conditions, where some of the assumptions mentioned above were not applicable. Therefore, in a second stage of model development, some modifications were introduced to the *basic constitutive law* in order to account for specific conditions characterizing the FCV testing phenomena, for example:

- confining stresses within FCV specimens increased during loading, from 10 *kPa* at initial conditions to over 1000 *kPa* at peak applied loads;
- stress-strain distributions were highly non-uniform;
- principal stress and strain directions rotated during testing; and
- progressive failure conditions developed as stress-strain gradients increased with load in a highly localized manner.

Since it is well known that the elastic modulus of sands is a stress-dependent property, (Janbu 1963, Kolymbas et al. 1990, Desai & Abel 1972, and Mazari & Dafalias 1997), a pressure-dependent elastic modulus was incorporated into the formulation of the stress-strain relationship. This formulation is referred to as the *pressure-dependent constitutive law*.

The stress-dependency of the elastic modulus also implied that different stress gradients acting in orthogonal directions could induce different elastic properties in those directions (Rothenburg & Bathurst 1989). As a result, it was further speculated that rotation of principal planes associated with highly non-uniform stress gradients could be responsible for generating or inducing anisotropic material properties. Owing to the dominance of confining stresses over the deviatoric stresses existing in the sand mass under FCV conditions, it seemed reasonable to assume that stress-induced anisotropy would mostly affect the elastic behavioral properties, particularly the stress-dependent elastic moduli. It was speculated that this stress-induced anisotropy could have a strong impact on the behaviour of FCV specimens, where some preferred directions would exhibit high values of strength while in the conjugate directions the material would be weaker; see, e.g., Oda et al. (1985). Moreover, since stress distributions in FCV specimens were non-uniform, it was assumed that the stress-induced anisotropy would also be subjected to spatial variations. In this context, it was believed that the rotation of principal stresses expected to occur within FCV specimens under loading would have important implications in the modeling of FCV tests. Although it seemed reasonable to assume that at initial conditions, the material properties were essentially isotropic and homogeneous, it may not be realistic to assume that the conditions in the specimens would remain so during loading.

An extended version of the *pressure-dependent constitutive law* was developed with the objective of evaluating the influence of stress-induced anisotropy on the behavior of sand in the FCV device under loading. This formulation was designated as the *anisotropic* *constitutive law*.

The following sections present the description of the finite element model incorporating the three constitutive relations; namely, the *basic*, the *pressure-dependent*, and the *anisotropic constitutive laws*.

3.2 The Finite Element Model

The mathematical formulation was in general restricted to problems where the loading is quasi-static and monotonic, and the material response is governed by an elasto-plastic constitutive law. The basic constitutive law considers isotropic, homogeneous, elastic material properties under axisymmetric stress-strain conditions.

3.2.1 Formulation of the Boundary-Valued Problem

The general boundary-valued problem is defined in this section by specifying the conditions for equilibrium, the kinematic relations, the constitutive law and the boundary conditions.

(i) Equilibrium. The equation of equilibrium for a soil mass is given by

$$L_\sigma^T \sigma + b = 0 \quad , \tag{3.1}$$

where the stress vector σ for axisymmetric problems is $\{ \sigma_r \;\; \sigma_z \;\; \sigma_{rz} \;\; \sigma_\theta \}^T$ with T indicating the transpose of a vector or a matrix. The subscripts r, z, and θ refer to the radial, axial, and circumferential directions, respectively. The body forces acting on the system are represented by $\boldsymbol{b}$. If we consider gravity loading, the body forces $\boldsymbol{b}$ can be written as $\{\ 0 \quad \rho g\ \}^T$ where ρ is mass density and g is the gravitational constant. The differential operator $\boldsymbol{L}_\sigma$ is

$$\boldsymbol{L}_\sigma = \begin{bmatrix} \left(\frac{1}{r}+\frac{\partial .}{\partial r}\right) & 0 & \frac{\partial .}{\partial z} & -\frac{1}{r} \\ 0 & \frac{\partial .}{\partial z} & \left(\frac{1}{r}+\frac{\partial .}{\partial r}\right) & 0 \end{bmatrix}^T . \tag{3.2}$$

(ii) Kinematics. The kinematic equation

$$\varepsilon = \boldsymbol{L}\,\boldsymbol{u} \tag{3.3}$$

relates the total strain $\varepsilon = \{\ \varepsilon_r \quad \varepsilon_z \quad \gamma_{rz} \quad \varepsilon_\theta\ \}^T$ to the displacement $\boldsymbol{u} = \{\ u_r \quad u_z\ \}^T$, where $\boldsymbol{L}$, the differential operator for displacements, is given by

$$\boldsymbol{L} = \begin{bmatrix} \frac{\partial .}{\partial r} & 0 & \frac{\partial .}{\partial z} & \frac{1}{r} \\ 0 & \frac{\partial .}{\partial z} & \frac{\partial .}{\partial r} & 0 \end{bmatrix}^T . \tag{3.4}$$

(iii) Constitutive law. The constitutive law is presented in its incremental form as

$$\Delta\sigma = \boldsymbol{D}\ \Delta\varepsilon^e \tag{3.5}$$

with $\boldsymbol{D}$ being the elastic constitutive matrix, while $\Delta\sigma$ and $\Delta\varepsilon^e$ represent the stress and elastic strain increments, respectively. For elasto-plastic material behavior, the total strain increment $\Delta\varepsilon$ vector can be decomposed into two parts, the elastic $\Delta\varepsilon^e$ and the plastic $\Delta\varepsilon^p$ components, i.e.,

$$\Delta\varepsilon = \Delta\varepsilon^e + \Delta\varepsilon^p \quad . \tag{3.6}$$

Substituting equation (3.6) into (3.5) yields

$$\Delta\sigma = \boldsymbol{D} \left(\Delta\varepsilon - \Delta\varepsilon^p \right) . \tag{3.7}$$

For axisymmetric problems $\boldsymbol{D}$ is given by

$$\boldsymbol{D} = \frac{E}{(1+\nu)(1-2\nu)} \begin{bmatrix} 1-\nu & \nu & 0 & \nu \\ & (1-\nu) & 0 & \nu \\ & & \frac{1-2\nu}{2} & 0 \\ \mathit{symm.} & & & 1-\nu \end{bmatrix} , \tag{3.8}$$

where the elastic modulus E and Poisson's ratio ν are the mechanical properties for the isotropic material.

(iv) Boundary conditions. Finally, the statement of the boundary-valued problem is completed by specifying either surface tractions $\boldsymbol{t}$ or prescribed displacements $\boldsymbol{u}_s$ at the boundary surface S. For example

$$\boldsymbol{t} - \sigma\,\boldsymbol{n} = \boldsymbol{0} \tag{3.9}$$

with $\boldsymbol{n}$ as the outward normal to the surface S.

3.2.2 Discretization of the Boundary-Valued Problem

Applying the principle of Virtual Work to the expression of equilibrium (Bathe 1982, Zienkiewicz & Taylor 1989, and Mirza 1992), we can write equation (3.1) as

$$\int_V \delta \boldsymbol{u}^T \left[\boldsymbol{L}_\sigma{}^T \sigma + \boldsymbol{b} \right] dV = 0 \quad . \tag{3.10}$$

Taking into account the axisymmetric nature of the model, and integrating the first term by parts, we have the following identity:

$$\int_V \delta \boldsymbol{u}^T \boldsymbol{L}_\sigma{}^T \sigma \; dV = \int_S \delta \boldsymbol{u}^T \boldsymbol{t} \; dS \; - \int_V \delta \varepsilon^T \sigma \; dV \quad . \tag{3.11}$$

This expression, which is derived using equations (3.3) and (3.9), is now substituted into equation (3.10) to yield

$$\int_V \delta \varepsilon^T \sigma \; dV = \int_V \delta \boldsymbol{u}^T \boldsymbol{b} \; dV + \int_S \delta \boldsymbol{u}^T \boldsymbol{t} \; dS \quad . \tag{3.12}$$

In order to express equation (3.12) in terms of stress and strain increments suitable for load-stepping, we consider that equation (3.12) corresponds to the end of the i^{th} load interval , with

$$\sigma_i = \sigma_{i-1} + \Delta\sigma_i \quad . \tag{3.13}$$

Substituting equations (3.5) and (3.13) into (3.12), the principle of Virtual Work at the end of the i^{th} load step is given by

$$\int_V \delta \varepsilon^T \boldsymbol{D}_T \, \Delta\varepsilon_i \; dV = \int_V \delta \boldsymbol{u}^T \boldsymbol{b} \; dV + \int_S \delta \boldsymbol{u}^T \boldsymbol{t}_i \; dS \; - \int_V \delta \varepsilon^T \sigma_{i-1} \; dV \quad , \tag{3.14}$$

where $\boldsymbol{D}_T$ represents the tangential constitutive matrix. In order to apply equation (3.14), the domain is discretized by dividing the volume of the body into finite elements. By using piecewise continuous interpolation functions, the displacement field can be defined in terms of the nodal displacements $\boldsymbol{a}$

$$\boldsymbol{u} = \boldsymbol{N}\,\boldsymbol{a} \tag{3.15}$$

where $\boldsymbol{N}$ is the matrix containing the interpolation functions. Replacing $\boldsymbol{u}$ in equation (3.5) with equation (3.15), the strains can be defined in terms of nodal displacements as

$$\varepsilon = \boldsymbol{L}\,\boldsymbol{N}\,\boldsymbol{a} = \boldsymbol{B}\,\boldsymbol{a} \quad , \tag{3.16}$$

which in the incremental form becomes

$$\Delta\varepsilon = \boldsymbol{B}\,\Delta\boldsymbol{a} \quad , \tag{3.17}$$

where $\boldsymbol{B}$ is the strain-displacement matrix. The discretized form for the Virtual Work can be derived as

$$\begin{aligned} \int_V \delta(\boldsymbol{B}\,\boldsymbol{a})^T \boldsymbol{D}_T\,(\boldsymbol{B}\,\Delta\boldsymbol{a})\; dV = \int_V \delta(\boldsymbol{N}\,\boldsymbol{a})^T \boldsymbol{b}\; dV + \int_S \delta(\boldsymbol{N}\,\boldsymbol{a})^T \boldsymbol{t}_i\; dS \\ - \int_V \delta(\boldsymbol{B}\,\boldsymbol{a})^T \sigma_{i-1}\; dV \quad , \end{aligned} \tag{3.18}$$

which after factoring out the virtual displacements $\delta\boldsymbol{a}^T$ can be written as

$$\int_V \boldsymbol{B}^T \boldsymbol{D}_T \boldsymbol{B}\; dV\; \Delta\boldsymbol{a} = \int_V \boldsymbol{N}^T \boldsymbol{b}\; dV + \int_S \boldsymbol{N}^T \boldsymbol{t}_i\; dS - \int_V \boldsymbol{B}^T \sigma_{i-1}\; dV \quad . \tag{3.19}$$

The discretized expression for incremental equilibrium in its compact form is

$$\boldsymbol{K}_T \, \Delta \boldsymbol{a} = \Delta \boldsymbol{f} \tag{3.20}$$

where $\Delta \boldsymbol{a} = \boldsymbol{a}_i - \boldsymbol{a}_{i-1}$ is the incremental nodal displacement vector and $\boldsymbol{K}_T$ is the tangential global stiffness matrix evaluated using

$$\boldsymbol{K}_T = \int_V \boldsymbol{B}^T \boldsymbol{D}_T \boldsymbol{B} \, dV \ . \tag{3.21}$$

The R.H.S. in equation (3.19) is the net external force increment Δf. Since in many geotechnical problems, including those discussed in this study, the initial state of stresses $\sigma_0 = \sigma_{initial}$ is defined by gravity loading, the following statement applies to the first term of the force increment

$$\int_V \boldsymbol{N}^T \boldsymbol{b} \, dV = \int_V \boldsymbol{B}^T \sigma_{initial} \, dV \ , \tag{3.22}$$

understanding that this initial state of stresses $\sigma_{initial}$ does not contribute to the straining of the body. The integral $\int_V \boldsymbol{B}^T \sigma_{initial} \, dV$ is the initial internal force vector at the onset of loading due to the initial state of stresses. Substituting equation (3.22) into (3.19) the load Δf producing straining is written as

$$\Delta \boldsymbol{f} = \boldsymbol{T}^i{}_S - \left[\int_V \boldsymbol{B}^T \sigma_{i-1} \, dV - \int_V \boldsymbol{B}^T \sigma_{initial} dV \right] \ , \tag{3.23}$$

where $\boldsymbol{T}^i{}_S$ represents the surface traction applied at the end of the i^{th} load interval.

3.2.3 Solution of the Nonlinear Problem

For linear elastic problems, expression (3.20) represents exactly the equilibrium conditions in the body at all stages. For nonlinear problems, the use of the tangential global stiffness matrix $\boldsymbol{K}_T$ requires, first, that the global stiffness matrix be updated periodically, and second, that the load-steps must be sufficiently small to ensure that $\boldsymbol{K}_T$ remains approximately constant during the load interval. Using an alternative procedure, the displacement increment $\Delta \boldsymbol{a}$ may be calculated assuming an elastic response at the global level. This first approximation is then corrected for the plastic straining of the body, which is executed at the element level (Bathe & Cimento 1980, Bathe 1982, and Zienkiewicz & Taylor 1991). The computational aspects of this initial stiffness approach, which was adopted in the present study, are described in the algorithm shown in Box 3.1. In this algorithm, the first approximation to the displacement increment $\Delta \boldsymbol{a}^*$ is obtained by solving

$$\boldsymbol{K} \, \Delta \boldsymbol{a}^* = \Delta \boldsymbol{f} \quad , \tag{3.24}$$

where $\boldsymbol{K}$ is the initial stiffness matrix. The corrections to the displacement increment $\delta \Delta \boldsymbol{a}^*$ are calculated with a residual load $\boldsymbol{R}$ by using the following recursive equation

$$\boldsymbol{K} \, \delta \Delta \boldsymbol{a}_j^* = \boldsymbol{R}_j \quad , \tag{3.25}$$

with j indicating the iteration number and $\boldsymbol{R}_j$ being given by

$$\boldsymbol{R}_j = \boldsymbol{T} - \left[\left\{ \int_V \boldsymbol{B}^T \sigma_i^* \, dV \right\}_j - \int_V \boldsymbol{B}^T \sigma_{initial} \, dV \right] \quad , \tag{3.26}$$

where σ_i^* is a trial estimate of the updated stresses. This trial stress is defined as

$$\left\{\sigma_i^*\right\}_j = \sigma_{i-1} + \boldsymbol{D}\left\{(\Delta\varepsilon - \Delta\varepsilon^p)\right\}_j \ , \tag{3.27}$$

where $\Delta\varepsilon$ is given by

$$\Delta\varepsilon_j = \boldsymbol{B}\ \Delta\boldsymbol{a}_j^* \ . \tag{3.28}$$

Initially we use the elastic approximation $\Delta\boldsymbol{a}_0^* = \Delta\boldsymbol{a}^*$. For the first iteration, the displacement increment in equation (3.28) is $\Delta\boldsymbol{a}_1^* = \Delta\boldsymbol{a}^* + \delta\Delta\boldsymbol{a}_1^*$, and for subsequent iterations $\Delta\boldsymbol{a}_j^* = \Delta\boldsymbol{a}_{j-1}^* + \delta\Delta\boldsymbol{a}_j^*$. The iterative process is repeated until the residual load vector is smaller than the specified tolerance. The plastic strain increment $\Delta\varepsilon^p$ is evaluated by means of the elasto-plastic constitutive law, which is incorporated into the iterative process at Step 7. The formulation of plasticity is introduced in the next section.

3.2.4 A Simplified Plasticity Model for Sands

The plasticity model considered in this study is based on the flow theory of plasticity. For the fundamental concepts of the theory the reader is referred to the work presented by Chen (1984), and Chen & Baladi (1985). The computational aspects of the theory may be found in the literature; see e.g., Christian et al. (1977), Zienkiewicz & Pande (1977), Owen & Hinton (1980), Mroz et al. (1984), and Zienkiewicz & Taylor (1991).

The implementation of the flow theory of plasticity requires the definition of

(a) the yield surface, given here by the Mohr-Coulomb failure criterion

Box 3.1 **Finite Element Algorithm: Basic Constitutive Law**

1. Assemble the external load vector $\boldsymbol{T}_S$. see eq.(3.19)
2. Define initial stresses and calculate the gravity load vector $\int_V \boldsymbol{B}^T \sigma_{initial}\, dV$.
3. Assemble the tangential elastic stiffness matrix $\boldsymbol{K}_T$. use eq.(3.21)
4. Determine the stresses at the beginning of the time interval σ_{i-1}, and calculate $\int_V \boldsymbol{B}^T \sigma_{i-1}\, dV$.
5. Calculate the load increment Δf for the i^{th} load step. use eq.(3.23)
6. Solve for the initial displacement increment $\Delta \boldsymbol{a}^*$ using the elastic solution,

   $$\boldsymbol{K}\, \Delta \boldsymbol{a}^* = \Delta f \ , \qquad \text{use eq.(3.24)}$$

7. With $\Delta \boldsymbol{a}^*$ calculate the stress increment $\Delta\sigma$ using the prescribed elasto-plastic stress-strain law.
8. Determine the residual load vector $\boldsymbol{R}$. use eq.(3.26)
9. Calculate the norm of the residual load vector with

   $$Norm = \frac{\| \boldsymbol{R} \|}{\| \Delta f \|} \ , \tag{3.29}$$

   and compare with the specified tolerance TOL. If *Norm* < TOL then stop iteration and continue on Step 12. Otherwise, continue with Step 10.

10. Using eq.(3.24) in Step 6 as the recursive relation and with $\boldsymbol{R}$ as the loading term, solve for the correction to the displacement increment $\delta\Delta \boldsymbol{a}^*$ due to plastic straining

    $$\boldsymbol{K}\, \delta\Delta \boldsymbol{a}_j^* = \boldsymbol{R}_j \ . \tag{3.30}$$

    For the first iteration use $\boldsymbol{R}_1 = \Delta f - \int_V \boldsymbol{B}^T \{\Delta\sigma\}_1\, dV$

    and for subsequent iterations $\boldsymbol{R}_j = \boldsymbol{R}_{j-1} - \int_V \boldsymbol{B}^T \{\Delta\sigma\}_j\, dV$ for $j > 1$.

11. Repeat the iteration cycle starting at Step 7, using $\delta\Delta \boldsymbol{a}_j^*$ and $\boldsymbol{R}_j$ instead of $\Delta \boldsymbol{a}^*$ and Δf, respectively.
12. Calculate the corrected displacement increment for the i load step with

    $$\Delta \boldsymbol{a}_i = \Delta \boldsymbol{a}^* + \sum_{j=1}^{n} \delta\Delta \boldsymbol{a}_j^* \ . \tag{3.31}$$

13. Update the total displacement with

    $$\boldsymbol{a}_i = \boldsymbol{a}_{i-1} + \Delta \boldsymbol{a}_i \ , \tag{3.32}$$

    and proceed with next load increment at Step 4.

$$f = \sqrt{3}\ \frac{\bar{\sigma}}{g_1(\theta)} - \eta\ \sigma_m = 0 \quad , \tag{3.33}$$

(b) the plastic potential, which, as presented by Pietruszczak & Stolle (1987), is written as

$$\Psi = \sqrt{3}\ \frac{\bar{\sigma}}{g_2(\theta)} + \eta_{cs}\ \sigma_m\ \ln\left(\frac{\sigma_m}{\sigma_{mo}}\right) = 0 \quad , \quad \text{and} \tag{3.34}$$

(c) a hardening rule, defined as

$$\eta = \eta_f\left(\frac{\varepsilon_q^p}{A + \varepsilon_q^p}\right) \quad . \tag{3.35}$$

The definitions of the stress invariants $\bar{\sigma}$, σ_m, and θ, which are similar to those introduced by Nayak et al. (1972), are presented in Appendix B. The functions $g_1(\theta)$ and $g_2(\theta)$ represent the shapes of the failure envelope and plastic potential in the π plane, respectively. The parameters η, η_{cs} and η_f correspond to the stress ratios at the current state, at critical state, and at failure conditions, respectively. In equation (3.35), A is the model parameter controlling the rate of hardening and ε_q^p is a scalar quantity representing the plastic deviatoric strain invariant, which is calculated incrementally with

$$\Delta\varepsilon_q^p = \Delta\lambda \left\{ \frac{2}{3}\ dev\left(\frac{\partial\Psi}{\partial\sigma}\right)^T dev\left(\frac{\partial\Psi}{\partial\sigma}\right) \right\}^{1/2} \quad . \tag{3.36}$$

In general, the plastic strain increment $\Delta\varepsilon^p$ in equation (3.31) is calculated as

$$\Delta\varepsilon^{p} = \Delta\lambda \frac{\partial\Psi}{\partial\sigma} , \tag{3.37}$$

where $\frac{\partial\Psi}{\partial\sigma}$ is the gradient of the plastic potential (flow vector), with $dev\left(\frac{\partial\Psi}{\partial\sigma}\right)$ being the deviatoric component of the flow vector, and $\Delta\lambda$ is a scale factor for plasticity calculated by means of the consistency condition; that is

$$\Delta f = \frac{\partial f}{\partial\sigma}^{T} \Delta\sigma + \frac{\partial f}{\partial\varepsilon_{q}^{p}}^{T} \Delta\varepsilon_{q}^{p} = 0 . \tag{3.38}$$

The scale factor $\Delta\lambda$ can be derived by substituting equations (3.32) and (3.36) into the consistency condition, yielding

$$\Delta\lambda = \frac{1}{(H_{e} + H_{p})} \frac{\partial f^{T}}{\partial\sigma} D^{e} \Delta\varepsilon . \tag{3.39}$$

For the numerical implementation (Stolle 1991), the scale factor $\Delta\lambda$ may be approximated by the simpler expression

$$\Delta\lambda = \frac{\langle f\rangle}{(H_{e} + H_{p})} , \tag{3.40}$$

where $\langle f \rangle = f$ if $f > 0$, and

$\langle f \rangle = 0$ if $f \leq 0$.

In equation (3.40), f is evaluated at a pseudo-elastic stress $\sigma_{i}^{e} = \sigma_{i-1} + D \Delta\varepsilon$. In the case that σ_i^e lies on the yield surface the value of f is zero.

In equations (3.39) and (3.40), H_e and H_p are known as the elastic and the plastic hardening moduli, respectively. The definitions of H_e, H_p, and the gradients of the yield function and the plastic potential are given in Appendix B.

3.3 The Pressure-Dependent Constitutive Law

The pressure-dependent constitutive law is similar to the basic law, the main difference being that the elastic stiffness matrix is now updated after each load increment to account for changes on the pressure-sensitive elastic modulus. The working hypotheses for this model are:

- The elastic modulus E is a variable material property depending on the confining stress $\bar{\sigma}_c$ while Poisson's ratio remains constant;
- elastic material properties, E and ν remain isotropic during loading;
- the formulation of plasticity is identical to the that of the basic model formulation; and
- in the case of zero confinement or tensile stresses, a minimum value of $E = 5\ MPa$ and a small amount of confining stresses are assumed.

The first assumption is a direct consequence of the analysis of experimental results obtained from the series of drained triaxial tests on saturated sand specimens presented in Chapter 2. In the pressure-dependent constitutive model, the stress-dependent elastic modulus is expressed using the exponential form

$$E(\bar{\sigma}_c) = E_{ref}\left(1 - e^{r}\right) , \qquad (3.41)$$

where E_{ref} is the limiting value of E measured from triaxial testing. For the Ottawa sand utilized in the experimental work, and for an average dry unit weight of 17.2 *kN/m³*, the value of E_{ref} is approximately equal to 240 *MPa*. The exponent r in equation (3.41) is given by

$$r = \frac{1000}{E_{ref}} \bar{\sigma}_c \quad . \tag{3.42}$$

For the adopted sign convention, e.g., negative compression, the exponent r is a negative dimensionless parameter. The elastic constitutive matrix is redefined as

$$\boldsymbol{D} = \frac{E(\bar{\sigma}_c)}{(1+\nu)(1-2\nu)} \begin{bmatrix} 1-\nu & \nu & 0 & \nu \\ & (1-\nu) & 0 & \nu \\ & & \frac{1-2\nu}{2} & 0 \\ \textit{symm.} & & & 1-\nu \end{bmatrix} \quad . \tag{3.43}$$

Here, increments in the elastic modulus lead to an incremental elastic stiffness matrix, given by

$$\Delta\boldsymbol{D} = \frac{\Delta E(\bar{\sigma}_c)}{E(\bar{\sigma}_c)} \boldsymbol{D} \quad , \tag{3.44}$$

where increments in the elastic modulus are determined with

$$\Delta E(\bar{\sigma}_c) = 1000 \ \Delta\bar{\sigma}_c \ e^r \quad . \tag{3.45}$$

In the adopted sign convention, the principal stresses are defined in the following order

$$\sigma_3 \le \sigma_2 \le \sigma_1 \tag{3.46a}$$

but in terms of absolute magnitude, the principal stresses are ordered as

$$|\sigma_3| \geq |\sigma_2| \geq |\sigma_1| \quad , \tag{3.46b}$$

with σ_1, σ_2, and σ_3 corresponding to the major, intermediate, and minor principal stresses, respectively. For the pressure-dependent constitutive law, the confining stress is always defined in terms of the principal stress with the minimum magnitude; that is with σ_1. Furthermore, since it is considered that cohesionless soils can not develop tensile stresses, the Mohr diagrams representing the state of stresses always span to the left of the vertical axis.

The triaxial results introduced in Chapter 2, Section 2.2.3, indicated some variations on plastic parameters with increasing levels of confinement. However, these variations were observed to be small in comparison to the substantial increase in the confining stresses. Then it seemed reasonable to assume that the plastic behavior is controlled by stress-independent material parameters. Owing to changes in the elastic constitutive matrix, equation (3.5) should be revised. For an updated elastic matrix, equation (3.5) should be written as

$$\Delta\sigma = \boldsymbol{D}\ \Delta\varepsilon^e + \Delta\boldsymbol{D}\ \varepsilon^e \quad , \tag{3.47}$$

or after substituting equation (3.44) into (3.47) ,

$$\Delta\sigma = \boldsymbol{D} \left[\Delta\varepsilon^e + \frac{\Delta E}{E}\ \varepsilon^e \right] \ . \tag{3.48}$$

The evaluation of elastic stress increase with expression (3.48) is viable but cumbersome and can be the source of numerical instabilities. A simpler alternative option was adopted; that is the second term in equation (3.48) was disregarded, while taking load steps sufficiently small as to ensure this term remains negligible.

Minimum values for confining stress and elastic modulus were specified to prevent zero division errors during computations. In the present algorithm, the global matrices ***K*** and ***D*** are updated at the beginning of each load step, but remain constant during the iterations, as indicated in the algorithm summarized in Box 3.2.

Box 3.2 Finite Element Algorithm: Pressure-Dependent Constitutive Law

```
1.   Assemble the external load vector $T_S$.                                   see eq.(3.19)
2.   Define initial stresses and calculate $\int_V B^T \sigma_{initial}\, dV$.
3.   Assemble the tangential elastic stiffness matrix $K$                        use eq.(3.21)
4.              :
5.              :
6.              :
7.   From Steps 4 to 13 the procedure is the same as indicated in Box 3.1 for the Basic Constitutive Law.
8.              :
9.              :
10.             :
11.             :
12.
13.  Update total displacements with
          $a_i = a_{i-1} + \Delta a_i$                                           (3.32)
14.  Calculate confining stress $\bar{\sigma}_c$ and form the stress-dependent $D$ matrix    use eq.(3.43)
15.  Proceed with the next load increment at Step 3.
```

The process of updating the global matrix ***K*** increases the computation time significantly. On the other hand, the use of the updated stiffness matrix improves the rate of convergence during the iterations, thereby reducing computation time. This approach corresponds to the actual modified Newton-Raphson method (Zienkiewicz & Taylor, 1991).

3.4 The Anisotropic Constitutive Law

The main objective in this section is to present an anisotropic constitutive model that can take into account more realistic aspects associated with an increase in confinement. The discussion begins by addressing the rationale for including anisotropy when modeling soils in the FCV device. A brief review on anisotropy for granular materials is also presented. At the end of this section, the assumptions and working hypothesis, on which the anisotropic constitutive model is founded, are introduced. Complementary information regarding the formulation of the anisotropic model is included in Appendix C.

3.4.1 Necessity for Modeling Anisotropic Behavior

The three models developed in this investigation can be classified within the general category of phenomenological approaches for the description of soil behaviour (Pietruszczak 1987b) . In this category, constitutive relations are conceptually described at the macroscopic level. The most important advantage of this class of approaches is that the elasto-plastic theories for continuum materials can be readily used for the description of granular or particulate media. There are limitations, however, in the type of phenomena that a macroscopic model can simulate.

Soil behaviour is very complex and, as explained by Chen (1984) and Chen et al.(1985), no single model can account for all aspects of a phenomena. It is necessary then to consider a practical engineering approach, in which only the dominant aspects of the phenomena for a specific soil-related problem are taken into account.

Consider for instance the problem of the drained triaxial compression test. Stresses and strains are considered to be distributed in a fairly uniform manner, and the response seems to be controlled by deviatoric stresses under constant confinement. This problem might be accurately described by the basic constitutive model. The response of FCV specimens, on the other hand, depends very much on increasing levels of confinement, high stress-strain gradients, rotation of principal planes, and by stress-dependent material properties, which the basic model is not capable to simulate. The model implementing the pressure-dependent constitutive law introduces some improvements with respect to basic model when simulating FCV responses, but during the model development stage it was clear that the observed behaviour may not be fully captured by the pressure-dependent law.

As previously mentioned, the concept of stress-induced anisotropy is believed to be a dominant aspect of FCV testing, and in the next section, anisotropy is briefly discussed with reference to the implementation of the anisotropic constitutive model.

3.4.2 Inherent and Induced Anisotropy

Experimental observations have shown that under specific circumstances the behaviour of granular soils can be strongly affected by the existence of inherent anisotropy, by the development of induced anisotropy, or by a combination of both. See, e.g., Pickering (1970), Arthur & Menzies (1972), and Wong & Arthur (1985). Feda (1982) has presented a good compilation of work done in the field of particulate material, in relation to anisotropy. Symes et al.(1988) have also reported important experimental results related to the effects of principal plane rotations and stress-induced anisotropy on the response of sands. Anisotropy has been observed in soil response for every strain range; for example, in very small, small, and large strains ranges, which might be correlated to elastic, quasi-elastic, and plastic deformations, respectively[1].

For the case of very small strains, wave propagation techniques have enabled researchers to evaluate with reasonable accuracy the effects of inherent and induced anisotropy on the behaviour of granular soils. On the other hand, for the cases of small and large strains, the measurement of anisotropic properties is not a simple task. Subtle changes in testing conditions can lead to large discrepancies in material response, with the consequence that the interpretation of experimental results is often contradictory or inconsistent (Feda 1982, Oda et al. 1978, and Bellotti et al. 1996). There have been many reports describing the observation of anisotropy from a qualitative prospective, but accurate measurements of anisotropic material properties, for the ranges of small and large strains are not abundant. Because of this, researchers have found it difficult to validate mathematical descriptions of anisotropy (Wong et al. 1985). With regards to induced anisotropy, it appears that the trend has been to include the description of anisotropy in the formulation of plasticity (Baker & Desai 1984, Pietruszczak 1997, and Mroz & Pietruszczak 1983), the argument being that the range of elastic behaviour for soils is small or negligible. However, experimental results from testing programs in the range of very small strains clearly indicates that stress-state induced anisotropy also occurs in the elastic range (Hardin & Black 1966, Yu & Richart 1984, Hardin & Blandford 1989, Jiang et al. 1997, and Jovičić & Coop 1997).

---

[1] As suggested by Atkinson & Sallfors (1991) very small strains are considered to be less than 0.001%. Small strains lie between 0.001 and 1%, and large strains are considered to be larger than 1%.

For the anisotropic model introduced in this section, a simplified approach is considered, which accounts for inherent and induced anisotropy. Specifically, stress-induced anisotropy is considered only in the determination of the elastic stress-strain relationship. The formulation of plasticity is considered to be controlled by material properties, which are essentially constant, stress-independent and isotropic. The reason for this simplification, i.e. anisotropic conditions within the elastic range only, is that the elastic behaviour appears to be a dominant aspect of the FCV testing phenomena, while plasticity and failure conditions associated with the deviatoric stresses appear to have a lesser influence in FCV specimen responses. Based on these assumptions, the isotropic deviatoric law is considered to be sufficient to handle plasticity in a simplified manner.

3.4.3 Working Hypothesis for Induced-Anisotropy

The elastic matrix for the anisotropic constitutive model is defined for the general case of orthotropic anisotropy, in which the stress-dependent elastic moduli are defined in the directions of the principal stresses, as explained in Appendix C, and given by

$$E_1 = E_{ref}\left(1 - e^{r_1}\right) \quad , \quad r_1 = \frac{1000}{E_{ref}}\left(\frac{\sigma_2 + \sigma_3}{2}\right) \; , \tag{3.49a}$$

$$E_2 = E_{ref}\left(1 - e^{r_2}\right) \quad , \quad r_2 = \frac{1000}{E_{ref}}\left(\frac{\sigma_3 + \sigma_1}{2}\right) \; , \tag{3.49b}$$

$$E_3 = E_{ref}\left(1 - e^{r_3}\right) \quad , \quad r_3 = \frac{1000}{E_{ref}}\left(\frac{\sigma_1 + \sigma_2}{2}\right) \; , \tag{3.49c}$$

$$G_{13} = G_{ref}\left(1 - e^{r_{13}}\right) \quad , \quad r_{13} = \frac{1000}{G_{ref}}\left(\frac{\sigma_3 + \sigma_1}{2}\right) \; . \tag{3.49d}$$

With the elastic moduli defined in the directions of the principal stresses, the constitutive matrix $\boldsymbol{D}_P$ (Lekhnitskii, 1968; and Du & Dusseault, 1994) is given by

$$\boldsymbol{D}_P = \frac{1}{G_{13}\,\Delta}\begin{bmatrix} \frac{1}{E_2}\left(\frac{1}{E_3}-\frac{\nu_3^2}{E_2}\right) & \frac{1}{E_1}\left(\frac{\nu_1}{E_3}+\frac{\nu_2\nu_3}{E_2}\right) & 0 & \frac{1}{E_1E_2}\left(\nu_2+\nu_3\,\nu_1\right) \\ & \frac{1}{E_1}\left(\frac{1}{E_3}-\frac{\nu_2^2}{E_1}\right) & 0 & \frac{1}{E_1}\left(\frac{\nu_3}{E_2}+\frac{\nu_1\,\nu_2}{E_1}\right) \\ \textit{symmetric} & & G_{13}^2\,\Delta & 0 \\ & & & \frac{1}{E_1}\left(\frac{1}{E_2}-\frac{\nu_1^2}{E_1}\right) \end{bmatrix} , \tag{3.50}$$

where the values of the Poisson's ratios ν_1, ν_2, and ν_3 are assumed to be constant material properties, and Δ, the determinant of the compliance matrix, is given by

$$\Delta = \frac{1}{E_1\,G_{13}}\left(\frac{1}{E_2E_3}-\frac{\nu_1^2}{E_1E_3}-\frac{\nu_2^2}{E_1E_2}-\frac{\nu_3^2}{E_2^2}-2\,\frac{\nu_1\,\nu_2\,\nu_3}{E_1\,E_2}\right) \quad ; \tag{3.51}$$

see, for example, Malvern (1969), Pickering (1970), and Du & Dusseault (1994). The principal stresses in equations (3.49) are obtained by using the stress transformation matrix

$$\sigma_P = \boldsymbol{T}\,\sigma_L \quad , \tag{3.52}$$

which express the principal stresses σ_P in terms of the stresses from the local system σ_L. The stress transformation matrix $\boldsymbol{T}$ is written as (see Lekhnitskii 1963, and Malvern 1969)

$$T = \begin{bmatrix} \cos^2\alpha & \sin^2\alpha & \sin 2\alpha & 0 \\ \sin^2\alpha & \cos^2\alpha & -\sin 2\alpha & 0 \\ -\dfrac{\sin 2\alpha}{2} & \dfrac{\sin 2\alpha}{2} & \cos 2\alpha & 0 \\ 0 & 0 & 0 & 1 \end{bmatrix}, \tag{3.53}$$

with the rotation angle α defined in terms of the local stresses as

$$\tan\alpha = \frac{\sigma_{rz}}{\left(\dfrac{\sigma_r - \sigma_z}{2}\right) - \dfrac{1}{2}\sqrt{\left(\sigma_r - \sigma_z\right)^2 + 4\,\sigma_{rz}^{\;2}}} \tag{3.54}$$

The constitutive matrix referred to the local system is then obtained with

$$D_L = T_d^{\;T}\, D_P\, T_d \tag{3.55}$$

where T_d is the strain transformation matrix given by

$$T_d = \left(T^T\right)^{-1} = \left(T^{-1}\right)^T = \begin{bmatrix} \cos^2\alpha & \sin^2\alpha & \dfrac{\sin 2\alpha}{2} & 0 \\ \sin^2\alpha & \cos^2\alpha & -\dfrac{\sin 2\alpha}{2} & 0 \\ -\sin 2\alpha & \sin 2\alpha & \cos 2\alpha & 0 \\ 0 & 0 & 0 & 1 \end{bmatrix}. \tag{3.56}$$

3.4.4 Implementation

Regarding the general solution algorithm, the anisotropic model differs with the pressure-dependent model in the formation of the stiffness or material matrix. The procedure implemented for the anisotropic model is outlined in Box 3.3.

In the anisotropic model, the influence of the second term in equation (3.47), is also neglected, for example $\{ \Delta \boldsymbol{D} \; \varepsilon^e \} \rightarrow 0$. Therefore, care must be taken to select a sufficiently small size for the load step.

Box 3.3 Finite Element Algorithm: Anisotropic Constitutive Law

```
1.  Assemble the external load vector $T_S$.                                  see eq.(3.19)
2.  Define initial stresses and calculate $\int_V B^T \sigma_{initial} \, dV$.
3.  Assemble the tangential elastic stiffness matrix $K$ with $D_L$.    use eqs.(3.21) & (3.50)
4.                 :
5.                 :
6.                 :
7.  From Steps 4 to 13 the procedure is the same as indicated in Box 3.1 for the Basic Constitutive Law.
8.                 :
9.                 :
10.                :
11.                :
12.                :
13. Update total displacements with
        $a_i = a_{i-1} + \Delta a_i$                                           (3.32)
14. Determine $\alpha$, the orientation of principal stress directions         use eq.(3.54)
15. Calculate principal stresses $\sigma_1$; $\sigma_2$; and $\sigma_3$        use eq.(3.52)
16. Define elastic moduli $E_1$; $E_2$; $E_3$; and $G_{13}$                    use eq.(3.49)
17. Form the $D_P$ matrix in the principal stress directions                   use eq.(3.50)
18. Transform $D_P$ back into the global system as $D_L$                       use eq.(3.55)
19. Proceed with the next load increment at Step 3.
```

3.5 Closure

This section presents a summary of the basic assumptions introduced in the three numerical models described in Chapter 3. The numerical performance of the three models developed in this thesis is evaluated in Chapter 4.

3.5.1 Assumptions for the FE Model: Basic Constitutive Law

The FE model assumes that the boundary-valued problem is governed by elasto-plastic behaviour defined in terms of a deviatoric hardening law. Elasto-plastic material properties are assumed to be stress-independent and isotropic. Different degrees of material inhomogeneities can be introduced by specifying different material properties within the discretized domain.

3.5.2 Assumptions for the Pressure-Dependent Law

Elasto-plastic behaviour is controlled by a deviatoric hardening law and the elasto-plastic material properties are assumed to be isotropic. A stress-dependent elastic modulus is defined in terms of the confining stress $\bar{\sigma}_c$, assumed to be the major principal stress σ_1.

3.5.3 Assumptions for the Anisotropic Law

Similar to the previous two constitutive laws, elasto-plastic behavior is described by the same deviatoric hardening law. Material properties are defined in the context of orthotropic anisotropy. Anisotropy is assumed to be stress-induced. The formulation can also accommodate inherent anisotropy, specified at the initial conditions. Anisotropy only affects the elastic moduli. The development of plastic strains is assumed to be controlled by constant, stress-independent, isotropic, material properties.

The choice of stress-dependent moduli defined in terms of principal stresses ensures that material constraints are satisfied automatically. Consequently, the principle of work invariance and the postulate of positive strain energy are preserved in the presented formulation.

Chapter 4

NUMERICAL ANALYSES

4.1 Introduction

The first objective of the numerical analyses undertaken in this chapter is to obtain insightful information, which could not be measured, regarding the behaviour of sand specimens in the current FCV device. Based on the knowledge gained from these simulations, the second objective of this chapter is to provide guidelines for the design of a new confining device in which stress conditions may be better controlled for the purpose of physical modeling of reduced-scale piles.

The problem of calibrating the finite element codes is addressed first by simulating triaxial test responses, and then by simulating the behaviour of FCV specimens tested under membrane loading; i.e. uniformly applied pressure. These simulations are primarily concerned with the comparison of observed and predicted behaviour. The simulations of triaxial test responses were completed using the three constitutive models mentioned in the previous Chapter, namely the basic, the pressure-dependent, and the anisotropic models. FCV loading conditions, on the other hand, were only simulated with the pressure-dependent and anisotropic models. The basic model is not considered to be suitable for this problem since it takes no account of the effects of confining stresses on material properties, which is one of the most relevant characteristics of FCV testing conditions on sands. The results of the calibrated models are then used to determine patterns of stresses and displacements for the entire domain of the FCV testing problem. This step is considered as the first application of the calibrated models.

During the interpretation of test results it is often presupposed that material properties are uniformly distributed. However, in the case of the FCV testing, it is worth considering by means of numerical modeling, the case where distributions of material properties are not uniform. The second application of the numerical models is to test the consequence of non-uniformities, with particular attention being paid to the numerical simulation of FCV specimens with random distributions of material properties. The idea is to determine whether or not non-uniformities have a significant influence on the measured responses of FCV specimens.

Finally, the third application of the numerical models is related to the optimization and design of a new confining vessel. The optimization process initially consists of defining typical stress conditions in the field, and then seeking an optimal shape for the confining vessel in which stresses are the closest to those assumed field conditions. A few basic trial shapes are simulated and the predicted stresses are evaluated in relation to typical stress conditions found in the field.

4.2 Simulations of Triaxial Testing

The triaxial testing series considered specimens tested under various levels of confinement. All levels of confinement were simulated using the three constitutive models mentioned previously. Given the fact that numerical simulations were considered successful in describing triaxial responses at all levels of confinement, and for the purpose of conciseness, only one representative case is described in the ongoing discussion. This is the case of triaxial test TT500, where the sample is tested under the effective confining pressure of 500 *kPa*.

4.2.1 Discretization and Loading

The finite element grid used for the simulations of test TT500 consisted of 650 six-noded triangular elements, with 1377 nodes. The initial configuration of the grid is illustrated in Figure 4.1(a), where it may be observed that only half of the sample domain is discretized. The specified boundary conditions include vertical rollers along the centerline, fixed nodes at the bottom, and free nodes at the right vertical side, while nodes on the top are constrained with a prescribed uniform displacement, i.e. the displacement-controlled loading of the actual test. The loading of the sample is described by the top displacement δ versus time t, as shown in Figure 4.1. The geometrical characteristics of the sample are also included in this figure.

The main assumptions of the analysis are uniform distributions of material properties and that there is no slippage at the contact locations with the base and the loading cap. Table 4.1 summarizes the list of material properties estimated from the interpretation of experimental data, and compares them with calibrated properties from the numerical analyses corresponding to each constitutive model.

For the case of the anisotropic constitutive model, the available experimental data is not sufficient to obtain a conclusive estimation of the three independent Poisson's ratios required by this model. Because of this, the values of ν_1, ν_2, and ν_3 were arbitrarily defined to be the same and equal to 0.37. It is further assumed that values of Poisson's ratios are stress-independent material properties.

Table 4.1 Summary of material properties utilized in the numerical analyses

	Elastic moduli $[MPa]$	Poisson's ratio ν	Stress ratio at failure η_f	Stress ratio at critical state η_{cs}	Hardening Parameter A
Experimental data	$E = 203$	0.36	1.39	1.07	0.00049
Basic constitutive law	$E = 203$	0.37	1.44	1.00	0.00070
Pressure-dependent constitutive law	$E_{ref} = 240$	0.37	1.44	1.00	0.00070
Anisotropic constitutive law	$E_{ref} = 240$ $G_{ref} = 95$	$\nu_1 = \nu_2 = \nu_3 =$ 0.37	1.44	1.14	0.00070

4.2.2 Comparison of Predicted and Observed Responses

Comparisons of the experimental and numerical responses in terms of the load-displacement and volumetric change characteristics of the triaxial test TT500 are shown in Figures 4.2(a) and 4.2(b), respectively. An important feature observed in these plots is the fact that the responses predicted with the three different constitutive models are essentially identical. As discussed in Chapter 3, under the prevailing conditions of constant confining stresses the three models should predict similar responses. This requirement is clearly satisfied by the three numerical models. Whereas the observed responses, i.e., load versus vertical displacements, are quite accurately predicted within both elastic and plastic ranges of deformation, the predicted volumetric changes exhibited some discrepancy when compared with the measured response. As observed in Figure 4.2(b), the numerical models overpredicted the amount of volumetric compaction during the initial or quasi-elastic stage of the test; i.e., for axial strains lower than 0.5%. Within the range of plastic deformations, the rate of volumetric deformation is accurately predicted, as both measured and predicted responses in Figure 4.2(b) showed the same slope.

Similar discrepancies were observed in simulations of triaxial tests performed under different levels of confinement; for example, TT50 to TT1050. It is not completely clear whether these discrepancies are due to experimental errors or to inadequacies in the constitutive laws, or a combination of both. In any case, the discrepancies between predicted and observed volumetric strains are considered to be relatively small. In general, the ability of the three constitutive models to describe the observed behaviour is considered to be satisfactory. The capability to simulated simple elasto-plastic behaviour of sands under drained conditions has been verified. It should be noted that during a sensitivity study, it was observed that values of Poisson's ratio between 0.45 and 0.49 improved predictions of volumetric change during the initial elastic deformations. However, the use of such high values of Poisson's ratio was considered inadequate, as such high values are typical for nearly incompressible materials.

4.2.3 Stress and Strain Fields

The distributions of vertical, radial, and shear stresses are represented by contour plots in Figures 4.3, 4.4, and 4.5, respectively. The stress fields are shown at three different stages of deformation, namely for axial strains ε_a equal to 0.5%, 2.1%, and 5.3%, shown in plots (a), (b), and (c) respectively. Volumetric strains are shown in the same manner in Figure 4.6.

As discussed in Section 2.2.5, the usual assumption that triaxial samples deform under relatively uniform stress-strain conditions is not always correct. In the cases where the presence of porous stones restrain the lateral displacement of the sample's top and bottom, the stress-strain fields are approximately uniform only for the range of small deformations, as seen when comparing plots (a) and (b) of Figure 4.1. It should be noted that displacements are magnified by a factor of two in order to visualize the non-uniform straining of the sample. By inspection of the predicted stress and volumetric strain fields, shown in Figures 4.3 to 4.6, approximate uniform conditions exist at axial strain levels of 0.5% or lower. This range approximately coincides with the strain range where compaction dominates volumetric changes. At the point of maximum compaction, shown as the absolute minimum in Figure 4.2(b), the entire sample is close to the critical state condition. Further straining of the sample results in dilation along with a rapid departure from the conditions of stress and strain uniformity. This is shown in plots (b) and (c) of Figures 4.3 to 4.6. The simulated stress fields also indicate that the non-uniform conditions are quite severe even at early stages of dilation. This observation may be inferred from the high stress gradients exhibited in Figures 4.3 to 4.6 for axial strain levels of 2.1% and 5.3%. Furthermore, in Figures 4.6(b) and 4.6(c), it is shown that the top and bottom portions of the sample are still contracting, even though the central portion of the sample is experiencing dilation. As a result, at high levels of axial strain, the volumetric changes measured during the actual test reflect net volumetric changes, which are not necessarily representative of the material response within the entire sample. Non-uniform stress-strain conditions become a very significant factor when triaxial samples are tested with restrained ends. Therefore, the analysis and interpretation of experimental results must take this factor into account.

4.2.4 Principal Stresses

In the present discussion, the adopted sign convention for stresses corresponds to that of soil mechanics, in which the major principal stress is defined as the maximum compressive stress, with the minor principal stress being the minimum compressive stress. Prior to the start of a triaxial test, the stress state in a consolidated drained sample is defined by hydrostatic loading. In the Mohr diagram, this stress state corresponds to one point on the horizontal axis. Immediately after the axial loading stage of the test begins, the principal stress directions are associated with the vertical and radial directions, respectively, as shown in Figure 4.7(a). The predicted principal stress directions, corresponding to 5.3 % of axial strains, are illustrated in Figure 4.7(b). From this figure it may be seen that the principal directions do not suffer significant rotations during triaxial testing conditions. This is in accordance with the common assumption that principal directions do not rotate during a triaxial test. It is worth mentioning that the numerical analysis also provides the values of the out-of-plane or hoop stresses.

4.3 Simulations of FCV Testing

In the present discussion, the description of numerical analyses of FCV testing is limited to the case of the uniform pressure configuration (membrane loading). The reasons not to include simulations of FCV testing using the uniform displacement configuration (piston loading) are related to some important limitations of this FCV loading configuration, namely, the tilting of the piston as the load is applied and the occurrence of sudden stick-slip jumps during loading. From an experimental point of view, these types of anomalies or erratic behaviour are not considered suitable for a testing device. Therefore the decision was made to discard the uniform displacement (piston loading) as an alternative option for controlling the confining stresses in FCV specimens. It should be mentioned, however, that numerical simulations were conducted for FCV test with the piston loading, confirming that such loading cannot produce the desired stress conditions in the control volume.

4.3.1 Discretization and Loading

A typical finite element mesh for an FCV specimen is shown in Figure 4.8(a). The grid has 713 six-noded triangular elements and 22 interface elements, with 1545 nodes. Geometric characteristics, as well as the material properties of the sand specimen are included in this figure. The boundary conditions are defined by rollers along the centerline on the left side, free nodes at the top and bottom boundaries, and fixed nodes on the right side boundary. The stresses acting on the specimen at initial conditions are defined in terms of the specimen's self-weight.

Owing to the fact that displacements at the bottom were relatively small, potential problems related to membrane effects were considered to be negligible, and therefore no attempt was made to include the membrane in the discretization. A uniformly applied pressure was specified along the bottom row of elements, increasing from zero to 500 *kPa* in 30 minutes, as defined by the ramp load shown in Figure 4.8.

Twenty two interface elements were placed on the right side boundary representing the specimen-vessel interface. The amount of unit friction mobilized along the interface was defined in terms of the normal stresses σ_n' acting on these interface elements and on the friction coefficient tanδ, namely $f_{int} = \sigma'_n \tan\delta$. Adequate results were obtained with values of the friction coefficient tanδ = 0.28.

The actual tests were carried out with a one-inch thick steel plate placed freely on top of the specimen, which had the function of enforcing uniform displacements at this boundary. The effect of the steel plate was included by defining the elements corresponding to the top row with elastic material properties of steel, i.e., elastic modulus $E_{st} = 210\ GPa$ and Poisson's ratio $\nu = 0.30$.

The general assumptions considered for these simulations are that the material properties of the sand specimen are uniformly distributed and that loading is quasi-static.

The distorted grid shown in Figure 4.8(b), which corresponds to the anisotropic constitutive model at the maximum applied load of 500 *kPa*, illustrates the displacements, magnified by a factor of 10. From this figure, one can observe the predicted sliding of the specimen along the wall in the lower part of the vessel. Also, the simulated metal plate can be identified on the top row of elements where no significant distortions are observed.

4.3.2 Comparison of Predicted and Observed Responses

A comparison of responses between measurements and simulations are presented in terms of the top and bottom vertical displacements versus applied load, shown in Figure 4.9, and the distributions of vertical and radial stresses along the centerline, as shown in Figure 4.10.

Vertical displacements at the top at the specimen are shown in Figure 4.9(a). This figure shows that, both, the pressure-dependent and anisotropic constitutive laws had problems to reproduce the measured response. Although better agreement in magnitude was obtained at high applied pressure with the anisotropic constitutive law, the rate of increase in displacements is better modeled using the pressure-dependent law. Both numerical models, which predicted vertical displacements at the bottom that were relatively accurate, showed a pattern of displacement versus load behaviour similar to that observed in the experimental data, as seen in Figure 4.9(b).

Figure 4.9(c) compares predicted and observed displacements at mid-height of the specimen-vessel interface. At this location, the anisotropic model predicted displacements that were more accurate than those predicted with the pressure-dependent model. Overall, both constitutive laws were able to capture the spatial deformation trends reasonably well.

With regard to the prediction of stresses, Figure 4.10 illustrates the variations of normalized vertical and radial stresses, and the stress ratio versus the normalized depth along the centerline, as shown in plots (a), (b), and (c), respectively. The experimental data points are provided with error bars representing the uncertainty on the measured stresses. It should be mentioned that these uncertainty errors, which were estimated from a series of calibration tests performed for each sensor[1], refer to uncertainties associated with instrumentation errors and do not take into account the possible variations of the actual stress field.

In general, the magnitude of the predicted vertical and radial distributions compared well with the measured stresses, with the exception of the measurements at the bottom sensor. At this particular sensor, the measured vertical stresses are somewhat higher than the actual pressure applied to the bottom of the specimen. Since it is unlikely that vertical stresses near the loading membrane are higher than the applied pressure, this inconsistency is attributed to

---

[1] These stress sensors are referred to the Force Sensing Resistors.

instrumentation errors. In this respect, predicted stresses near the bottom provide a stress distribution, which are believed to be more reasonable than those indicated by measurements.

Figure 4.10(c) shows discrepancies between predicted and observed distributions of the *k* values. The error bars associated with values of *k* are larger than those corresponding to the stresses, indicating the cumulative effect of errors in the predicted stresses. An important observation here is that the numerical simulations confirmed the increase of *k* when going from the bottom to the top.

The behaviour of sand in a FCV device is complex, presenting difficulties for both experimental and mathematical methods of analyses. The observation that material properties of granular materials are strongly sensitive[2] to principal stress directions, as has been suggested by some researchers, indicates that a constitutive law should consider the influence of stress change and rotation of principal stress directions on the mechanical properties; see e.g., Oda et al. 1985, Hardin et al. 1989, Symes et al. 1988, and Bellotti et al. 1996. The anisotropic constitutive law describes the observed behaviour slightly better than the pressure-dependent model. This is attributed to the anisotropic constitutive law accommodating the directional stress dependency of the elastic modulus, which is believed to be important at the high levels of confinement provided by the FCV device. In general, it can be said that the numerical predictions are similar in magnitude and distribution to the experimental observations. The main difficulty with the proposed anisotropic model lies in the selection of constitutive parameters. Since there is insufficient experimental information for the verification of the

---

[2] The sensitivity of material properties to changes in the principal stresses and their directions is considered to be significant mainly for cases where the state of stresses is dominated by confining stresses, as in the case of FCV loading, rather than shearing stresses.

anisotropic model, further studies should be conducted addressing this topic.

4.3.3 Stress Fields

The predicted vertical and radial stresses are shown at the moment of maximum applied pressure in the contour plots of Figures 4.11(a) and 4.11(b), respectively. The stress distributions were simulated using the pressure-dependent constitutive model. The resulting distributions of stresses offer valuable information with respect to the stress fields that develops in an FCV. The vertical stress field is characterized by a smooth distribution of stresses; i.e., with no significant high gradients. The distribution of radial stresses, on the other hand, exhibits some areas of stress concentration, particularly where the inclined wall ends at the lower vertical part of the vessel, and at the interface of the specimen with the top metal plate. It is also interesting to note the intensity of radial stress in the vicinity of the outer wall near the bottom. The lower stress level suggests that soil arching may have developed around this zone. The distribution of shear stress, shown in Figure 4.12(a), is characterized by low values of shear stress in an area surrounding the centerline, and by the concentration of stresses shown at the lower part of the inclined wall. Contrary to what might have been expected, the shear stresses developed along the interface between the top part of the specimen and the steel plate appears to be insignificant. It should also be mentioned that the shear stresses considered in Figure 4.12(a) correspond to the global *x-y* frame of reference.

Given the distribution of *k* values, shown in the contour plot of Figure 4.12(b), it may be observed that for most of the middle portion of the specimen the stress ratio is approximately equal to one. For the lower part it is less than one, and for the upper part it is greater than one. With respect to the problem of physical modeling, this aspect of the FCV loading phenomena is considered to be a weak feature of the current FCV device. For the case of normally consolidated natural sand deposits, realistic values of the stress ratio lie between 0.35 and 0.60. On the other hand, for overconsolidated deposits *k* values may be close to one, see Bowles (1996). What is more important in the case of uniform sand deposits, the values of the stress ratio remain approximately constant with depth. This characteristic constant distribution of *k* with depth is not being reproduced in the current FCV device around the control volume. Therefore, one of the criteria to be considered for the optimization of a new device is the ability of the vessel to produce a more uniform distribution for the stress ratio.

4.3.4 Principal Stresses

The principal stress directions for stress conditions at the start and at the end of loading are presented by using the streamline plots of Figures 4.13(a) and 4.13(b), respectively. As was the case for the triaxial problem, the directions of principal stresses shown in Figure 4.13 are defined in terms of the sign convention used in soil mechanics, where the major principal direction is always given by the maximum compressive stress at a point.

With reference to the numerical analysis of the FCV test responses, the streamline plots shown in Figure 4.13(b) confirm the assumption, as discussed in Chapter 3, Section 4.1, that principal stress directions are subjected to important rotations during FCV testing. At the beginning of the test, the major principal directions are vertical while minor principal directions are horizontal. By the end of the test, the principal directions for the portion of the specimen adjacent to the inclined wall have suffered rotations ranging between 40° and 50° with respect to the original orientation. Meanwhile, in the upper half of the specimen, and close to the centerline, principal directions have rotated a full 90°, concluding that rotation of principal stress directions is an important aspect of FCV loading.

In relation to the problem of physical modeling, the rotation of principal stress directions, particularly in the upper half of the specimens, reflects the inadequacy of the current FCV device to reproduce scaled field stresses, as ideal stress conditions in the field are usually consistent with a vertical orientation of the major principal directions. With this in mind, the orientation of principal stresses will be used, in Section 4.5 of this Chapter, as a design consideration during the optimization process.

4.4 Influence of Non-Uniform Distribution of Material Properties

One of the conclusions emerging from the evaluation of experimental results was that FCV test responses are reproducible, provided the specimens are formed with the same compaction procedure. The underlying assumption was that if observed responses from two identical tests were the same or very similar, then the material properties for both specimens were reproduced during the testing events. Furthermore, it was assumed that the specimen's material properties, specifically density, are uniformly distributed at the start of a FCV test. However, based on experimental observations alone, it was felt that it may not be feasible to determine whether these assumptions are valid. The assumption of uniform distributions of material properties is addressed in this section by means of simulating the responses of FCV specimens with non-uniform distributions of density, and comparing these results with those obtained from simulations of FCV specimens with initial uniform densities.

Within the context of FCV testing, and depending on the degree of complexity, three levels of non-uniform distributions may be considered. For the simplest case, non-uniform conditions are randomly distributed in two directions and symmetrically distributed around the vertical axis. In this case the problem can still be modeled with the current axisymmetric mathematical description. The intermediate case considers non-random (lumped or biased distributions) non-uniform distributions in two directions (2-D), with the final case corresponding to biased non-uniform distributions extended in three directions (3-D). In the present study, the simulations of non-uniform conditions are directed only to the first case where density is represented by a normal random distribution in 2-D.

4.4.1 Model Parameters Affected by Non-Uniformities

Even though the model parameters representing the constitutive behaviour of FCV specimens, namely, E_{ref}, ν, η_f, η_{cs}, and A, are all related or influenced by changes in density, the present evaluation of non-uniformities is limited to random distributions of E_{ref} and η_f, as they represent the most important aspects of the elasto-plastic characteristics of the behaviour. Variations of these two parameters are considered to be independent of each other in order to separate the effects of each random distribution.

The assumed non-uniform normal distribution of values for the dry unit weight is $\gamma_{dry} = 17.2 \pm 1.0\, kN/m^3$, which represents a coefficient of variation of 5.8%. The mean value, 17.2 kN/m^3, corresponds to the bulk unit weight of FCV specimens formed with the *high compaction* procedure, and the variation ± 1.0 kN/m^3 was chosen in a way that includes all realistic possibilities of γ_{dry}. Incidentally, it should be mentioned that experimentally, the bulk unit weight γ_{dry} is a highly repeatable property. Since the same amount of dry sand is always employed for all tests, and the initial volume of the specimens are always the same, add or take one part in 40000, it is reasonable to assume that all specimens have the same bulk density or dry unit weight.

Using some empirical relations proposed by Hardin et al. (1989), it can be shown that a variation of ±5.8% in values of γ_{dry} corresponds approximately to ±13.5% variation on the reference modulus, that is $E_{ref} = 223 \pm 30 MPa$.

4.4.2 Responses Predicted with Uniform and Random Variations of E_{ref} and η_f

The non-uniform distribution of the reference elastic modulus, shown in Figure 4.14(a), was produced with a routine that generates normal random variables based on the given mean value and the variation or deviation. In relation to changes of E_{ref}, the actual values of the elastic moduli E also depend on the principal stresses as given by expressions (3.49), for instance

$$E_i = E_{ref}\left(1 - e^{r_i}\right) \quad , \quad r_i = \frac{1000}{E_{ref}}\left(\frac{\sigma_j + \sigma_k}{2}\right) \tag{4.1}$$

where i, j, and k refer to the principal stress directions. The simulated distribution for the values of the elastic moduli E_{max} at the end of the loading stage is shown in Figure 4.14(b). Since cross-confinement anisotropy was assumed for the definition of the elastic moduli, values of E_{max} and E_{min} were always related to the minor and major principal stress direction. In Figure

4.14(b) it may be observed that the effects of non-uniformities are most visible in the areas of high stresses, at the bottom of the specimen for example.

The displacements at the top and bottom versus applied pressure predicted for the case of non-uniform distribution of E_{ref} differed very little from those predicted for the uniform case, as illustrate in Figure 4.15(a) and 4.15(b), thereby indicating that random variation of density does not influence the measured displacement.

Figure 4.16 illustrates contour plots of (a) vertical, and (b) radial stresses, while Figure 4.17 shows (a) shear stresses, and (b) values of the stress ratio. The contour plots shown in these figures were predicted for the case of non-uniform distribution of E_{ref}.
The blurry appearance of stress distributions in Figure 4.16 (a)(b) and 4.17(a) clearly exhibit the effects of non-uniform elastic moduli on the distribution of stresses. For the case of the stress ratio, Figure 4.17(b), the color contours are more smoothly distributed, and there seems to be no indication that non-uniform E_{ref} values had any effect on the stress ratio. Incidentally, the stress distributions shown in Figures 4.16 and 4.17 can not be directly compared with those of Figures 4.11 and 4.12. The stresses shown in Figures 4.16 and 4.17 were predicted with the anisotropic constitutive law, while in the case of Figures 4.11 and 4.12 the stresses were predicted with the pressure-dependent constitutive law.

Provided that the non-uniform distributions are truly random, the evaluation of non-uniform distributions indicates that even though varying values of the reference elastic moduli affected the stress distributions in a localized manner, the overall response of the FCV specimen is dominated by the bulk or average characteristics of the reference elastic moduli.

So far, the effects of non-uniformities have been described by means of contour plots.

These effects may also be quantified by plotting variables from the non-uniform simulation versus those with uniform distributions, and estimating the dispersion characteristics of these plots in a manner similar to that used in regression analysis, where dispersion or scatter is measured by standardized norms. Figure 4.18 illustrates the dispersion plots corresponding to (a) maximum elastic modulus E_{max}, (b) radial stresses σ_r, (c) vertical stresses σ_z, (d) shear stresses σ_{zr}, (e) horizontal displacements u, (f) vertical displacements v, and (g) stress ratio k. It should be noted that for the case of displacements, plots (e) and (f), all degrees of freedom are included. The plots corresponding to the elastic moduli and stresses represent the variables evaluated at integration points.

The dispersion characteristics of the distributions shown in these plots provide a visual image of the influence of non-uniformities for each aspect of the response. Quantification of these characteristics was conducted with two dispersion norms, defined as the mean absolute dispersion

$$\Delta = \left\{ \frac{1}{(n-2)} \sum_{i=1}^{n} \left(V_i^{NU} - V_i^{U} \right)^2 \right\}^{1/2} , \tag{4.2}$$

and the relative mean dispersion

$$\varepsilon\,\% = \left\{ \frac{1}{(n-2)} \sum_{i=1}^{n} \left(\frac{V_i^{NU} - V_i^{U}}{V_i^{U}} \right)^2 \right\}^{1/2} \tag{4.3}$$

with V^{NU} and V^{U} representing the values of the variables for the non-uniform and uniform cases, respectively. The parameter n is the number of points in the distribution. The application of these norms to the distributions of moduli, stresses and displacements are summarized in Table 4.2.

Table 4.2 Dispersion norms for non-uniform distribution of E_{ref}

Variable	$\pm\Delta$	$\pm\varepsilon$ %
E_{ref}	24.7 [MPa]	11.3
E_{max}	9.8 [MPa]	5.6
σ_r	11.8 [kPa]	4.3
σ_z	17.5 [kPa]	4.0
σ_{rz}	4.2 [kPa]	10.9
k	0.01	0.9
u	$3\text{x}10^{-4}$ [mm]	0.7
v	$3\text{x}10^{-4}$ [mm]	0.3

For the case of the maximum elastic moduli E_{max}, the absolute and relative norms provide measures of the average or mean value of the dispersion. The values of the dispersion for E_{max} increase proportionally with values of the variable, as shown in Figure 4.18(a). This aspect of the distribution, which is a direct consequence of the dependency of values of E_i on the confining stress levels as in equation (4.1), is not fully represented by the norms. A similar trend was observed for the distributions of vertical and horizontal stresses, where the amount of dispersion is directly related to the stress levels, as shown in Figures 4.18(b) and (c). The characteristics of shear stress distribution, on the other hand, exhibited approximately uniform values of dispersion on the entire range of stresses, which were then well represented by the mean value norms. This aspect of the shear stress distribution, shown in Figure 4.18(d), may be explained by the fact that a certain amount of shear transfer had developed between weak and strong pockets of the soil. The distribution of shear stresses was the most affected variable as indicated by a relative mean dispersion of 10.9 %, in Table 4.2. The downloading of stresses from weak elements to stronger ones by means of shear redistribution may in turn explain in part the fact that non-uniform distribution of elastic moduli had little impact on the displacements. Illustrated in Figures 4.18(e) and (f), the horizontal and vertical displacements had showed no significant dispersion, clearly demonstrating that non-uniform values of E_{ref} had little effect on the displacements throughout the entire specimen. As a result, surface measurement of displacements can not be used to make conclusive statements about relative uniformity of specimens. Finally, the dispersion for values of the stress ratio were relatively small, as shown in Figure 4.18(g).

A similar analysis was conducted to estimate the effects of non-uniform distributions of the stress ratio η_f at failure. The coefficient of variation for η_f was arbitrarily selected as 13.5%, with a mean value of 1.44; that is $\eta_f = 1.44 \pm 0.19$. This corresponds to a distribution of values for the peak friction angle of $\phi_f = 35.5° \pm 4.5°$. The results from the simulations, however, indicated that the effects of the non-uniformity of η_f are negligible for both local and global aspects of the simulated response. The estimated values of the relative mean dispersion for stresses and displacements were all smaller than 0.3%. The fact that non-uniform distributions of η_f had little effects on the predicted FCV responses supports the notion that FCV behaviour is mainly dominated by a quasi-elastic stress-strain regime. Since the effects of non-uniform η_f are negligible, plots and figures from these simulations are omitted.

4.5 Optimization of the Confining Vessel

The design of a new FCV device requires a clear definition of the criteria to be met by the trial designs. The selection criteria, which depends on stress conditions existing in the field, is discussed in this section. With regard to the numerical aspects of the optimization, all numerical analyses were carried out with the pressure-dependent constitutive model. Even though the anisotropic constitutive law appears to predict FCV responses, which are somewhat better that those of the pressure-dependent law, the decision not to use the former model was made on the basis that the anisotropic model could not be fully validated.

4.5.1 Characteristic Stress Conditions in the Field

The soil conditions encountered in the field are complex, depending on a number of factors such as the type of soil, processes of deposition, and stress history. From an analytical point of view, many of the complex conditions found in the field may be readily accommodated in a finite element analysis. On the other hand, for the problem of the physical modeling of piles, the focus is placed on adopting simplified ideal soil conditions: (*i*) homogeneous sandy soil, (*ii*) horizontal soil surface, (*iii*) free-field conditions (no surface loads are applied in the vicinity), and (*iv*) uniform effective unit weight γ', constant with depth. For such an ideal case and prior to pile installation, the only stresses acting in the soil are those produced by its own weight, for instance, at a depth z from the surface the stresses in the soil are:

$$\sigma'_v = \sigma'_z = \gamma' z \qquad \text{vertical stresses} \qquad (4.4a),$$

$$\sigma'_h = \sigma'_x = \sigma'_y = k_o \gamma' z \qquad \text{horizontal stresses} \qquad (4.4b),$$

$\sigma_{vh} = 0$ shear stresses (4.4c),

Since the shear stresses acting on vertical and horizontal planes are presumed to be zero, the normal stresses acting in those planes coincide with the major and minor principal stresses, respectively. The intermediate and minor principal stresses are assumed to be equal in magnitude. Implicit in equations (4.4a) and (4.4b) is the assumption that k_o, the coefficient of earth pressure at rest, is constant with depth.

4.5.2 Optimization Criteria

As stated previously, the usable region of an FCV specimen in which stress conditions are suitably controlled for the purposes of physical modeling of piles, is referred to as the control volume. The control volume is the cylindrical portion of an FCV specimen that stretches from top to bottom along the centerline. The selection of an optimal design is then based on the capability of an FCV to produce scaled field conditions on the control volume. In this respect, the stress conditions within the control volume of an optimal device should meet the following criteria:

(a) The distribution of stresses need to ensure

  i. linear distributions of vertical and radial stresses with depth,

  ii. zero shear stresses in the vertical and horizontal planes, $\sigma_{rz} \rightarrow 0$,

  iii. constant values of the stress ratio k with depth, and

  iv. admissible values of the stress ratio, i.e., $0.30 < k < 0.80$.

(b) The stress levels must be adjustable. By means of controlling the pressure applied to the loading membrane, it is required that an FCV device should produce different levels of stress, while preserving the stress characteristics enumerated in (a). Specifically, for a constant value of the applied basal pressure p_{app}, the stress distributions should be defined by linear relations similar to the following expressions:

$$\sigma'_z \propto C_1\, p_{app}\, \frac{z}{H} \qquad \text{vertical stress} \qquad (4.5a),$$

$$\sigma'_r \propto C_2\, p_{app}\, \frac{z}{H} \qquad \text{radial stress} \qquad (4.5b),$$

where C_1 and C_2 are constant parameters related to a particular vessel design, and H represents the height of the specimen at the centerline.

(c) The rotation of principal planes must be minimized during FCV loading.

(d) The artificial boundaries should have minimum effects of the stress distributions.

4.5.3 Basic Vessel Shapes

Numerical analyses of FCV testing revealed that the current device has some shortcomings with respect to reproducing properly scaled field conditions. For instance, values of the stress ratio along the centerline varied significantly, ranging from 0.8 to 1.6. In addition, principal stress rotations were shown to be severe for the upper portion of the control volume. The elimination or minimization of these shortcomings is numerically evaluated in this section by considering three basic shapes. The basic trial shapes, represented by their finite element grids with their relevant geometric characteristics, are shown in Figure 4.19. While grids 1 and 2 only differed in their wall inclination and the size of load membrane, grid 3 has a narrow opening in the top and the loading base has the shape of a spherical cap. For the simulations with these trial shapes, the top of the specimens are free, i.e., the metal plate has been eliminated, and the maximum applied loading is p_{max}= 500 *kPa*. All three FCV trial designs were able to produce stresses which are controllable as required by the criteria described in point (b).

A comparison of the principal stress directions is presented in Figure 4.20. In this figure is evident that stresses within the control volume predicted for grid 3 are the closest to meeting the vertical/horizontal principal planes criteria, provided that one eliminates the region at the top and the bottom for the control volume. While grid 2 shows some improvement over grid 1, the upper portion of the control volume exhibits the typical 90° rotation of principal planes, which is similar to what is observed in the simulations of the existing device. An examination of the results indicates that a narrower opening at the top is more appropriate than the wide openings. For narrower openings, less arching develops in the upper region. With respect to the rotation of principal planes observed on the lower portions of the three basic shapes, it is not clear whether this characteristic is due to confining conditions or shear stresses acting on the lower portion of the specimen. This, however, is not a serious problem, as the control volume can be made just long enough to avoid this region.

In terms of stresses predicted along the centerline, it appears that grid 1 produces a distribution of vertical stresses, shown in Figure 4.21(a), which is closest to a linear variation. On the other hand, the variation of the stress ratio for this vessel, plotted in Figure 4.21(c), is the least desirable as it ranges from k = 3.0 on the top, to k = 0.8 close to the bottom. In general, grid 3 appears to provide the most reasonable variations in stresses when considering the selection criteria indicated in (c). For the case of the stress ratio, even though values of *k* are not constant, the variation of the *k* values with depth is small when compared with the variations produced in trial designs 1 and 2. With respect to the predicted shear stresses within the control volume, not shown in the figures, all three grids produced small or close to zero values of shear stresses, readily satisfying the third criterion.

None of the three trial shapes satisfied all aspects of the selection criteria simultaneously. For reasons that will be made clear in Chapter 5, the trial shape that produces a near linear variation for radial stresses and uniform *k* value is assumed to have the optimal shape. Consequently, grid 3 is selected for further evaluations in terms of different friction conditions at the wall interface and different angles for the wall inclination.

4.5.4 Friction at the Wall Interface

The inner surface of a confining vessel can be physically treated to reduce or increase the friction between the specimen and the wall. In this section, stresses predicted with values of the friction coefficient tanδ equal to 0.05 and 0.60 are compared with the results obtained in the previous section in which tanδ is equal to 0.28. The aim of performing simulations with different values of tanδ is first to determine the effects of interface friction on stresses within the control volume, and second to assess the possibility of improving the distribution of the stresses in relation to the testing of model piles.

An examination of the stresses predicted along the centerline reveals that reducing the friction at the interface results in undesirable distributions of vertical and radial stresses with depth, as shown in plots (a) and (b) of Figure 4.22, respectively. It is further noticed that values of the stress ratio produced by using a reduced friction are almost constant and equal to one from normalized depths of 0.2 and down, thereby suggesting that the stress conditions are closely resembling hydrostatic pressure conditions. Increasing the friction from 0.28 to 0.60 at the interface caused small changes in the vertical stresses along the centerline, and an increased departure from linearity with respect to the radial stress distribution, shown in (b).

These numerical simulations demonstrated that the development of interface friction is beneficial to the stress distributions at the centerline, while a non-frictional interface is highly detrimental. It is also observed that an enhancement of interface friction is not necessary. In most cases, untreated steel surfaces may provide sufficient roughness to ensure adequate values of friction coefficient at the interface of a confining vessel.

4.5.5 Effect of Wall Inclination

The effect of wall inclination is considered by simulating the cases with values of β equal to 30° and 60°, and comparing the responses with that obtained for grid 3 with $\beta = 45°$. The grids corresponding to the different wall inclinations are shown in Figure 4.23. The simulations were carried out using the same material properties and discretization as indicated in Section 4.3.1

The stresses predicted along the centerline for the three values of β are shown in Figure 4.24. This figure illustrates a direct relation between stress distributions and wall inclination. The trend indicates that low values of β are detrimental while higher values are beneficial for the generation of desired vertical and horizontal stress distributions. As may be observed in (c), the distributions of the stress ratio with depth are similar for the three wall inclinations, suggesting that both radial and vertical stresses are affected simultaneously in the same manner.

Based on this results, it may be concluded that, first, the inclination of the wall has a significant effect on the stress distributions along the centerline, and second, that an inclination of the wall $\beta = 60°$ (grid 5) results in a distribution of vertical stress which is better than those produced by using lower values of β. The control volume predicted for this vessel, however, was narrow and very close to the vessel wall.

Overall, it is concluded that the results obtained with grids 3 and 5 are the most suitable for the purpose of testing of model piles. The predicted stress fields for these two cases illustrated in the contour plots in Figures 4.25 and 4.26.

With respect to the high values of the stress ratio observed in the upper part of the specimens for grids 3 and 5, it is concluded that, although significantly reduced, these distortions can not be eliminated by making changes on the shape alone. An alternative remedy for this situation is to place a protective sleeve around the model pile to minimize the influence of this disturbance.

From the previous discussion of results, it may be appreciated that grids 3 and 5 exhibit some benefits and drawbacks. The philosophy adopted in developing a new shape for the confining vessel is to accept some limitations on those aspects of the selection criteria that may be considered of secondary importance. As previously mentioned and in relation to testing of model piles, linear distributions of radial stresses with depth and artificial boundaries placed as far as possible are considered the most important requirements for the soil conditions within the control volume. Therefore, the author believes that a vessel with a shape represented by grid 3, offers the best alternative for the design of a new confining vessel.

4.6 Closure

Based on the numerical analyses conducted in this chapter, the following conclusions may be drawn:

- With respect to the simulations of triaxial testing it was observed that some minor discrepancies exist between the predicted and measured volumetric changes. In general, an appropriate set of material properties was defined. Good agreement between predicted and measured displacements was obtained with the three constitutive models.
- The simulation of the FCV testing conditions, using the existing geometry, was conducted with the pressure-dependent and the anisotropic models. The responses simulated with both models were found to be in good agreement with the measured responses. Since further study is required to evaluate the validity of the anisotropic law, the pressure-dependent model was adopted for the task of numerical optimization.
- Non-uniform values of E_{ref} affect the distribution of stress on the local scale. However, the global aspects of the specimen's response are not significantly affected by these changes.
- Non-uniform values of η_f did not have a significant effect on the responses at the local or global scales.
- Although plastic straining occurs at the FCV boundary, the responses seem to be dominated by elastic stress-strain behaviour.
- Vessel shapes represented by grids 3 and 5 are deemed to be the most appropriate for the purposes of physical modeling of reduced-scale piles.
- A non-frictional surface at the specimen-wall interface was found to be highly

detrimental on the stress distributions along the centerline. Increasing the friction conditions at the specimen-wall interface did not significantly alter the distribution of stresses along the centerline.

- Stress distributions acting on the control volume were found to improve with increasing values of the angle β.

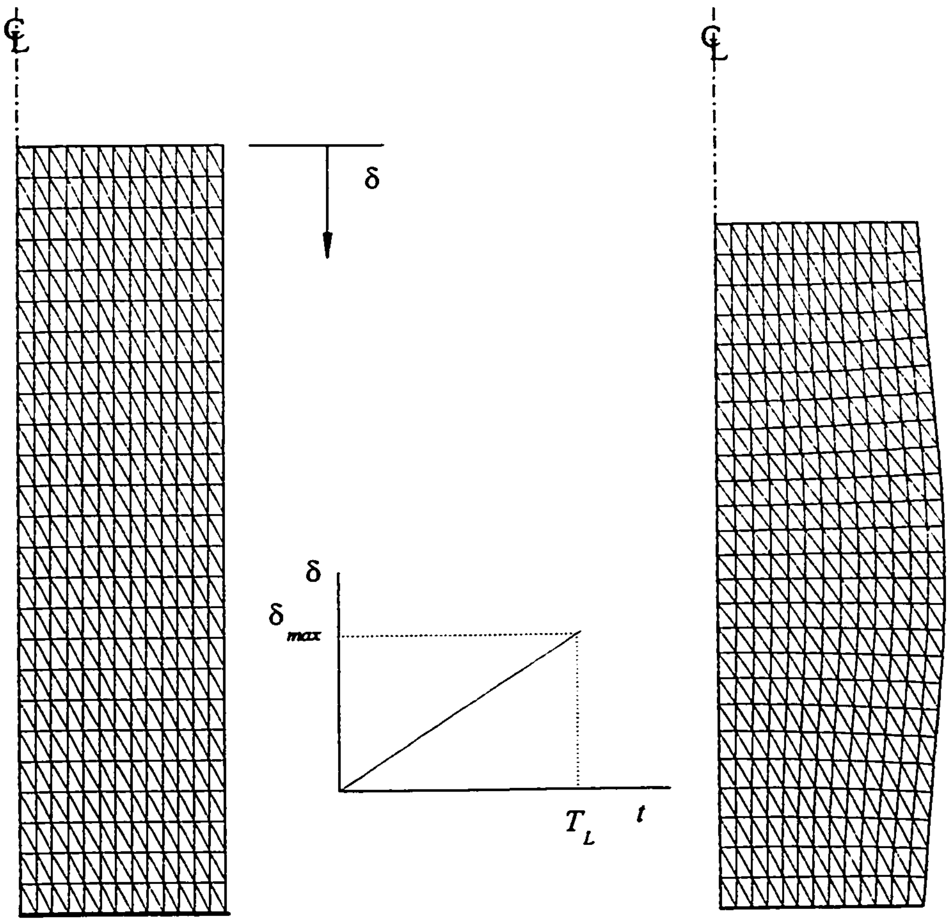

(a) (b)

Sand Specimen		
radius	R	$= 0.018\ m$
height	H	$= 0.075\ m$
Poisson's ratio	ν	$= 0.37$
friction coef. at failure	$\sin\phi_f$	$= 0.58$
friction coef. at crit. state	$\sin\phi_c$	$= 0.46$
hardening parameter	A	$= 0.00070$

Elastic Moduli		
Basic Constitutive Law	E	$= 203\ MPa$
Pressure-Dep. Const. Law	E_{ref}	$= 240\ MPa$
Anisotropic Const. Law	E_{ref}	$= 240\ MPa$
	G_{ref}	$= 95\ MPa$
	$\nu_1 = \nu_2 = \nu_3$	$= 0.37$

Loading		
max. axial displacement	δ_{max}	$= 7.5\ mm$
loading interval	T_L	$= 4\ 0\ min$
confining stress	σ'_3	$= 500\ kPa$

Finite Element Mesh	
No. of nodes	1377
No. of triangular elements	650
No. of dof	2624

(a) Undistorted mesh used for the axisymmetric triaxial sample problem. (b) Deformed mesh at a loading stage corresponding to 5 % of axial strain. Displacements were magnified by a factor of 2 in order to enhance the view of the non-uniform strain conditions at the top and bottom loading platens.

Figure 4.1. Discretization of triaxial sample

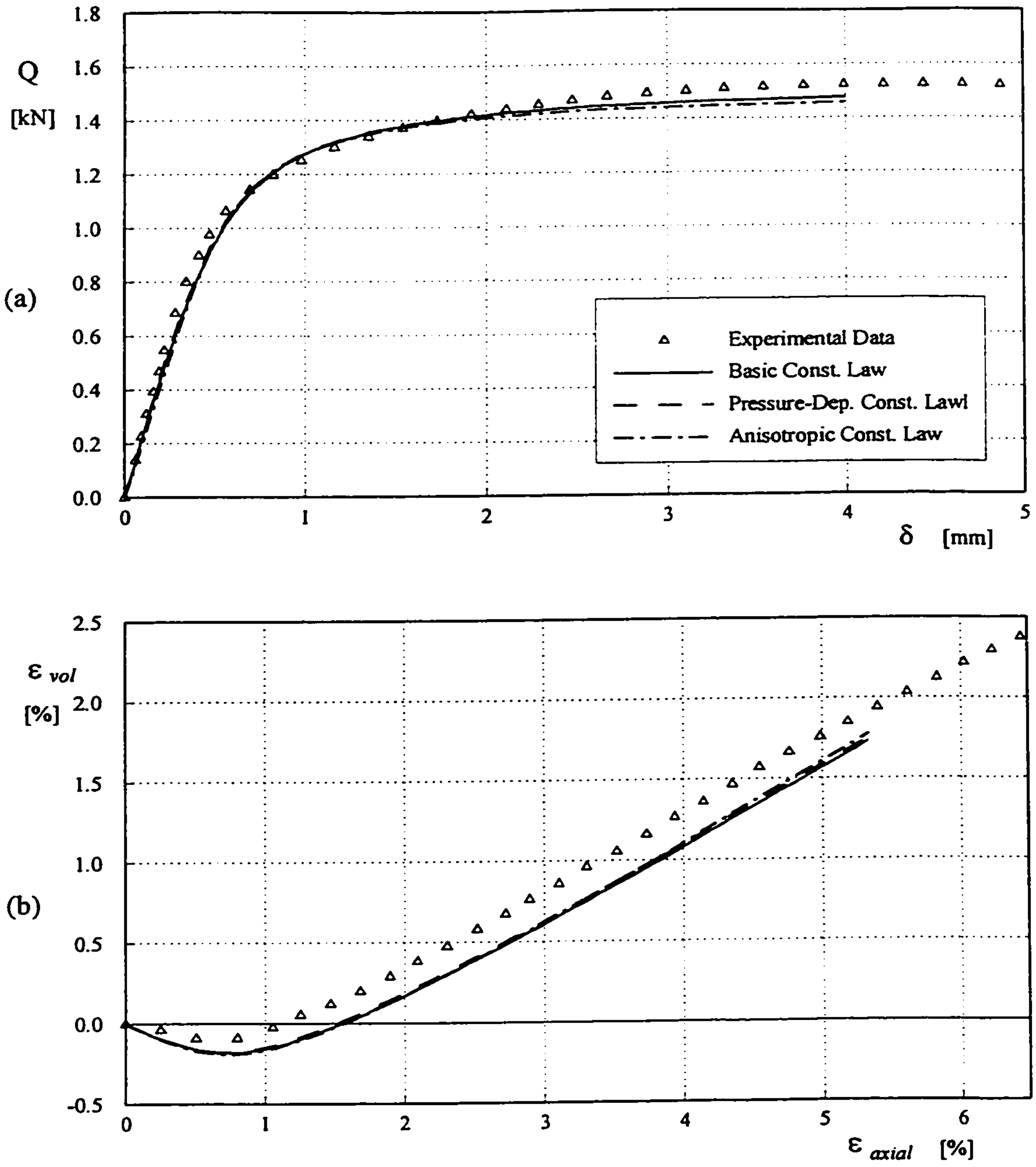

The observed triaxial response is compared with numerical predictions for the case of effective confinement of 500 *kPa*. The finite element simulations were obtained using the three constitutive laws; Basic, Pressure-Dependent, and Anisotropic constitutive laws. The triaxial response is shown in terms of (a) applied load versus axial displacements, and (b) net volumetric strains versus axial strains.

Figure 4.2. Comparison of experimental and numerical triaxial responses

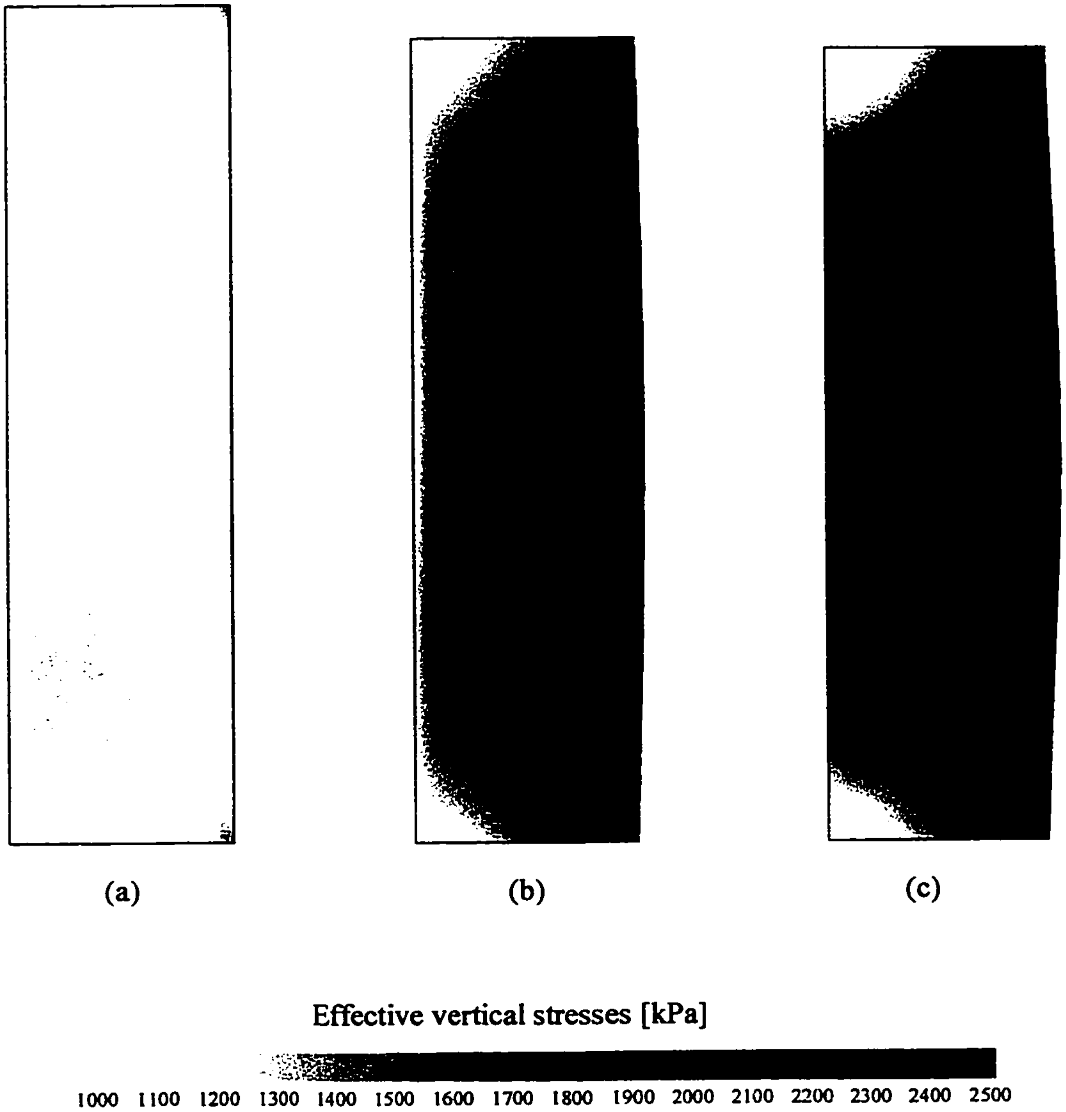

Contour plots representing the distribution of effective vertical stresses, at three different levels of axial strain, namely: (a) ε_{axial} = 0.5% , (b) ε_{axial}= 2.1% , and (c) ε_{axial} = 5.3% . No magnification factor was used to display sample displacements.

Figure 4.3. Triaxial test response: Vertical stress field

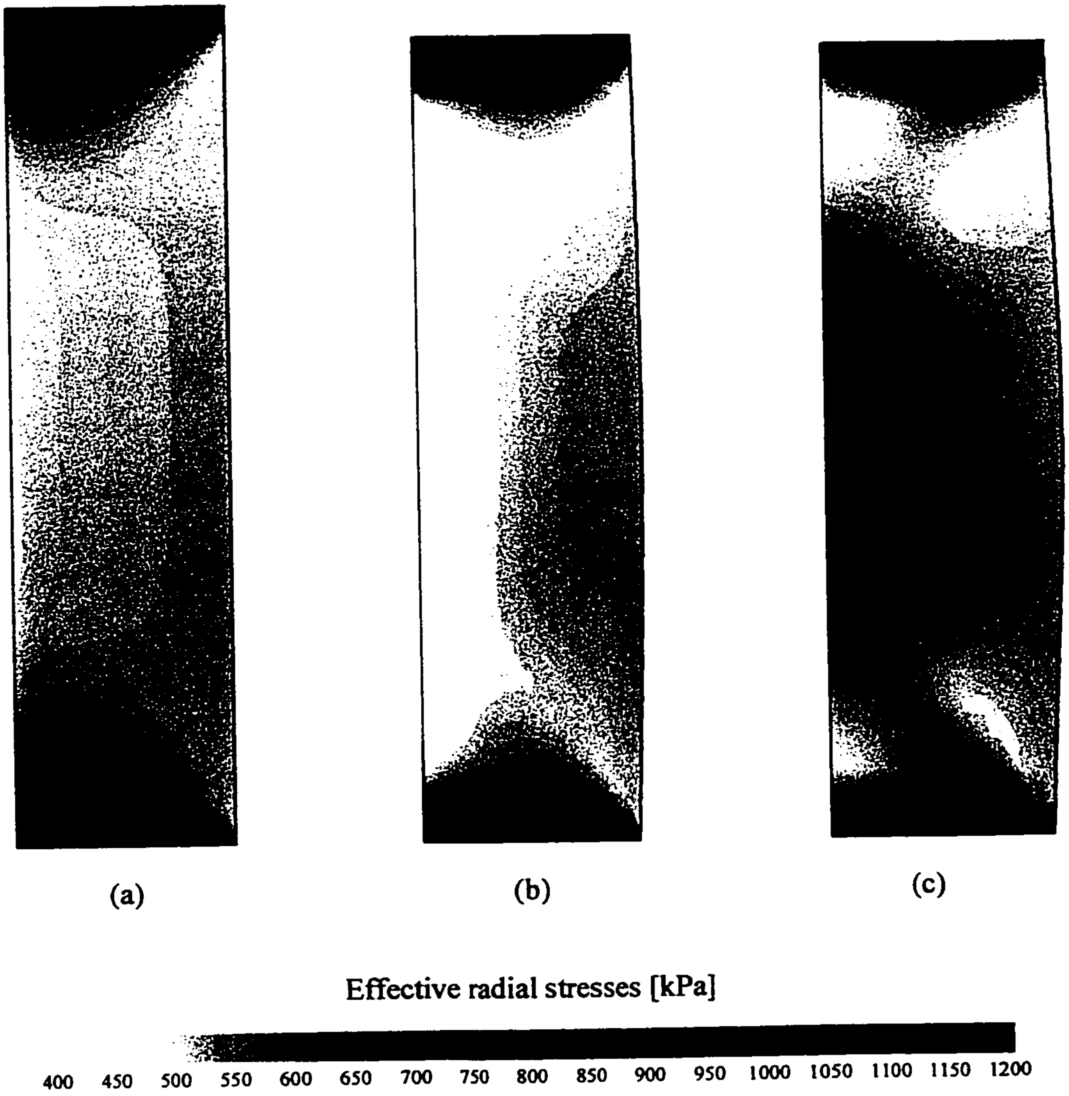

Contour plots representing the distribution of effective radial stresses, at three different levels of axial strain, namely: (a) $\varepsilon_{axial} = 0.5\%$, (b) $\varepsilon_{axial} = 2.1\%$, and (c) $\varepsilon_{axial} = 5.3\%$. No magnification factor was used to display sample displacements.

Figure 4.4. Triaxial test response: Radial stress field

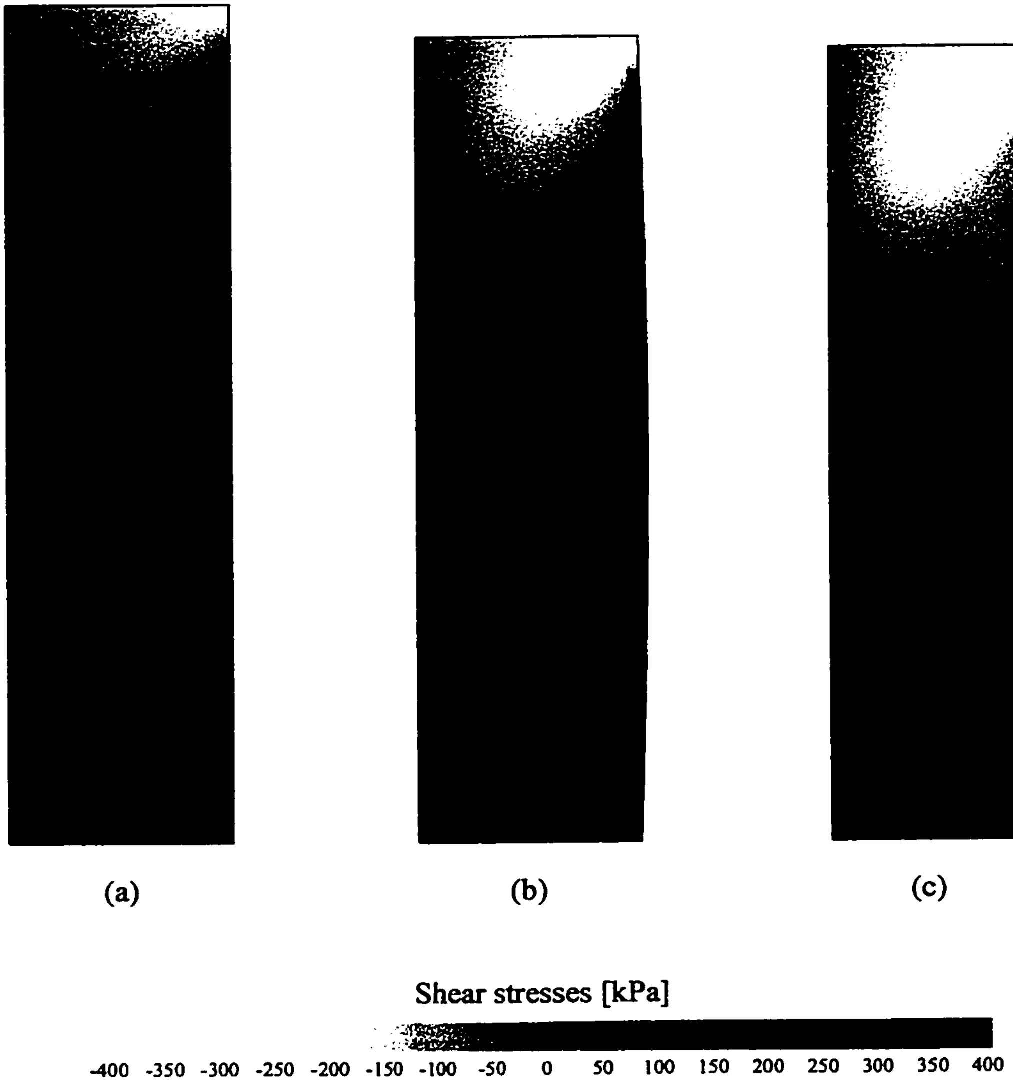

(a) (b) (c)

Contour plots representing the distribution of shear stresses, at three different levels of axial strain, namely: (a) ε_{axial} = 0.5% , (b) ε_{axial}= 2.1% , and (c) ε_{axial} = 5.3% . No magnification factor was used to display sample displacements.

Figure 4.5. Triaxial test response: Shear stress field

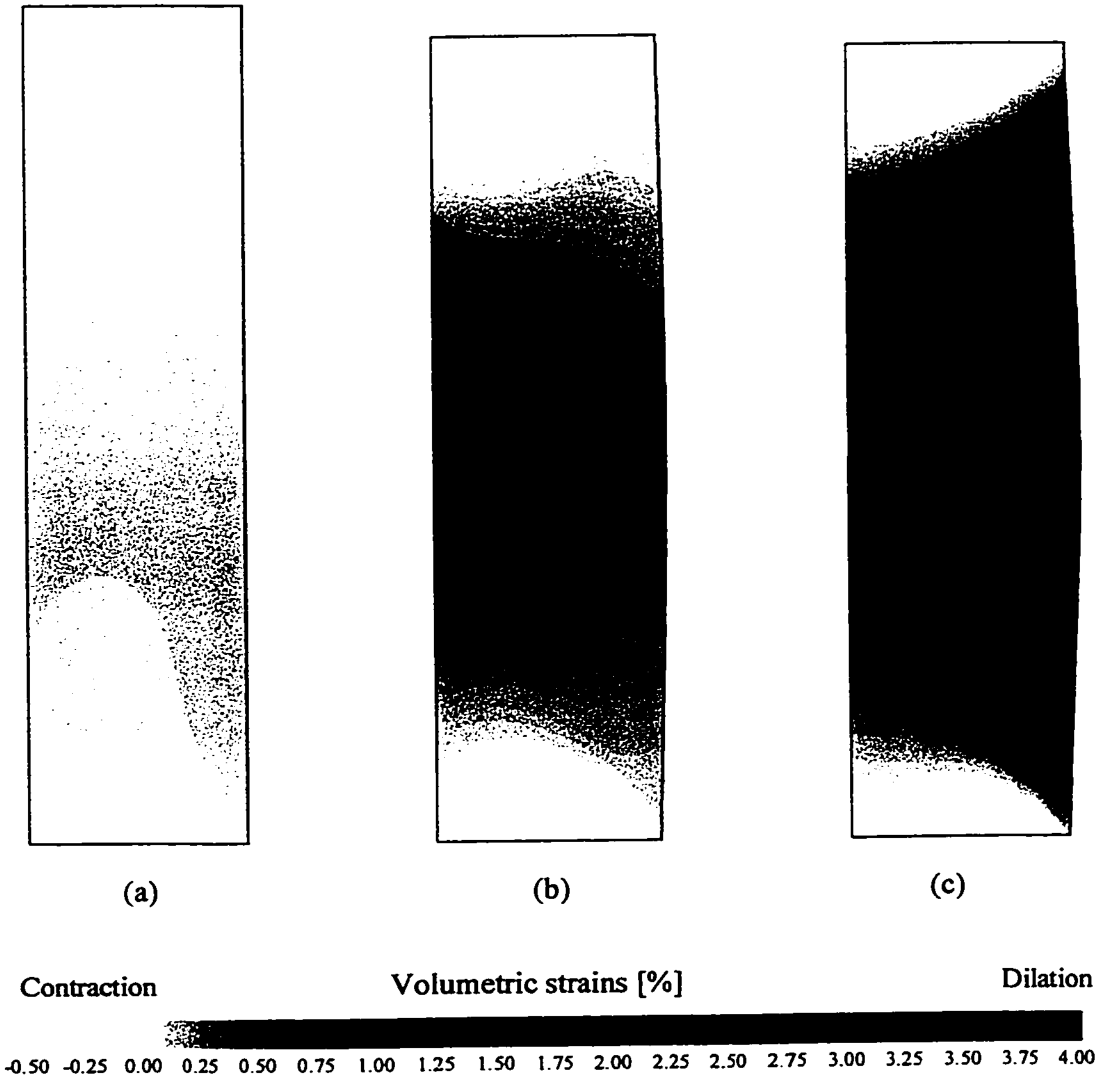

Contour plots representing the distribution of volumetric strains during a triaxial test, at three different levels of axial strain, namely: (a) $\varepsilon_{axial} = 0.5\%$, (b) $\varepsilon_{axial} = 2.1\%$, and (c) $\varepsilon_{axial} = 5.3\%$. No magnification factor was used to display sample displacements.

Figure 4.6. Triaxial test response: Volumetric change

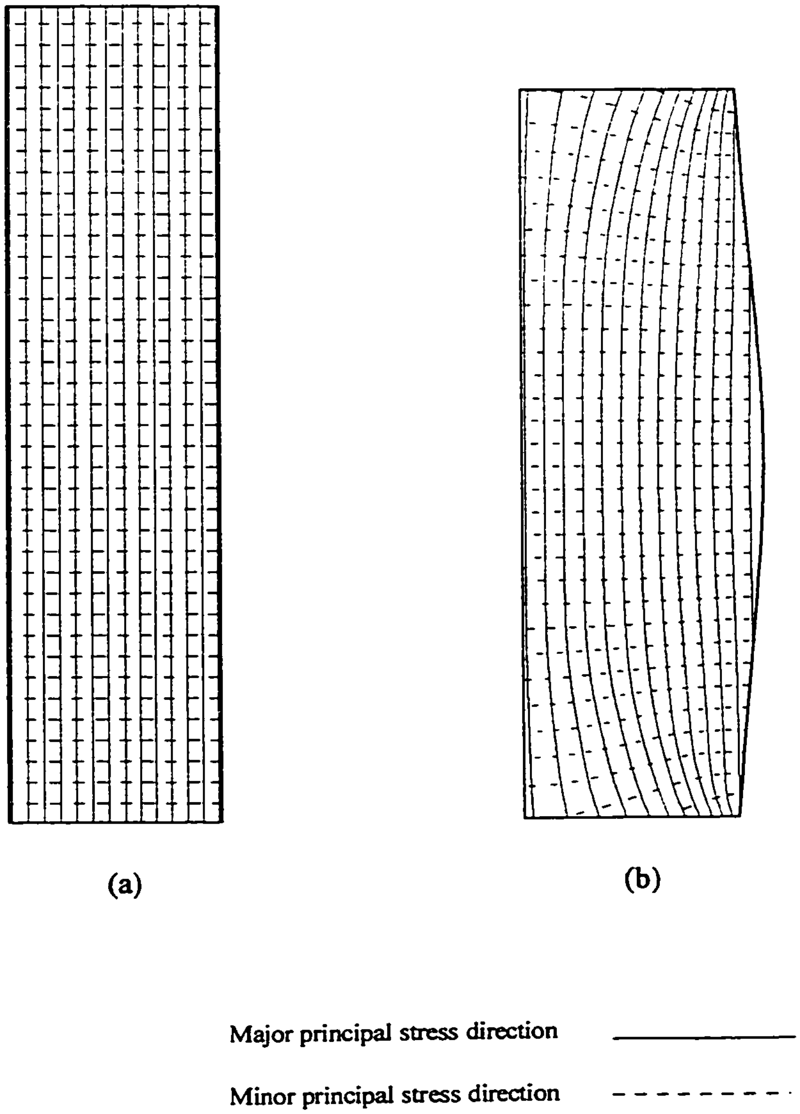

The streamline plots illustrate the orientation of the principal stresses in a triaxial sample (a) at the start and (b) at the end of the test. The predicted stress distributions clearly indicated that principal stresses do not suffer significant rotations during triaxial testing.

Figure 4.7. Triaxial test response: Principal stress directions

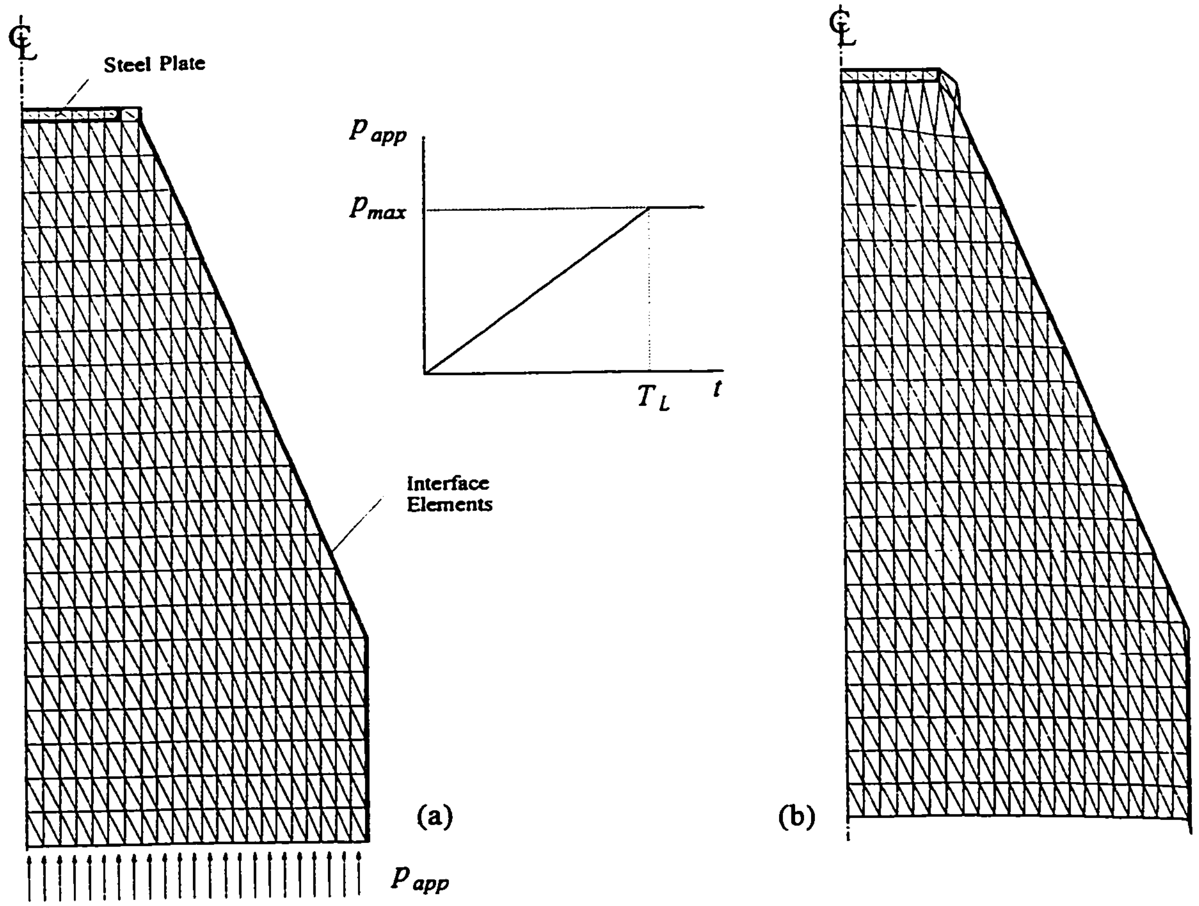

Sand Specimen					
top radius	R_t	$= 0.076\ m$	Pressure Dep. Law	E_{ref}	$= 223\ MPa$
bottom radius	R_b	$= 0.227\ m$		ν	$= 0.35$
height	H	$= 0.540\ m$			
friction coef. at failure	$\sin\phi_f$	$= 0.58$	Anisotropic Law	E_{ref}	$= 223\ MPa$
friction coef. at crit. state	$\sin\phi_c$	$= 0.48$		G_{ref}	$= 90\ MPa$
hardening parameter	A	$= 0.00070$		$\nu_1 = \nu_2 = \nu_3$	$= 0.37$
dry unit weight	γ_{dry}	$= 16.4\ kN/m^3$	interface friction coef.	$\tan\delta$	$= 0.28$

Loading			**Finite Element Mesh**	
max. applied pressure	p_{max}	$= 500\ kPa$	No. of nodes	1545
loading interval	T_L	$= 30\ min$	No. of triangular elements	713
			No. of interface elements	22
			No. of dof	2955

(a) Undistorted mesh used for the axisymmetric problem of a FCV sand specimen tested under the uniform load configuration. b) Typical deformed mesh at the maximum applied pressure of 500 *kPa*. In this case, the displacements were magnified by a factor of 10.

Figure 4.8. Discretization of a FCV specimen

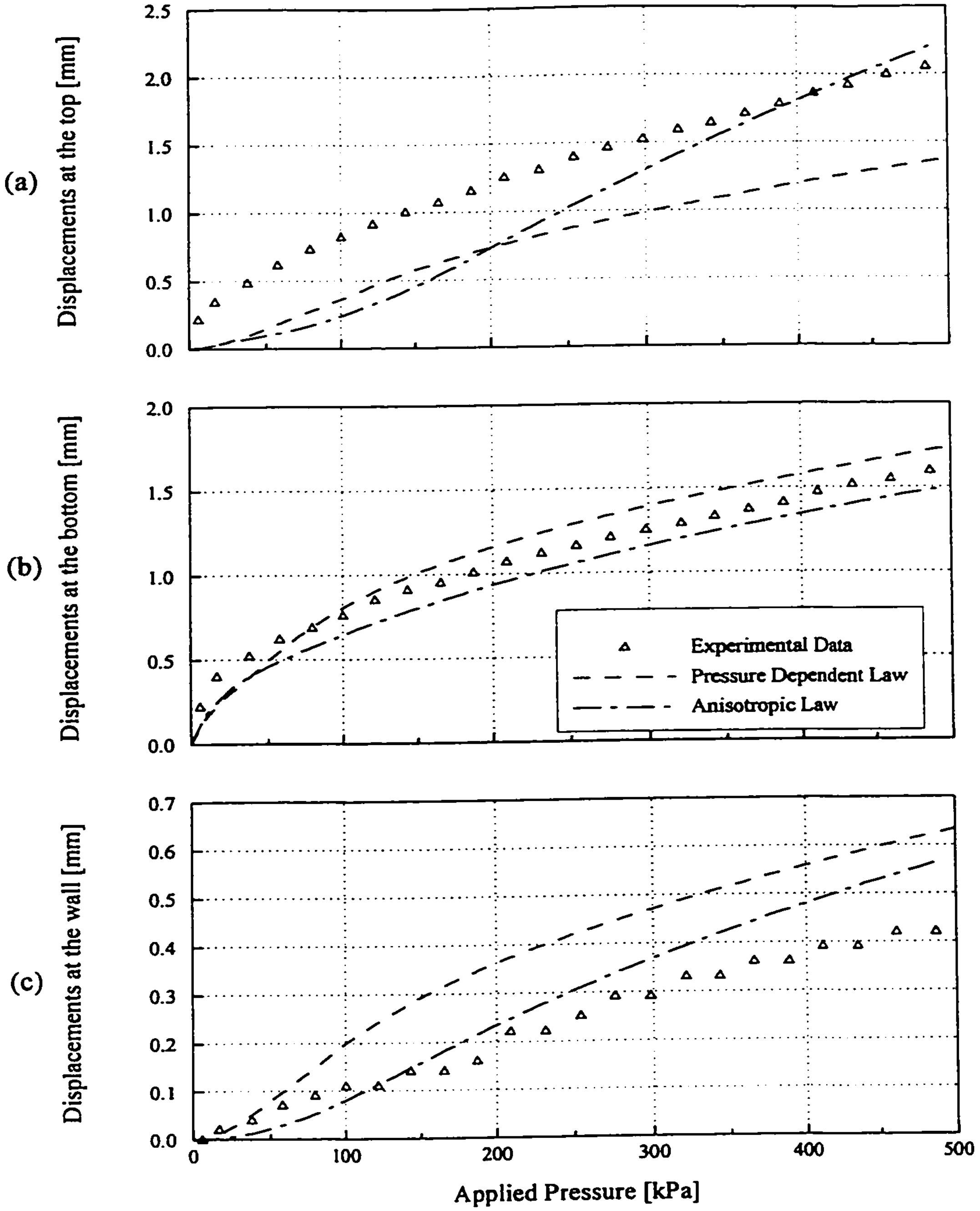

Only the Pressure-Dependent and the Anisotropic laws were used in these simulations. The displacements (a) at the top and (b) the bottom of the specimens are plotted versus the applied pressure to the loading membrane. Plot (c) shows the sliding of the specimen at the inclined wall (mid-height).

Figure 4.9. Comparison of experimental and numerical FCV responses

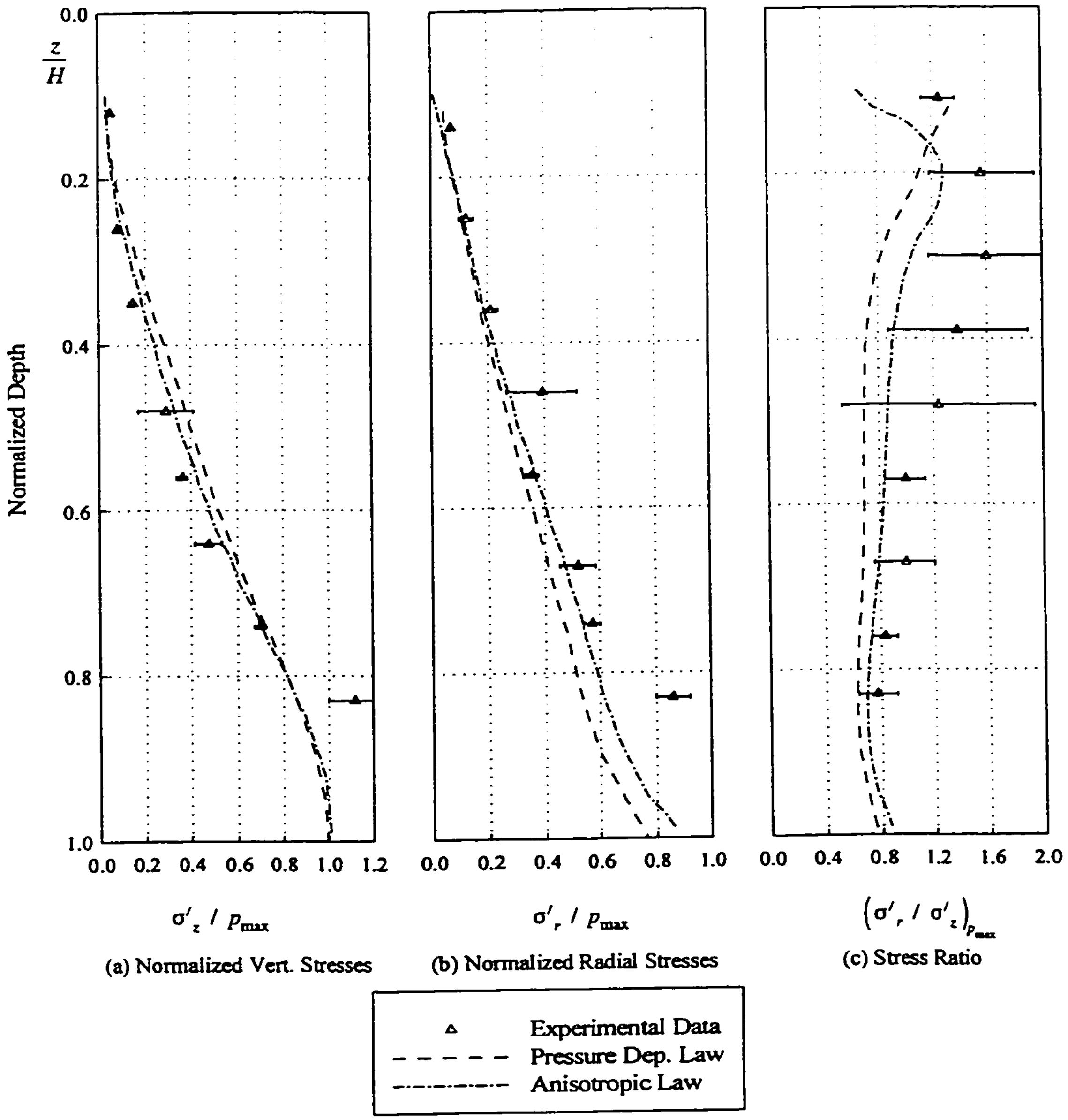

(a) Normalized Vert. Stresses (b) Normalized Radial Stresses (c) Stress Ratio

Variation of normalized (a) vertical and (b) radial stresses along the centerline. The stresses were normalized with respect to the applied pressure of 500 *kPa* and plotted versus normalized depth *z/H*. Plot (c) shows the stress ratio $k = \sigma'_r / \sigma'_z$ versus *z/H*. The error bars attached to the experimental data points indicate the uncertainty associated with the stress measurements due to instrumentation errors.

Figure 4.10. Comparison of experimental and numerical FCV responses: Centerline stresses

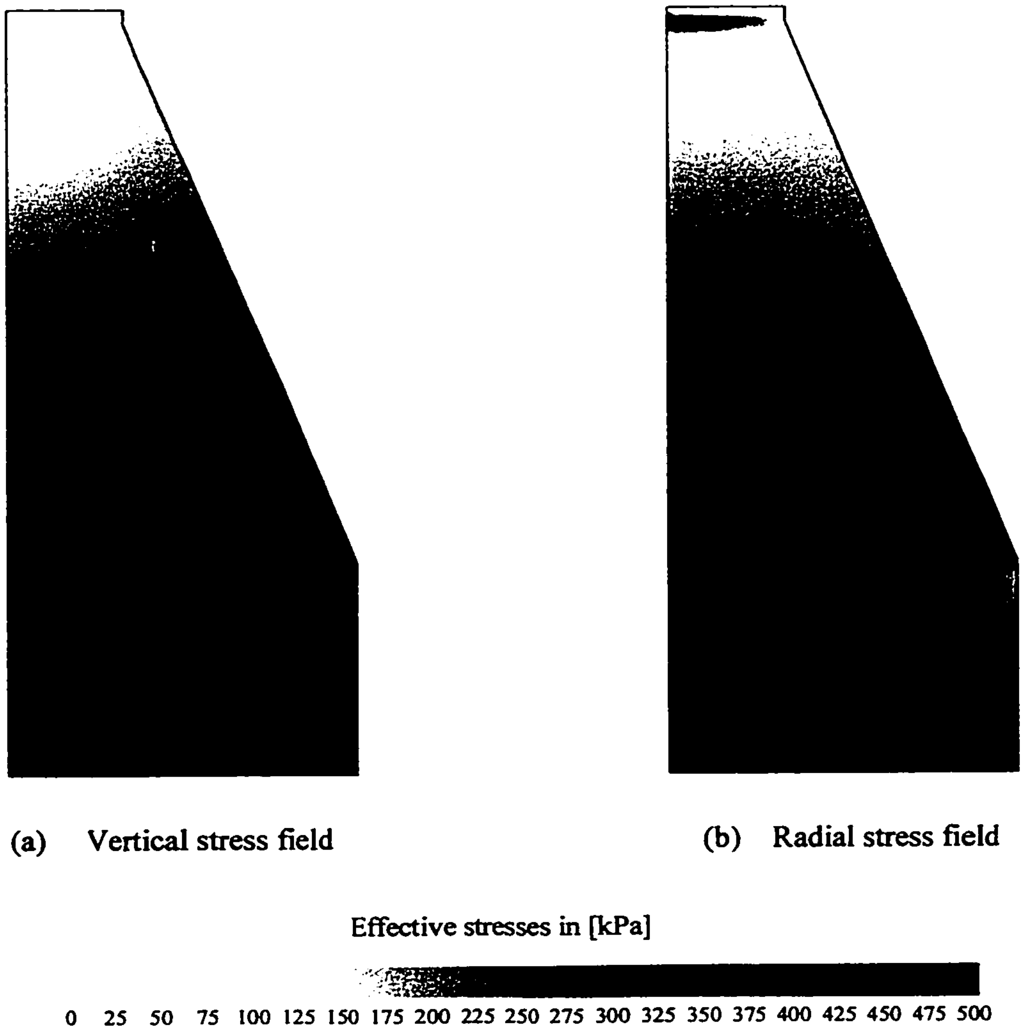

(a) Vertical stress field

(b) Radial stress field

Effective stresses in [kPa]

Contour plots representing the distribution of (a) vertical and (b) radial effective stresses in a FCV specimen at 500 *kPa* of applied pressure. The predicted stress fields shown the figure were produced with the Pressure-Dependent constitutive law.

Figure 4.11. FCV test response: Vertical and radial stresses

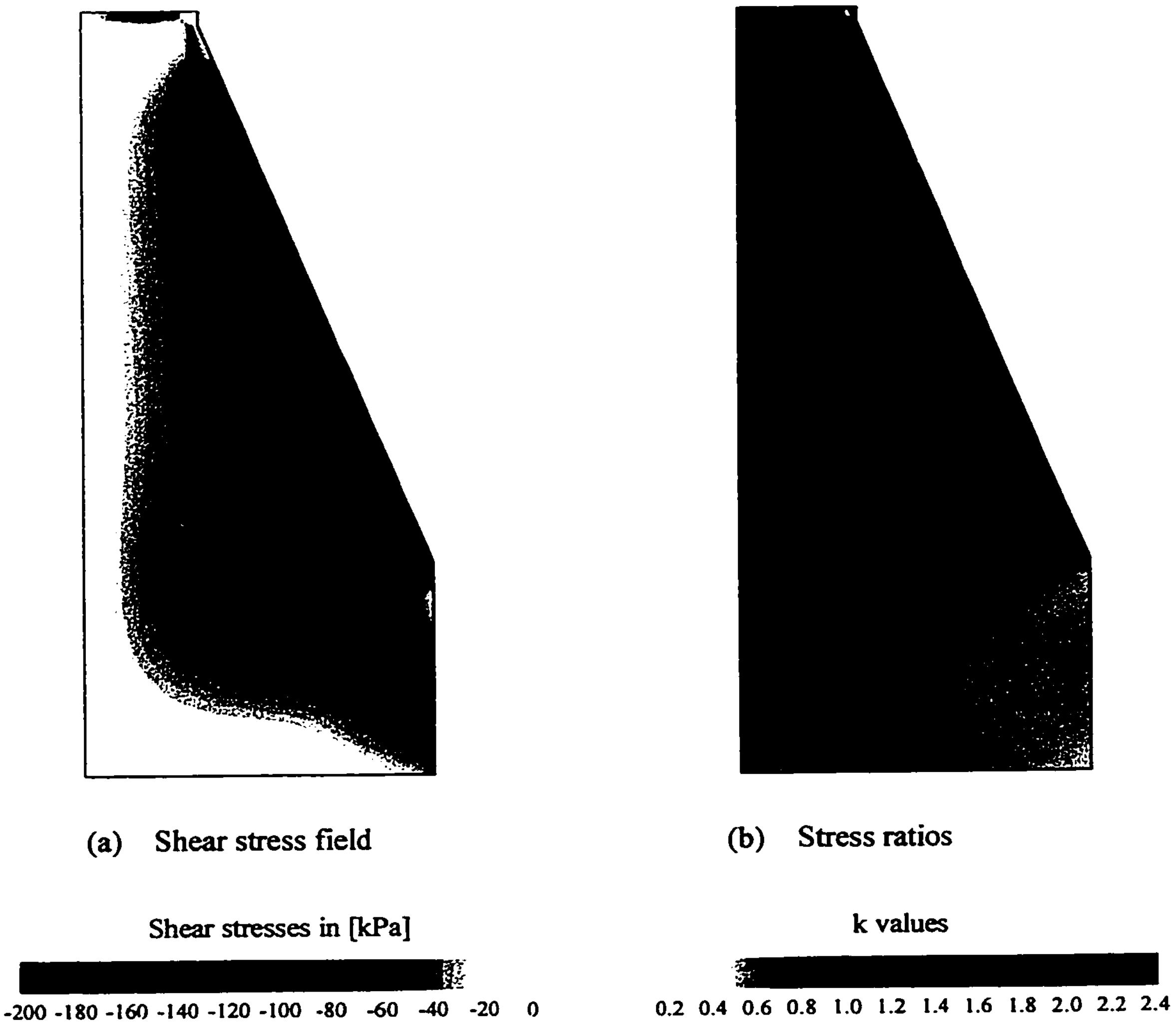

(a) Shear stress field

(b) Stress ratios

Contour plots shown the distributions of (a) shear stresses and (b) values of the *k* ratio in a FCV specimen at 500 *kPa* of applied pressure. The shear stresses shown in the figure are referred to the r-z directions. The metal plate on the top of the specimen is clearly visualized in red color.

Figure 4.12. FCV test response: Shear stresses and *k* values

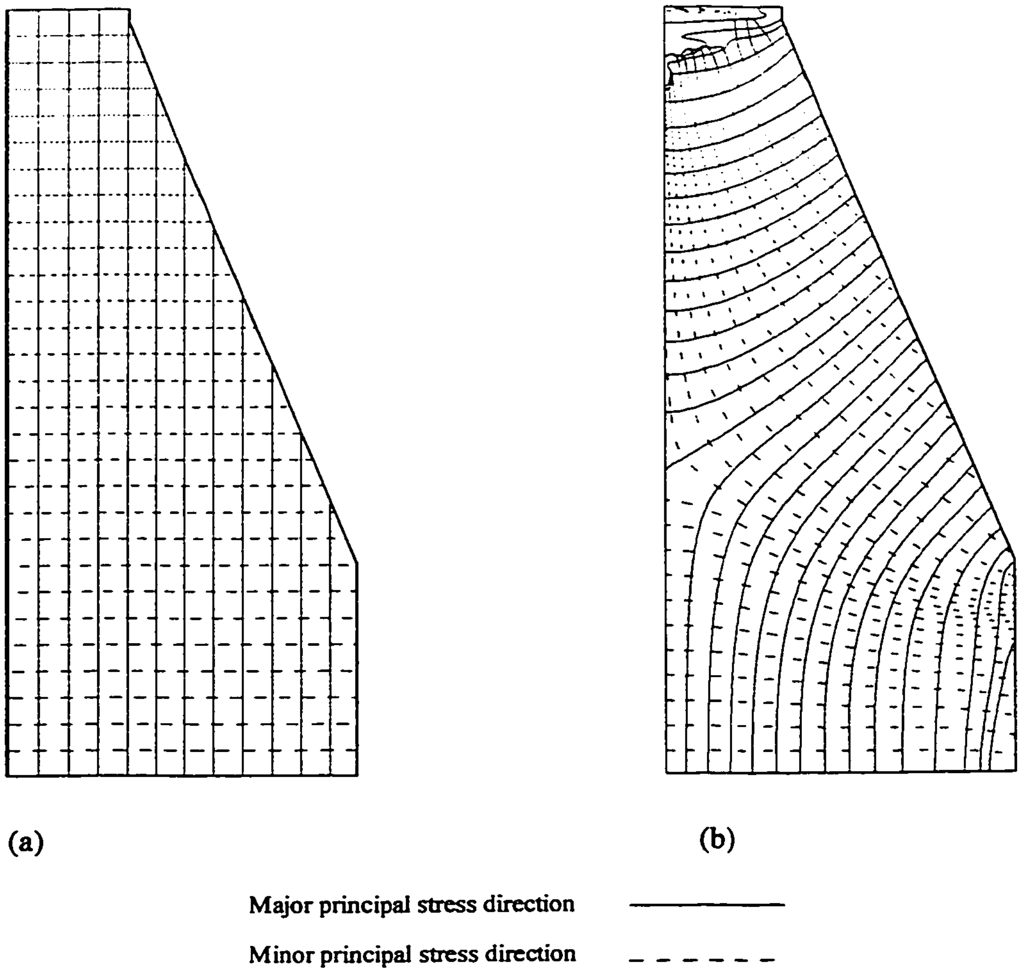

The principal stress directions on a FCV specimen are shown at (a) the start and (b) the end of the membrane loading. The predicted distributions of stresses suggested that principal stress directions were subjected to significant rotations, for instance, up to 90°, as it may be observed in the upper half of the specimen.

Figure 4.13. FCV test response: Principal stress directions

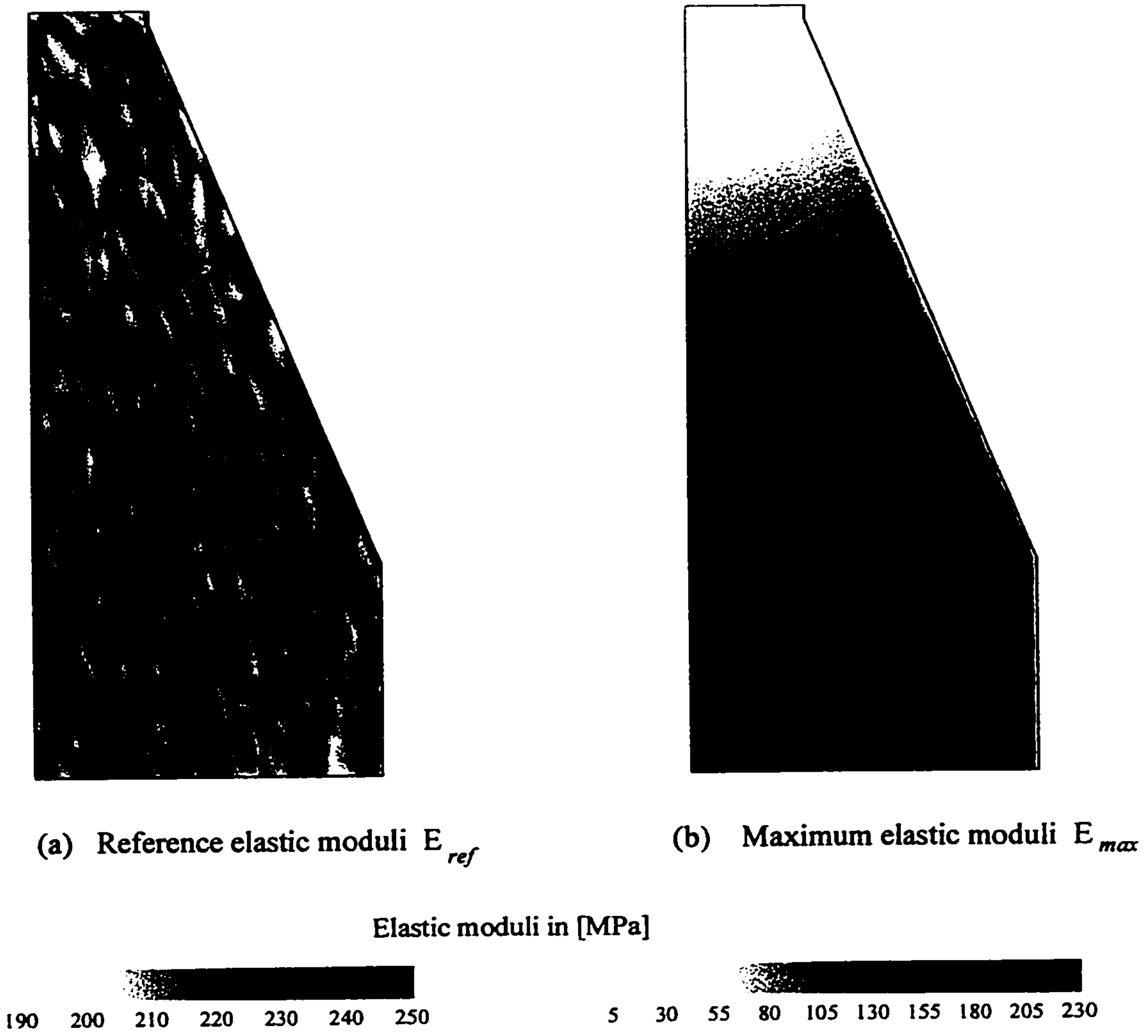

(a) Reference elastic moduli E_{ref}

(b) Maximum elastic moduli E_{max}

The influence of non-uniform distribution of elastic moduli was numerically evaluated by using a random variation of the reference elastic modulus E_{ref} as shown in contour plot (a) at initial conditions. Plot (b) represents the distribution of maximum values of the elastic moduli predicted at the end of the loading stage.

Figure 4.14. Non-uniform distribution of elastic moduli

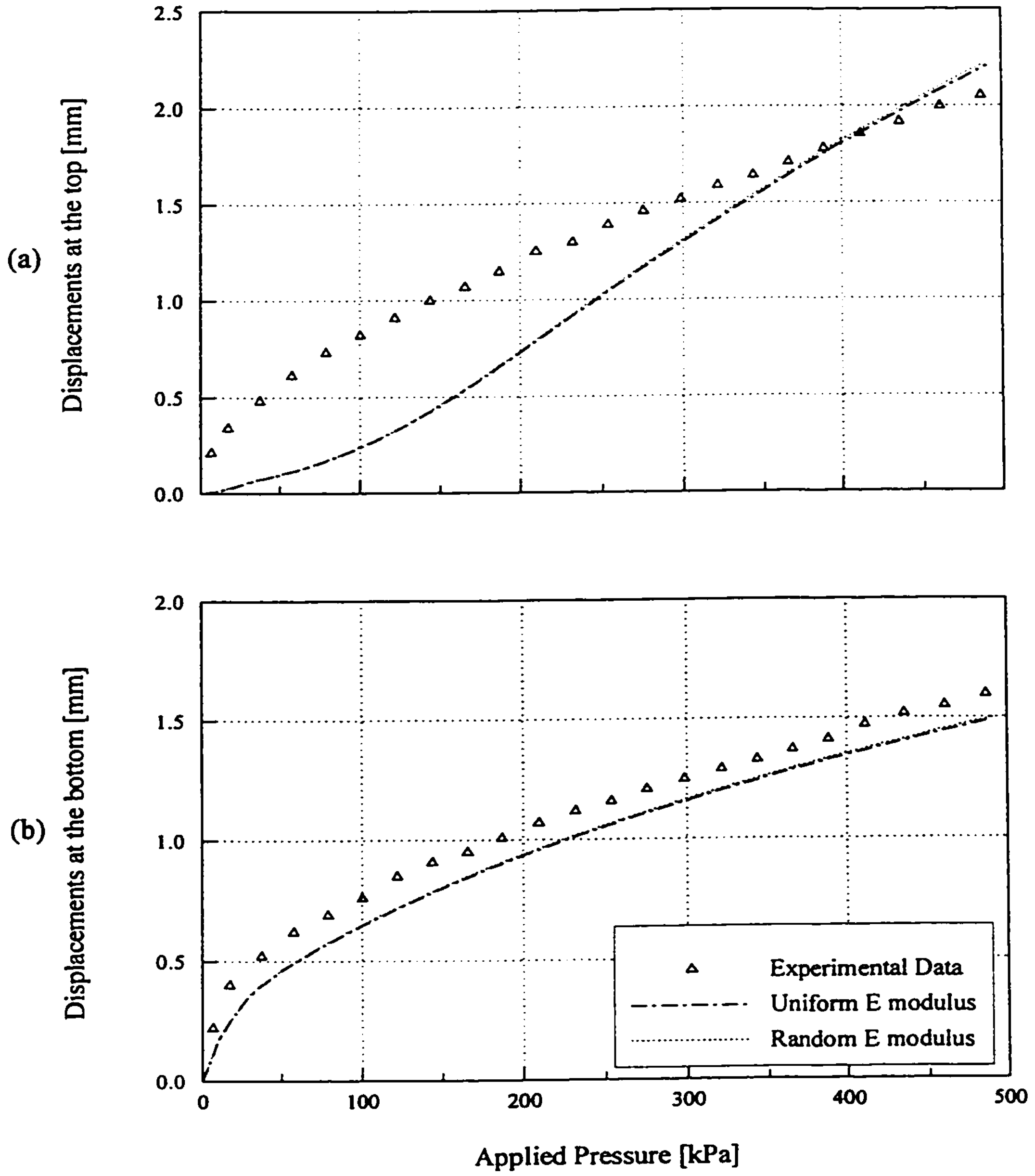

The FCV test responses predicted for the cases of uniform and random distributions of the reference modulus E_{ref} are shown for the (a) top and (b) bottom displacements versus applied membrane pressure. The simulations were obtained using the Anisotropic constitutive law and compared with experimental results.

Figure 4.15. Comparison of uniform and non-uniform responses

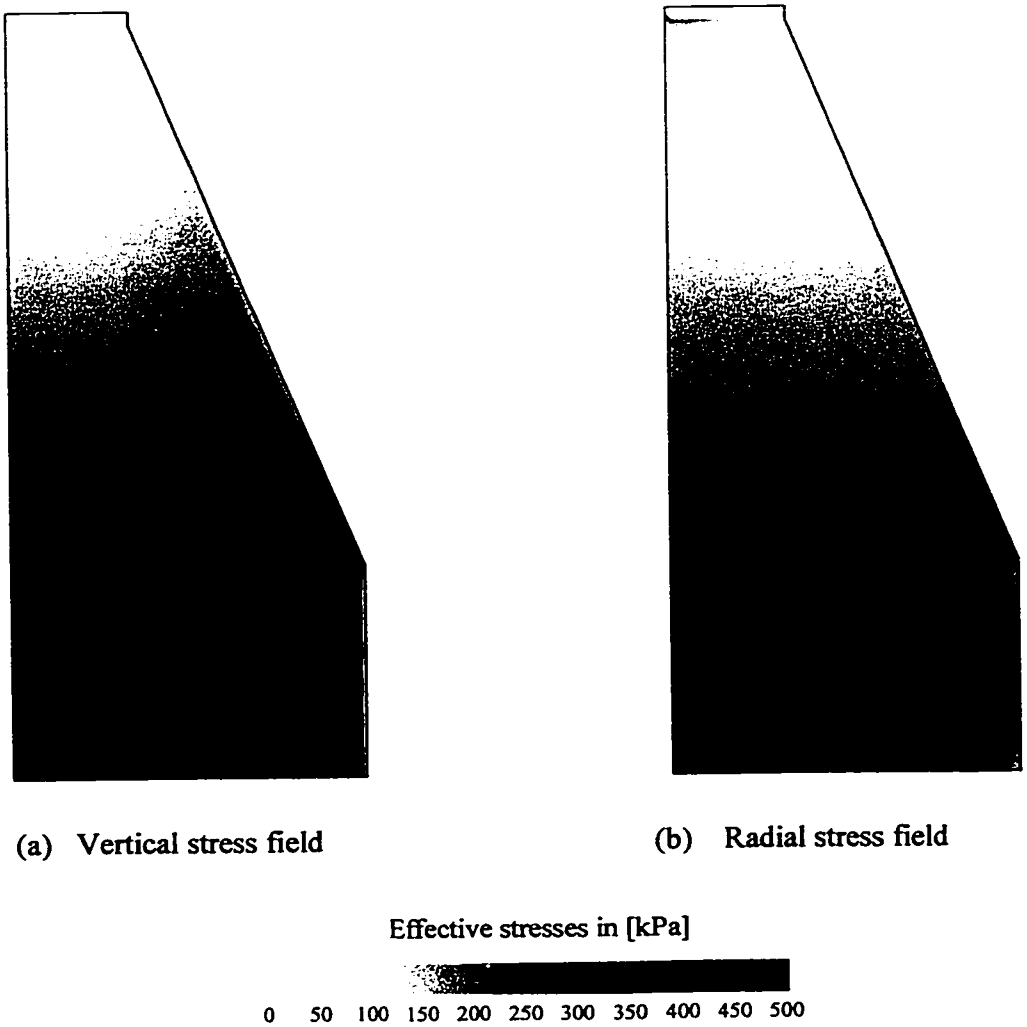

(a) Vertical stress field

(b) Radial stress field

The contour plots illustrate the predicted distributions of (a) vertical and (b) radial effective stresses at the end of the loading stage for a random distribution of the reference modulus E_{ref}. The stresses were predicted using the Anisotropic constitutive law.

Figure 4.16. FCV test response for random E_{ref}: Vertical and radial stresses

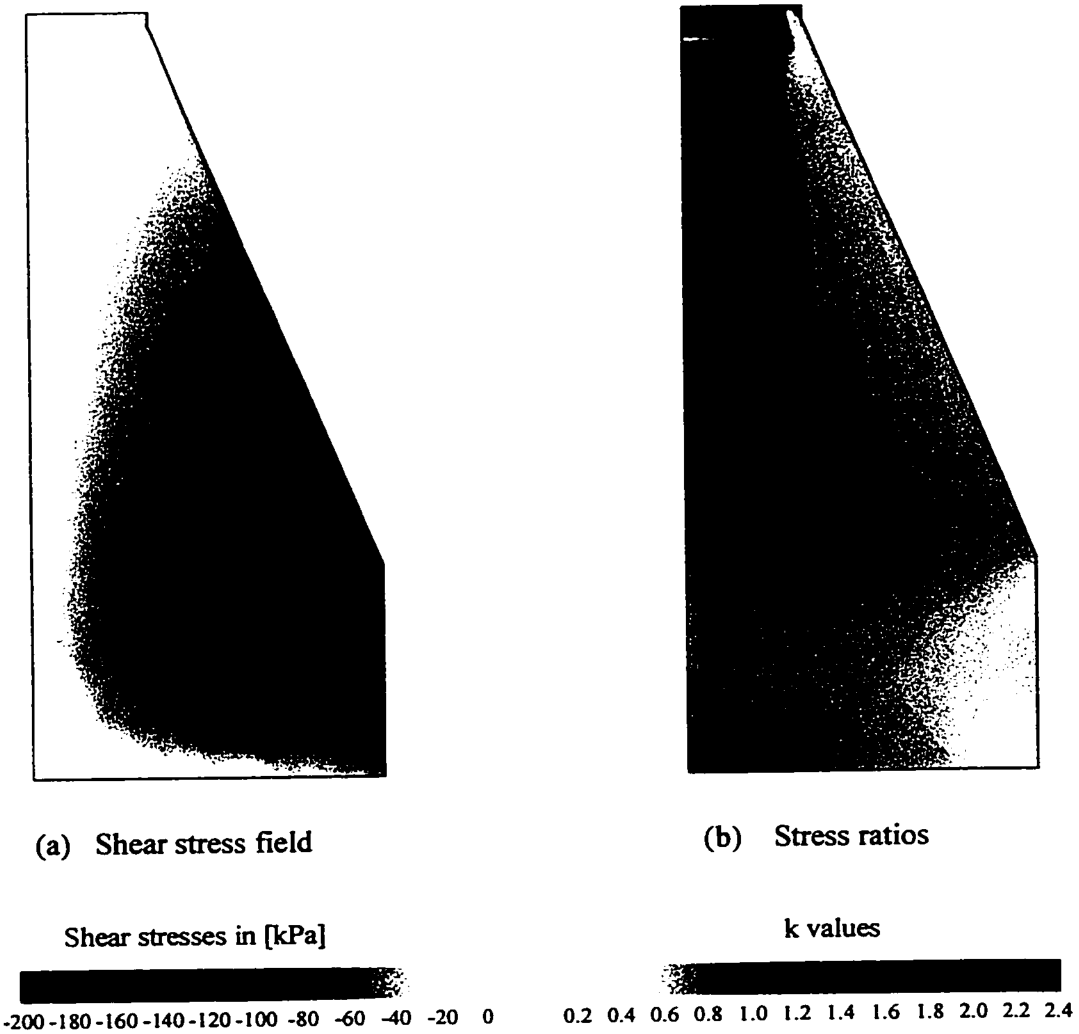

(a) Shear stress field

(b) Stress ratios

The contour plots illustrate the predicted distributions of (a) shear stresses and (b) values of the stress ratio at the end of the loading stage for a random distribution of the reference modulus E_{ref}. The stresses were predicted using the Anisotropic constitutive law.

Figure 4.17. FCV test response for random E_{ref}: Shear stresses and k values

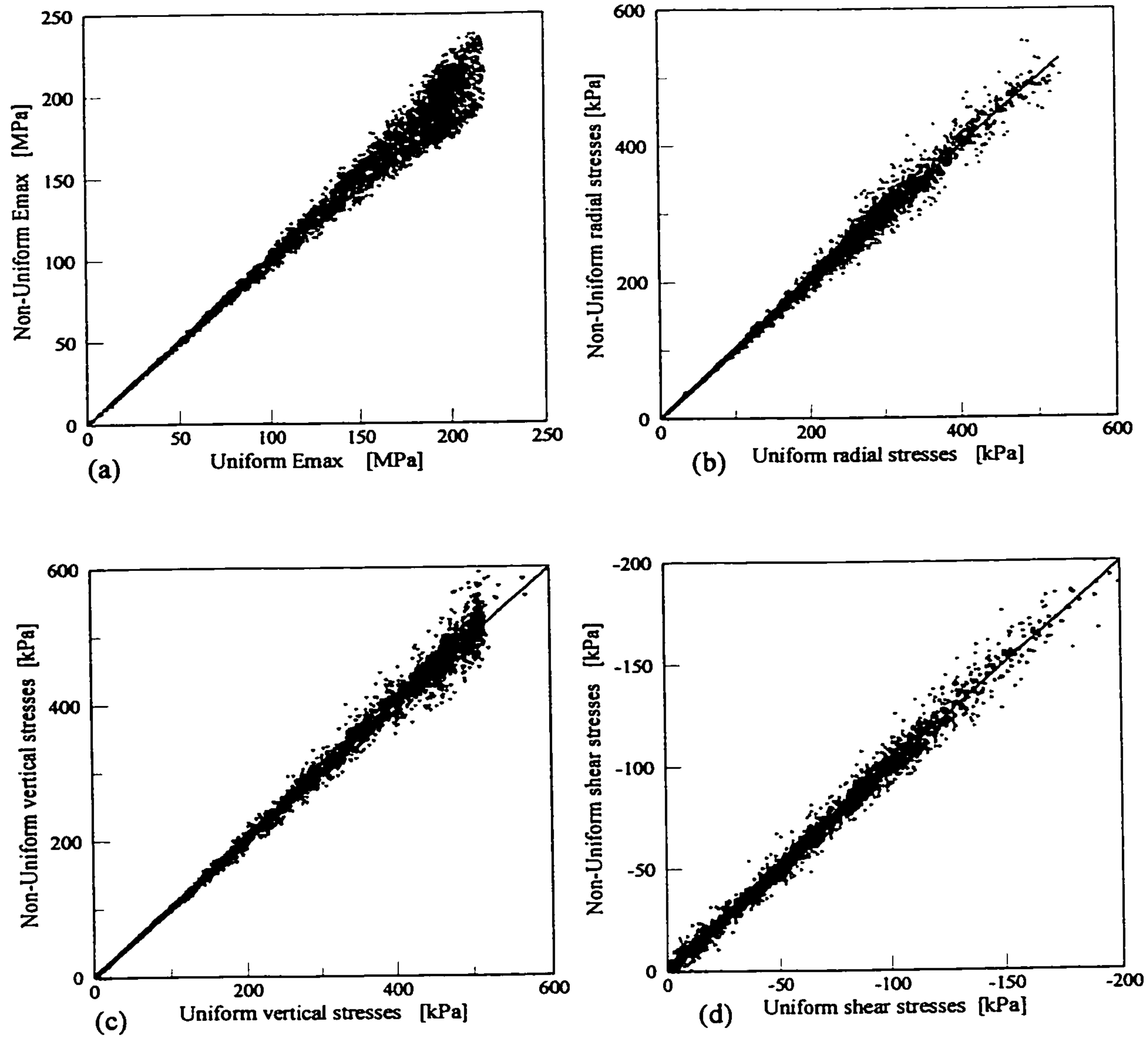

The influence of random distribution of E_{ref} on FCV responses was quantified by comparing results from uniform and non-uniform simulations. The scattering observed in the responses is evaluated in terms of (a) maximum predicted elastic moduli E_{max}, (b) radial stresses σ'_r, (c) vertical stresses σ'_z, and (d) shear stresses σ_{zr}.

Figure 4.18. Influence of non-uniform distribution of E_{ref}

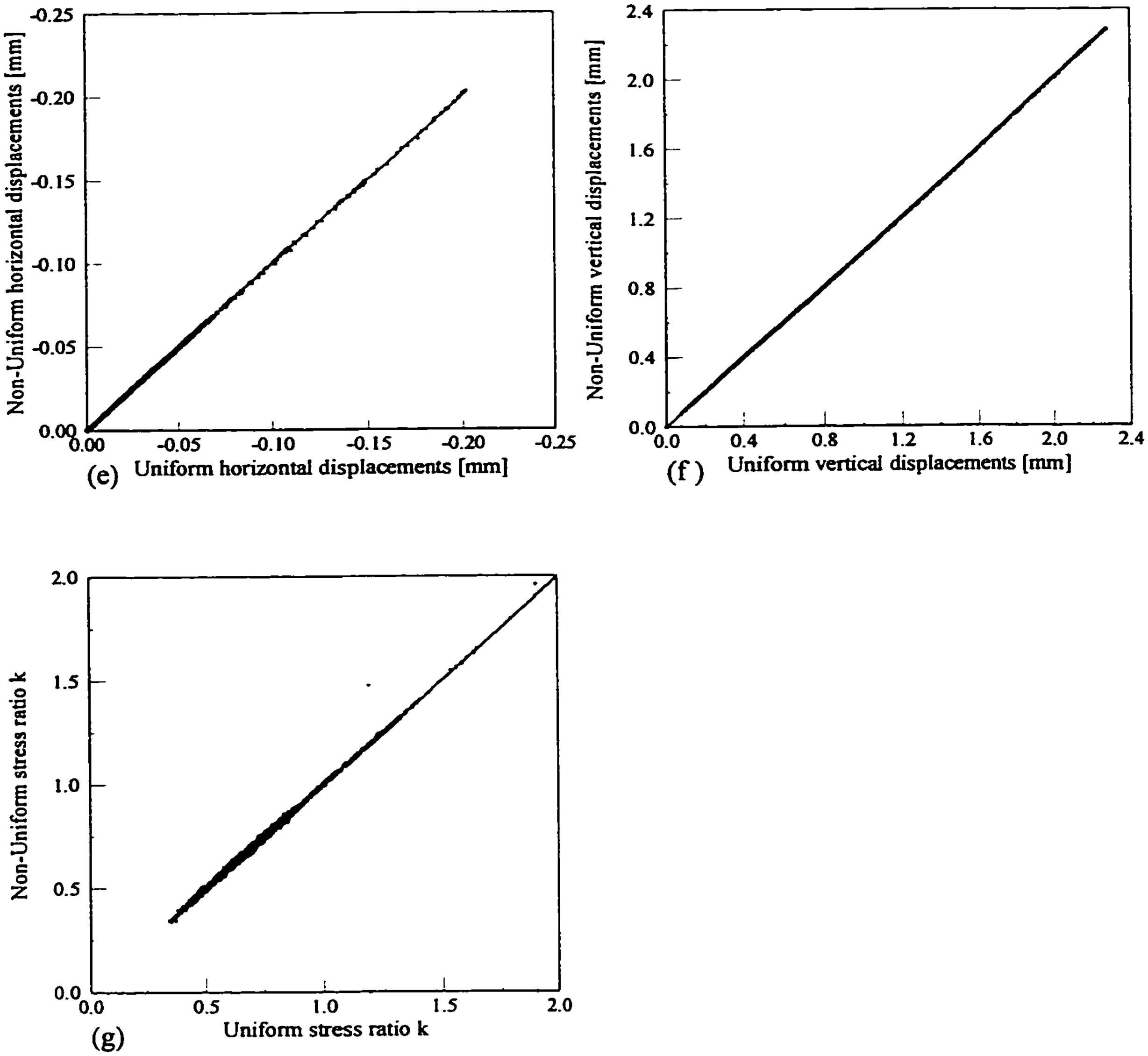

The scattering observed in the responses is evaluated in terms of (e) horizontal displacements *u*, (f) vertical displacements *v*, and (g) values of the stress ratio *k*. The effects of non-uniform E_{ref} are illustrated at the moment of maximum applied pressure $p_{max} = 500$ *kPa*.

Figure 4.18. Influence of non-uniform distribution of E_{ref} (Continuation)

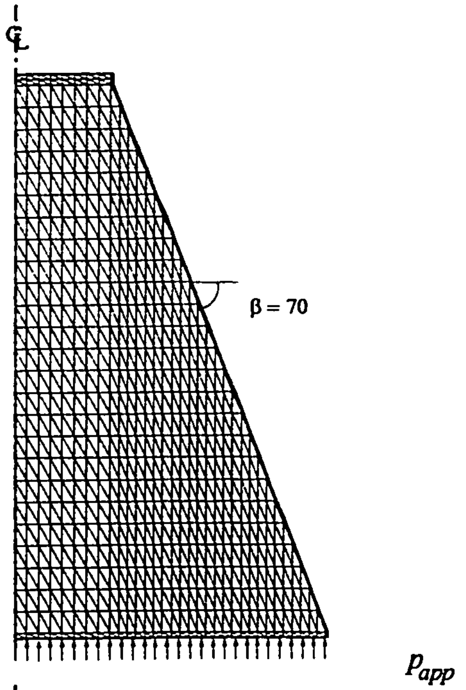

grid 1

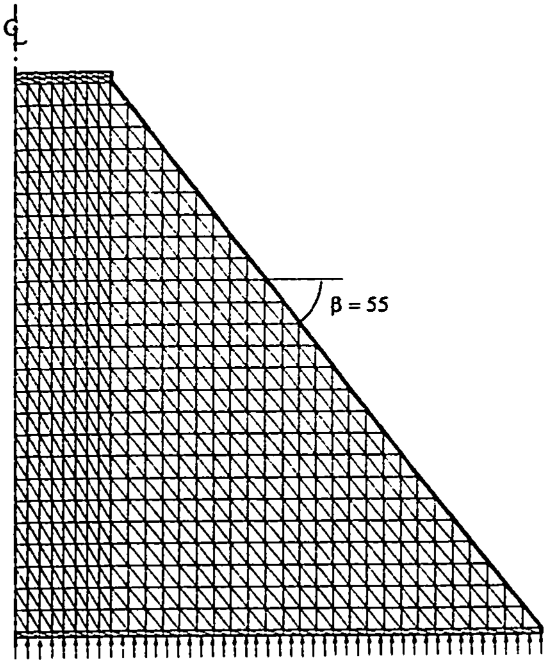

grid 2

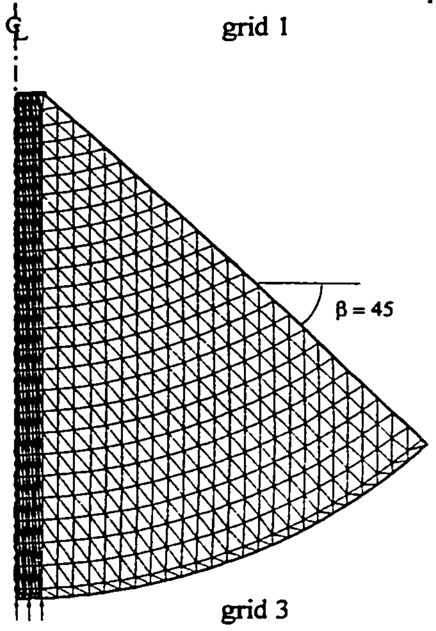

grid 3

Geometry				
grid designation		#1	#2	#3
top radius	R_t [m]	0.15	0.15	0.04
bottom radius	R_b [m]	0.50	0.85	-
height (centerline)	H [m]	1.00	1.00	0.87

Finite Element Meshes	
No. of nodes	2401
No. of triangular elements	1123
No. of interface elements	28
No. of dof's	4631

Figure 4.19. Basic vessel shapes

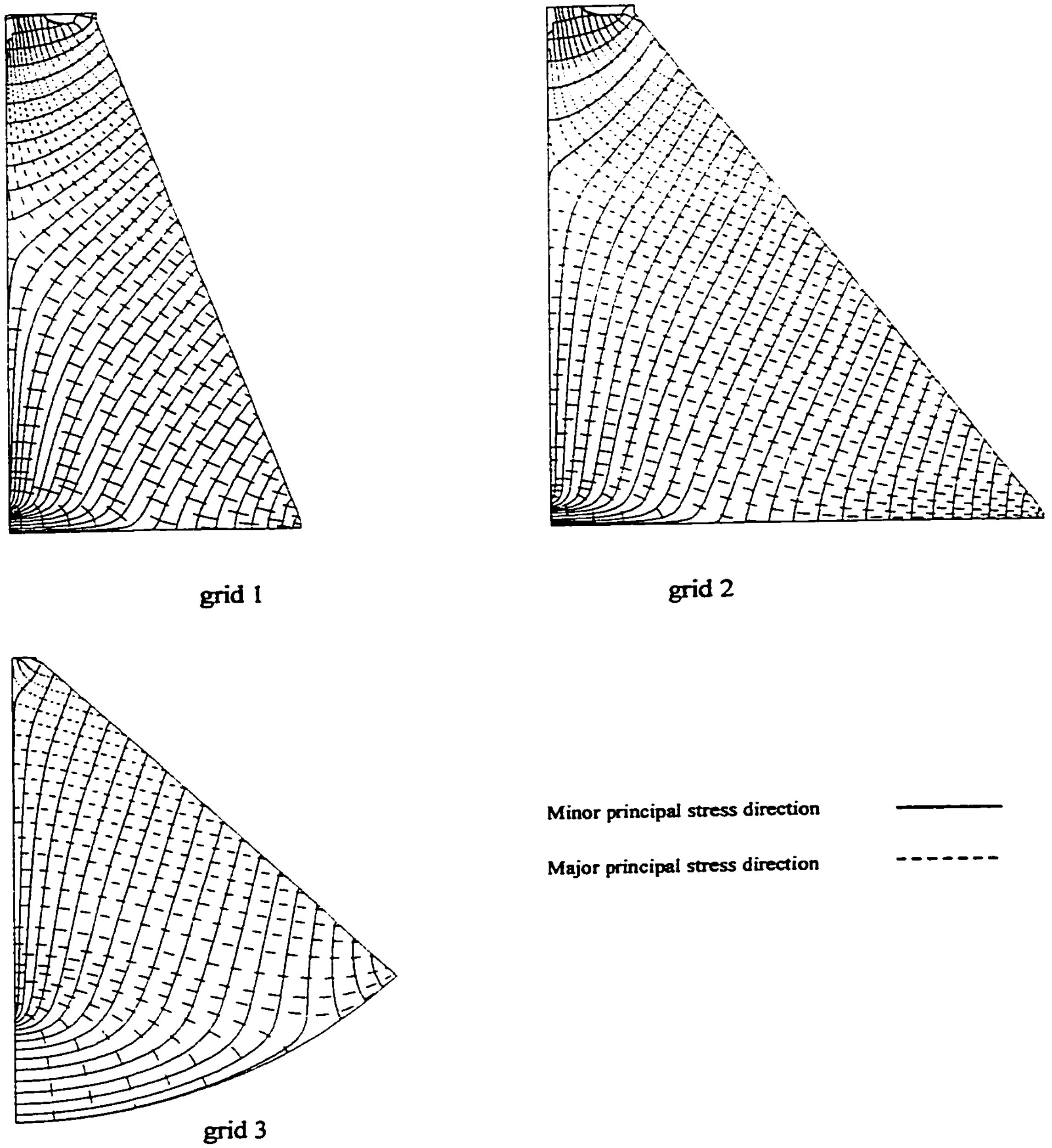
grid 1

grid 2

grid 3

The numerical predictions of principal stress directions for the three trial vessel shapes correspond to an applied pressure of 500 *kPa*, using membrane loading.

Figure 4.20. Predicted principal stress directions

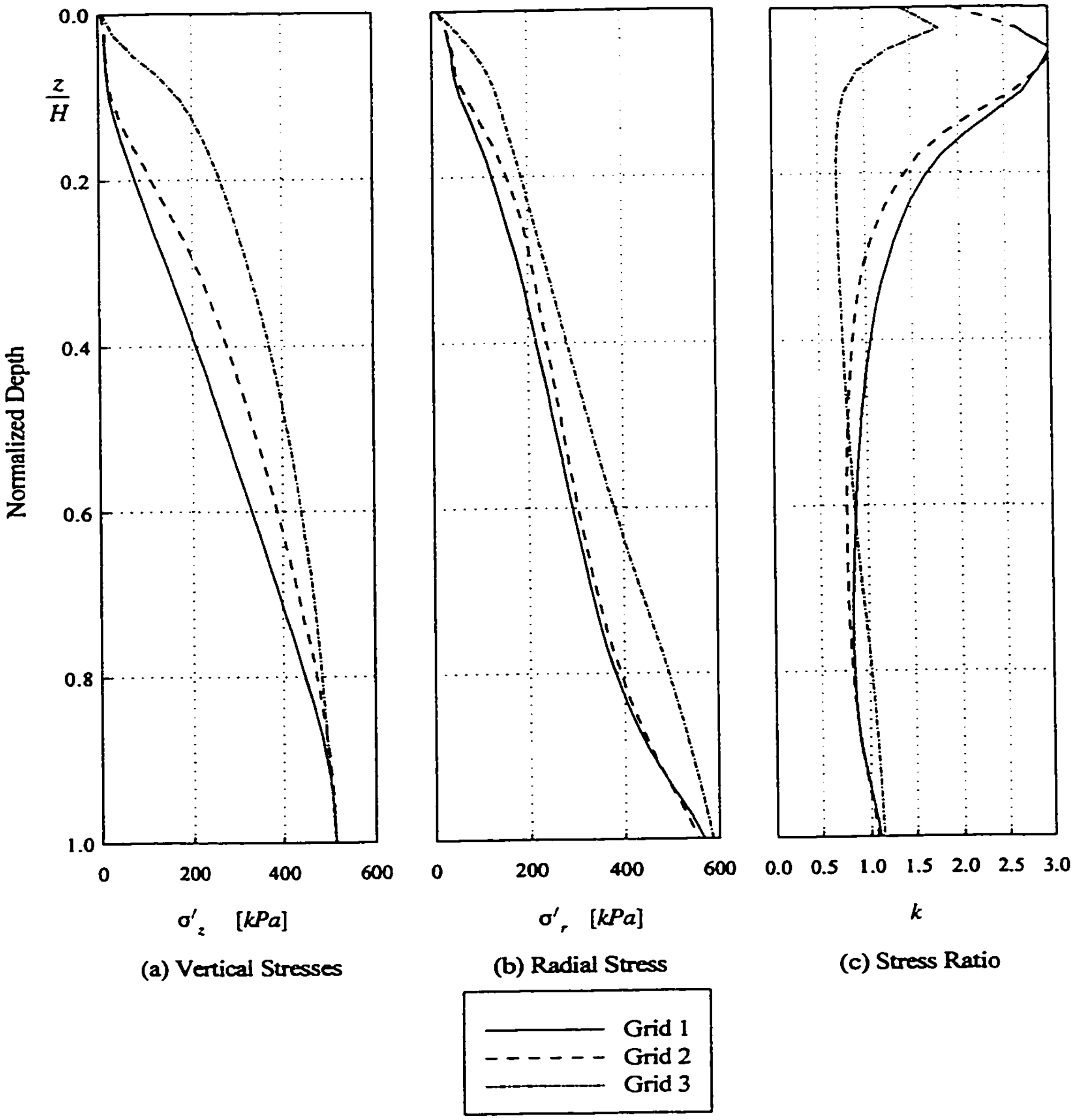

The predicted stresses acting along the centerline of the three basic shapes are shown for (a) vertical and (b) radial effective stresses, and (c) the stress ratio versus the normalized depth *z/H*. Stresses are illustrated at the moment of maximum applied pressure $p_{max} = 500$ *kPa*.

Figure 4.21. Centerline stresses for basic shapes

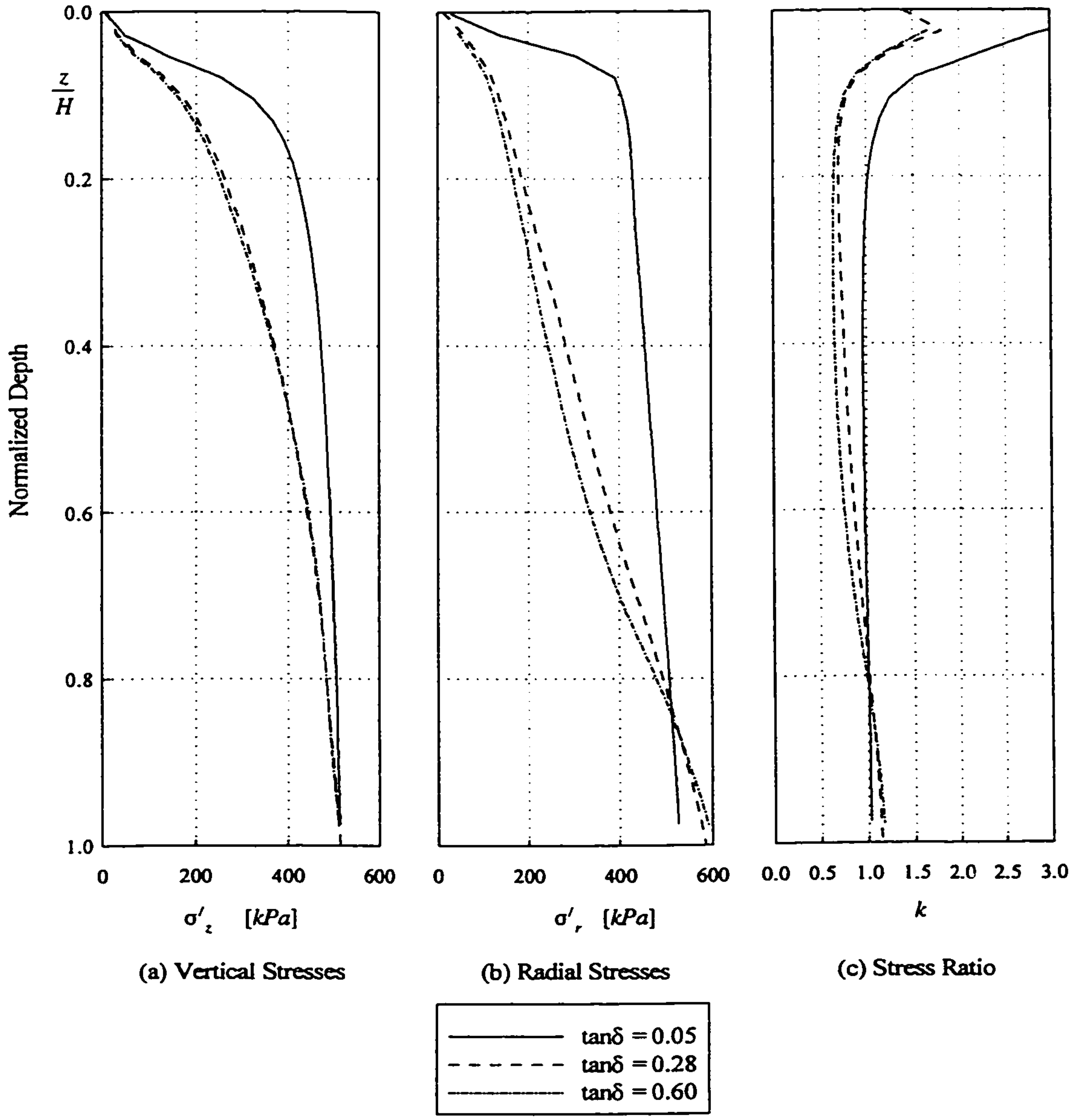

The stresses acting along the centerline of grid #3, for (a) vertical and (b) radial effective stresses, and (c) the stress ratio versus the normalized depth z/H, were predicted for three different values of the friction coefficient tanδ at the wall interface.

Figure 4.22. Centerline stresses for grid #3: Interface friction tanδ

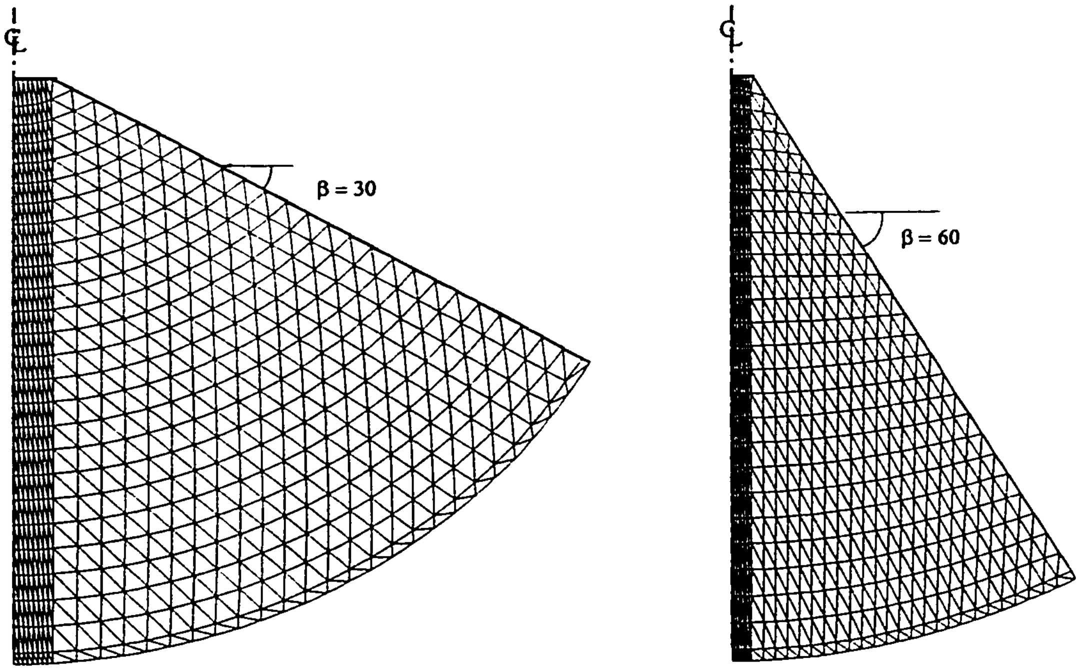

grid 4

grid 5

Finite element simulations of vessel shapes represented by grid #4 and grid #5 were conducted in order to evaluate the effects of wall inclination on the distribution of stresses.

Figure 4.23. Vessel shapes with different wall inclination

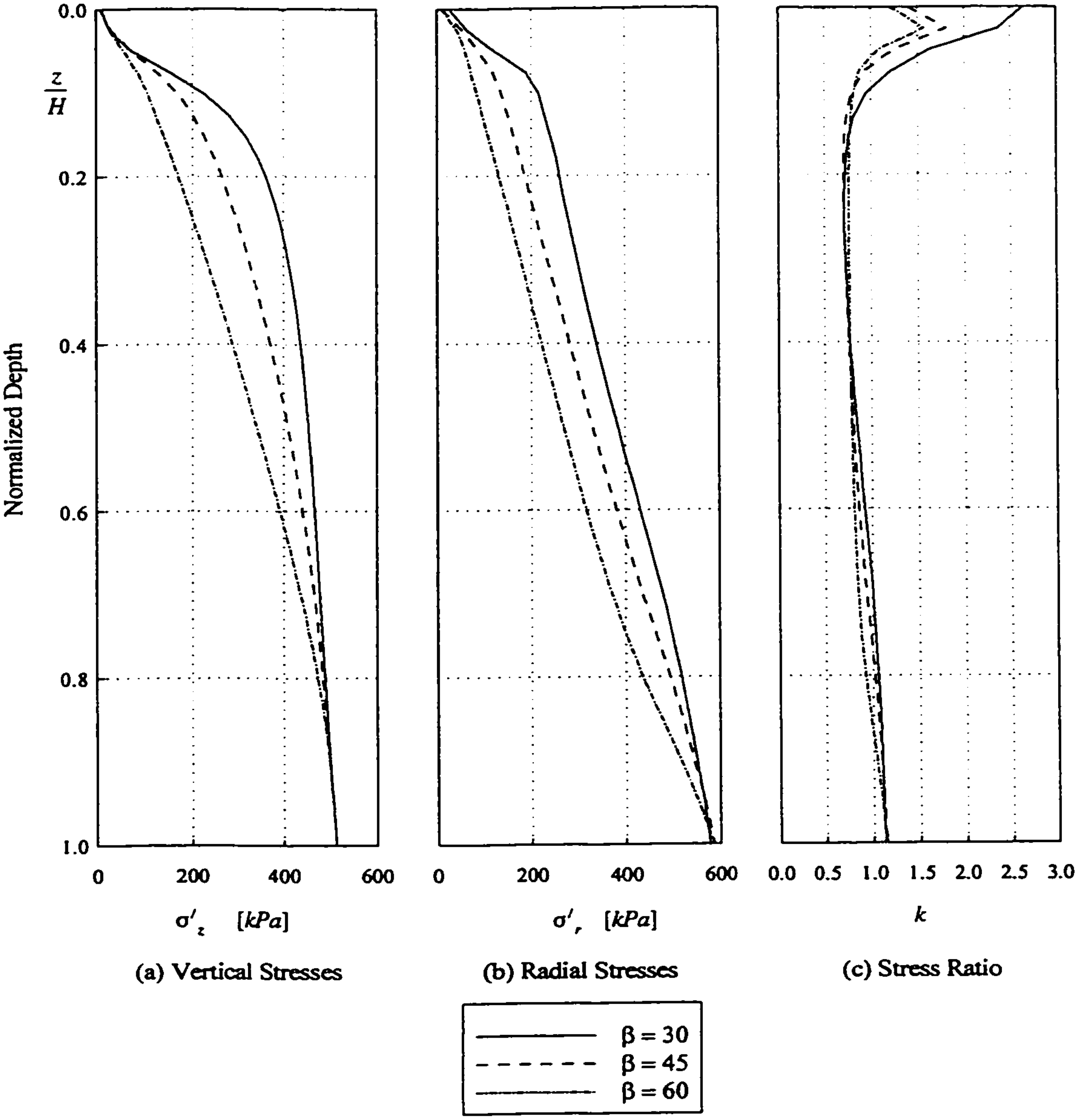

(a) Vertical Stresses

(b) Radial Stresses

(c) Stress Ratio

The stresses acting along the centerline were predicted for values of β equal to 30, 45,and 60° corresponding to grids #4, #3, and #5, respectively. The centerline stresses are shown in terms of (a) vertical and (b) radial effective stresses, and (c) the stress ratio versus the normalized depth z/H.

Figure 4.24. Centerline stresses for grids #3 #4 and #5: Wall inclination β

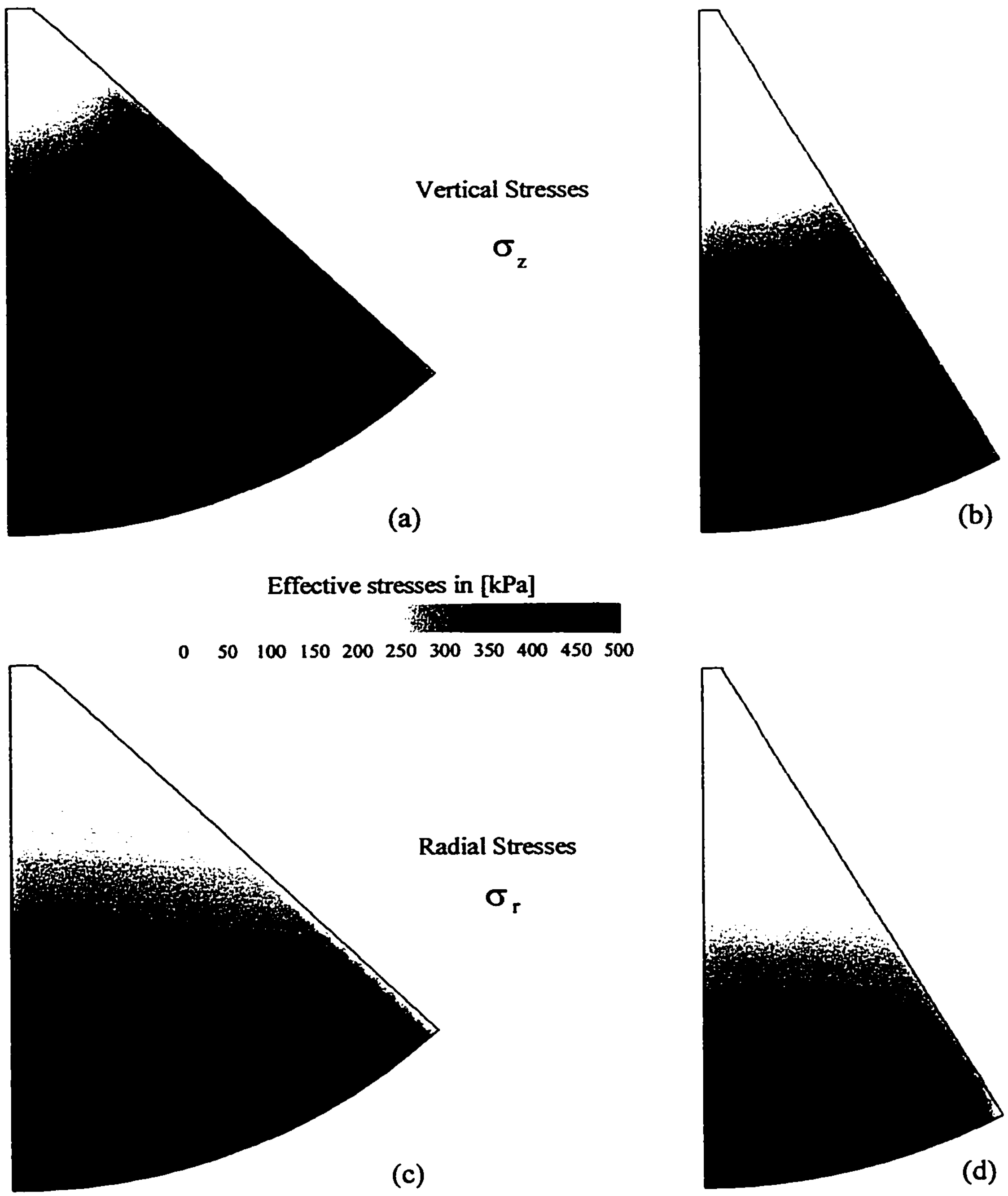

The contour plots of vertical and radial stresses predicted for grid #3 are shown in (a) and (c), while the vertical and radial stresses predicted for grid #5 are shown in (b) and (d).

Figure 4.25. Vertical and horizontal stresses for grids #3 and #5

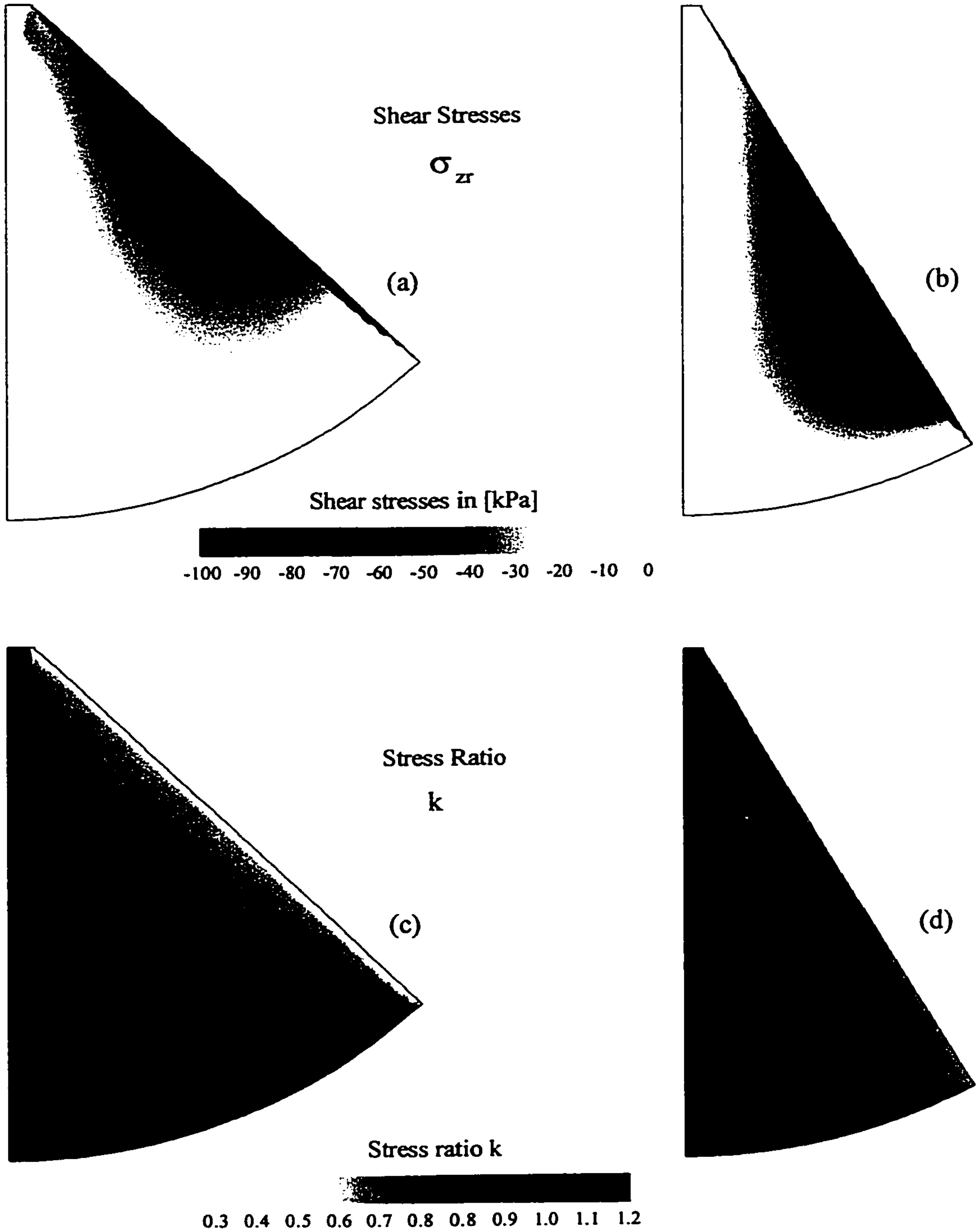

The contour plots of shear stresses and *k* values predicted for grid #3 are shown in (a) and (c), while shear stresses and *k* values predicted for grid #5 are shown in (b) and (d).

Figure 4.26. Shear stresses and *k* values for grids #3 and #5

Chapter 5

PHYSICAL MODELING

5.1 Background

The theoretical background for physical modeling may be expressed using dimensional and similarity analyses. Although both types of analyses are usually considered to be equivalent within the context of model testing, dimensional and similarity analyses are conceptually different. In the ongoing discussions, dimensional analysis is understood as the process of transforming a limited number of variables and parameters, which control a given type of phenomena, into a reduced set of dimensionally homogeneous groups, often dimensionless. This process is based on the Buckingham π theorem. The resulting set of normalized variables are known as π groups. If testing is performed on either model or prototype conditions, the presentation of results in terms of these π groups conveys the essential aspects of the phenomena without redundancies as would be the case when presenting the same results in terms of a primitive set of variables. In other words, dimensional analysis allows for the systematic elimination of subjectivity in the evaluation of test results, regardless of the scale of the problem.

Similarity analysis, on the other hand, investigates the required conditions that a scaled model must comply with, in order to respond in a similar or homologous manner as the prototype. A thorough understanding of the phenomena at hand, together with a careful similarity analysis, provides the scaling factors necessary to extrapolate results from model to prototype conditions. As indicated by Altaee & Fellenius (1994), numerous papers published on the topic of model foundations do not make reference to scaling relations, nor do they explain how results can be extrapolated to prototype conditions. If similarity conditions are not fulfilled, then distortions can be expected when extrapolating results. Consequently, in such cases, the interpretation and the validity of test results are limited, as they are only applicable to reduced scale conditions.

This chapter deals with the reduced-scale testing of model piles embedded in sandy soils. Moreover, test conditions are limited to problems defined in terms of effective stresses and axial loading conditions. Similarity analysis is performed in order to investigate a suitable set scaling factors. Also, a set of basic variables are defined for the problem of load tests on piles, and by means of dimensional analysis, a reduced set of normalized parameters is presented for the cases of quasi-static and dynamic loads.

5.2 Similarity Conditions

5.2.1 Definitions

From a mathematical viewpoint, the basic concept of similarity may be presented as follows,

- *"The function f' is similar to the function f, provided the ratio f'/f is a constant when the* *functions are evaluated for homologous points and homologous times. The constant* $\lambda_f = f'/f$ *is called the scale factor for the function* f'*.*" (Langhaar 1951)

In engineering applications, and according to the degree of complexity of the system being studied, four levels of similarity conditions can be distinguished, including:

- Geometric similarity. "*Two systems are geometrically similar if the ratio* $\lambda_L = L_m / L_p$ *is constant throughout the systems, where L is any distance in the systems*" (Langhaar 1951).

  The subscripts *m* and *p* refer to model and prototype systems, respectively.

- Kinematic similarity. "*The motions of two systems are similar, if homologous particles lie at homologous points at homologous times. If kinematic similarity exists, then corresponding components of velocity and acceleration are similar.*" (Langhaar 1951).

  Within the context of similitude analysis, the term homologous refers to the concept of one to one correspondence, as in a functional relation.

- Dynamic similarity. "*Two systems are said to be dynamically similar if homologous parts of the systems experience homologous net forces. If the systems are kinematically similar and if mass distributions are similar, then dynamic similarity exists.*" (Baker, Westine & Dodge, 1973).

- Constitutive similarity. "*Models do not have to be constructed from the same material as in the prototype. One can define homologous constitutive properties of materials. Provided the non-dimensionalized stress-strain curves of homologous material are similar, constitutive similarity exists*" (Baker, Westine & Dodge, 1973).

We are going to consider the problem of a model pile embedded in cohesionless soil and tested under a half-sine impulsive axial loading. The purpose of analyzing the dynamic behaviour of the pile is to lend some generality to the investigation so that pile driving and Statnamic Load Test conditions may be included in the analysis. Typical field procedures for pile load tests such as the Quick- and Slow-Maintained Load and the Constant Rate of Displacement are readily included in the present analysis as particular cases of dynamic loading.

5.2.2 Governing Equations

In order to establish a suitable set of scaling factors, we must ensure that the governing equations, i.e. those which describe the load-displacement phenomena, for both model and prototype systems are dynamically and constitutively similar[1]. The most important aspects of the phenomena are controlled by: *(i)* the equation of motion; *(ii)* the dependency of the sand's elasto-plastic material properties on the void ratio and stress confinement; and *(iii)* the unit skin friction along the shaft. A brief description of each one of these aspects is introduced next.

(i) The Equation of Motion. For the given full scale or prototype system, the equation of motion is given by

$$M_p \ddot{A}_p + C_p \dot{A}_p + K_p A_p = F_p(t_p) \quad , \tag{5.1}$$

and correspondingly, for the reduced scale or model system, the equation of motion is

$$M_m \ddot{A}_m + C_m \dot{A}_m + K_m A_m = F_m(t_m) \quad , \tag{5.2}$$

---

[1] Geometric and kinematic similarities are implicitly included in the concept of dynamic similarity.

where ***M***, ***C***, and ***K*** refer to the mass, damping, and stiffness matrices of the system with distributed material properties, and A represents the system displacements. The load term is given by the force F, and t is the time variable. Superimposed dots indicate differentiation with respect to time, and subscripts m and p refer to the model and prototype systems, respectively.

(ii) Dependency of Material Properties of Sand on Void Ratio and Confining Stresses. With respect to the constitutive similarity between the model and the prototype, the pile and soil subsystems are treated differently. Pile behaviour is considered to be linear elastic and its material properties are stress independent. Consequently, the requirements for constitutive similarity are readily satisfied since the model and prototype of the pile subsystem are often built with the same material. The elasto-plastic material properties of sands, on the other hand, are known to depend on a number of variables, such as initial void ratio or density, over-consolidation ratio OCR, material fabric, straining range, and perhaps the most important of all, stress confinement. For the purposes of the ongoing analysis, the discussions are limited to the dependency of the elastic modulus E on initial void ratio and the stress level. This is consistent with experimental results reported in the literature, where the elastic modulus of sand is related to void ratio and stress levels by the expression (Hardin & Blandford 1989, and Yu & Richart 1984):

$$E_i = A_{OCR} \frac{1}{F(e)} \sigma_{ref} \left(\frac{\sigma_i}{\sigma_{ref}} \right)^{0.5} , \tag{5.3}$$

where σ_{ref} is a reference stress, A_{OCR} is a parameter that depends on the overconsolidation ratio and on the material fabric, and σ_i, with $i = 1, 2, 3$, represents the principal stresses. *F(e)* may be defined in terms of the void ratio *e* as

$$F(e) = 0.3 + 0.7\, e^2 \quad . \tag{5.4}$$

(iii) Unit Skin Friction. For the prototype, the unit skin friction acting along the shaft is defined as

$$f_s = k\, \sigma'_v \tan\delta \quad , \tag{5.5}$$

where δ is the angle representing the static friction between the pile and the soil, σ'_v is the vertical effective stress, and *k* is the coefficient of lateral earth pressure. Expression (5.5) does not include the effects of surcharges on the skin friction. Such surcharges can however be readily implemented in the physical model as well as in expression (5.5).

5.2.3 Scaling Requirements

Appropriate scaling factors for the model pile-soil system may be directly obtained by scaling the equations of motion indicated in expressions (5.1) and (5.2). The set of scaling factors required for the pile-soil system are summarized in Table 5.1. While the strain ratio is always equal to one, the geometric ratio λ_L is imposed by the chosen size of the model with respect to the prototype. Area and volume ratios are directly related to λ_L. For instance, $\lambda_{Area} = \lambda_L^2$, and $\lambda_{Volume} = \lambda_L^3$. In the present approach, the densities of the model materials, pile and sand, are specified to be identical to those of the prototype, therefore the density ratio, $\lambda_\rho = 1$, is an imposed condition. The mass ratio is then constrained by scaling factors 3 and 4, for instance $\lambda_M = \lambda_L^3$.

The stress, force, time, velocity, acceleration, stiffness, elastic moduli and damping scaling factors have yet to be established. Using the corresponding ratios, i.e. substituting M_m by $\lambda_M M_p$ and so forth, in expression (5.2), the equation of motion of the model can be expressed in terms of prototype variables. For example

Table 5.1 **Scaling factors λ required for the pile-soil problem.**

1.	λ_L	$= L_m / L_p$	Length & Displacement
2.	λ_{Area}		Area
3.	λ_{Volume}		Volume
4.	λ_ρ		Density
5.	λ_M		Mass
6.	λ_σ		Stress
7.	λ_ε		Strain
8.	λ_F		Force
9.	λ_T		Time
10.	λ_{vel}		Velocity
11.	λ_{acc}		Acceleration
12.	λ_K		Stiffness
13.	λ_C		Damping
14.	λ_E		Elastic moduli

$$\left\{\frac{\lambda_L^2}{\lambda_T}\right\}^2 M_p \ddot{A}_p + \left\{\frac{\lambda_C \lambda_L}{\lambda_T}\right\} C_p \dot{A}_p + \left\{\lambda_K \lambda_L\right\} K_p A_p = \left\{\lambda_F\right\} F_p(t_p) \quad . \tag{5.6}$$

Dynamic and constitutive similarity between model and prototype is achieved if the factors within brackets in expression (5.6) are all equal to one. It should be noted that it is possible to factorize expression (5.6) in different ways to produce alternative sets of scaling factors. The set of scaling factors, typically adopted for physical models tested in centrifuge devices, is presented in Table 5.2 (Prakash & Sharma 1990). If the model performance is to be undistorted with respect to the prototype response, then all factors listed in Table 5.2 must be fulfilled.

As mentioned previously, Table 5.2 only presents one particular set of scaling factors, but other sets are possible; see, e.g., Altaee & Fellenius (1994), Dancygier (1995), and Kumae et al. (1997). Different sets of scaling factors produce physically different models. This implies that if different models are tested, all fulfilling their corresponding set of scaling factors, their behaviors will be exactly similar to that of the prototype. There are, however, technical aspects that must be considered, as it might be difficult or not feasible to meet certain scaling criteria. For those models in which the scaling criteria can not be fully satisfied, distortions are introduced to the scaling. In such cases, the choice of a set of scaling factors is restricted to the set which would introduce the least amount of distortion into the model response.

Table 5.2		**Particular set of scaling factors**	
1.	λ_L	$= L_m / L_p$	Length & Displacement
2.	λ_{Area}	$= \lambda_L^2$	Area
3.	λ_{Volume}	$= \lambda_L^3$	Volume
4.	λ_ρ	$= 1$	Density
5.	λ_M	$= \lambda_L^3$	Mass
6.	λ_σ	$= 1$	Stress
7.	λ_ε	$= 1$	Strain
8.	λ_F	$= \lambda_L^2$	Force
9.	λ_T	$= \lambda_L$	Time
10.	λ_{vel}	$= 1$	Velocity
11.	λ_{acc}	$= 1/\lambda_L$	Acceleration
12.	λ_K	$= \lambda_L$	Stiffness
13.	λ_C	$= \lambda_L^2$	Damping
14.	λ_E	$= 1$	Elastic moduli

According to Table 5.2, the model is required to have densities and stresses identical to those of the prototype, i.e. λ_ρ and λ_σ equal to one. This is of key importance for achieving constitutive similarity of the model, and particularly so for the soil subsystem, since no scaling of material properties is then required. Given that material properties of sand depend on density and stress levels, any other set of scaling factors in which either λ_ρ or λ_σ are not equal to one, would require appropriate scaling of material properties, namely: elastic modulus E; Poisson's ratio ν; friction angle at failure and at critical state ϕ_f and ϕ_{cs}; hardening parameters; etc. The scaling of these material properties would require the definition of functional relations between those material properties with density and stress confinement levels, such as that presented in expression (5.3) for the elastic modulus.

While most of the scaling factors in Table 5.2 are technically easy to enforce, the scaling of acceleration, stress, and damping present some difficulties that must be dealt with.

(i) **The Acceleration Ratio $\lambda_{acc} = 1 / \lambda_L$.** Acceleration quantities enter the equation of motion by the terms related to inertial and gravity loads, as well as by the term containing the time-dependent forcing function. The acceleration related to the inertial term is a natural response of the system and does not require any constraint in the physical model. Therefore, there is no technical difficulty associated with acceleration; thus it is relatively easy to scale. The forcing function, on the right-hand side of expression (5.1), consists of the applied force plus the gravity load ($M g$). Gravity loads cannot be properly scaled with the factor $\lambda_{acc} = 1/\lambda_L$ unless a centrifuge device is use for the testing of the model. However, if we consider that in the pile-soil system gravity loads do not produce strains nor displacements, and also that the gravity load due to the pile mass is usually very small when compared with the applied force, as is the case for load test to failure, it is possible to conclude that gravity loads do not have a significant impact on the response of the model, whether a test is performed in a centrifuge or in any $1g$ device.

(ii) The Stress Ratio $\lambda_\sigma = 1$. The limitations associated with the lack of proper gravity scaling in the so-called $1g$ devices are not derived from the equation of motion but rather from the unit skin friction, which is controlled by equation (5.5). For the prototype, the unit skin friction at a certain depth z is

$$f_{s_p} = \sigma'_h \tan\delta = k\left(\rho_p\, g_p\, z_p\right) \tan\delta \tag{5.7}$$

with σ'_h as the effective horizontal stress at depth z, while for the model

$$f_{s_m} = k\left(\rho_m\, g_m\, z_m\right) \tan\delta \ . \tag{5.8}$$

If we assume that k and $\tan\delta$ are the same in model and in prototype, then the stress scale factor for the unit skin friction is

$$\lambda_\sigma = \frac{f_{s_m}}{f_{s_p}} = \lambda_\rho \frac{g_m}{g_p} \lambda_L \ , \tag{5.9}$$

where density ratio is $\lambda_\rho = 1$. In the case of pile-soil models tested in the centrifuge, the acceleration ratio is $g_m = (\lambda_{acc} g_p) = (g_p/\lambda_L)$. Thus the stress ratio $\lambda_\sigma = 1$ has been fulfilled in expression (5.9).

Using $1g$ devices, where the gravitational acceleration is not scaled, i.e. $g_m = g_p$, expression (5.9) yields a distorted stress ratio $\lambda_\sigma = \lambda_L \neq 1$. This means that the unit skin friction of piles tested in $1g$ devices are misrepresented by a factor of λ_L, for instance, $f_{s_m} = \lambda_L f_{s_p}$. Obviously, this type of distortion represents a severe handicap for model piles tested in $1g$ devices.

The inspection of equation (5.7) reveals that the unit skin friction of model piles can be scaled by means of controlling gravity, as in the case of centrifuges, or by scaling horizontal stresses. The later alternative is considered useful in the case of testing model piles in the FCV device, in which σ_r can be controlled by varying the pressure applied to the membrane p_{app}.

(iii) The Damping Scale Factor $\lambda_C = \lambda_L^2$. The direct measurement of soil damping is a difficult task, and is not always attempted in field conditions. Since material damping may not be measured, a practical approach to control or impose soil damping in the model is considered not to be feasible. As a result, what remains to be established is to determine how important is the influence of material damping on the pile-soil response. This influence has been evaluated by means of the numerical simulations described in Section 5.2.5.

5.2.4 Influence of the Size of the Sand Particles

For practical considerations, the model is assumed to be constructed with the same sand as in the prototype, and with the scaling relations discussed in the preceding section. The size of the sand grains in the reduced model is not scaled with λ_L the length factor[2], begging the question of how much influence it exerts on the model response. This problem, common to both centrifuge and 1*g* devices, should not be disregarded as it represents an important aspect of physical modeling in sands. Franke & Muth (1985) reported work done by Ovesen (1980) which presented experimental evidence demonstrating that for circular footings embedded in sand with a ratio of footing diameter to grain size d/d_g greater than 30 the influence of grain size effects on model response can be neglected. In lieu of a specific criteria for model piles, the foundation width to grain size ratio, or aspect ratio, described above is applied to FCV model piles. For a model pile with 17*mm* in diameter and for the Ottawa sand with a mean grain size $D_{50} = 0.39mm$ the aspect ratio is 44, suggesting that particle size effects may not influence model responses.

5.2.5 Numerical Simulations

The validity of the similarity criteria for the pile-soil system, presented in Table 5.2, is confirmed by comparing numerical predictions of prototype and model responses. The sand is modeled as an elasto-plastic material, using the pressure-dependent constitutive model, while the pile is treated as a linear elastic material. The pile-soil interface is modeled with interface elements, and the transient behaviour is modeled via a Galerkin time-stepping algorithm (Stolle 1995), which accounts for the transfer of momentum between time increments.

With regards to the boundary-valued problem for the prototype, the soil domain is

---

[2] Besides the fact that reducing the grain size is impractical, scaling of grain size would result in drastic changes in the material properties of the soil.

assumed to have a radius of 13.4 *m* with a depth to bedrock of 15.3 *m*, and the concrete-filled, steel pipe pile is 9.0 *m* long and 0.34 *m* in diameter. Appropriate values for material properties and soil parameters were obtained from the literature; see, e.g. Janes et al.(1994), and Mabsout et al. (1995). The finite element mesh, shown in Figure 5.1, is formed by 1860 nodes and 840 six-noded triangular elements, plus 30 six-noded interface elements at the pile-soil interface. The boundary conditions are defined by: *(i)* free displacement for nodes on the upper boundary; *(ii)* fixed nodes on the right boundary (since the right boundary is placed far away[3] from the centerline there is no need to define a transmitting boundary); (*iii*) nodes at the centerline are constrained in the horizontal direction; and *(iv)* fixed nodes at the lower boundary. The loading function corresponds to a 100 millisecond half-sine pulse of a uniform distributed vertical stress applied to the head of the pile, which is similar to that of an Statnamic Load Test (see, e.g. Horvath et al. 1990, and Middendorp et al. 1992).

Two reduced scale models are considered in the present simulations, that of a hypothetical centrifuge model and that of a FCV model. For both models, a geometric ratio of 1/20 is selected along with the scaling factors specified in Table 5.2. While the centrifuge model uses the same node and element disposition as in the case of the prototype, the FCV model corresponding to an optimized shape is discretized with the mesh shown in Figure 5.2. This mesh has 2401 nodes and 1067 six-noded triangular elements, plus 56 six-noded interface elements used at the pile-soil interface and at the walls of the vessel. The simulation of the pile load test in the FCV model consists of a two-stage loading. In a first stage, with the model pile already installed inside the control volume, uniform pressure is applied to the bottom of the

---

[3] For instance, over 10-pile diameters away.

vessel in order to generated appropriate initial stresses in the control volume. In a second stage, the model pile is loaded according to the load test specifications, while keeping constant pressure on the bottom of the sand specimen.

The results from the simulations are presented in Figures 5.3 and 5.4 in terms of load and time versus displacements at the pile head and toe, respectively. In these figures the variables have been normalized in a way that responses from the models can be compared with that of the prototype, specifically, *(i)* applied stresses are normalized with respect to the reference elastic modulus of the sand E_s; *(ii)* time is normalized according to an estimation of the fundamental period of the pile [4]; and *(iii)* displacements are normalized with respect to pile length. These normalizations are justified in Section 5.3.2, which addresses dimensional analysis.

The normalized response of the hypothetical centrifuge model, as seen in Figures 5.3 and 5.4 directly overlapped with the normalized response of the prototype, verifying in this way the theoretical aspects of the scaling criteria discussed in the previous sections. It should be noted that these simulations only represent model and prototype responses in an idealized manner, while conditions, and therefore results, from actual physical modeling may be slightly different. The normalized response of the FCV model differs somewhat from that of the prototype. Nevertheless, the most important aspects of the phenomena, both, in terms of the magnitude of displacements and dynamic characteristics of the response, are considered to represent field conditions appropriately. In other words, although the scaling is not exact,

---

[4] For example, considering the static mode of deformation as a single degree of freedom, which is consistent for both prototype and model.

reasonable results can be achieved when using an FCV device.

With regards to material damping, the numerical simulations for the prototype were performed using different damping ratios. By using damping ratios of 2 and 10% it was observed that no noticeable changes occurred in the dynamic responses. This supports the notion that for cases of Statnamic or even pile-driving loading, the damping properties associated with the velocity term in the equation of motion is not significant with respects to the overall response, as most of the energy dissipation is associated with the nonlinear sliding friction along the pile-soil interface.

5.3 Dimensional Analysis

5.3.1 The Buckingham π Theorem

The set of scaling factors introduced in Table 5.2 is sufficient to specify model characteristics and to extrapolate results from model testing to full-scale conditions. In this section we seek a set of normalized parameters representing the pile loading phenomena, which can be used for a comprehensive interpretation of test data, regardless of the size of the physical problem. This is done by means of dimensional analysis. As presented by Baker, Westine & Dodge (1973), the conceptual definition of dimensional analysis can be stated as follows

- *"The Buckingham π theorem which is the basis of most dimensional analyses asserts that any complete physical relationship can be expressed in terms of a set of independent dimensionless products composed of the relevant physical parameters."*

Mathematically, the Buckingham π theorem states that, if a given physical phenomena admits a functional $\mathcal{F}(p_1\, p_2\, p_3 \,.....p_n) = 0$, then it is also possible to define another functional such as $\mathcal{G}(\pi_1\, \pi_2\, \pi_3 \,.....\pi_{n-k}) = 0$. The parameters p_i are the *n* primitive variables representing the phenomena, and π_j are the dimensionless π groups. The number of dimensionless π groups is less than the numbers of primitive variables. If the physical problem admits three fundamental dimensions such as length [L], mass [M] and time [T], then *k* may be equal to three or less.

5.3.2 Particular Set of π Groups for the Pile-Soil System

Let it be assumed that the dynamic load tests on a pile-soil system is completely defined by the set of primitive variables listed in Table 5.3.

Table 5.3 Primitive set of variables for pile-soil system under dynamic loading

	variable		units	dimensions
p_1	σ_{app}	applied stress on pile head	*kPa*	$M\,L^{-1}\,T^{-2}$
p_2	T_L	loading interval	*s*	T
p_3	d	pile diameter	*m*	L
p_4	L_p	pile embedded length	*m*	L
p_5	w	pile axial displacements	*m*	L
p_6	E_p	pile elastic modulus	*kPa*	$M\,L^{-1}\,T^{-2}$
p_7	$\tan\delta$	friction at pile-soil interface	-	dimensionless
p_8	E_s	reference elastic modulus of sand	*kPa*	$M\,L^{-1}\,T^{-2}$
p_9	ν_s	Poisson's ratio of sand	-	dimensionless
p_{10}	γ_s'	effective unit weight of sand	*kN/m³*	$M\,L^{-2}\,T^{-2}$
p_{11}	k	coefficient of lateral earth pressure	-	dimensionless
p_{12}	$\sin\phi_f$	friction coefficient at failure	-	dimensionless
p_{13}	$\sin\phi_{cs}$	friction coefficient at critical state	-	dimensionless
p_{14}	A_s	hardening parameter	-	dimensionless

Any other variable, such as the unit weight and Poisson's ratio of the pile material for instance, is considered to be irrelevant to the problem of pile-soil interaction. It can be shown that the pile-soil system defined in Table 5.3 only admits two normalizing variables, thus reducing the original numbers of parameters from 14 to 12. According to what primitive parameters are taken as normalizing variables, different sets of π groups can be produced. For instance, if E_s and L_p are considered to be the normalizing variables, then the Buckingham π theorem yields the set of π groups listed in Table 5.4.

The inclusion of time in the primitive set of variables lends some generality to the present dimensional analysis, thereby allowing one to treat quasi-static problems as particular cases of dynamic loading conditions. Provided that the set of primitive variables is complete and that they represent the behaviour of the system accurately, then the dimensionless π groups shown in Table 5.4 are strictly independent from each other. These π groups present an objective basis for the evaluation of data obtained from test programs, either in prototype conditions or reduced scale models. For instance, given the dimensionless properties $\{\pi_2, \pi_4, \pi_5$, and π_7 through $\pi_{12}\}$, the normalized loading conditions $\{\pi_1$ and $\pi_6\}$, and the normalized response $\{\pi_3\}$ of the system, a parametric characterization of the pile-soil system may be carried out.

5.3.3 Experimental Determination of Functional Relationships

Considering a testing program on model piles, data from test results can be systematically evaluated on the basis of a parametric approach, from which functional relations may be established. This section presents two examples of how the results of a hypothetical

Table 5.4 π Groups for pile-soil system under dynamic loading

π_1	$\left(\frac{\sigma_{app}}{E_s}\right)$	normalized applied stress
π_2	$\left(\frac{d}{L_p}\right)$	pile aspect ratio
π_3	$\left(\frac{w}{L_p}\right)$	normalized displacements
π_4	$\left(\frac{E_p}{E_s}\right)$	modular ratio
π_5	$\left(\frac{\gamma_s' L_p}{E_s}\right)$	normalized unit weight of sand
π_6	$\left(\frac{T_L}{T_p}\right)$	time ratio, with $T_p = L_p \sqrt{\frac{\rho_p}{E_p}}$, approximation to the fundamental frequency of the pile
π_7	$(\tan\delta)$	friction at pile-soil interface
π_8	(ν_s)	Poisson's ratio of sand
π_9	(k)	coefficient of lateral earth pressure
π_{10}	$(\sin\phi_f)$	friction coefficient at failure
π_{11}	$(\sin\phi_{cs})$	friction coefficient at critical state
π_{12}	(A_s)	hardening parameter

testing program, performed via finite elements simulations, can be used to construct functional relationships. We are going to consider the basic problem of the pile-soil prototype of Section 5.2.5, for cases of different pile lengths and different values of the lateral earth pressure coefficient *k*.

Figure 5.5 shows the sequence of a possible condensation of π groups using data from a series of tests on model piles where the only parameter that changes is the pile length. Initially, the responses of piles with different lengths are shown in Figure 5.5(a), in terms of the π_1 versus π_3 curve. In a second stage, the ordinate axis is condensed by properly combining π_3 and π_2 into a new dimensionless group π_{II}, as illustrated in Figure 5.5(b). In a third stage, the previous plot is linearized. From Figure 5.5(c) an approximate functional relation may be identified, namely

$$\left(\frac{w}{L_p}\right) \cong a \left(\frac{d}{L_p}\right)^3 \left(\frac{\sigma_{app}}{E_s}\right)^2 , \tag{5.10}$$

where a is the slope of the π_{II} versus π_1^2 curve shown in Figure 5.5(c). For the case of a series of tests on model piles with different k values, a similar process yields

$$\left(\frac{w}{L_p}\right) \cong b \; (k)^{-0.78} \left(\frac{\sigma_{app}}{E_s}\right)^2 , \tag{5.11}$$

where b is the slope of the π_{III} versus π_1^2 curve, as shown in Figure 5.6(c). Similar to the examples presented above, other relationships may be obtained. The intent of the exercise presented here is to show the benefits of applying dimensional analysis to the evaluation of a comprehensive set of experimental data. It is reasonable to state that even though a perfect condensation may not be possible, significant improvement can be achieved by defining approximate correlations.

5.4 Physical Modeling of Pile Tests in the FCV Device

The development of the FCV device and the corresponding model testing technique is justified in this section by enumerating the advantages of testing model piles in a FCV device as opposed to model testing in centrifuges or 1*g* devices.

5.4.1 Testing of Model Piles in 1*g* Devices

The inability of the 1*g* devices to properly scale soil stresses in model piles results in severe distortions in similarity conditions, as discussed in previous sections. For the case of 1*g* model foundations embedded in sand, some procedures have been developed in order to account for distortions in model responses; see e.g., Hettler & Gudehus (1985), and Franke & Muth (1985). These procedures, however, are mostly developed for simple problems under service state or quasi-elastic soil responses, and cannot be applied to the problem of load test on 1*g* model piles. Foray et al. (1998), tried to minimize distortions associated with the lack of gravity scaling by testing model piles in sand within a cylindrical confinement vessel, in which lateral and vertical stresses could be controlled. In spite of that, the control in the lateral and vertical stress levels did not produce realistic stress gradients, especially the linear increase of stresses with depth. For this reason, similarity conditions are fulfilled only segmentwise. Although the overall pile-soil response might not be properly reproduced in their confining device, it presents an improvement when compared with other 1*g* devices. The main advantage of the FCV device when compared with other 1*g* testing environments for piles is the capability to provide more realistic lateral pressures and distribution on the pile's shaft.

5.4.2 Testing of Model Piles in Centrifuge Devices

The most direct advantages that the FCV testing technique offers over the use of centrifuge devices are its comparatively low running cost, and the simplicity associated with its operation. FCV models also present technical advantages with respect to the volume and size of models. In the case of the centrifuge, the size and weight of the payload is limited to the capacity of the machinery. Typical geometric ratios for model piles in centrifuges are between 1/60 and 1/100, compared with the 1/15 to 1/30 of FCV models [5]; see e.g., Schofield (1980), Craig & Sabagh (1994), Scott (1981), and Prakash et al. (1990). Some of the consequences of size limitations in centrifuge models are:

i. The ratios of model pile diameter to the sand effective grain size are small numbers, and as indicated in Section 5.2.4, grain size effects can introduce distortions in the conditions for similarity.

ii. Model imperfections and distortions are magnified by a factor of 60 or 100 when results are extrapolated to prototype conditions. In comparison, similar imperfections in FCV models are magnified by a factor of 15 or 30.

iii. The ratio between the length of a model pile and the length of the centrifuge rotating arm is a sizable number, indicating that centripetal acceleration varies linearly along the model pile. Thus acceleration is controlled only in an average sense.

iv. Small size models are affected by close or near boundary effects. Reports on the chamber size effects indicate that close artificial boundaries are responsible for

---

[5] These geometric ratios are based on an optimized FCV device with a control volume which is about 1.0 to 2.0*m* long.

substantial distortions in the stress distributions on the soil (Houlsby & Hitchman 1988, Schnaid & Houlsby 1991, and Al-Douri et al. 1993).

v. Difficulties in the instrumentation of pile-soil model increase as the size of the model becomes smaller.

Owing to all these considerations related to model size, it is suggested that larger FCV models are technically better suited than centrifuge models for the testing of model piles. Notwithstanding, centrifuge machines still offer the possibility of performing lateral load tests while FCV models may not. Another limitation of FCV models is that undrained problems may not be reasonably replicated, as fluid pressure cannot be controlled, as is the case of centrifuge devices.

5.5 Closure

The current scaling criteria for the testing of model piles has been analyzed. It is concluded that scale ratios for density and stresses equal to one are essential to fulfill constitutive similarity. It is also recognized that the scaling of gravity is relevant to the problem of model piles insofar as gravity controls stress levels and stress distributions. However, if stress levels and distributions can be controlled by properly constrained boundary conditions, then is not necessary to scale gravity. By means of numerical analysis, it is shown that the material damping does not affect the pile response to loading, in either model or prototype. Therefore the scaling of material damping is not required. Advantages and limitations of using the FCV device in the testing of model piles have been addressed.

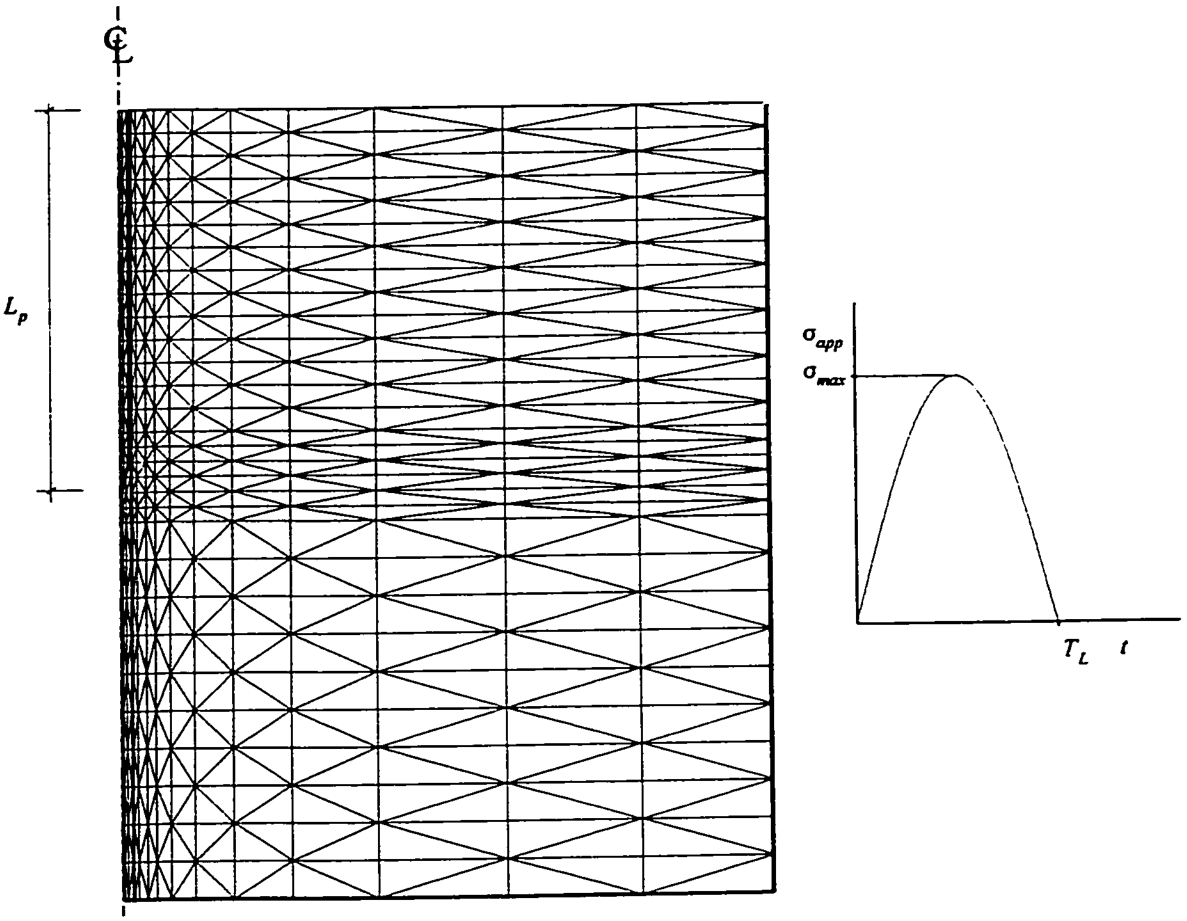

Sand		
radius	R	$= 13.4\ m$
height	H	$= 17.8\ m$
elastic modulus	E_s	$= 240\ MPa$
Poisson's ratio	ν	$= 0.35$
friction coef. at failure	$\sin\phi_f$	$= 0.58$
friction coef. at crit. state	$\sin\phi_c$	$= 0.50$
hardening parameter	A	$= 0.00080$

Pile		
diameter	d	$= 0.34\ m$
embedded length	L_p	$= 9.00\ m$
elastic modulus	E_p	$= 1500\ MPa$
Poisson's ratio	ν	$= 0.30$
interface friction	$\tan\delta$	$= 0.55$

Loading		
maximum applied stress	σ_{max}	$= 12\ MPa$
loading interval	T_L	$= 100\ ms$

Finite Element Mesh	
No. of nodes	1860
No. of triangular elements	840
No. of interface elements	30
No. of dof	3479

Figure 5.1. Discretization of the pile-soil problem: Prototype and centrifuge model

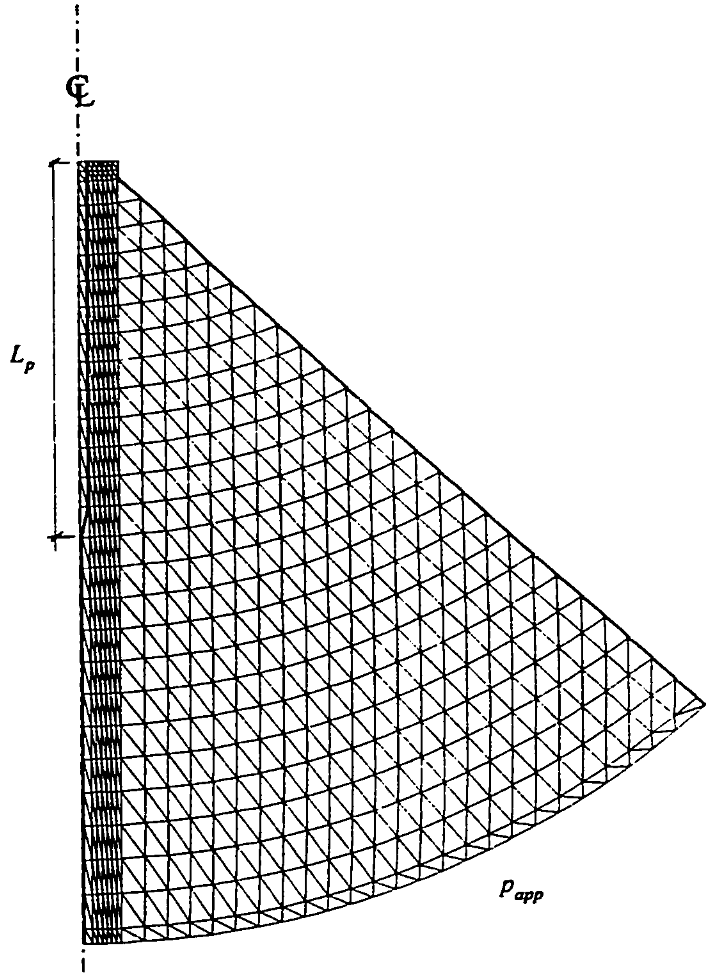

Applied pressure

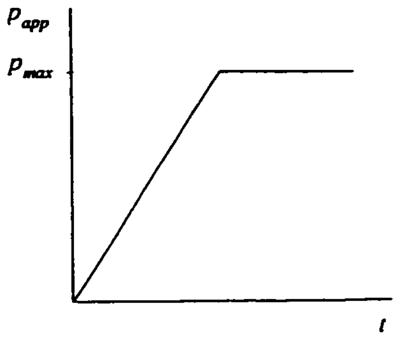

Initial loading stage

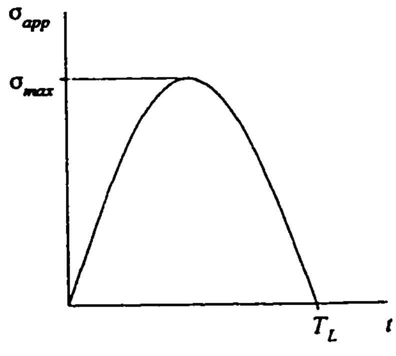

Secondary loading stage

FCV Sand Specimen		
height	H	= 0.890 *m*
elastic modulus	E_s	= 240 *MPa*
Poisson's ratio	ν	= 0.35
friction coef. at failure	$\sin\phi_f$	= 0.58
friction coef. at crit. state	$\sin\phi_c$	= 0.50
hardening parameter	A	= 0.00080

Pile		
diameter	d	= 0.017 *m*
embedded length	L_p	= 0.450 *m*
elastic modulus	E_p	= 1500 *MPa*
Poisson's ratio	ν	= 0.30
interface friction	$\tan\delta$	= 0.55

Loading		
initial loading stage: membrane load		
applied pressure	p_{max}	= 145 *kPa*
secondary loading stage: pile load test		
maximum applied stress	σ_{max}	= 12 *MPa*
loading interval	T_L	= 5 *ms*

Finite Element Mesh	
No. of nodes	2401
No. of triangular elements	1608
No. of interface elements	56
No. of dof	4517

Figure 5.2. Discretization of the pile-soil problem: FCV model

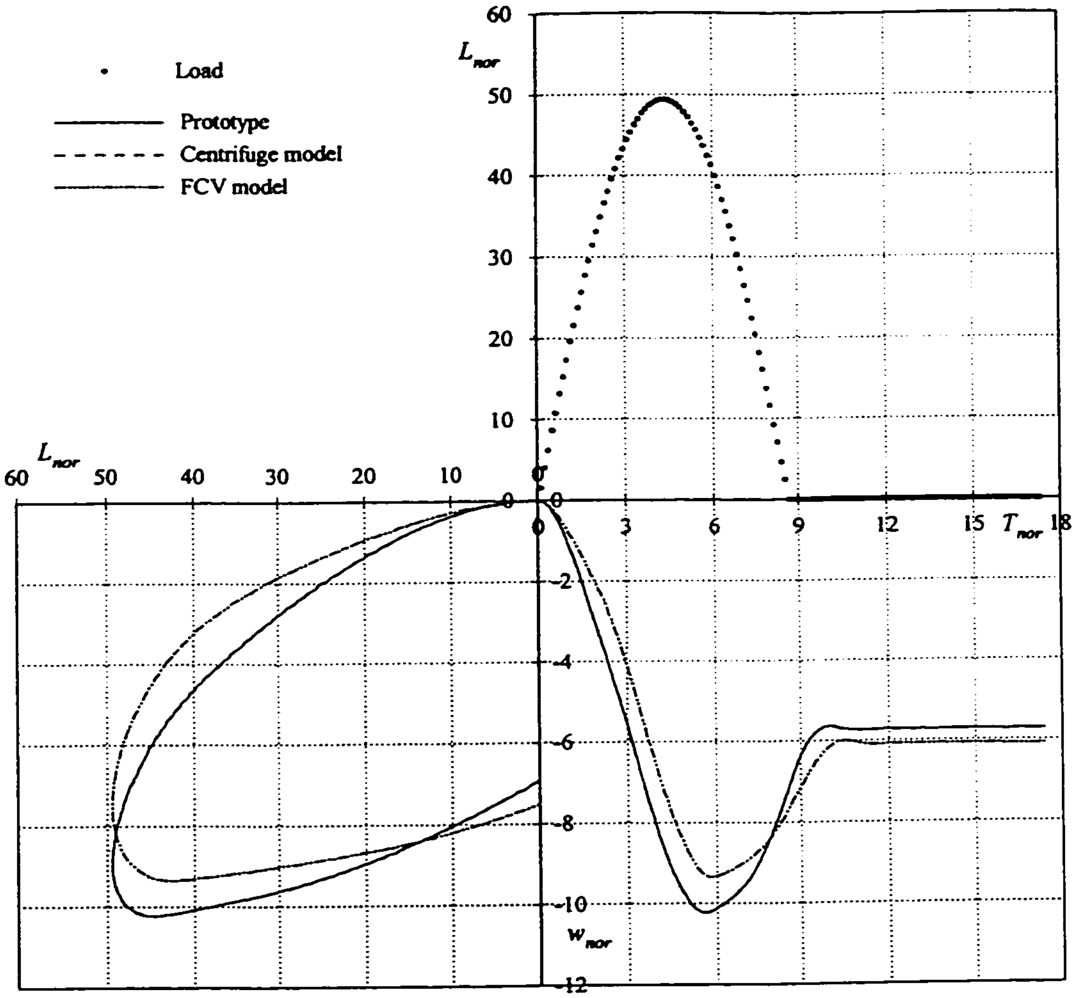

Normalized Loading $L_{nor} = \frac{\sigma_{app}}{E_s} \times 10^{-3}$

Normalized Time $T_{nor} = \frac{t}{T_p}$

Normalized Displacements $w_{nor} = \frac{w}{L_p} \times 10^{-3}$

Comparison of normalized responses from prototype with those of the centrifuge and FCV models. The pile-soil interaction problem was simulated with the Pressure-Dependent constitutive law.

Figure 5.3. Normalized displacements at the pile head

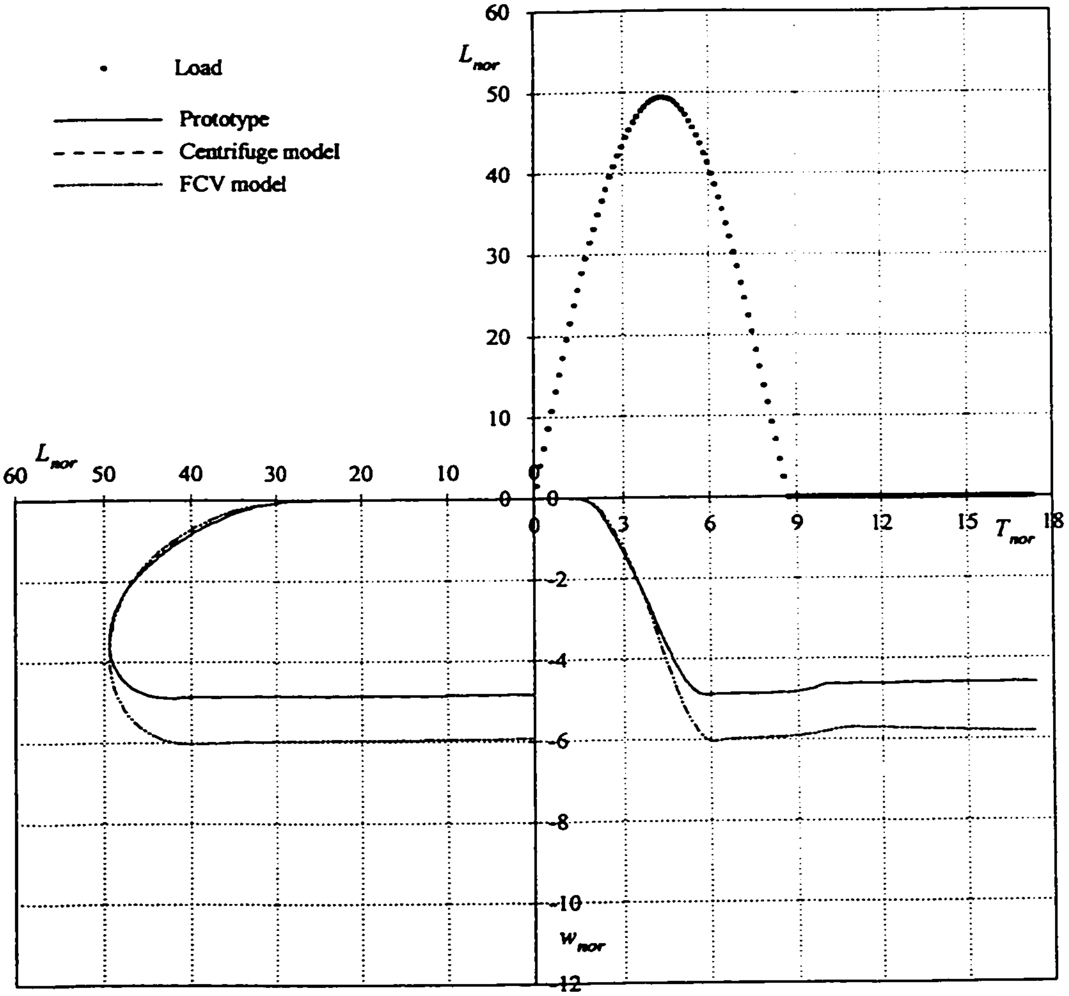

Normalized Loading $L_{nor} = \frac{\sigma_{app}}{E_s} \times 10^{-3}$

Normalized Time $T_{nor} = \frac{t}{T_p}$

Normalized Displacements $w_{nor} = \frac{w}{L_p} \times 10^{-3}$

Comparison of normalized responses from prototype with those of the centrifuge and FCV models. The pile-soil interaction problem was simulated with the Pressure-Dependent constitutive law.

Figure 5.4. Normalized displacements at the pile toe

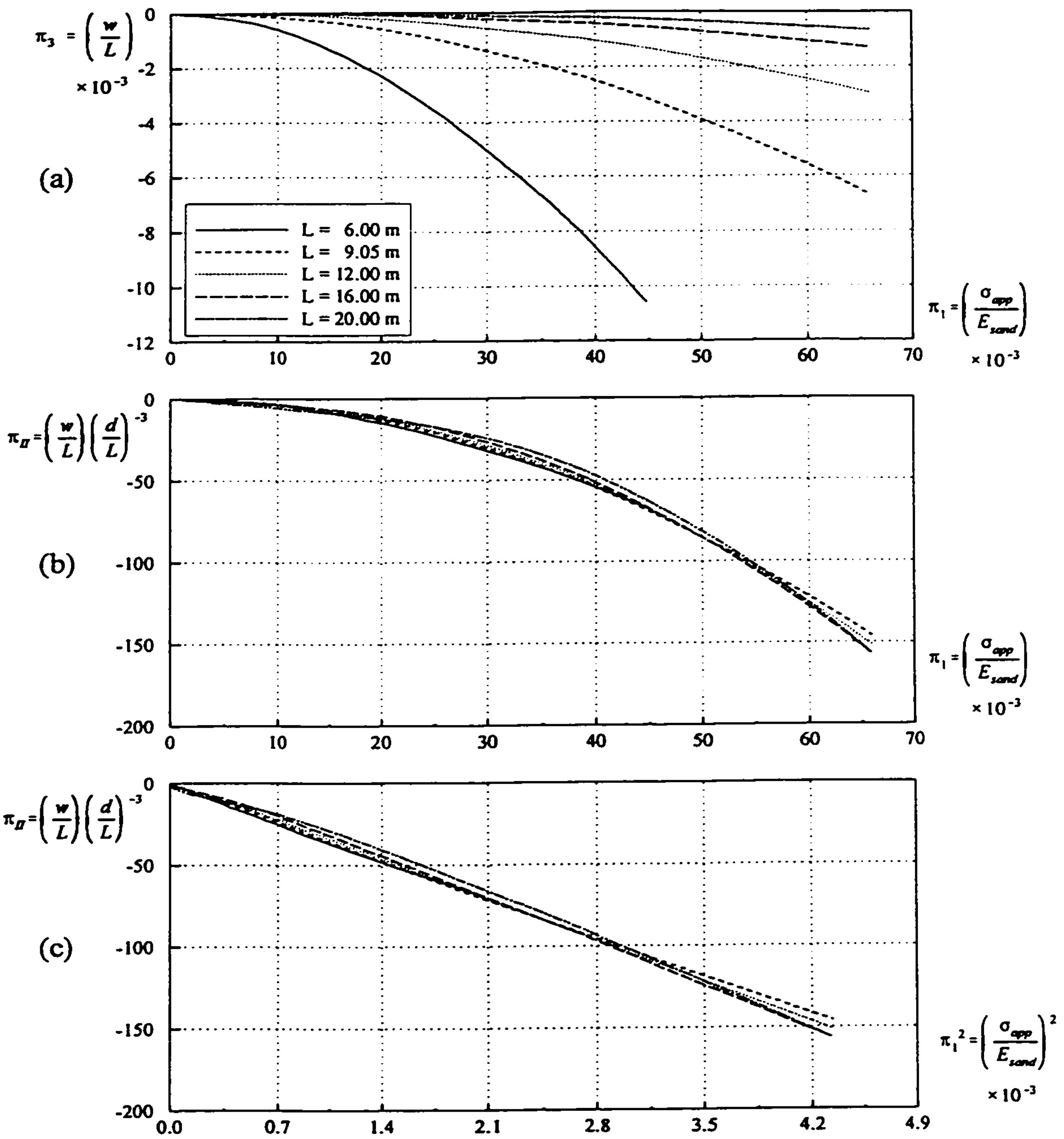

Possible condensation of π groups was attempted by using numerical predictions. (a) Normalized displacements versus normalized load, i.e., π_3 vs. π_1 for different values of normalized length π_2. (b) Condensation of π_2 and π_3 into a new dimensionless group π_Π. (c) Linearization of the π_Π vs. π_1 curve.

Figure 5.5. Condensation of π groups: Pile length L

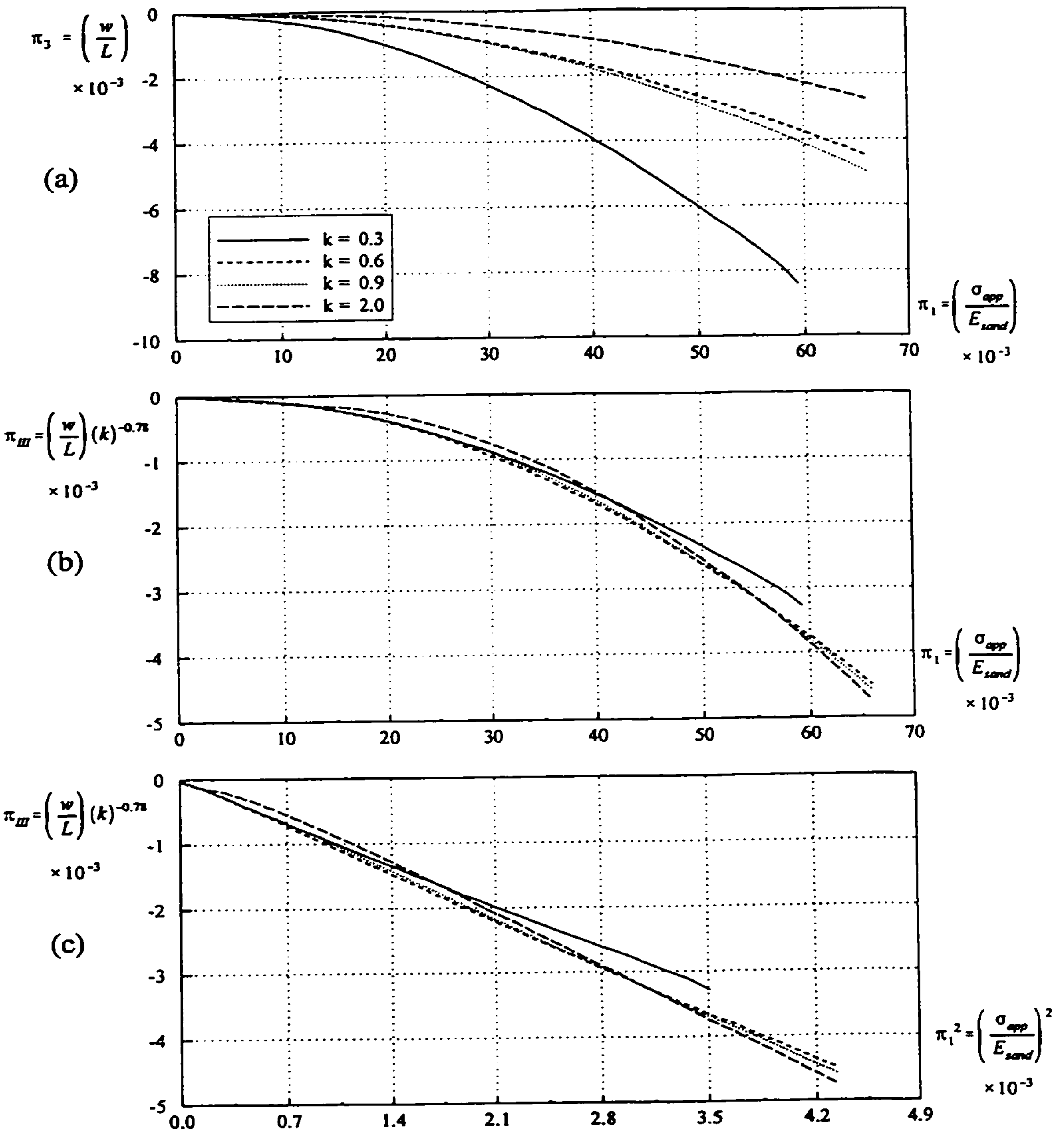

Possible condensation of π groups was attempted by using numerical predictions. (a) Normalized displacements versus normalized load, i.e., π_3 vs. π_1 for different values of the stress ratio k. (b) Condensation of π_3 and π_9 into a new dimensionless group π_{III}. (c) Linearization of the π_{III} vs. π_1 curve.

Figure 5.6. Condensation of π groups: Stress ratio k

Chapter 6

CONCLUSIONS

An experimental and analytical investigation of the Frustum Confining Vessel was completed in order to gain an understanding of the behaviour of sand specimens within the FCV device. Based on the results of this investigation, the following sections present conclusions and recommendations, which are summarized in accordance with the thesis objectives.

6.1 FCV Testing Procedures

Several procedures for compaction were considered for the preparation of specimens, and from these results it is concluded that high-density specimens are best suited for ensuring test reproducibility.

With respect to the loading procedures, the ramp load applied in one or more cycles was found to provide repeatable conditions. The application of the load to the specimens must be slow enough to avoid time-rate effects on the responses. A period of time of 400 *s* or longer to reach the peak loading was considered to be appropriate.

As a result of problems associated with tilting of the piston and stress concentrations in the lower portion of the specimens, where the inclined wall meets the lower cylinder, the uniform displacement configuration (piston loading) was considered to be not suitable for FCV testing. The uniform pressure configuration (membrane loading), on the other hand, minimized the problem of stress concentrations in the same portion of the specimens. The membrane loading did not require expensive loading equipment for the application of confinement to FCV specimens. Membrane pulling effects were considered negligible for the small displacements observed during the experiments, 3 *mm* or less. Since small displacements are ensured by testing high-density specimens, membrane pulling effects are not a concern.

The effects of non-uniform density distributions were addressed from a numerical prospective. It was observed that random variations of density at initial conditions affected stresses in a localized manner, while displacements were unaffected. This implies that reproducibility of test responses based on measured surface displacements may not guarantee reproducibility of stresses. Average values of scattering were observed to be less than 5 % for both the vertical and radial stresses, and about 11 % for the shear stresses. This study, however, was based on simplifying assumptions with respect to non-uniformity. Thus, conclusions drawn from the exercise only provided an indication of possible effects of non-uniform densities on the reproducibility of FCV tests.

Normal stresses within FCV specimens were estimated by using an intrusive measuring technique. Although some scatter was observed on the measured stresses, it is recognized that the Force Sensing Resistors® and the capacitive stress sensors are valuable for acquiring test data related to magnitude and distribution of normal stresses. The intrusive stress measuring technique requires further development in relation to calibration procedures for FCV conditions. It is recommended that in future FCV testing, an array of stress sensors be deployed around the control volume. Monitoring of vertical and radial stresses at the surface of the control volume would help determine the appropriate pressure levels at the membrane to ensure that target conditions within the control volume are realized. It would also provide valuable information with respect to the stress changes occurring during the testing of model piles.

6.2 Optimized Vessel

A selection criterion, based on idealized field conditions that are to be scaled within the FCV, was provided to evaluate different vessel shapes. The evaluation of trial designs for the vessel was accomplished by means of numerical simulations. It was established that a minimum amount of friction at the wall surface is necessary to ensure appropriate distribution of stresses at the control volume.

Three basic shapes were evaluated with respect to the selection criterion, and it was concluded that a frustum vessel with the shape of grid #3 provided the best results. Two important characteristics of the vessel's shape were the spherical bottom and a narrow opening at the top.

6.3 Physical Modeling

The concept of dimensional analysis was reviewed and a set of primitive variables was defined for the pile-soil interaction problem. Subsequently, a set of dimensionless π groups was derived. These dimensionless π groups can be used as the basis for a comprehensive study of the pile-soil problem by means of physical modeling using the FCV device. The possibility of studying empirical relationships between dimensionless groups was demonstrated with the help of numerical simulations.

Scaling relations were examined and it was shown that is not necessary to scale gravity. As long as the stress scaling ratio is enforced to be equal to one, the physical modeling of reduced-scaled piles satisfies similarity requirements. The ability of an optimized FCV device to enforce the stress scaling ratio is considered to be fundamental to ensure undistorted conditions for the physical modeling of reduced-scale piles. Furthermore, it is concluded that the FCV device is a suitable alternative to centrifuge testing of model piles.

In comparison to centrifuge devices, the FCV models are inexpensive and much easier to set up. The testing of larger models is also possible. The use of larger models, as discussed in Chapter 5, Section 5.4.2, presents a number of important advantages over centrifuge models. On the other hand, pore water pressures can not be scaled within FCV specimens, as is the case when using centrifuge models, thereby limiting the FCV capabilities to the modeling of drained problems.

6.4 Mathematical Modeling

Three constitutive models were implemented for the present study. The numerical analysis of stress conditions within FCV sand specimens confirmed the assumptions that increasing levels of confining and rotation of principal stress planes are dominant aspects of the behaviour of sand specimens within an FCV.

The assumption that stress-state induced anisotropy affects the specimen behaviour was taken care of by implementing stress-dependent anisotropic elasticity. The anisotropic moduli were evaluated using the notion of cross-confinement, which depends on the magnitude of transverse principal stresses. The anisotropic model produced reasonable predictions. However, at this stage of model development, and due to the lack of experimental data to properly validate the model, one cannot make a definitive statement whether or not stress-induced anisotropy is a significant aspect of the responses. This aspect was beyond the scope of the reported study.

Experimental studies should be conducted to evaluate the effects of stress-induced anisotropy in sands, particularly within the range of quasi-elastic deformations. It is suggested that a suitable testing setup, similar to that of the hollow cylindrical sand samples presented by Symes et al. (1988), might help in the investigation of the effects of principal stress rotations on anisotropic elastic moduli. When interpreting the data from such a testing program, it is strongly recommended that experimental results be complemented with finite element simulations.

6.5 Recommendations for Future Studies

Based on the experience gained in this investigation the author recommends the manufacturing of a new FCV device, as suggested previously. The next step would be the development of a comprehensive testing programme to conduct load tests on model piles. It is also suggested that a study should be conducted to establish an appropriate technique to instrument the model piles.

Once testing results become available, it is suggested that the experimental data be extrapolated to the full-scale problem using the guidelines for similarity conditions described in Section 5.2.3. The experimental results should also be analyzed in terms of the π groups as suggested in the dimensional analysis carried out in Section 5.3.2. The use of π groups will aid in developing functional relations using the measured variables characterizing the pile-soil interaction.

APPENDIX A:

STRESS MEASUREMENTS IN SAND

A.1 Overview

The different procedures for measuring stresses may be placed in one of two categories; that is active and passive measurements (Dunnicliff 1982, and Hanna 1985). While active measurements produce large soil displacements in order to probe stresses, passive stress measurements do not displace the soil during the measurements. Most of the field methods to measure in-situ stresses are considered to be of the active type. For example, penetration devices such as those used in SPT, CPT, Vane Shear, and Flat Dilatometer testing, fall within this category. In this category the stresses are estimated indirectly by means of empirical correlations which are specific to each testing technique.

The state of stresses at any point is fully defined by three orthogonal normal stresses and three shearing stresses, in this regard, stress measuring devices can not capture the full state of stresses. Some devices are capable of probing stresses in the radial or normal direction with respect to the probing axis, while some other devices are sensitive to a combination of confining stresses.

In situations where a stress measuring device can be placed in position before the soil is backfilled, the measuring technique is considered to be of the passive form. Such cases include stress measurements on retaining walls; braced cuts; embankments; silos; or similar related research applications.

This Appendix presents the description of stress measurements in FCV specimens using three types of passive stress transducers, namely diaphragm-based stress transducers, capacitive transducers, and resistive transducers. Most of the stress measurements in geotechnical applications are done by using earth pressure cells. The transduction of stresses from the cell to a signal-processor may operate according to different principles, including for example, pressure transducers, strain gauges, vibrating wire, inductive and piezoelectric transducers. One aspect that all these devices have in common is that they interact with the soil by means of a flexible member or diaphragm (Hanna, 1985). These diaphragms introduce distortions in the stresses intended to be measured, thereby resulting in under- or over-registration of the free-field stresses. The diaphragm's deflection together with a stiff housing usually causes a redistribution of stresses on the soil surrounding the pressure cell. The resulting stress redistribution is due to soil arching for the case of under-registration, or inverse soil arching in the case of over-registration.

Weller and Kulhawy (1982) introduced the concept of the registration ratio

$$R = \frac{\sigma_c}{\sigma_s} \ , \qquad \text{(A.1)}$$

where σ_c is the normal stress measured by the pressure cell during calibration under fluid pressure , and σ_s is the free-field normal stress present in the soil. In the case of over-registration R is greater than one, and for under-registration R is less than one. This ratio depends primarily on the cell's aspect ratio and the overall cell stiffness (Hanna 1985). In general, diaphragm stress cells with very small thickness-to-diameter aspect ratio tend to minimize the effects of soil disturbance.

For those earth pressure cells for which the registration ratio is approximately constant and repeatable, a suitable correction factor might be applied to the output readings in order to correlate measured stresses with free-field stresses.

Ullidtz et al. (1996) reported the results of loading experiments in dry granular material using two different diaphragm stress cells in which stress measurements could be reasonably well estimated. In their report, the free-field stresses were evaluated by correcting the outputs from the stress cells using an algebraic expression that accounted for the applied normal stress as well as for lateral confinement acting around the stress cell. Such an algebraic expression was said to be derived from calibration procedures under fluid and soil pressure loading. In these experiments the stress cells were embedded in a shallow layer of dry sand and the normal stress distributions acting over the surface of the cell were approximately uniform, for instance, very low normal stress gradients. Under these nice testing conditions, the use of diaphragm stress cells to measure normal stresses provided satisfactory results. However, in most geotechnical application, stress conditions in the soil are far from being as nice as in case of the experiment reported above. In most cases measurements with diaphragm pressure cells are frequently erratic and difficult to interpret (Filz & Duncan 1993, and Filz & Brandon 1994).

In terms of transducer output, most of these instruments provide highly accurate, linear, and repeatable readings. The fundamental limitation of these stress cells is the uncertainty associated to the estimation of distorted stresses at the soil-diaphragm interface. Owing to this limitation, earth pressure cells are not intended to measure accurate values of in-situ stresses but rather to acquire an approximate estimation of stress changes. A common application of earth pressure cells is to monitor stress changes due to loading in large masses of soil (Dunnicliff 1982).

With regards to this thesis, the stress characterization of sand specimens tested in the Frustum Confining Vessel required the deployment of stress transducers inside the specimen or at its interface with the vessel. The three types of stress transducers improvised for this purpose were: (a) two prototypes of diaphragm stress cells; (b) a capacitive type of stress cell; and (c) a resistive type of stress cell.

A.2 Diaphragm Stress Transducers

The first prototype of diaphragm stress cell consisted of a single strain gauge attached to a brass diaphragm. The schematic for this pill-box configuration is shown in Figure A.1(a). The pressure cell was 12.7 *mm* in diameter and 4.0 *mm* thick, and its calibration was conducted by pressure loading. For instance, the cell was fixed to the pedestal and sealed with a rubber membrane. The cell response to air or water pressure exhibited linear and repeatable output signals. This output signal, measured in micro strain units, was directly correlated to the pressure of the fluid by a constant calibration factor. The registration ratio was then estimated by measuring the readings of the stress sensor when it is placed inside a triaxial sample and tested under isotropic or hydrostatic loading. The comparisons of cell readings under isotropic loading with the calibration curve are shown in Figure A.2. The comparison reveals a very low registration ratio. Such a severe under-registration problem may have been caused in part by the high aspect ratio of the cell, and in part by the fact that the stress cell was very stiff at the rim and soft over the diaphragm sensitive area. Similar results were observed in the case of the cell placed in a triaxial sample and tested under axial compression.

Placing the stress cell within sand in a direct shear box provided clear confirmation that soil arching was occurring at the sand-diaphragm interface. Under a constant normal stress of 38 *kPa* the initial stress cell output read 17 *microstrain units*, which corresponded to a normal stress of 20 *kPa* on the calibration curve, indicating under-registration. In Figure A.2(b) the *y* axis on the left represents the applied shear load, while the scale on the right indicates the stress cell output. Even though the normal load was kept constant throughout the test, the stress cell readings increased approximately proportionally to the applied shear force T. The increasing output was attributed to the fact that the soil arch, which formed above the sand-diaphragm interface, was being dislodged by the straining at the shear plane. For a horizontal displacement of 1.35 *mm* the stress cell reading increased to 28 *micro strain units*. Which corresponded to the applied pressure of 37 *kPa*. The under-registration effect was not constant, as it was observed that the sensors output depended on levels of confinement and on the density of the sample. These results indicated that the pill-box configuration cell, with the given stiffness and aspect ratio, was not capable of reading normal stresses in a reliable manner.

An improved type of diaphragm stress cell was assembled by mounting a diaphragm between two stiff aluminum shields, as shown in Figure A.1(b). The advantage of this design, with respect to the previously described pill-box cell, was its lower aspect ratio and its uniform stiffness across the measuring surface. A preliminary set of calibration tests was conducted using a high capacity triaxial cell under fluid pressure and isotropic loading. The test results, not presented here, indicated that this stress cell over-registered stresses. The over-registration was believed to be a consequence of the stiff aluminum shields and their thicknesses. Due to time constraints, no further work was conducted with this type of cells. However, it is believed that such a configuration might be properly calibrated in order to produce a registration ratio of one.

A.3 Capacitive Stress Transducers

The problem associated with soil arching can be minimized if a thin cell with uniform stiffness and low aspect ratio is used instead of the pill-box diaphragm configuration. Such a cell was constructed in the Geotechnical Laboratory at McMaster University, using a multilayer capacitive sensor. Several prototypes were tested with different number of layers and with different dielectric materials. All cells were 30.0 *mm* in diameter, 1.3 *mm* thick, and consisted of 8 layers of brass foil separated by insulating tape. The cells were protected from background electromagnetic noise by a grounded shield of aluminum foil. The stress cell was connected to a signal conditioning unit, which converted changes in capacitance into output voltage in mV. Since this stress cell introduced negligible volume change, no disturbance was introduced to the soil mass surrounding the sensor.

The relation between applied stresses and output voltage for the capacitance transducer was found to be nonlinear. In addition the output voltage was subjected to slow drifting. The effects of drifting in the output signal could be compensated for by estimating the rate of drifting before and after a load was applied, and then subtracting from the acquired signal an average value of drift for the particular length of the loading time. With respect to the nonlinear output response of the transducer, the calculation of stresses was estimated by using the nonlinear calibration curves.

The calibration curve for one of theses sensors is shown in Figure A.3(a), which was obtained with the stress cell placed within a sand specimen in a triaxial setup and loaded isotropically up to cell pressures of 3100 *kPa*. The same calibration curve is shown in Figure A.3(b) in semilogarithmic scale. By using a non-linear regression analysis a suitable calibration expression was established, where

$$SC = A + B \ln(\sigma_N) \quad , \tag{A.2}$$

with $A = -81.82 \pm 1.90$ and $B = 20.707 \pm 0.638$. This expression relate the values of applied stress σ_N in *kPa* to the stress cell output *SC* in *mV*. Solving for σ_N

$$\sigma_N = A^* e^{B^* SC} \quad , \tag{A.3}$$

with $A^* = 52.0$ and $B^* = 0.0483$. These values of A, B, A^*, and B^* are characteristics of a particular prototype. It was concluded that it was feasible to measure total stresses in sand with a mean deviation less than 10% when using a capacitive stress cell. Although this is not a high level of accuracy, it was considered to be sufficiently good for the purposes at hand.

A.4 Force Sensing Resistors®

Stress distributions within FCV specimens were also estimated with the help of Force

Sensing Resistors® (FSR). The FSR's are made with thin polymer films imprinted with semi-conductor that changes its resistivity with changes in the applied normal stress. The use of these FSRs in stress measurements also eliminates the problem of soil arching associated with diaphragm-based transducers. As reported by Paikowsky & Hajduk (1997), some of the limitations associated with FSRs are related to the fact that stress measurements may be distorted if the sensing pads are subjected to twisting or bending. The output signal is also nonlinear, and for long term measurements the possibility of drifting in the output signal may become important. Since the disturbances introduced in the free-field stresses by the presence of the FSR transducers are greatly minimized, this stress measurement technique represents a significant improvement in the area of stress measurements within granular soil masses.

Eight FSR transducers were tested and calibrated for the measurement of stresses in FCV specimens. Four sensors had circular shape with 12.7 *mm* in diameter, while the other four were square pads 38.1 *mm* aside. Both types of pads were 0.46 *mm* thick. The FSR's were calibrated first using fluid pressure up 650 *kPa*, and then by isotropic loading up to 6000 *kPa*. The latter set of calibrations was conducted with the sensors embedded within triaxial sand samples. From these two sets of calibrations it was possible to calculate the registration ratio for each sensor.

Figure A.4(a) shows the nonlinear responses of a circular FRS sensor under fluid pressure and under isotropic loading. Similarly the response of a square FSR sensor is shown in Figure A.4(b). These figures were used to define calibration curves for each sensor, for example, the average resistivity between the curves would define the stress measurement. An estimation of the variation at each load level was also obtained for each sensor, and it may be observed that the range of variation or uncertainty depends on the stress level.

Owing to the nonlinear responses of the FSR sensors, the resolution was shown to decrease with increasing stress levels. This load-dependent resolution was evaluated by comparing FSR output responses with the calibration response from one of the capacitive stress sensors. Figures A.5(a) and A.5(b) show the comparisons between capacitive and resistive transducers in normal and semilogarithmic scales, respectively. Output readings corresponding to the capacitive sensor, in *mV*, are located at the left side scale, while output reading for the FSR sensors, in *ohms*, are on the right. The FSR sensor responses shows that output signals are saturated for normal stresses higher than about 1000 *kPa*, while the capacitive transducer is shown to still respond to increasing stresses. In summary, the following conclusions may be drawn:

- The insertion of resistive or capacitive stress sensors in dry sand specimens does not introduce significant distortions to the normal stresses to be measured.
- Calibration curves from tests using hydraulic pressure can be employed for interpretation of sensor data by postprocessing the output signal.
- FSR sensors are more appropriate than the capacitive transducer for measuring normal stresses below 800 kPa. For stress levels higher than 800 *kPa*, the capacitive sensors offer better resolution than FSR sensors.
- Both types of stress transducers should only be used in areas where shear distortions are minimal.
- Both types of sensors can be permanently fixed to a hard surface or interface, in order to measure normal stresses. For such cases pad distortion are eliminated.

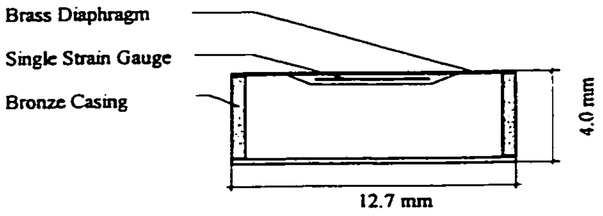

(a) Pill box configuration.

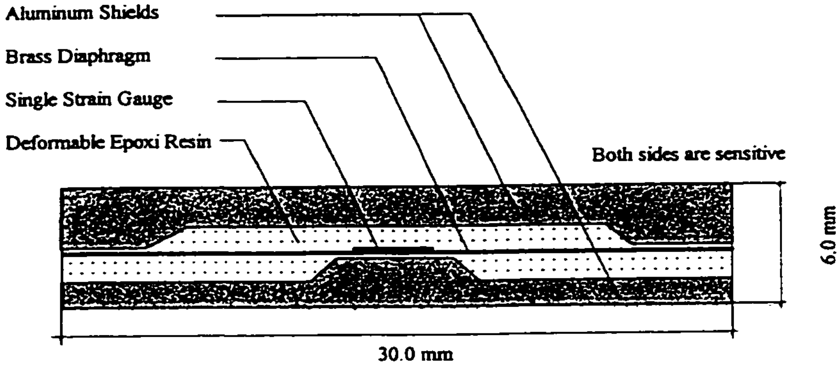

(b) Shielded box configuration.

Figure A.1. Schematics of diaphragm stress transducers

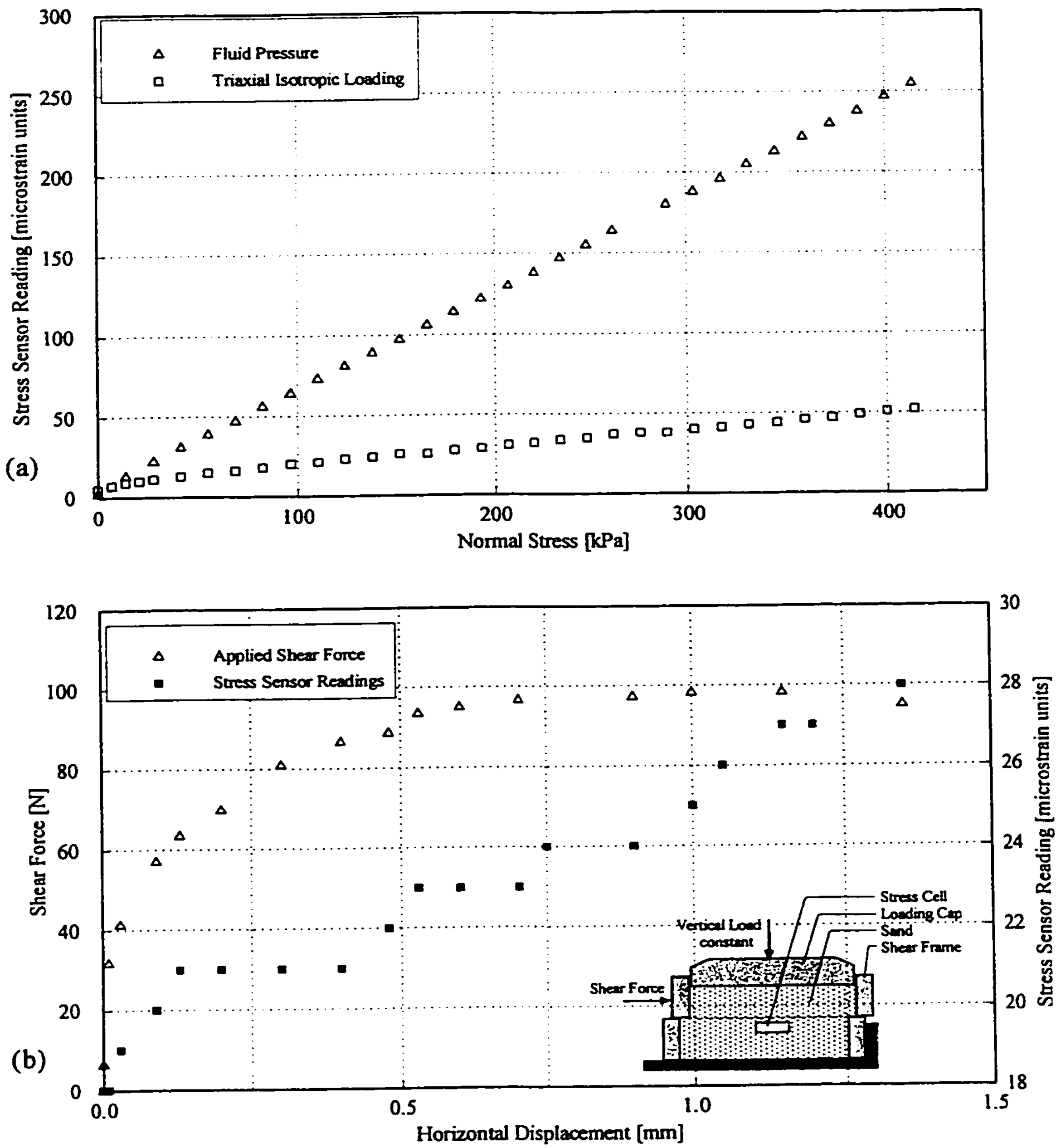

(a) Transducer's outputs under both, fluid pressure and triaxial isotropic loading. (b) Increased output response of the transducer as the soil arch is sheared inside a sample tested in a shear box.

Figure A.2. Performance of the diaphragm stress transducer: Pill box

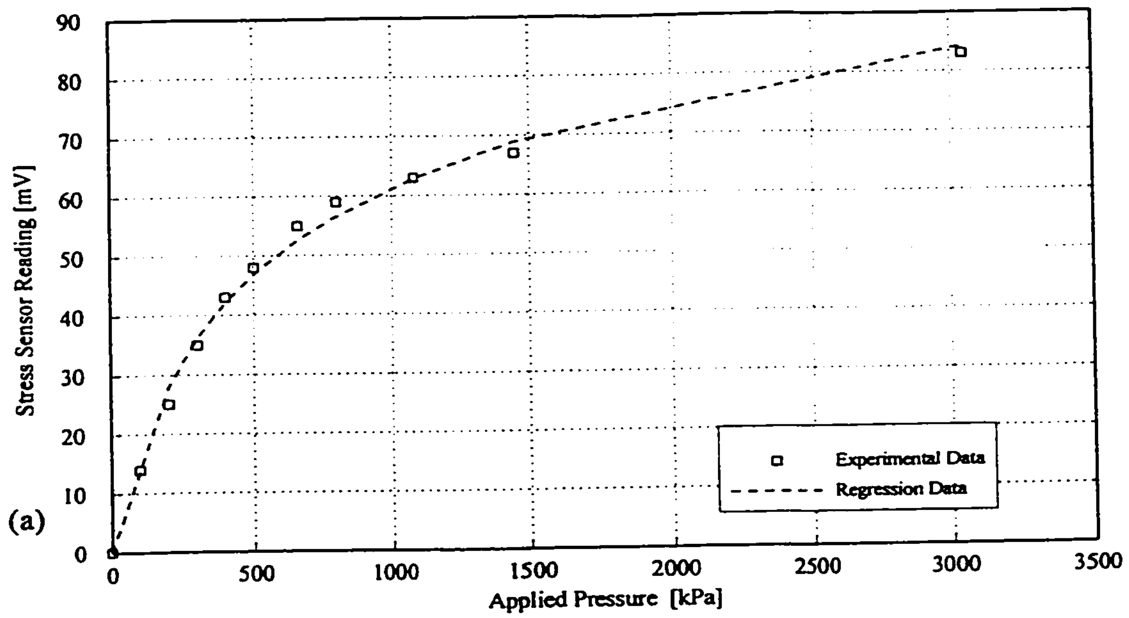

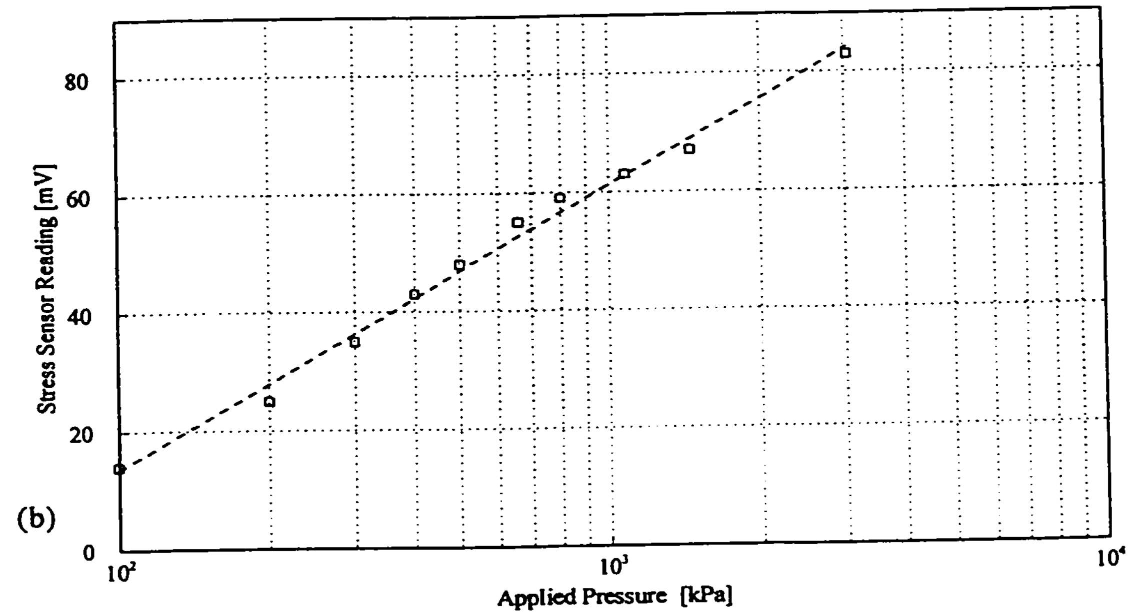

Output response of the capacitive stress transducer under fluid pressure. The experimental data points and the adopted regression curve are shown in terms of output in *mV* versus applied pressure in (a) normal, and (b) semilogarithmic scales, respectively.

Figure A.3. Performance of the capacitive stress transducer

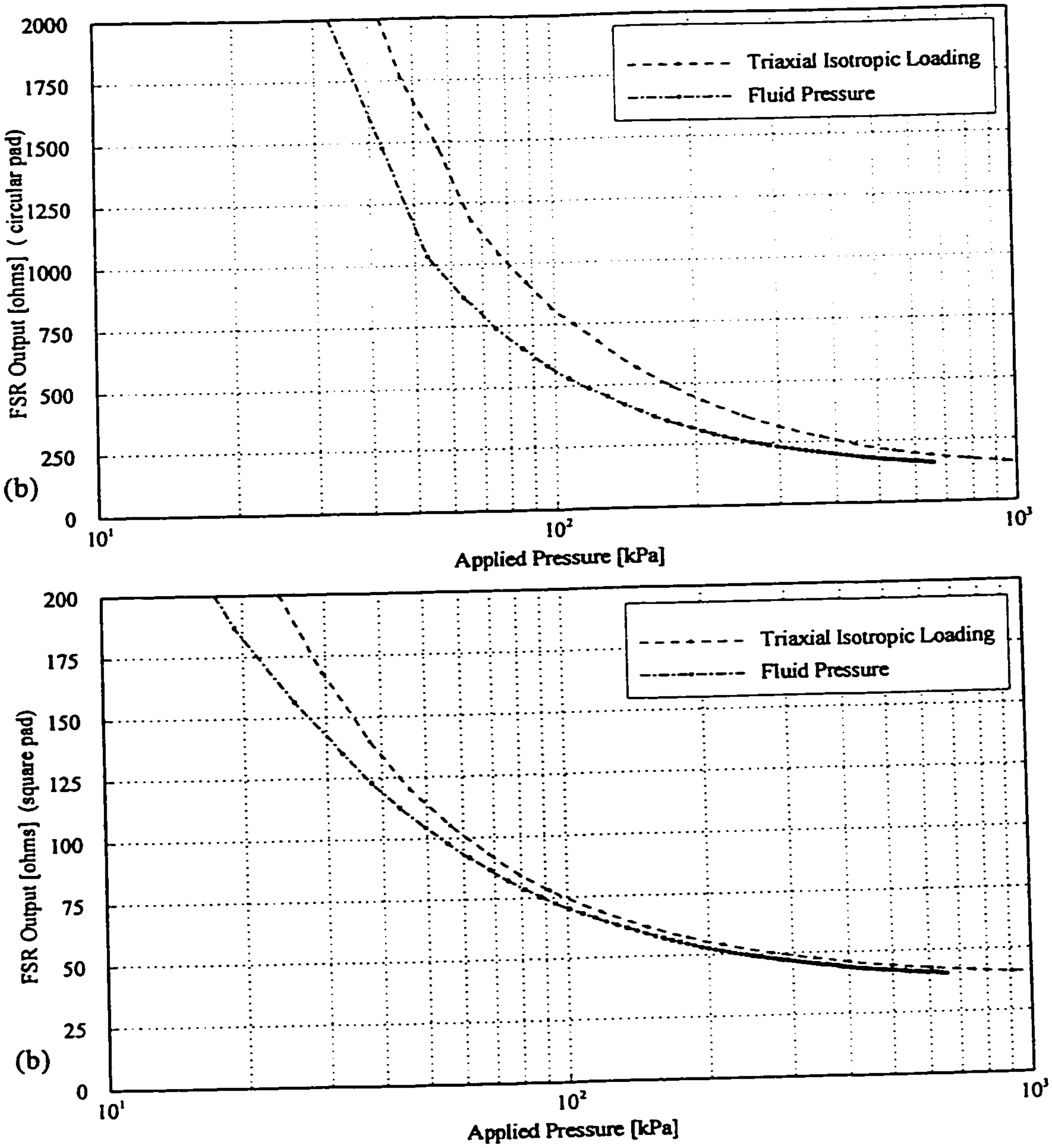

Output response of the FSR's transducer under both, fluid pressure and triaxial isotropic loading. The output measured in *ohms* is plotted against the applied pressure in *kPa*, in semilogarithmic scale. The response obtained with the circular and square pads are shown in (a) and (b), respectively.

Figure A.4. Performance of the Force Sensing Resistors (FSR®)

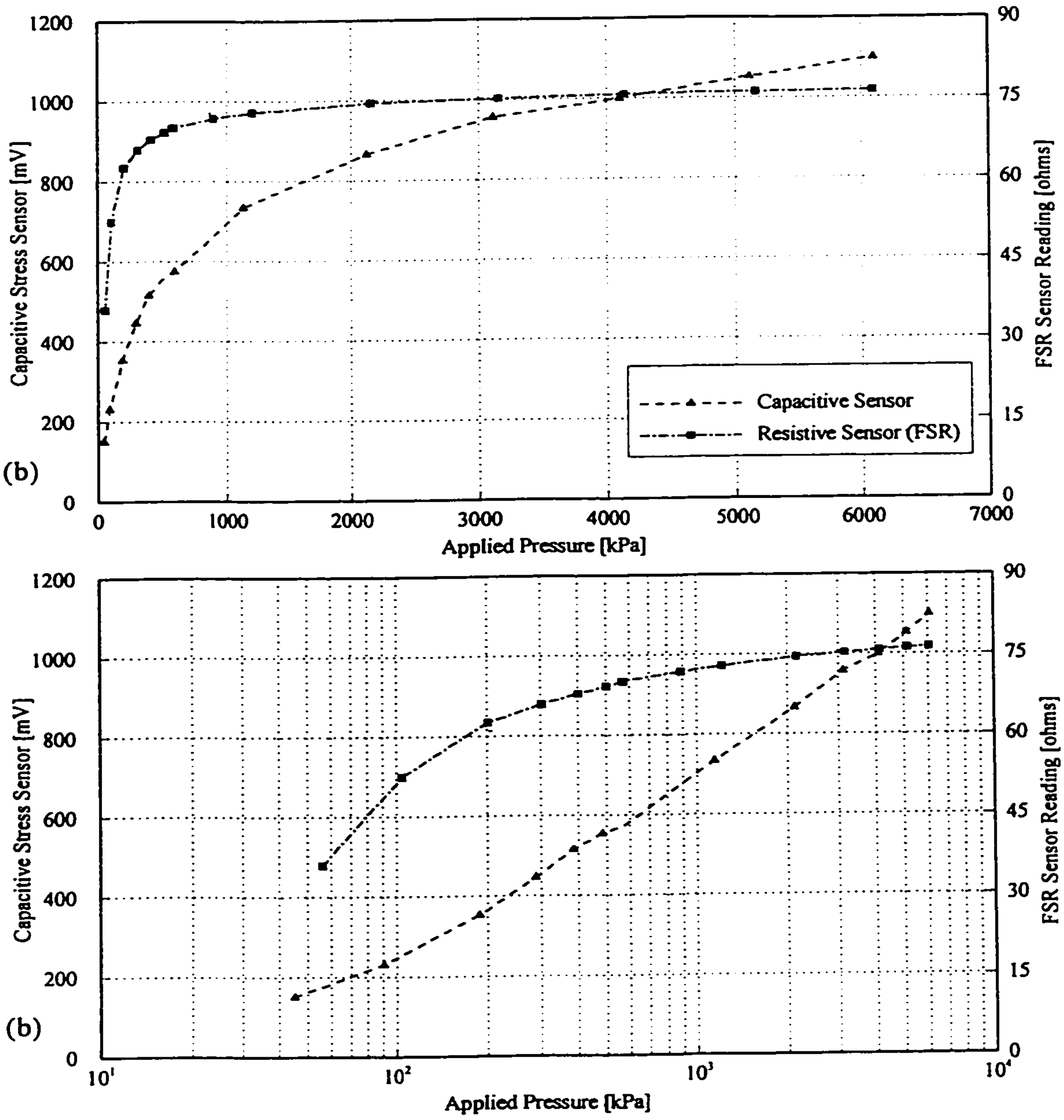

The output responses from a FSR and a capacitive transducers under fluid pressure are shown in (a) normal, and (b) semilogarithmic scales.

Figure A.5. Comparison of performances from capacitive and resistive stress transducers

APPENDIX B

DEFINITION OF PLASTICITY VARIABLES

This appendix summarizes several variables utilized by the mathematical formulation of plasticity for the case of axisymmetric problems. The continuum mechanics sign convention is adopted.

$\sigma = \left[\sigma_r \;\; \sigma_z \;\; \sigma_{rz} \;\; \sigma_\theta \right]^T$	Effective stress tensor.
$\sigma_m = -\tfrac{1}{3}\,\sigma_{kk} = -\tfrac{1}{3}\,(\sigma_r + \sigma_z + \sigma_\theta)$	First invariant of the effective stress tensor.
$\boldsymbol{s} = \sigma + \sigma_m \boldsymbol{I} = \left[s_r \;\; s_z \;\; s_{rz} \;\; s_\theta \right]^T$	Deviatoric effective stress tensor.
$\boldsymbol{I} = [\,1 \;\; 1 \;\; 0 \;\; 1\,]^T$	Unit vector.
$J_2 = \bar{\sigma}^2 = \tfrac{1}{2}\left(s_{ij}\, s_{ij}\right) = \tfrac{1}{2}\left(s_r^2 + s_z^2 + s_\theta^2\right) + s_{rz}^2$	Second invariant of the deviatoric stress tensor.
$J_3 = \tfrac{1}{3}\left(s_{ij}\, s_{jk}\, s_{ki}\right) = s_r s_z s_\theta - s_\theta\, s_{rz}^2$	Third invariant of the deviatoric stress tensor, given by Christian & Desai (1977), or
$J_3 = \tfrac{1}{3}(s_r^3 + s_z^3 + s_\theta^3) + s_{rz}^2\,(s_r + s_z)$	as given by Nayak & Zienkiewicz (1972).
$g_1(\theta) = \dfrac{2k}{(1+k) - (1-k)\,sin3\theta}$	Shape of the yield function in the π-plane, and *k*
$k = \dfrac{3 - \sin\phi_f}{3 + \sin\phi_f}$	with ϕ_f defined as the friction angle at failure.
$g_2(\theta) = \dfrac{2k^*}{(1+k^*) - (1-k^*)\,sin3\theta}$	The shape of the plastic potential in the π-plane, with

$$k^{*} = \frac{3 - \sin\phi_c}{3 + \sin\phi_c}$$

ϕ_c defined as the friction angle at critical state.

$$sin3\theta = -\frac{3\sqrt{3}}{2}\frac{J_3}{\bar{\sigma}^3}$$

Lode's angle θ (Chen 1989).

$$H_e = \frac{\partial f^T}{\partial \sigma} \boldsymbol{D}^e \frac{\partial \Psi}{\partial \sigma}$$

Elastic hardening modulus.

$$H_p = -\frac{\partial f}{\partial \varepsilon_q{}^p}\left\{\frac{2}{3}\, dev\left(\frac{\partial \Psi^T}{\partial \sigma}\right)\, dev\left(\frac{\partial \Psi}{\partial \sigma}\right)\right\}^{1/2}$$

Plastic hardening modulus.

$$\frac{\partial f}{\partial \sigma} = \frac{\partial f}{\partial \sigma_m}\frac{\partial \sigma_m}{\partial \sigma} + \frac{\partial f}{\partial \bar{\sigma}}\frac{\partial \bar{\sigma}}{\partial \sigma} + \frac{\partial f}{\partial g_1(\theta)}\frac{\partial g_1(\theta)}{\partial \sigma}$$

Gradient of the yield function.

$$\frac{\partial f}{\partial \sigma} = A_1\, \boldsymbol{I} + A_2\, \boldsymbol{S}_a + A_3\, \boldsymbol{S}_b$$

where the scalar constants A_1, A_2 and A_3 are given by

$$A_1 = \left(\frac{1}{3}\eta - \frac{1}{2}\eta_f\right)$$

$$A_2 = \frac{\sqrt{3}}{2}\frac{1}{\bar{\sigma}}\left(\frac{1}{g_1(\theta)} + \frac{1}{2}\eta_f\, sin3\theta\right)$$

$$A_3 = \frac{3}{4}\eta_f\frac{1}{\bar{\sigma}^2}$$

$$\boldsymbol{S}_a = \left[\, s_r \quad s_z \quad 2s_{rz} \quad s_\theta \,\right]^T$$

$$\boldsymbol{S}_b = \left[\, \left(s_r^2 + s_{rz}^2\right) \; \left(s_{rz}^2 + s_z^2\right) \; \left(2\left(s_r + s_z\right)s_{rz}\right) \; \left(s_\theta^2\right) \,\right]^T$$

$$\frac{\partial \Psi}{\partial \sigma} = \frac{\partial \Psi}{\partial \sigma_m}\frac{\partial \sigma_m}{\partial \sigma} + \frac{\partial \Psi}{\partial \bar{\sigma}}\frac{\partial \bar{\sigma}}{\partial \sigma} + \frac{\partial \Psi}{\partial g_2(\theta)}\frac{\partial g_2(\theta)}{\partial \sigma}$$

Gradient of the plastic potential or flow vector

$$\frac{\partial \Psi}{\partial \sigma} = B_1\, \boldsymbol{I} + B_2\, \boldsymbol{S}_a + B_3\, \boldsymbol{S}_b$$

$$B_1 = \left(\frac{1}{3} \frac{g_1(\theta)}{g_2(\theta)} \eta - \frac{5}{6} \eta_{cs} \right)$$

$$B_2 = \frac{\sqrt{3}}{2} \frac{1}{\bar{\sigma}} \left(\frac{1}{g_2(\theta)} + \frac{1}{2} \eta_{cs} \sin 3\theta \right)$$

$$B_3 = \frac{3}{4} \eta_{cs} \frac{1}{\bar{\sigma}^2}$$

APPENDIX C

ANISOTROPIC CONSTITUTIVE MODEL

C.1 Introduction

The implementation of an anisotropic constitutive model is developed for the case of orthotropic anisotropy. We consider stress-induced anisotropy limited to the elastic deformations, where the stress-dependent elastic moduli and Poisson's ratios are defined according to the principal stress directions. The implementation of this anisotropic constitutive model requires the transformation of the material matrix from the principal stress system into the local system. In order to remain positive definite, the constitutive matrix must comply with a specific set of material constraints.

C.2 Orthotropic Anisotropy

The constitutive relations for the general case of stresses and strains in orthotropic materials are expressed in terms of any (x, y, z) orthogonal reference system (see e.g., Feda 1982, and Pickering 1970), as follows:

$$\varepsilon_x = \frac{1}{E_x}\sigma_x - \frac{\nu_{yx}}{E_y}\sigma_y - \frac{\nu_{zx}}{E_z}\sigma_z \tag{C1.a}$$

$$\varepsilon_y = -\frac{\nu_{xy}}{E_x}\sigma_x + \frac{1}{E_y}\sigma_y - \frac{\nu_{zy}}{E_z}\sigma_z \tag{C1.b}$$

$$\varepsilon_z = -\frac{\nu_{xz}}{E_x}\sigma_x - \frac{\nu_{yz}}{E_y}\sigma_y + \frac{1}{E_z}\sigma_z \tag{C1.c}$$

$$\gamma_{xy} = \frac{\sigma_{xy}}{G_{xy}} \tag{C.1d}$$

$$\gamma_{yz} = \frac{\sigma_{yz}}{G_{yz}} \tag{C.1e}$$

$$\gamma_{zx} = \frac{\sigma_{zx}}{G_{zx}} \tag{C.1f}$$

where ν_{ij} is Poisson's ratio for transverse strain in the j^{th} direction due to stress in the i^{th} direction, E_i is the elastic modulus in the i^{th} direction, and G_{ij} is the shear modulus in the plane containing the i^{th} and j^{th} directions.

In accordance with the Maxwell-Betti postulate of reciprocal work, the constitutive relationship must be symmetric. As a result the following relations apply to equations (C.1):

$$\frac{\nu_{yx}}{E_y} = \frac{\nu_{xy}}{E_x} \quad \rightarrow \quad \nu_{yx} = \nu_{xy}\frac{E_y}{E_x}\ , \tag{C.2a}$$

$$\frac{\nu_{zx}}{E_z} = \frac{\nu_{xz}}{E_x} \quad \rightarrow \quad \nu_{zx} = \nu_{xz}\frac{E_z}{E_x}\ , \tag{C.2b}$$

$$\frac{\nu_{zy}}{E_z} = \frac{\nu_{yz}}{E_y} \quad \rightarrow \quad \nu_{zy} = \nu_{yz}\frac{E_z}{E_y}\ , \tag{C.2c}$$

The number of independent materials properties is reduced from 12 to 9. Also, for the axisymmetric type of problems considered in this thesis, out-of-plane shear strains are zero; for instance, if z is the hoop direction, then $\gamma_{yz} = \gamma_{zx} = 0$. The number of necessary independent constants is thus further reduced to 7, namely $\{E_{xy}, E_{xz}, E_{yz}, \nu_{xy}, \nu_{xz}, \nu_{yz}, G_{xy}\}$[1].

After substitution of equations (C.2) into (C.1), the constitutive relations for axisymmetric problems with orthotropic anisotropy can be presented in the matrix form by

$$\begin{Bmatrix} \varepsilon_x \\ \varepsilon_y \\ \gamma_{xy} \\ \varepsilon_z \end{Bmatrix} = \begin{bmatrix} \frac{1}{E_x} & -\frac{\nu_{xy}}{E_x} & 0 & -\frac{\nu_{xz}}{E_x} \\ -\frac{\nu_{xy}}{E_x} & \frac{1}{E_y} & 0 & -\frac{\nu_{yz}}{E_y} \\ 0 & 0 & \frac{1}{G_{xy}} & 0 \\ -\frac{\nu_{xz}}{E_x} & -\frac{\nu_{yz}}{E_y} & 0 & \frac{1}{E_z} \end{bmatrix} \begin{Bmatrix} \sigma_x \\ \sigma_y \\ \sigma_{xy} \\ \sigma_z \end{Bmatrix} \tag{C.3}$$

or, in compact notation, as $\varepsilon = \boldsymbol{C}\,\sigma$, where $\boldsymbol{C}$ is the compliance matrix. Solving for stresses, for example $\sigma = \boldsymbol{D}\,\varepsilon$, the constitutive or material matrix $\boldsymbol{D}$ is given by

$$\boldsymbol{D} = \frac{1}{G_{xy}\Delta} \begin{bmatrix} \frac{1}{E_y}\left(\frac{1}{E_z} - \frac{\nu_{yz}^2}{E_y}\right) & \frac{1}{E_x}\left(\frac{\nu_{xy}}{E_z} + \frac{\nu_{xz}\nu_{yz}}{E_y}\right) & 0 & \frac{1}{E_x E_y}\left(\nu_{xz} + \nu_{yz}\,\nu_{xy}\right) \\ & \frac{1}{E_x}\left(\frac{1}{E_z} - \frac{\nu_{xz}^2}{E_x}\right) & 0 & \frac{1}{E_x}\left(\frac{\nu_{yz}}{E_y} + \frac{\nu_{xy}\,\nu_{xz}}{E_x}\right) \\ \textit{symmetric} & & G_{xy}^2\,\Delta & 0 \\ & & & \frac{1}{E_x}\left(\frac{1}{E_y} - \frac{\nu_{xy}^2}{E_x}\right) \end{bmatrix} \tag{C.4}$$

where Δ is the determinant of the compliance matrix, which is calculated using the expression

$$\Delta = \frac{1}{E_x\,G_{xy}}\left(\frac{1}{E_y E_z} - \frac{\nu_{xy}^2}{E_x E_z} - \frac{\nu_{xz}^2}{E_x E_y} - \frac{\nu_{yz}^2}{E_y^2} - 2\,\frac{\nu_{xy}\,\nu_{xz}\,\nu_{yz}}{E_x\,E_y}\right) \tag{C.5}$$

---

[1] *Gxz* and *Gyz* still remain as independent material constants but they drop out of the axisymmetric formulation.

C.3 Material Constraints

The fact that strain energy is always a positive quantity imposes some limitations on the selection of the material properties $\{E_{xy}, E_{xz}, E_{yz}, \nu_{xy}, \nu_{xz}, \nu_{yz}, G_{xy}\}$. The definition of these material constraints is based on the characteristics of the constitutive relations. Considering, for example, that the compliance and material matrices, $\boldsymbol{C}$ and $\boldsymbol{D}$, are symmetric matrices, then the expression for the strain energy

$$U_o = \frac{1}{2}\, \varepsilon^T \boldsymbol{D}\, \varepsilon = \frac{1}{2}\, \sigma^T \boldsymbol{C}\, \sigma \qquad \text{(C.6)}$$

is a pure quadratic form (Mirza 1992). Since U_o is always positive it follows that C and $\boldsymbol{D}$ must be positive definite matrices. We can use the properties of positive definite matrices to establish the materials constraints. For instance the following equivalent conditions are necessary and sufficient for positive definiteness:

i. For any given ε, the expression $\varepsilon^{T} \boldsymbol{D}\ \varepsilon > 0$ must be true.

ii. All eigenvalues of the constitutive matrix $\boldsymbol{D}$ are real positive numbers.

iii. The determinants of all co-minors along the diagonal of $\boldsymbol{D}$ are real positive numbers.

iv. The determinant of the compliance matrix Δ must be a real positive number.

Also, a necessary condition, but not sufficient, for positive definite systems is that all diagonal terms of either $\boldsymbol{D}$ or $\boldsymbol{C}$ must be real positive numbers. An inspection of diagonal terms in equation (C.4) yields the following necessary constraints:

$$\nu_{xy} < \sqrt{\frac{E_x}{E_y}} \ ; \ \nu_{xz} < \sqrt{\frac{E_x}{E_z}} \ ; \ \nu_{yz} < \sqrt{\frac{E_y}{E_z}} \ , \tag{C.7a}$$

and from condition iv,

$$\nu_{xy}\,\nu_{xz}\,\nu_{yz} < \frac{1}{2}\left(\frac{E_x}{E_z} - \frac{E_y}{E_z}\,\nu_{xy}^{\,2} - \nu_{xz}^{\,2} - \frac{E_x}{E_y}\,\nu_{yz}^{\,2} \right) \ . \tag{C.7b}$$

Furthermore, all materials properties must be positive (Malvern 1969),

$$\{E_{xy},\, E_{xz},\, E_{yz},\, \nu_{xy},\, \nu_{xz},\, \nu_{yz},\, G_{xy}\} > 0 \ . \tag{C.7c}$$

The next section is related to the selection of parameters for the anisotropic model based on the constraints imposed by equations (C.7).

C.4 Cross-Confinement

As discussed in Section 3.4.2 of the thesis for the anisotropic constitutive model, the stress dependency of the elastic moduli is controlled by the lateral confinement, in the principal stress directions.

In the present formulation we assume that the constitutive matrix ***D*** can be oriented with the principal stress directions, for example, the reference system (*x, y, z*) in equation (C.4) can be aligned with the principal stress planes directions (*1, 2, 3*). Specifically, *x* relates to the major principal direction, *y* relates to the intermediate principal direction, and *z* relates to the minor principal direction. For the sign convention employed in solid mechanics, and adopted for the formulation, the principal stresses are ordered by magnitude as

$$\sigma_3 \le \sigma_2 \le \sigma_1 \quad , \tag{C.8a}$$

and in terms of absolute magnitudes, for cohesionless soils (no tension allowed)

$$|\sigma_3| \ge |\sigma_2| \ge |\sigma_1| \quad . \tag{C.8b}$$

In other words, for soil mechanics problems Mohr diagram spans the left side of the τ-σ plane, and σ_3 represents the maximum compression even though it is referred to as the minor principal stress. The stiffness matrix ***D***, defined in the direction of the principal stresses, is given by

$$\boldsymbol{D} = \frac{1}{G_{13}\Delta}\begin{bmatrix} \frac{1}{E_2}\left(\frac{1}{E_3}-\frac{\nu_3^2}{E_2}\right) & \frac{1}{E_1}\left(\frac{\nu_1}{E_3}+\frac{\nu_2\nu_3}{E_2}\right) & 0 & \frac{1}{E_1E_2}\left(\nu_2+\nu_3\nu_1\right) \\ & \frac{1}{E_1}\left(\frac{1}{E_3}-\frac{\nu_2^2}{E_1}\right) & 0 & \frac{1}{E_1}\left(\frac{\nu_3}{E_2}+\frac{\nu_1\nu_2}{E_1}\right) \\ \textit{symmetric} & & G_{13}^2\Delta & 0 \\ & & & \frac{1}{E_1}\left(\frac{1}{E_2}-\frac{\nu_1^2}{E_1}\right) \end{bmatrix} , \tag{C.9}$$

and the determinant Δ by

$$\Delta = \frac{1}{E_1\,G_{13}}\left(\frac{1}{E_2E_3}-\frac{\nu_1^2}{E_1E_3}-\frac{\nu_2^2}{E_1E_2}-\frac{\nu_3^2}{E_2^2}-2\frac{\nu_1\nu_2\nu_3}{E_1E_2}\right) \quad . \tag{C.10}$$

The stress-dependency of elastic moduli on the orientation of principal stress planes has been discussed by Oda et al.(1985) for granular assemblies, and by Hardin and Blandford (1989) for the case of sandy soil. In this approach we define the stress dependent elastic moduli in terms of the cross-confining stresses with

$$E_1 = E_{ref}\,(1 - e^{r_1}) \quad , \quad r_1 = \frac{1000}{E_{ref}} \left(\frac{\sigma_2 + \sigma_3}{2} \right) \tag{C.11a}$$

$$E_2 = E_{ref}\,(1 - e^{r_2}) \quad , \quad r_2 = \frac{1000}{E_{ref}} \left(\frac{\sigma_3 + \sigma_1}{2} \right) \tag{C.11b}$$

$$E_3 = E_{ref}\,(1 - e^{r_3}) \quad , \quad r_3 = \frac{1000}{E_{ref}} \left(\frac{\sigma_1 + \sigma_2}{2} \right) \tag{C.11c}$$

$$G_{13} = G_{ref}\,(1 - e^{r_{13}}) \quad , \quad r_{13} = \frac{1000}{G_{ref}} \left(\frac{\sigma_3 + \sigma_1}{2} \right) \tag{C.11d}$$

The reference moduli E_{ref} and G_{ref} are stress-independent material properties, which depend on density and grain characteristics of the sand. From the testing of dense samples during the triaxial series, E_{ref} and G_{ref} were found to be 900 and 350 *kPa*, respectively. The orthotropic Poisson's ratios, ν_1, ν_2, and ν_3, are assumed to be stress-independent material parameters.

In what follows, the intermediate stress direction is assumed to be associated with the out-of-plane stress direction. Furthermore, if we consider that the Poisson's ratios for real world materials can not be less than zero nor greater than 0.50 (Malvern 1969), then the inequality

$$\nu_1\ \nu_2\ \nu_3 < 0.125 = \left(0.50^3\right) \tag{C.12}$$

will always apply. In this case, it can be proven that the material constraint indicated in equation(C.7b) is satisfied as long as the relation

$$E_1^{\,2} \geq E_2\ E_3 \tag{C.13}$$

holds true.

According to the adopted sign convention, equation (C.11a) will always yield values of elastic moduli complying with the condition expressed in equation (C.13); for example, $E_1 \geq E_2 \geq E_3$. Therefore, it can be concluded that the positive definiteness of the material matrix is ensured by the assumption that the orthotropic axes of anisotropy are coaxial with the principal stress directions.

C.5 Stress transformation

This section considers the stress transformation necessary to define the principal stresses and principal directions. Since the stress tensor is invariant with respect to the reference system, it is possible to write

$$\sigma_P = T\, \sigma_L \ , \tag{C.14}$$

where σ_P is the principal stress vector, σ_L is the stress vector referred to the local system, and T is the stress transformation tensor.

The local system of reference is attached to the cylindrical coordinate system (r, z, θ), where r, z and θ stand for radial, vertical, and out-of-plane directions. The stresses corresponding to this cylindrical system are $\sigma_L = \{\ \sigma_r\ \ \sigma_z\ \ \sigma_{rz}\ \ \sigma_\theta\ \}^T$.

As mentioned before, the out-of-plane direction is free of shear stresses, and σ_θ is permanently a principal stress, which is assumed to be associated with the intermediate principal stress σ_2. Imposed by axisymmetric constraints, this assumed intermediate principal direction remains fixed with the out-of-plane direction. It follows then that the stress transformation T

can be reduced to a rotation around the θ direction; for example, equation (C.14) can now be written as

$$\begin{Bmatrix} \sigma_3 \\ \sigma_1 \\ 0 \\ \sigma_2 \end{Bmatrix} = \boldsymbol{T} \begin{Bmatrix} \sigma_r \\ \sigma_z \\ \sigma_{rz} \\ \sigma_\theta \end{Bmatrix} , \tag{C.15}$$

where $\boldsymbol{T}$ is defined as

$$\boldsymbol{T} = \begin{bmatrix} \cos^2\alpha & \sin^2\alpha & \sin 2\alpha & 0 \\ \sin^2\alpha & \cos^2\alpha & -\sin 2\alpha & 0 \\ -\dfrac{\sin 2\alpha}{2} & \dfrac{\sin 2\alpha}{2} & \cos 2\alpha & 0 \\ 0 & 0 & 0 & 1 \end{bmatrix} , \tag{C.16}$$

and where the rotation angle α from Figure C.1 is uniquely defined by

$$\tan\alpha = \frac{\sigma_{rz}}{\left(\dfrac{\sigma_r - \sigma_z}{2}\right) - \dfrac{1}{2}\sqrt{\left(\sigma_r - \sigma_z\right)^2 + 4\,\sigma_{rz}^{\,2}}} . \tag{C.17}$$

According to equation (C.15), the transformation matrix $\boldsymbol{T}$ given in equation (C.16) confirms the requirement that $\sigma_2 = \sigma_\theta$ for any rotation α. The ordering of stresses in the L.H.S. of expression (C.15) corresponds to the stress convention specified in equations (C.8). Also, in equation (C.17) counter-clockwise rotations are considered negative.

C.6 Strain Transformation

Using the strain transformation, we would like to transform the stiffness matrix $\boldsymbol{D}_P$ from the principal stress directions, where it was formed, to the original cylindrical coordinate system, where $\boldsymbol{D}_L$ will be used by the solution procedure.

If transformation $\boldsymbol{T}$ in equation (C.16) were to be used for strains the resultant $\boldsymbol{D}_L$ matrix would be nonsymmetric, even though $\boldsymbol{D}_P$ is symmetric. This nonsymmetry violates the principle of invariance of the constitutive relations with respect to the reference system. Therefore, it is concluded that strains do not transform like stresses. A suitable form for strain transformation $\boldsymbol{T}_d$ may be obtained by invoking the principle of invariance mentioned above. Consider first two reference systems, one is the cylindrical coordinate system where stresses, strains, and the constitutive matrix are defined as σ_L, ε_L, and $\boldsymbol{D}_L$ respectively, and the other is the system of the principal directions where stresses, strains, and constitutive matrix are defined as σ_P, ε_P, and $\boldsymbol{D}_P$. The relation between these two systems of reference is defined by transformations $\boldsymbol{T}$ and $\boldsymbol{T}_d$ as follows

$$\sigma_P = \boldsymbol{T}\,\sigma_L \ , \tag{C.18}$$

$$\varepsilon_P = \boldsymbol{T}_d\,\varepsilon_L \ . \tag{C.19}$$

Then, the work done by stresses along the strain field must be independent of the reference system. This work invariance can be represented by

$$\sigma_L^{\,T}\,\varepsilon_L = \sigma_P^{\,T}\,\varepsilon_P \ , \tag{C.20}$$

where the L.H.S. represents the work done in the original system of reference, while the R.H.S. is the work done in the principal direction system. Substituting equations (C.18) and (C.19) in the R.H.S in equation (C.20) the work invariance might be written as

$$\sigma_L^{\,T}\,\varepsilon_L = \left(\boldsymbol{T}\,\sigma_L\right)^T\left(\boldsymbol{T}_d\,\varepsilon_L\right) = \sigma_L^{\,T}\;\boldsymbol{T}^T\,\boldsymbol{T}_d\;\varepsilon_L \tag{C.21}$$

which implies that $T^T\ T_d = I$, I being the identity matrix. The strain transformation is thus defined as

$$T_d = \left(T^T\right)^{-1} = \left(T^{-1}\right)^T = \begin{bmatrix} \cos^2\alpha & \sin^2\alpha & \frac{\sin 2\alpha}{2} & 0 \\ \sin^2\alpha & \cos^2\alpha & -\frac{\sin 2\alpha}{2} & 0 \\ -\sin 2\alpha & \sin 2\alpha & \cos 2\alpha & 0 \\ 0 & 0 & 0 & 1 \end{bmatrix} . \tag{C.22}$$

The transformation of the constitutive matrix D_L is then defined in terms of the strain transformation by the expression

$$D_L = T_d^T\, D_P\, T_d\ . \tag{C.23}$$

The constitutive matrix D_L obtained with expression (C.23) is symmetric and fully populated, indicating that dilation and distortion strain modes are now coupled. This is an important characteristic of an anisotropic continuum where, in general, strain directions are not coaxial with the stress directions (see Jaunzemis 1967, Malvern 1969, and Antman 1995). It is only in the principal stress directions that dilation and distortion modes are uncoupled as might be observed in equation (C.9). The reason for this peculiarity is that only for the principal direction system are the stresses and strains coaxial. For any other orientation strains and stresses are not coaxial and dilation and distortion strain modes are coupled.

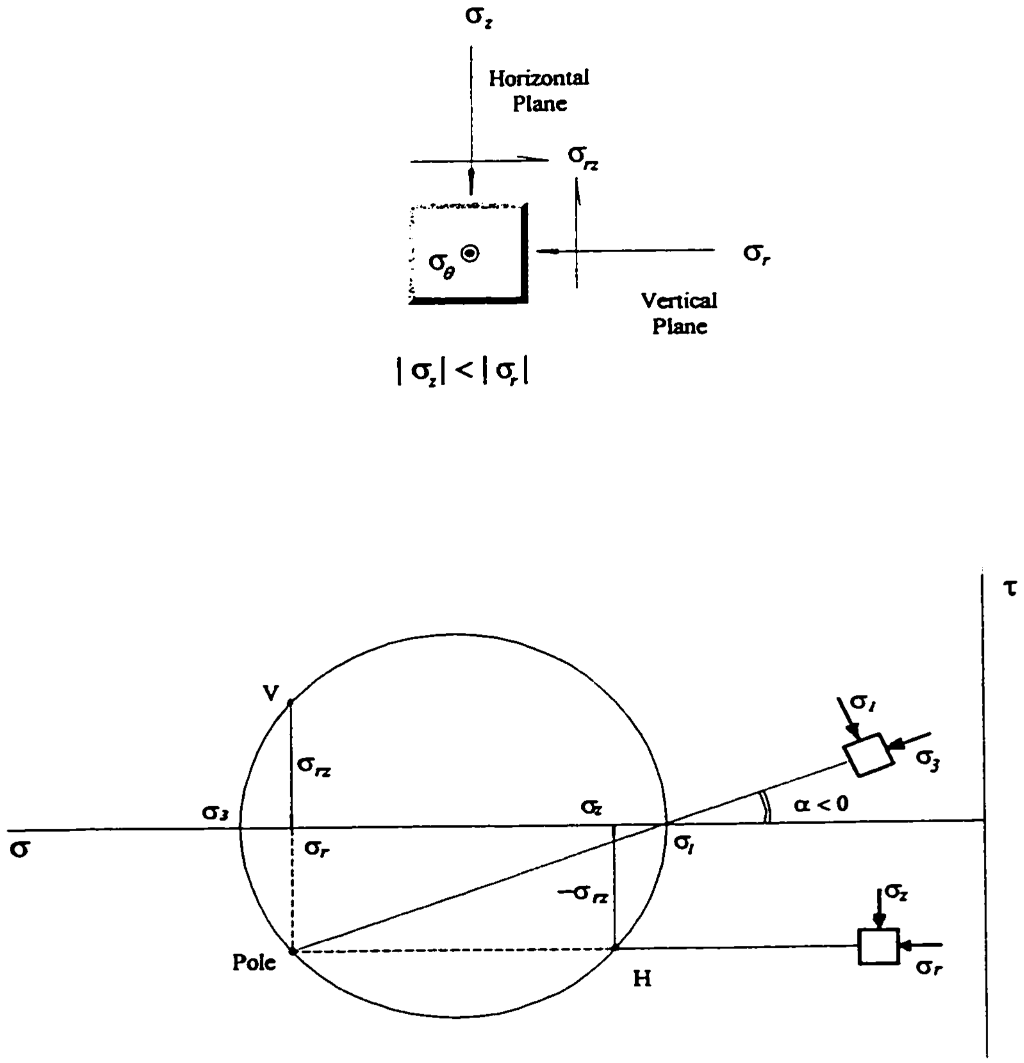

Figure C.1 Mohr diagram and the principal stress planes.

REFERENCES

Agaiby, S.W., Kulhawy, F.H. & Trautmann, C.H. 1996. On large-scale model testing of laterally loaded drilled shafts in sand. *ASTM Geotechnical Testing Journal*, 19(1): 32-40.

Al-Douri, R.H., Hull, T. & Poulos, H., 1993. Influence of test chamber boundary conditions on sand bed response. *ASTM Geotechnical Testing Journal*, 16(4): 550-562.

Altaee, A. & Fellenius, B.H. 1994. Physical modeling in sand. *Canadian Geotechnical Journal*, 31: 420-431.

Antman, S.S. 1995. *Nonlinear Problems in Elasticity*. Springer-Verlag. New York.

Arthur, J.R.F. & Menzies, B.K. 1972. Inherent anisotropy in a sand. *Geotechnique*, 22(1): 115-128.

Atkinson, J.H. & Bransby, P.L. 1978. *The Mechanics of Soils. An Introduction to Critical State Soil Mechanics*. McGraw Hill Book Company.

Atkinson, J.H. & Sallfors, G. 1991. Experimental determination of soil properties. *Proc. of the X European Conference of Soil Mechanics & Foundation Engineering*, Florence, Italy, Vol. 3: 915-956.

Baker, W.E., Westine P.S., & Dodge, F.T. 1973. *Similarity Methods in Engineering Dynamics. Theory and Practice of Scale Modeling*. Rochelle Park, New Jersey: Hayden Book Company.

Baker, R. & Desai, C.S. 1984. Induced anisotropy during plastic straining. *Intern. Journal for Numerical & Analytical Methods in Geomechanics*, 8: 167-185.

Bathe, K.J. & Cimento, A.P. 1980. Some practical procedures for the solution of nonlinear finite element equations. *Computer Methods in Applied Mechanics and Engineering*, 22: 59-85.

Bathe, K.J. 1982. *Finite Element Procedures in Engineering Analysis*. Prentice-Hall, Inc.

Been, K. & Jefferies, M.G. 1985. A state parameter for sands. *Geotechnique*, 35(2): 99-112.

Been, K., Jefferies, M.G. & Hachey, J. 1991. The critical state of sands. *Geotechnique*, 41(3): 365-381.

Bellotti, R., Jamiolkowski, M., LoPresti, D.C.F. & O'Neill, D.A. 1996. Anisotropy of small strain stiffness in Ticino sand. *Geotechnique*, 46(1): 115-131.

Bishop, A.W. & Henkel, D.J. 1962. *The Measurement of Soil Properties in the Triaxial Test.* 2nd Edition, Edward Arnold Publishers Ltd.

Bowles, J.E. 1986. *Engineering Properties of Soils and their Measurement.* 3rd Edition, McGraw-Hill Book Company.

Bowles, J.E. 1996. *Foundation Analysis and Design.* 5th Edition, McGraw-Hill Company.

Chen, W.F. 1984. Constitutive Modelling in Soil Mechanics. Chapter 5 in *Mechanics of Engineering Materials.* Edited by Desai & Gallagher. John Wiley & Sons Ltd.

Chen, W.F. & Baladi, G.Y. 1985. *Soil Plasticity: Theory and Implementation.* Elsevier.

Craig, W.H. 1985. Modelling pile installation in centrifuge experiments. *Proc. of the XI Intern. Conference of Soil Mechanics & Foundation Engineering,* San Francisco, USA, Vol. 2: 1101-1104.

Craig, W. & Sabagh, S. 1994. Stress-levels in model tests on piles. *Canadian Geotechnical Journal,* 31: 28-41.

Christian, J.T. & Desai, C.S. 1977. Constitutive laws for geologic media. Chapter 2 in *Numerical Methods in Geotechnical Engineering.* McGraw-Hill.

Dancygier, A.N. 1995. Qualitative evaluation of effect of gravity on small-scale modeling. *ASCE Journal of Engineering Mechanics,* 121(7): 773-777.

Desai, C.S. & Abel, J.F. 1972. *Introduction to the Finite Element Method.* Van Nostrand Reinhold.

Du, J. & Dusseault, M.B. 1994. A generalized D matrix for anisotropic elastic granular media. *Intern. Journal for Numerical & Analytical Methods in Geomechanics,* 18: 107-120.

Dunnicliff, J. 1982. Geotechnical Instrumentation for Monitoring Field Performance. *National Cooperative Highway Research Program.* Synthesis of Highway Practice 89. TRB, NRC, Washington, DC, USA.

Feda, J. 1982. *Mechanics of Particulate Materials-The Principles.* Developments in Geotechnical Engineering 30. Elsevier Scientific Publishing Company.

Filz, G.M. & Duncan, J.M. 1993. Drift of Flush-Mounted Pressure Cell Readings. *ASTM Geotechnical Testing Journal,* 16(4): 432-441.

Filz, G.M. & Brandon, T.L. 1994. Static and Dynamic Measurements Using Embedded Earth Pressure Cells. *Transportation Research Record 1432,* TRB, Washington, DC: 86-95.

Foray, P., Balachowski, L. & Colliat, J.L. 1998. Bearing capacity of model piles driven into dense overconsolidated sands. *Canadian Geotechnical Journal,* 35: 374-385.

Franke, E. & Muth, G. 1985. Scale effect in 1g model tests on horizontally loaded piles. *Proc. of the XI Intern. Conference of Soil Mechanics & Foundation Engineering,* San Francisco, USA, Vol. 2: 1011-1014.

Garga, V. K. & Zhang, H. 1997. Volume change in undrained triaxial tests on sands. *Canadian Geotechnical Journal*, 34: 762-772.

Hanna, T.H. 1985. *Field Instrumentation in Geotechnical Engineering*. Volume 10, Trans Tech Publications.

Hardin, B.O. & Black, W.L. 1966. Sand stiffness under various triaxial stresses. *ASCE Journal of the Soil Mechanics & Foundations Division*, 92(2): 27-42.

Hardin, B.O. & Blandford, G.E. 1989. Elasticity of particulate materials. *ASCE Journal of Geotechnical Engineering*, 115(6): 788-805.

Hassini, S. & Woods, R.D. 1989. Dynamic experiments with model pile foundations. *Proc. of the XII Intern. Conference of Soil Mechanics & Foundation Engineering*, Rio de Janeiro, Brazil: 1135-1138.

Hettler, A. & Gudehus, G. 1985. A pressure-dependent correction for displacement results from 1*g* model tests with sand. *Geotechnique*, 35(4): 497-510.

Horvath, R.G., Bermingham, P. & Janes, M. 1990. The Statnamic loading test. An innovative method for predicting capacity of deep foundations. *Proc. of the 43rd Canadian Geotechnical Conference.* Laval University, Sainte Foy, Quebec, Canada: 143-150.

Horvath, R.G. 1995. Influence of loading rate on the capacity of a model pile in clay. *Canadian Geotechnical Journal*, 32: 364-368.

Horvath, R.G. & Stolle, D.F.E. 1996. Frustum confining vessel for testing model piles. *Canadian Geotechnical Journal*, 33: 499-504.

Houlsby, G.T. & Hitchman, R. 1988. Calibration chamber tests of a cone penetrometer in sand. *Geotechnique*, 38(1): 39-44.

Janbu, N. 1963. Soil compressibility as determined by oedometer and triaxial tests. *Proc. of the European Conference of Soil Mechanics & Foundation Engineering*, Wiesbaden, Germany, 1: 19-25.

Janes, M., Sy, A. & Campanella, R.G. 1994. A comparison of Statnamic and static pile load tests on steel pipe piles in the Fraser Delta. *Vancouver Geotechnical Society Symposium on Deep Foundations*, Vancouver, B.C., Canada.

Jaunzemis, W. 1967. *Continuum Mechanics*. The MacMillan Company.

Jiang, G.L., Tatsuoka, F., Flora, A. & Koseki, J. 1997. Inherent and stress-state-induced anisotropy in very small strain stiffness of a sandy gravel. *Geotechnique*, 47(3): 509-521.

Jovičić, V. & Coop, M.R. 1997. Stiffness of coarse-grained soils at small strains. *Geotechnique*, 47(3): 545-561.

Kenneth, L.L. & Bolton Seed, H. 1967. Drained strength characteristics of sands. *ASCE Journal of the Soil Mechanics & Foundations Division*, 93(6): 117-141.

Kolymbas, D. & Wu, W. 1989. A device for lateral strain measurement in triaxial tests with unsaturated specimens. *ASTM Geotechnical Testing Journal*, 12(3): 227-229.

Kolymbas, D. & Wu, W. 1990. Recent results of triaxial tests with granular materials. *Powder Technology*, 60: 99-119.

Konrad, J.M. 1997. In situ sand state from CPT: evaluation of a unified approach at two CANLEX sites. *Canadian Geotechnical Journal*, 34: 120-130.

Kumae, S., Itoh, Y., Saizuka, K. & Usami, T. 1997. Pseudodynamic testing of scaled models. *ASCE Journal of Structural Engineering*, 123(4): 524-526.

Langhaar, H.L. 1951. *Dimensional Analysis and Theory of Models*. Robert E. Krieger Publishing Company Inc., Malabar, Florida. Reprinted by John Wiley & Sons.

Lekhnitskii, S.G. 1963. *Theory of Elasticity on an Anisotropic Elastic Body*. Holden-Day.

Lekhnitskii, S.G. 1968. *Anisotropic Plates*. Gordon & Breach, Science Publishers.

Malvern, L.E. 1969. *Introduction to the Mechanics of a Continuous Medium*. Prentice-Hall.

Manzari, M.T. & Dafalias, Y.F. 1997. A critical state two-surface plasticity model for sands. *Geotechnique*, 47(2): 255-272.

Mabsout, M.E., Reese, L.C. & Tassoulas, J.L. 1995. Study of pile driving by finite element method. *ASCE Journal of Geotechnical Engineering*, 121(7): 535-543.

Middendorp, P., Bermingham, P. & Kuiper, B. 1992. Statnamic load testing of foundation piles. *Proc. of the 4th Intern. Stress Wave Conference*, The Hague, September 21-24.

Mirza, F.A. 1992. Energy Methods. *CE712 Lecture Notes*. Department of Civil Engineering, McMaster University, Hamilton, Ontario, Canada.

Mroz, Z. & Pietruszczak, S. 1983. A constitutive model for sand with anisotropic hardening rule. *Intern. Journal for Numerical & Analytical Methods in Geomechanics*. Vol. 7: 305-320.

Mroz, Z. & Zienkiewicz, O.C. 1984. Uniform Formulation of Constitutive Equations for Clays and Sands. Chapter 22 in *Mechanics of Engineering Materials*. Edited by Desai & Gallagher. John Wiley & Sons Ltd.

Nayak, G.C. & Zienkiewicz, O.C. 1972. Convenient form of stress invariants for plasticity. *ASCE Journal of the Structural Division*, 98(4): 949-954.

Oda, M., Koishikawa, I. & Higuchi, T. 1978. Experimental study of anisotropic shear strength of sand by plane strain test. *JSSMFE Soils and Foundations*, 18(1): 25-38.

Oda, M., Nemat-Nasser, S. & Konishi, J. 1985. Stress-induced anisotropy in granular masses. *JSSMFE Soils and Foundations*, 25(3): 85-97.

Ovesen, N.K. 1980. The use of physical models in design. *Proc. of the 7th European Conference of Soil Mechanics & Foundation Engineering*, Brighton, 4: 319-323.

Owen, D.R.J. & Hinton, E. 1980. *Finite Elements in Plasticity. Theory and Practice.* Pineridge Press.

Paikowsky, S.G. & Hajduk, E.L. 1997. Calibration and Use of Grid-Based Tactile Pressure Sensors in Granular Material. *ASTM Geotechnical Testing Journal,* 20(2): 218-241.

Pickering, D.J. 1970. Anisotropic elastic parameters for soils. *Geotechnique,* 20(3): 271-276.

Pietruszczak, S. & Stolle, D.F.E. 1987a. Modelling of sand behaviour under earthquake excitation. *Intern. Journal for Numerical & Analytical Methods in Geomechanics,* 11: 221-240.

Pietruszczak, S. 1987b. Some recent trends in modelling of soil response to fluctuating load. In *Constitutive Laws for Engineering Materials: Theory and Applications.* Desai et al. Editors. Elsevier.

Pietruszczak., S. 1997. On inelastic behaviour of anisotropic frictional materials. Private communication.

Prakash, S. & Sharma, H.D. 1990. *Pile Foundations in Engineering Practice.* Wiley Interscience.

Robertson, P.K. & Campanella, R.G. 1983. Interpretation of cone penetration tests. Part I: Sand. *Canadian Geotechnical Journal,* 20: 718-733.

Rothenburg, L. & Bathurst, R.J. 1989. Analytical study of induced anisotropy in idealized granular materials. *Geotechnique,* 39(4): 601-614.

Schanz, T. & Vermeer, P.A. 1996. Angles of friction and dilatancy of sand. *Geotechnique,* 46(1): 145-151.

Schnaid, F. & Houlsby, G.T. 1991. An assessment of chamber size effects in the calibration of in situ tests in sand. *Geotechnique,* 41(3): 437-445.

Schofield, A.N. 1980. Cambridge centrifuge operations. *Geotechnique,* 30(3): 227-268.

Scott, R.F. 1981. Pile testing in a centrifuge. *Proc. of the X Intern. Conference of Soil Mechanics & Foundation Engineering,* Stockholm, Sweden, Vol. 2: 839-842.

Sully, J.P. & Campanella, R.G. 1991. Effect of lateral stress on CPT penetration pore pressure. *ASCE Journal of Geotechnical Engineering,* 117(7): 1082-1088.

Steenfelt, J.S., Randolph, M.F. & Wroth, C.P. 1981. Instrumented model piles jacked into clay. *Proc. of the X Intern. Conference of Soil Mechanics & Foundation Engineering,* Stockholm, Sweden, Vol. 2: 857-864.

Stolle, D.F.E. 1991. An interpretation of initial stress and strain methods, and numerical stability. *Intern. Journal for Numerical & Analytical Methods in Geomechanics,* 15: 399-416.

Stolle, D.F.E. 1995. A direct integration algorithm and the consequence of numerical stability. *Journal of Sound and Vibration,* 180(3): 513-518.

Symes, M.J., A. Gens, A. & Hight, D.W. 1988. Drained principal stress rotation in saturated sand. *Geotechnique*, 38(1): 59-81.

Ullidtz, P., Askegaard, V. & Sjølin, F.O. 1996. Normal Stresses in a Granular Material Under Falling Weight Deflectometer Loading. *Transportation Research Record 1540*, TRB, Washington, DC: 24-28.

Weller, W.A. & Kulhawy, F.H. 1982. Factors Affecting Stress Cell Measurements. *ASCE Journal of the Geotechnical Engineering Division*, 108(12): 1529-1548.

Wong, R.K.S. & Arthur, J.R.F. 1985. Induced and inherent anisotropy in sand. *Geotechnique*, 35(4): 471-481.

Wood, M.W. 1990. *Soil Behaviour and Critical State Soil Mechanics*. Cambridge University Press.

Yu, P. & Richart, F.E. 1984. Stress ratio effects on shear modulus of dry sands". *ASCE Journal of Geotechnical Engineering*, 110(3): 331-345.

Zienkiewicz, O.C. & Pande, G.N. 1977. Some useful forms of isotropic yield surfaces for soil and rock mechanics. Chapter 5 in *Numerical Methods in Geomechanics*. Edited by G.Gudehus. Wiley.

Zienkiewicz, O.C. & Taylor, R.L. 1989. *The Finite Element Method*. Vol. 1. 4th Edition. McGraw-Hill.

Zienkiewicz, O.C. & Taylor, R.L. 1991. *The Finite Element Method*. Vol. 2. 4th Edition. McGraw-Hill.